Technical University of Denmark

DTU

3D-SEM Metrology for Coordinate Measurements at the Nanometer Scale

Carli, Lorenzo; De Chiffre, Leonardo; Hansen, Hans Nørgaard; Horsewell, Andy; Dirscherl, Kai

Publication date:
2010

Link back to DTU Orbit

DTU Library
Technical Information Center of Denmark

Philosophiæ Doctor Thesis

3D-SEM Metrology for Coordinate Measurements at the Nanometer Scale

Lorenzo Carli

November 2010

Technical University of Denmark

Department of Mechanical Engineering

To my dearly beloved Valentina

"Perché ho bisogno della tua presenza,

per capire meglio la mia essenza".

"The worthwhile problems are the ones you can

really solve or help solve,

the ones you can really contribute something to..

No problem is too small or too trivial if we can

really do something about it".

Published in Perfectly Reasonable Deviations from

the Beaten Track: The Letters of Richard P. Feynman (2005).

iv

Preface

This thesis has been prepared as one of the requirements of the Ph.D. degree at the Technical University of Denmark (DTU), Department of Mechanical Engineering. The work was funded by the Technical University of Denmark and has been carried out from September 2007 to August 2010 under the supervision of Prof. Leonardo De Chiffre, Prof. Hans Nørgaard Hansen, Prof. Andy Horsewell, from the Department of Mechanical Engineering at DTU, and Dr. Kai Dirscherl from the Danish Fundamental Metrology Institute (DFM).

I would like to thank all my supervisors for their inspiration and contribution to my work. In particular I would like to express my gratitude to Prof. Leonardo De Chiffre for his great collaboration and for giving me the opportunity to carry out the Ph.D. programme at DTU. I strongly believe that opportunities I have been given during these three years of my Ph.D. have deeply affected my personality and broaden my perspective, apart of having increased my working skills and experiences. I would also like to express my heartfelt gratitude to Prof. Andy Horsewell, for the inspiring suggestions regarding the topics related to Scanning Electron Microscopy, to Dr. Kai Dirscherl for the fruitful discussions on the experimental results, especially regarding the uncertainty evaluation issues and to Prof. Hans Nørgaard Hansen for his highly valuable advices, not only related to the work itself.

I would like to extent my best thanks to my closest family, Giovanni, Chiara e Giulia, and to my girlfriend Valentina, who really helped me to keep my spirit up especially in the last period of the work. Without her love, support and inspiration all the efforts I put in this work would not have been feasible. We reached this goal together.

A consistent help was also received by other DTU employees, in particular Rene Sobiecki and Jakob Rasmussen, for the reference measurements performed at the Center for Geometrical Metrology (CGM) and A. Nicole MacDonald from DTU CEN (Center for Electron Nanoscopy) for the assistance when performing SEM measurements.

A part of the work presented in this Ph.D. has been carried out in collaboration with the NanoCMM (Universal and Flexible Coordinate Metrology for Micro and Nano Components Production, NMP- IP Project FP6-026717-2). This gave me the opportunity to broaden my knowledge and to meet many experts in this field of micro and nano-metrology.

Abstract (English)

The present work deals with a study concerning 3D-SEM metrology as a tool for coordinate measurements at the nanometer scale. The relevance of 3D-SEM, based on stereophotogrammetry technique, has been highlighted with respect to the other measuring instruments nowadays available and the main issues to be addressed concerning uncertainty evaluation have been discussed.

Most recent developments in the field of micro and nano-metrology, in terms of measuring machines and techniques, are described pointing out advantages and limitations. The importance of multi-sensor and multi-orientation strategy for geometrical reconstructions is discussed through an experimental example, together with point cloud stitching methodology and the currently used algorithms for feature extraction.

Theoretical basis of stereo-pair technique, based on two SEM images obtained by tilting the SEM stage of a desired amount, leading to 3D reconstructions, are given and the main phases involved in stereophotogrammetry technique are described underlying the most relevant error sources in the case of 2D and 3D-SEM metrology. An uncertainty evaluation has been thus carried out in accordance with ISO GUM, following a holistic approach, to quantify the influence of the different error sources on the stereo-pair reconstruction procedure. As a case study, a wire gauge with a known reference diameter has been employed. Although stereo-pairs are more commonly obtained trough a SEM stage tilting, a new methodology has been developed based on object rotations inside the SEM chamber, since the item under consideration had a cylindrical shape. This technique permits multi-orientation measurements enabling the reconstruction of the complete object geometry.

The main error sources considered, when performing 3D-SEM reconstructions, are point cloud processing and feature extraction, instrument setting parameters and image quality. Moreover, a comparison of the results obtained trough a theoretical and an experimental uncertainty evaluation of stereo-pair technique has been performed. All these effects have been quantified through a series of experimental investigations often based on the Design of Experiments (DOE) approach. A final uncertainty budget table has been produced for the case of multi-orientation reconstructions obtained by applying 3D-SEM technique to three cylindrical items: two reference wire gauges and a hypodermic needle.

In the last part of the work, the development and application of two novel multiple-step heights artefacts, intended for 3D-SEM calibration, is addressed. Experimental results of the different step-height values, measured from 3D-SEM reconstructions, are compared with the calibrated ones obtained from reference measurements performed by means of stylus profilometer and with measurements carried out using an Infinite Focus instrument.

Resumé (Dansk)

Afhandlingen vedrører den metrologiske anvendelse af tredimensional Scanning Electron Microscopy (3D-SEM) til koordinatmåling på nanometer skala. Relevansen af 3D-SEM, der baseres på stereofotogrammetri, fremhæves her i forhold til andre tilgængelige måleteknikker, og en række problemstillinger vedrørende måleusikkerhedsestimering diskuteres.

De nyeste udviklinger indenfor mikro- og nanometrologien, såvel maskiner som teknikker, beskrives i forhold til deres fordele og begrænsninger. Den vigtige anvendelse af multisensor- og multiorientering-teknikker for geometriske rekonstruktioner diskuteres på baggrund af et eksperimentelt eksempel. Ligeledes diskuteres metodologien i forbindelse med sammenstykning af punktskyer samt de nyeste algoritmer for uddragning af geometriske elementer.

Det teoretiske grundlag for stereopar-teknikken beskrives. Teknikken baseres på tredimensionale rekonstruktioner ud fra to billeder taget under en given vinkel opnået ved at tilte SEM-mikroskopets emneholder. De forskellige trin i stereofotogrammetrien beskrives, og de vigtigste fejlkilder behandles for både 2D- og 3D-SEM målinger. En usikkerhedsestimering foretages i overensstemmelse med ISO GUM, idet en holistisk tilgang anvendes til at kvantificere indflydelsen fra de forskellige fejlkilder på stereopar-rekonstruktionsproceduren. En kalibreret måletråd anvendes som praktisk eksempel. Medens stereopar-billeder almindeligvis opnås ved tiltning af emneholderen, præsenteres her en ny fremgangsmåde baseret på rotation af emnet i SEM-mikroskopets vakuumkammer, som er egnet for emner med cylindrisk form. Denne fremgangsmåde muliggør målinger ved multiorientering og derved rekonstruktion af hele emnets geometri.

De vigtigste fejlkilder, som identificeres og behandles i forbindelse med rekonstruktioner i 3D-SEM er: Sammenstykning af punktskyer, uddragning af geometriske elementer, indstilling af instrumentets parametre samt billedkvalitet. En sammenligning af resultater fra en teoretisk og en eksperimentel estimering af måleusikkerheden ved brug af stereopar-teknikken præsenteres. Fejlkildernes effekter kvantificeres gennem en række eksperimentelle undersøgelser gennemført ved anvendelse af statistisk forsøgsplanlægning (Design of Experiment – DOE).

I en opsamlingstabel præsenteres usikkerhedsbudgetter for rekonstruktioner efter multiorientering udført ved anvendelse af 3D-SEM på tre cylindriske emner: To forskellige måletråde og en hypodermisk nål.

I afhandlingens sidste del præsenteres arbejdet med fremstilling og anvendelse af en ny type multistep referenceemne for kalibrering af z-aksen i et 3D-SEM. Eksperimentelle resultater af de forskellige stephøjde-værdier opnået ud fra 3D-SEM rekonstruktioner sammenlignes med referenceværdier fra kalibrering ved brug af et sporbart tastinstrument samt med resultater fra et Infinite Focus instrument.

Table of contents

1 Background and objectives

1.1 Micro and nanotechnology scenario

Although studies in the field of biological systems, medicine, material science and chemistry have been in the nanometer regime for decades, the ability to image, manufacture and manipulate systems on the nanoscale is a recent achievement. Shrinkage of the device scale, from the macro to the micro and nano-world, has been pushed by an increasing economical and technological interest for many different kind of industries such as semiconductor, optoelectronic, biomedical and information technology. On the other hand, in the last years an exponential growth was observed in the ability to manipulate and assemble individual atoms, moving up from the atomic level (0.1 nm) to the 10-100 nanometer regime (Schattenburg *et al.*, 2001). The convergence of these two top-down and bottom-up approaches will soon lead to new discoveries in the different fields of applications of these technologies. Moreover this will create new challenges and issues to be solved. The word 'nanotechnology' was popularized in the 1980's by K. Eric Drexler when ideas such as building machines on the scale of molecules, motors, robot arms, and even whole computers, far smaller than a cell were discussed (Drexler, 1981). Therefore, nanotechnology, in its traditional sense, means building things from the bottom up, with atomic precision. This theoretical capability was envisioned as early as 1959 by the renowned physicist Richard Feynman (Feynman, 1960). Nevertheless, much of the activities carried out nowadays under the name 'nanotechnology' refers to different concepts and ideas, much different from the original meaning of the word. From a technological perspective, some define nanotechnology by simply requiring that a critical dimension (CD) of a structure is below 100 nm, even though, *a* control and restructuring of matter at the nanoscale is a necessary element (Roco, 2006). The development of the traditional scientific fields such as physics, biology and chemistry into nanoscience and technology can be seen in Fig.1.1.
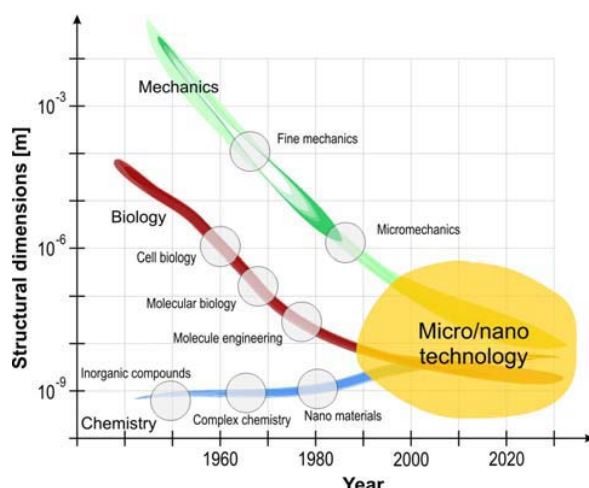
Figure 1.1. Overview on the development in the traditional scientific fields such as physics, biology and chemistry into nanoscience and technology (Hansen *et al.*, 2006).

In the next few years, nanotechnology will not only allow making many high-quality products at very low cost, but it will also allow making new nano-factories at the same low cost and at the same rapid speed. This unique ability to reproduce its own means of production is why nanotech is said to be an exponential technology (Drexler, 1992). Four generations of nanotechnology development has been described by (Roco, 2006; see Fig.1.2). Among the four different eras described there, human kind is currently facing the question of active nanostructures for multitasking, such as actuators, drug delivery devices, and sensors.
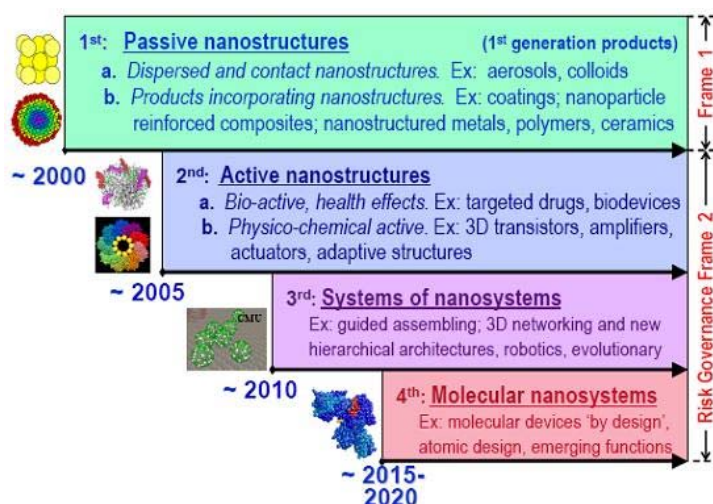
Figure 1.2. Description of the four generation nanotechnology developments as described by Roco (2006).

1.2 Challenges for micro and nanometrology

Metrology is an integral part of each step in the chain of development, through the run-in of production, purchasing and process control, down to the inspection of sold and purchased parts. If the metrology hardware and software exists, it is possible to define product specifications, measurement rules and standards for the manufactured parts. This means also that traceability can be established allowing instrument calibration and uncertainty evaluation. In Fig.1.3 a graph is shown where a number of different measuring instruments, nowadays available, are categorized based on dimensions of the part to be measured and on the resulting measuring uncertainty (Savio *et al.*, 2007). It can be noticed that, as part dimensions are scaled down, systems for micro and nanometrology should be employed if measuring uncertainties in the sub-micro range are desired. The task of reducing measuring uncertainty is more challenging when the geometrical complexity of objects is increasing. Nevertheless, the available technologies appear to be insufficient to fulfil this requirement. Furthermore, ISO (International Organization for Standardization) standards and measuring procedures have not been implemented yet for establishing traceability at the macro and nanoscale level.
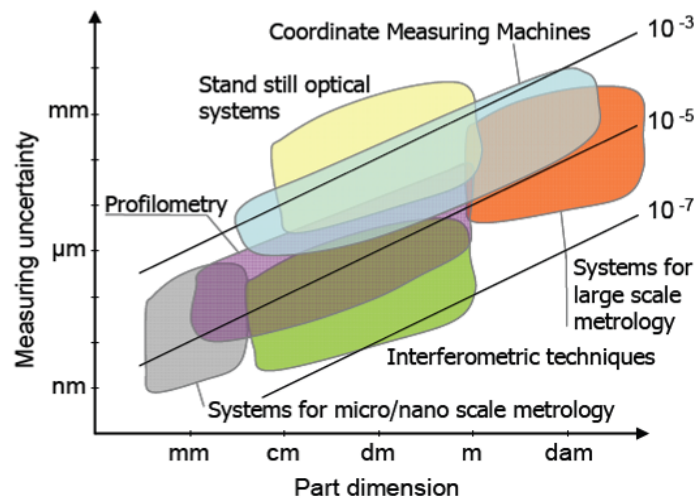
Figure 1.3. Graph showing a number of different measuring instruments, nowadays available, categorized based on dimensions of the part to be measured and on the resulting measuring uncertainty (Savio *et al.*, 2007).

Methods currently available for dimensional micro and nanometrology can be divided into the following categories (Hansen *et al.,* 2006):

- Technologies based on inteferometric solutions.
- Microtopography measuring instruments.
- Scanning electron microscopy.
- Micro and nano coordinate metrology.
- Other techniques.

The geometrical and structural complexity of an object to be measured can be estimated based on the characteristics of its features. For this reason, the methods for micro and nanometrology can be classified based on their measuring capabilities. Instruments capable of measuring features with aspect ratios below 1, are usually called 2D techniques. Measurement of features with aspect ratios of one or more is referred to as 2½D. Measurement of undercuts, free-forms or features within cavities, are described as 3D measurement tasks (Hansen *et al.*, 2006). A classification of the above mentioned equipments, based on their measuring capabilities, with regards to the geometrical and structural complexity, is shown in Fig. 1.4.
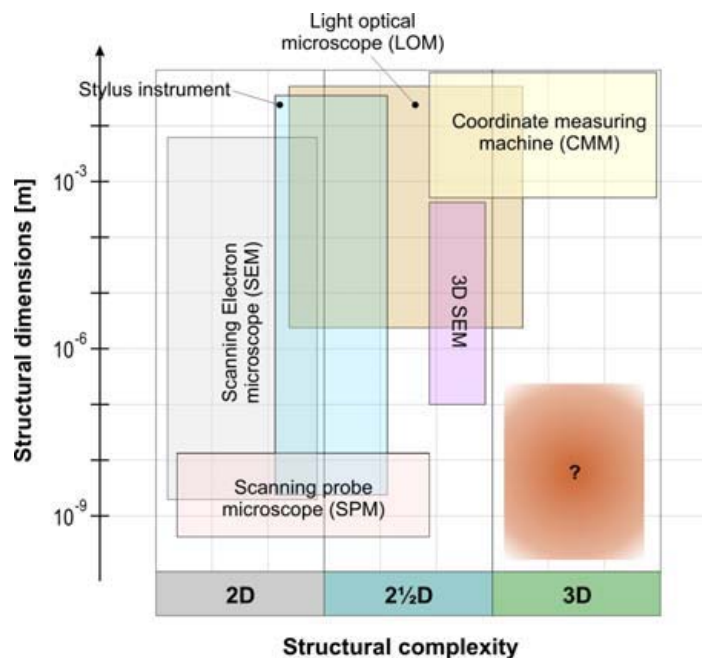
Figure 1.4. Classification of different instruments based on their measuring capabilities, with regards to the geometrical and structural complexity (2D, 2½D or 3D; Hansen *et al.*, 2006).

A recent study of the German VDI Technology Centre led to the following conclusion:

"… between 1996 and 2003, the world market for micro-systems grew from $ 14 billion to $US 50 billion. It is expected to have risen again to $US 68 billion by 2005. Longer-range estimates for the period up to 2010 predict continued growth in the markets for micro-engineered products, to a total volume of over $US 200 billion".

Moreover, a Nexus Market Analysis forecast that the MST (Microsystems Technologies) market will grow at a rate of 20% *per annum* at least until 2010. Therefore, since micro and nanotechnologies rely on the availability of micro and nanometrology, attributing just a 5-10% of their economical value to metrology would mean a tremendous potential, based on the above mentioned numbers. A number of new measuring tasks, arising from such micro-components, should serve as inspiration for developing new measuring strategies and technique leading to fully developed 3D metrology systems at the micro and nanometre scale. Moreover, current traceability gaps need to be fulfilled by means of newly developed ISO standards and calibration artefacts. These are some of the tasks of the NanoCMM European Project in which the author has also been involved (Project FP6-026717-2, "Universal and Flexible Coordinate Metrology for Micro and Nano Components Production").

1.3 Three-dimensional Scanning Electron Microscope metrology

Scanning Electron Microscopy (SEM) has some unique properties that, combined together, are not matched by any other microscopy technique. SEM is a multi-scale technique which allows image ranges from 1 mm² down to 1 μm² with an ultimate resolution as small as about 1 nm (at high magnifications), comparable to Scanning Probe Microscopes. Other unique capabilities are the large depth of field (i.e. the area in an image from front to back that is in focus) and the long working distance usable which allows development of measuring strategies based on multiple positioning (Marinello *et al.*, 2008a).

In Lonardo *et al.* (2002), the relevance of a true 3D characterization of surface topography, was pointed out. It is claimed that one of the difficulties posed by non-conventional surfaces, is the measurement of the relevant features. Contact probing is often impossible due to the lack of accessibility and to the steep slopes where optical techniques encounter problems created by the reflectivity and Atomic Force Microscopy (AFM) which suffers from measuring range limitations. Furthermore, current techniques are not fully 3D but somewhat less than 2½D, meaning by this, that only portions of the surface, with respect to the third dimension, can be accessed and characterized. Regarding this particular issue SEM seems to be a very promising technique with respect to measuring surfaces having high aspect ratios. Many application areas are foreseen specifically for this technique such as the semiconductor industry, life sciences, materials research and many industrial fields related to nanotechnology. Furthermore another possible use is for Nanoscale Sample Preparation and Modification using Dual Beam techniques, which combines a field emission SEM column with a gallium source focused ion beam (FIB) column (Lawrence, 2006). Nevertheless, many developments are still needed in order to transform SEM into a technique where the complete topography can be determined by a truly 3D characterization of the surface, developing metrologically correct techniques and producing traceable measurement results. In fact, although SEM images have a striking three dimensional appearance, they are in fact purely two dimensional, as they are built up by sensing intensity variations revealed when an electron beam is scanned over the specimen surface (secondary emission detection). A possible way to overcome these limitations is to use SEM in conjunction with image processing from stereographs (Sato, 1990). This method, called 3D-SEM technique, is based on photogrammetry and allows reconstructing the third dimension of surface features.

The stereophotogrammetry technique has been extensively studied (Boyde, 1973; Hillmann, 1980; Kolednik, 1981; Schubert *et al.*, 1996; Scherer, 2002) starting from the theoretical description, applied to Scanning Electron Microscopy, given by Piazzesi (1973). Some other authors (Bariani, 2005; Marinello *et al.*, 2008b) have already discussed the influence of various factors on reconstruction accuracy divided into two main classes of variables: the first one related to the measurement operation and the instrument set-up and the second concerning the quality of scanned images and software reconstruction. In this work the error sources belonging to both classes of variables were considered when performing uncertainty evaluation of 3D-SEM technique.

1.4 Problem identification

This work deals with an investigation concerning three dimensional Scanning Electron Microscopy (3D-SEM) for coordinate measurements at the nanometer scale. A number of issues must be addressed when performing stereophotogrammetry technique, to obtain 3D reconstructions of a given object's geometry. These issues are listed here, referring to the chapters of this thesis where they have been discussed:

➢ The 3D reconstructions performed using stereophotogrammetry technique, result typically in a very dense point cloud. Thus, a number of point cloud processing operations, such as trimming, outliers removal and filtering, are needed before carrying out feature extraction and measurements. The main problem to be faced in this case is that there is still a lack of standards prescribing how to perform these point cloud processing operations. As a consequence, different software for point cloud processing and feature extraction implements diverse algorithms, leading to results which are not always directly comparable. The point cloud processing operations are described in <u>chapter 4</u> through an example based on 3D-SEM reconstructions of a wire gauge with a known reference diameter. Moreover, three different software performing feature extraction and measurements are tested in <u>chapter 8</u>.

➢ When employing 3D-SEM technique a number of influencing factors are playing a relevant role, as discussed in the previous section. Among these, the quality of the images composing the stereo-pair, the instrument setting parameters and the measuring procedure have to be considered as uncertainty contributors when performing the uncertainty budget.

These topics are discussed in chapters 5 and 6, while the final uncertainty budget, for 3D-SEM reconstructions, has been produced in chapter 8, based on a case study regarding three cylindrical items.

➢ For a given measuring task, the uncertainty related to stereophotogrammetry technique has to be evaluated from a theoretical and experimental point of view. This can be made by applying ISO standards currently available, such as the Procedure for Uncertainty Management (PUMA) (ISO 14253-2:1999) and the Guide to the expression of Uncertainty in Measurement (GUM) (JCGM - Joint Committee for Guides in Metrology- 100100:2008). The former is from 1999 and an updated version is currently under development, while the latter has been recently revised (2008). The theoretical bases of stereophotogrammetry technique are given in chapter 3, where the SEM working principle is also described. Moreover, a theoretical and an experimental investigation of stereo-pair technique have been carried out in chapter 7, based on the case of a cylindrical item, tilted or rotated inside the SEM chamber, to perform 3D reconstructions.

➢ The z-coordinate calibration in SEM is a crucial issue to establish measurement traceability. Nevertheless, none or few reference artefacts are nowadays available for calibration and performance verification of 3D-SEM technique (Bariani *et al.*, 2005). Moreover, the possibility to perform the vertical elevation calibration at different magnifications and different working distances is also a desirable prerequisite. This requirement can be fulfilled, for instance, by means of multiple-step heights geometries. The main limitation of the currently available calibration artefacts is that, they typically require artefact relocation when different heights have to be measured. The fabrication and application of two novel artefacts, for 3D-SEM calibration, is described in chapter 9.

Besides chapters 3 to 9, addressing issues specifically related to 3D-SEM technique, chapters 1 and 2 deals with the following topics:

Chapter 1 consists of an overview on the current micro and nano technology scenario, followed by a description of the main challenges for micro and nano metrology. The relevance of 3D-SEM technique, as a tool for coordinate metrology at the nanoscale level, is highlighted and the main issues to be addressed, when performing this technique, are described.

Chapter 2 deals with the interaction of different probes with objects to be measured, describing the main advantages and limitations of these measuring techniques. Moreover, a number of measuring strategies and procedures, currently under development to decrease measuring uncertainty, are described. In particular multi-sensor and multi-orientation measuring strategies are addressed together with the issues of point cloud stitching and feature extraction at the micro and nano-level.

References

Bariani P, De Chiffre L, Hansen HN, Horsewell A. Investigation on the traceability of three-dimensional scanning electron microscope measurements based on the stereo-pair technique. *Precis. Eng.* 2005; **29**: 219-228.

Boyde A. Quantitative photogrammetric analysis and qualitative stereoscopic analysis of SEM images. *J. Micros.* 1973; **98**: 452-71.

Drexler KE. Molecular engineering: An approach to the development of general capabilities for molecular manipulation. *Proc. Natl. Acad. Sci. USA* 1981; **78/9**: 5275-5278.

Drexler KE. Nanosystems: Molecular Machinery, Manufacturing, and Computation**.** 1st edition, Wiley, 1992.

Feynman RP. There's plenty of room at the bottom. *Engineering and Science* (Caltech) 1960; **23/5:** 22-36.

Foucher J, Ernst T, Pargon E, Martin M. Critical dimension metrology: perspectives and future trends 3D-metrology is becoming mandatory for nanofabrication in the production environment. *Proc. SPIE* 2008; DOI: 10.1117/2.1200811.1345.

Hansen HN, Carneiro K, Haitjema H, De Chiffre L. Dimensional Micro and Nano Metrology. *CIRP Annals - Manufacturing Technology* - 2006; **55/2**: 721-743.

Hillmann W. Rauheitsmessung mit dem Raster – Elektronenmikroskop (REM). In: *Technisches Messen tm*, 1980; V 9116-6.

ISO 14253-2:1999. Geometrical Product Specifications (GPS) - Inspection by measurement of workpieces and measuring equipment -- Part 2: Guide to the estimation of uncertainty in GPS measurement, in calibration of measuring equipment and in product verification, ISO, 1999.

JCGM (Joint Committee for Guides in Metrology)100:2008. Evaluation of measurement data - Guide to the expression of uncertainty in measurement (GUM), 2008.

Kolednik O. A Contribution to Stereo-photogrammetry with the Scanning Electron Microscope. *Prakt. Metallogr.* 1981; **18**: 562-73.

Lawrence P. The Dualbeam (FIB/SEM) and its Applications - Nanoscale Sample Preparation and Modification. *Proc. of the Vacuum Nanoelectronics Conference,* China, 2006; 127-128.

Lonardo PM, Lucca D, De Chiffre L. Emerging Trends in Surface Metrology. *CIRP Annals* 2002; **51**: 701-723.

Marinello F, Carmignato S, Savio E, Bariani P, Carli L, Horsewell A, De Chiffre L. Metrological performance of SEM 3D techniques. *Proc. of 18th IMEKO TC 2 Symposium on Photonics in Measurements*, Prague, 2008a.

Marinello F, Bariani P, Savio E, Horsewell A, De Chiffre L. Critical factors in SEM 3D stereo microscopy. *Meas. Sci. Technol.* 2008b; **19;** 065705.

Piazzesi G. Photogrammetry with the scanning electron microscope. *J. Phys. D Appl. Phys.* 1973; **6/4**: 392-396.

Roco M. Nanotechnology social implications. 1st edition, Hardcover, 2006.

Sato H. A way to measurement for submicron meter: surface profile by scanning electron microscopy. *Proc. of Manufacturing Intern.* 1990; Book NO H0580C, ASME: 63-73.

Savio E, De Chiffre L, Schmitt R. Metrology of freeform shaped parts. *CIRP ANNALS.* 2007; **56/2**: 810-835.

Schattenburg ML, Smith HI. The critical role of metrology in nanotechnology. *Proc. SPIE* **4608**, *Nanostructure Science, Metrology, and Technology*, eds. Peckerar MC Postek MT, Jr. (SPIE, Bellingham, WA), 2001, **116-124**. (*CSR Reprint 01-105*).

Scherer S. 3D Surface Analysis in Scanning Electron Microscopy. *G.I.T Imaging and Microscopy* 3/2002: 45-46.

Schubert M, Gleichmann A, Hemmleb M, Albertz J, Köhler JM. Determination of the height of a microstructure sample by a SEM with a conventional and a digital photogrammetric method. *Ultramicroscopy* 1996; **63**: 57-64.

2 Coordinate metrology at the micro and nanoscale level

2.1 Introduction

A new generation Coordinate Metrology Machine (CMM) should be capable of measuring the majority of geometrical features of micro and nano parts and of systems assembled from such parts. This particularly means the ability to measure inside holes and gaps, on steep slopes, and behind obstructions. In order to fulfil this task, this CMM should have a very small effective probe tip, meaning a "structural resolution" and the flexibility to rotate the object and/or the probe in order to enter holes and gaps. Pursuing this defined project goal, a number of identified technologies are still lacking and their development falls within the parameters of the NanoCMM project (EU FP6, 2006). One of the tasks is therefore to develop a number of different complementary probe systems, not existing in the required form so far, in order to cover the different micro- and nano-applications. This takes into account the fact that applications might differ in point density required, uncertainty required, probe tip size required (*i.e.* size of structures to be measured), accessibility of the features, and object surface properties. This set of probes can be divided into two different classes: <u>tactile probes</u>, *i.e.* SPMs and 3D-tactile probes and <u>optical point and area probes</u>, *i.e.* White Light Interferometers and Confocal Microscopes. This chapter deals with the interaction of such kinds of different probes with objects to be measured, describing the main advantages and limitations of these measuring techniques. Moreover, a number of measuring strategies and procedures, currently under development to improve measuring uncertainty of the tactile and optical probes, are described. In particular multi-sensor and multi-orientation measuring strategies are provided together with the issues of feature extraction at the microscale and point cloud stitching. Regarding the latest, the main software and hardware solutions, in terms of the use of fiducial marks as external reference, will be presented and discussed in detail.

2.2 Probe-object interaction

Significant problems arise when measurements are performed on objects at the micro and nanoscale using conventional measuring techniques. In almost all the cases, the probing system is the limiting factor of the measurement; either it is not possible to access the feature (main challenge for optical and SPM systems), or the forces associated with tactile CMM-like probes, which can damage or destroy the surface or the feature. Although there is a wide range of probing systems used for nanoscale metrology tools, generally these are not suitable for measuring three-dimensional features. Most of the probing systems intended for measurements of micro-size features are miniaturizations of relatively conventional CMM probes or microscopy techniques being enhanced for 3D capability and better repeatability, giving the possibility of accurate calibration (Weckenmann *et al.*, 2004). Measuring systems use a wide range of physical phenomena to match the needs of specific measuring tasks. These must be compared to the requirements which can be derived from the categories of part dimension, shape complexity, surface conditions and material properties (see Table 2.1). In fact, more than simply understanding the underlying physical phenomena during the measuring process, it is important to comprehend the restrictions and boundary conditions for evaluating a geometric feature and the interaction of the specimens' properties with the measuring instrument; *e.g.* bandwidth-limiting and thus resolution decreasing effects whilst scanning a feature with a high shape complexity (Savio *et al.*, 2007). Resolution and range of some techniques for surface topography analysis are shown in Table 2.1. In the diagram of Fig.2.1, the vertical and horizontal resolution achievable with different instruments for surface topography measurements are shown.

Instrument	Vertical axis		Horizontal axes	
	Resolution/nm	Range/mm	Resolution/nm	Range/mm
Stylus	<1	10	2000	>100
Confocal	0.1	1	200	>100
WLI	0.1	1	500	<10
AFM	<0.1	0.01	1	0.1
WLI White Light Interferometry AFM Atomic Force Microscopy				

Table 2.1. Resolution and range of some techniques for surface topography analysis.
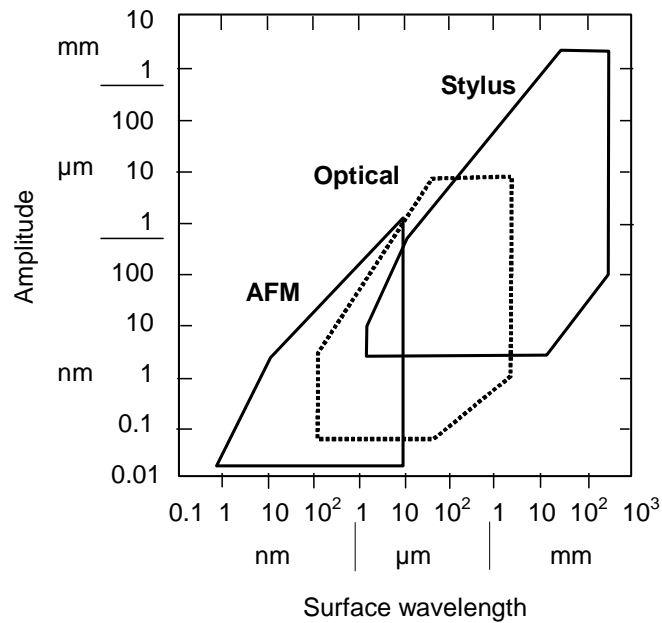
Figure 2.1. Diagram showing the vertical and horizontal resolution achievable with different instruments for surface topography measurements, after Stedman (1987).

	Tactile measuring instruments		Optical measuring instruments	
	μ-probe	*AFM*	*WLI*	*Confocal*
Part dimensions				
Macro (mm)	Optimal instrument choice depends on the desired vertical and horizontal resolution of the measurements. Additional information is given in Fig. 2.1 and Table 2.1.			
Micro (μm)				
Nano (nm)				
Material				
Metal	Soft material suffers from indentation problems when scanned by tactile probes while polymer exhibits light absorption phenomena when scanned with optical probes.			
Ceramic				
Polymer				
Surface				
Rough	Tactile techniques are preferable for investigating surface roughness because a mechanical interaction takes place.			
Smooth				
Geometry and features				
Free-form	Both tactile and optical systems are limited when measuring slopes or undercuts. Object multi-positioning is a potential way to overcome these limitations, but many issues still need to be solved.			
Random				
Undercuts / slopes				
External factors				
Noise and vibrations	By measuring at the room conditions with controlled temperature and humidity these influencing factors can be partially avoided or compensated. Noise and vibrations are critical for tactile measurements since they can contaminate the probe or affect surface estimations.			
Temperature				
Humidity				
Dust				
Object				
Mechanical behaviour	Wear and friction of probe or surfaces often occur when measuring with tactile probes. Optical surface behaviour is instead relevant when optical measurements are performed.			
Tribological behaviour				
Thermal behaviour				
Optical behaviour				

Table 2.2. Classification of probes, object characteristics and their interactions.

2.2.1 Probes description and classification

Contact measuring techniques require physical accessibility for the probing unit. Moreover when contact measuring methods are applied to objects having feature sizes of 200 μm or smaller, the contact forces are not negligible anymore and could produce significant tool deflection, which would affect the measurement results. The finiteness of the dimensions of the probing unit, and thereby the value of the tip radius and tip cone angle, also limits the reliability of contact measuring methods, since this implies that the contact point on the probing unit is not maintained constantly during the measuring path. Among the non contact methods, optical techniques are commonly applied in dimensional metrology. However, accessibility is still a problem even with optical methods. The main advantages and disadvantages of the optical methods are here listed.

General advantages of the optical methods:

1 Capability to measure 2D patterns (*e.g.* plates in the offset industry, printed circuits, cross sections of cables, network on metal etc.);

2 Non contact methods; in this way the risk of probable deformation is eliminated. In contact probing the stylus might scratch the object. Special applications regarding soft materials (*e.g.* plastic, rubber, textiles, wax, paper etc.), workpieces with hygienic requirements (*e.g.* parts for injection needles etc.) and markings on specimens of glass (*e.g.* scales, glass rulers etc.);

3 The possibility of reaching difficult points, especially when the measuring object has very small dimensions. Using contact probes it is difficult to reach every point of the surface due, for example, to recesses and/or protrusions of surface shape (*e.g.* small holes, nozzles, threads, etc.; Piron, 2003);

4 Acquisition of more data in less time.

General disadvantages of the optical methods comprehend:

1 Difficulties in measuring deep cavities or pores;

2 Limitation of the working distance (distance between the sample surface and the objective lens);

3 The quality of the lenses, in terms of distortions, spherical aberration and astigmatism, influences the measuring process;

4 Chemical and physical characteristics of the object's surface play a relevant role, thus they have to be taken into account when planning measurements by means of optical instruments.

In Table 2.3 the instruments analyzed are: Atomic Force Microscope belonging to the contact measuring methods, the Confocal Microscope and the White Light Interferometer belonging to the optical ones.

Probe	Advantages in measuring micro-objects:	Disadvantages in measuring micro-objects:
Atomic Force Microscope (AFM)	• nanometres / sub nanometres resolution. • easy sample preparation. • accurate height information. • works in vacuum, air and liquids.	• slow method. • limited lateral (~150 μm) and vertical ranges (~15 μm). • data dependent on the tip size and geometry. • tip or sample can be damaged.
Confocal Microscope	• Sharper images and hence better resolution than conventional methods. • By scanning many thin sections through your sample, a very clean three-dimensional image of the sample can build up.	• The speed which an image with a given signal-to noise ratio can be acquired is quite slow. • Limited lateral resolution in some commercially available instruments. • Limited vertical resolution in some commercially available instruments. • The best horizontal resolution of a confocal microscope is about 0.2 μm, and the best vertical resolution is about 0.5 μm. • Maximum detectable slope up to 75°.
White Light Interferometer (WLI)	• Fast method. • Resolution up to 1 nm. • Measurement range ≤ 100 μm. • High vertical resolving power (down to 0,1 nm).	• Limited lateral resolution (worse than 0,3 μm). • Maximum detectable slope up to about 30°.

Table 2.3. Summary of the main advantages and disadvantages when using different tactile and optical probes for measuring micro objects. In particular Atomic Force Microscope, belonging to the contact measuring methods, and the Confocal Microscope and the White Light Interferometer belonging to the optical ones were considered for comparison.

More information about the measuring techniques described in Table 2.3 can be found in (Wilkening, 2006; Carli, 2007; Schwenke, 2002; Bining, 1986). Nowadays small ultra-precision CMM are developed to achieve measurements of micro and nano parts. They are typically characterized by a working volume of less than 100 mm and uncertainties less than 0,2 µm. Nevertheless, issues to be solved still persist such as their measuring accuracy and the probe size. In Table 2.4 a comparison between conventional and small ultra-precision CMM is given. Weckenmann *et al.* (2004) reported a series of probing systems which are typically used with tip balls between 1 mm and 0.1 mm diameter and stem lengths of a few millimetres. The achievable probing reproducibility with these probing systems can reach down to a few nanometres depending on stylus, measurement task, material and surface characteristics of the specimen and environmental conditions such as cleanliness and temperature constancy. In Table 2.5 the probes presented in the above mentioned paper are compared according to some main characteristics.

	CONVENTIONAL CMM	Small ultra-precision CMM
Size of machine [mm^3]	2000	200
Weight [kg]	1000	10
Measuring range [mm^3]	10^9	10
Resolution [nm]	1000	10
Accuracy [nm]	5000	50
Probe diameter [µm]	5000	50
Measuring force [N]	10^{-1}	10^{-3}
Accuracy of scales [nm]	1000	10

Table 2.4. Specifications of small ultra-precision CMM (Bariani, 2005).

	TUE Micro-probe	NPL Micro-probe	METAS 3D Micro-probe	PTB/Werth Fiber probe
Resolution	1 nm	3 nm	< 1 nm	0.1 μm
Measuring Range	25 μm	± 20 μm	± 100 μm	± 0.4 mm
Stiffness	100 N/m – 450 N/m	10 N/m	20 N/m	0.1 N/m
Moving mass	20 mg	370 mg	7000 mg	< 1mg
Probing force	< 1 mN	0.2 mN	0.5 mN (dynamic)	Few μN

Table 2.5. Comparison among small and ultra-precision CMM (Weckenmann, 2004).

A classification of reviewed methods is attempted in Table 2.6. Instrumentation suitable for measurements of features, with aspect ratios below 1, is referred to as 2D techniques. Therefore the measuring tasks will be referred to as a 2D measurement tasks. Measurements of features with aspect ratios of 1 or bigger are referred to as 2½D, while detection of undercuts, or features within cavities is described as 3D tasks. CD indicates the critical dimension that is the smaller dimension, which is to be measured. Regarding probing systems for micro and nano components there is already a large variety of them available on the market but none can fulfil all the required tasks satisfactorily.

	2D	**2½D**	**3D**
Mesoscale 0,5 mm < CD < 10mm	Surface topography measuring instruments	Small ultra-precision CMMs	
Microscale 100 μm < CD < 0,5 μm		WLI Confocal	Small ultra-precision CMMs
Nanoscale CD > 100 nm	AFM	μCMMs	

Table 2.6. Instrument classification table adapted from (Bariani, 2005).

Because of the differing measuring capabilities of the probing principles, in micro- and nanometrology today, only a sophisticated combination of several probing systems seems to be adequate for quality assurance. The way to multisensorics nanometrology still poses a lot of challenges arising from insufficient compatibility of the results of different probing systems and from the lack of calibration artefacts being measurable in the variety of the existing probing systems. Nowadays three of the main producers of μCMMs in Europe, are SIOS Meßtechnik GmbH (Ilmenau, Germany), IBS Precision Engineering (Eindhoven, The Netherlands), both partners of the NanoCMM European Project, and Carl Zeiss (Oberkochen, Germany). The characteristics of their last generation μCMMs are summarized in Table 2.7 to allow capabilities comparison.

	SIOS	**IBS**	**ZEISS**
Machine	NMM1	ISARA 400	F25
Measuring volume XYZ [mm]	25 x 25 x 5	400 x 400 x100	100 x 100 x 100 (touch and optical)
Uncertainty of measurement	0.1 nm resolution (not further details available)	100nm in the 3D space	250 nm at a resolution of 7.5 nm
Tactile sensor	- AFM sensor head - 3D-Microprobe (GannenXP)	- Yes, own design - AFM possible	Sensitive 3D micro-stylus for stylus diameters of 50 – 500 μm and stylus tip diameters of 100 – 700 μm.
Optical sensor	Fix-focus sensor and white light interferometer	Yes	ViSCAN camera sensor based
Multi directional measurements	Yes	Yes	Information not available
Rotary table	Yes in future	Yes in future	Information not available

Table 2.7. Main characteristics comparison for the last generation μCMMs produced by SIOS Meßtechnik GmbH, IBS Precision Engineering and Carl Zeiss.

2.3   Multi-sensor   and   multi-orientation   strategies   for   geometrical reconstructions

Complete 3D characterisation of micro components, with measurement of dimensions, form and surface topography, cannot find a solution in a single sensor instrument. An effective approach should involve multiple view measurements (integration of sensor with linear and rotational displacement stages) as well as multiple probing measurements (integration of several sensors for probing different areas on the same part). Both multiple views and multiple probing are performed through a repositioning of the sensor relatively to the sample. Because the measurement of some parts will require both multi-sensor and multi-directional measurement, it is necessary to facilitate methods and algorithms to combine sub-point clouds of the measured object in one common coordinate system to describe the entire object.

Generally speaking, three different approaches can be envisaged for multiple view and multiple probe measurements, depending on the references used to relate the different sub-measurement sets to each other and with the object coordinate system:

1. Positioning system as reference. Information about the work piece position in space is used to connect the acquired surface points. This approach is typical of conventional CMMs. High accuracy is achieved through the use of computer correction of systematic geometrical errors in the machine movements.

2. External reference. Fiducial elements, *e.g.* spheres that are fixed relatively to the workpiece, allow generation of a reference coordinate system. This approach provides very high accuracy but requires access to probing workpiece and fiducial elements during the same measurement (see section 2.4.1).

3. Workpiece as reference. Features on the workpiece, e.g. texture details, are identified to provide stitching of the acquired surface points. This approach is used, *e.g.*, in SEM-stereo-photogrammetry and in the AFM-CMM (Bariani, 2005; Marinello, 2007; Marinello *et al.*, 2007). Very high accuracy can be achieved provided that the workpiece contains clearly identifiable details (see section 2.4.2).

Methods 2 and 3 could be suitable for an approach at a microscale level. A method based on the workpiece as a reference may eventually fail if the identifiable details can not be identified in 3D with sufficient accuracy by using merely 1D-accurate probes.

In the NanoCMM European Project, for instance, the approach based on external references was chosen and implemented. The use of fiducial marks seems to be preferable in the case of axial-symmetric workpieces to be measured but it requires the positioning of these fiducial elements on the workpiece itself or on the fixturing stage.

When calculating the surface of the object as a best fit of all measured points, the uncertainty must be taken into account. In general it will be necessary to define the data set describing a probing point in a much more complex way than done today. Some elements have to be taken into account:

1. Different from computer tomography and photogrammetry – there is only one high resolution direction, not two. Thus the object topography influences significantly the quality of the results;

2. The measurement of an object located in the working space of the μCMM will not always be possible from the direction that shows the lowest uncertainty. The measured piece may contain "hidden" points where the probe cannot access. Therefore, it will be necessary to turn the measured piece. By adding further degrees of freedom, through a rotary stage, the uncertainty of measurement will increase.
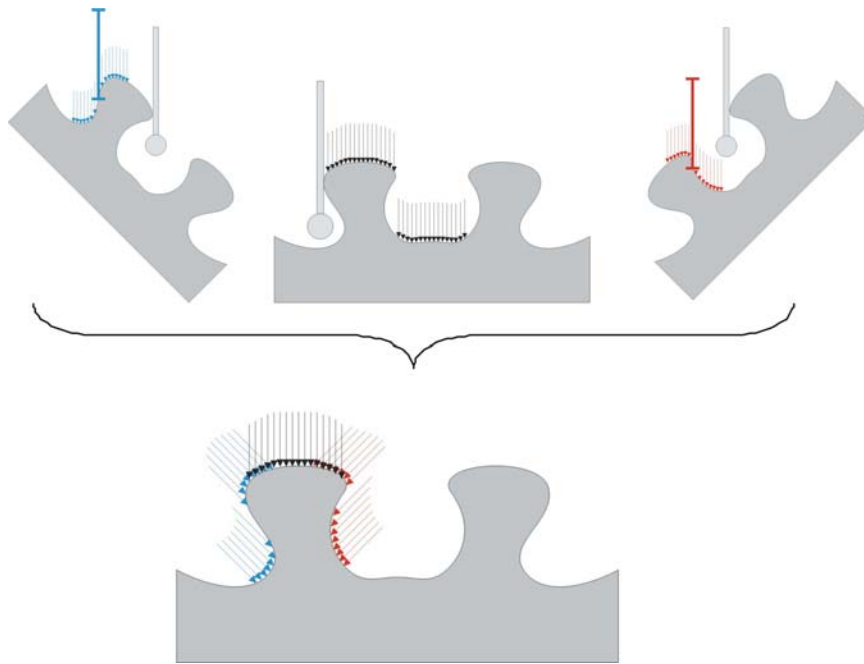
Figure 2.2. Example of probing in the direction showing the minimum uncertainty and the resulting combined uncertainty (source: Dr. Eugen Trapet, ISM3D, Gijón, Spain).

The task is to reconstruct the actual geometry of a surface on the object with the lowest possible uncertainty using stitching techniques based on clouds of points. The object rotations and the directional sensitivity of the probes contribute to increase the uncertainty. A list of the tools that can be applied to achieve low uncertainties can be produced. A general solution encompasses the use of:

- Theoretical model (CAD);

- Reference elements;

- Multiple probing (probe changer) and Multiple viewing (positioning by rotations and translations);

- Stitching (best fit, cross correlation etc.);

- Probe calibration (optical fiber, optical flat etc.);

- Scanning strategy;

- Simulation (Monte Carlo etc.);

- Data Filtering and Modelling (polynomial fitting etc.);

- Substitution.

2.4 Point cloud stitching

Some measuring systems are not able to measure the complete surface of interest in one single setup, due to intrinsic limitations of the measuring principle and for practical and economical reasons. When a single setup is not sufficient, multiple measurement views are taken with the part placed in different orientations in front of the measuring system, or vice versa. The relative alignment of data points measured in multiple orientations is a process called registration (Vàrady *et al.*, 1997). Registration of multiple views is based on the overlapping of measured information and different approaches have been proposed.

- <u>Hardware solutions</u> based on multiple sensors or accurate rotating/ positioning systems is one possibility, although the cost increase may not be acceptable for some applications. An alternative simple solution is to add some reference objects (*e.g.* spheres or other targets) in such a way that at least some of them are measured in each view; the registration in then based on the measured position of the added reference objects;

- Many <u>software solutions</u> have been proposed for the registration of the multiple views on the basis of overlapping measured data only, with and without use of the nominal geometry as a reference (CAD based). This approach is very popular in computer graphics literature, where accuracy is not critically restricted.

In the following sections the main hardware and software solutions will be discussed and presented in more details.

2.4.1 Stitching based on fiducial marks as external reference

The method to create artificial reference points in order to stitch together partial measurements of an object is, in principle, nothing new, it is called "leap-frogging". This method is much used in the classical metrology of large parts with theodolites, laser trackers and articulated arm CMMs. Here, frequently, reference spheres are glued to the object in order to transfer the coordinate system with high accuracy from one measurement to another when the measuring device must be moved between measurements to gain access to all features of the (large) object to be measured (with a too small measuring instrument). Note that often the object coordinate system can not be measured in all positions of the measuring system. This is a typical case where the reference elements method can be applied.

The fiducial mark method eliminates the rotary axes from the uncertainty budget. It also establishes the relationship of different probes with the work piece coordinate system, provided that this work piece coordinate system has been referenced against the fiducial marks.

The fiducial mark system works well if measurement with real 3D probes and with sufficiently accurate fiducial marks (*e.g.* using tactile micro probes with spherical tips) carried out. The work piece coordinate system is established with the same accuracy for each new probe and for each new rotary position, independent of the angle of rotation and independent of the probe used. Stitching is trivial as all point coordinates are equally valid coordinates.

However, as soon as sensors which lack resolution and accuracy in certain directions (as optical probes do) are employed, this system fails, as the different "views" can not be fitted or stitched together in 3D anymore without loss of accuracy. The same happens if the object surface itself is used for the stitching, in any case the sensor does not establish a "lateral" relationship with sufficient accuracy. In some cases a probe may very well be able to measure certain parts of the work piece surface, but these parts of the object surface may have overly large inclinations to achieve a small uncertainty. Optical point probes were reported to have a very high accuracy, *e.g.* sub-nanometre, in Z-direction (axial direction) and to be substantially worse for inclined surfaces. The reason for this described anisotropic behaviour of high accuracy optical point probes is, in most cases, simply because of the diffraction limit of the light spot projected on the surface or because of the resolution limit of the imaging optics. Hence techniques shall be developed to use all micro probes on the same CMM in the same reference coordinate system, one after the other. Thus different features on the same work piece can be measured each related to the other, or to the same feature measured with different probes for reasons of access, where the object can be precisely localized with one probe and measured then with a higher resolving probe; this in itself, being not so suited to first time localization of the object due to its small field of view. Note that in classical metrology, the referencing of probes, one to another on a reference sphere is a common technique, but in micro metrology this first requires the development of micro- reference marks to be placed on the object holder.

These fiducial marks must be equally measurable with all different probes from different directions. Different kinds of spheres are available, each of them with different dimensional qualities or characteristics (sphericity, thermal expansion coefficient, radii, hardness, density, relative abrasion resistance, optical refraction, etc). Some of them are shown in Fig.2.3:
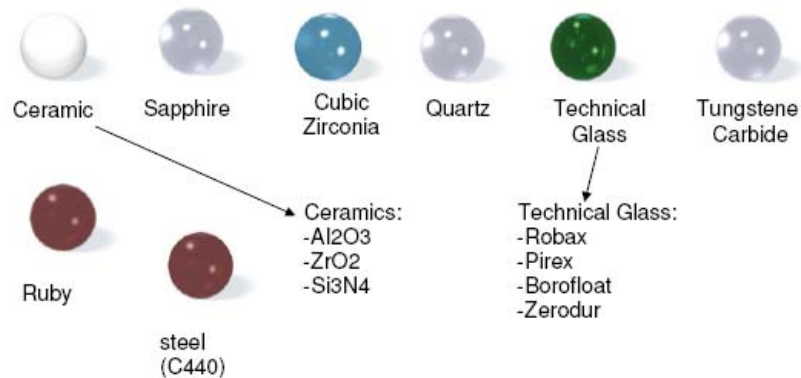
Figure 2.3. Different kind of spheres available on the market, to be used as fiducially elements (provided from different manufacturers).

The geometry selected for such fiducial marks are based on natural forms, such as spheres or flat prisms. Different materials are available for such fiducial marking types. Ceramic can be selected as a suitable material for the spheres in order to achieve grade 1 accuracy. On the other hand, silicon is a suitable material for the prisms. The base plate can be made of Zerodour or Robax which can be polished to a very high accuracy and have a nearly-zero thermal expansion with 3D homogeneity.

An example of solving the anisotropic uncertainty and limited measurable surface slope problems using spheres as reference elements is shown in Fig.2.4. Tilting and rotations of the sample can help to overcome measurements difficulties. Ideally a measurement should be always carried out orthogonally (normally) to the object surface, but this is not possible in practice. Thus, different measuring uncertainties derive from the diverse measuring directions. The problem is expected to be different for mono-dimensional optical or tactile probes with $U_{XY} \gg U_Z$ and 3D SEM probes with $U_{XY} < U_Z$.
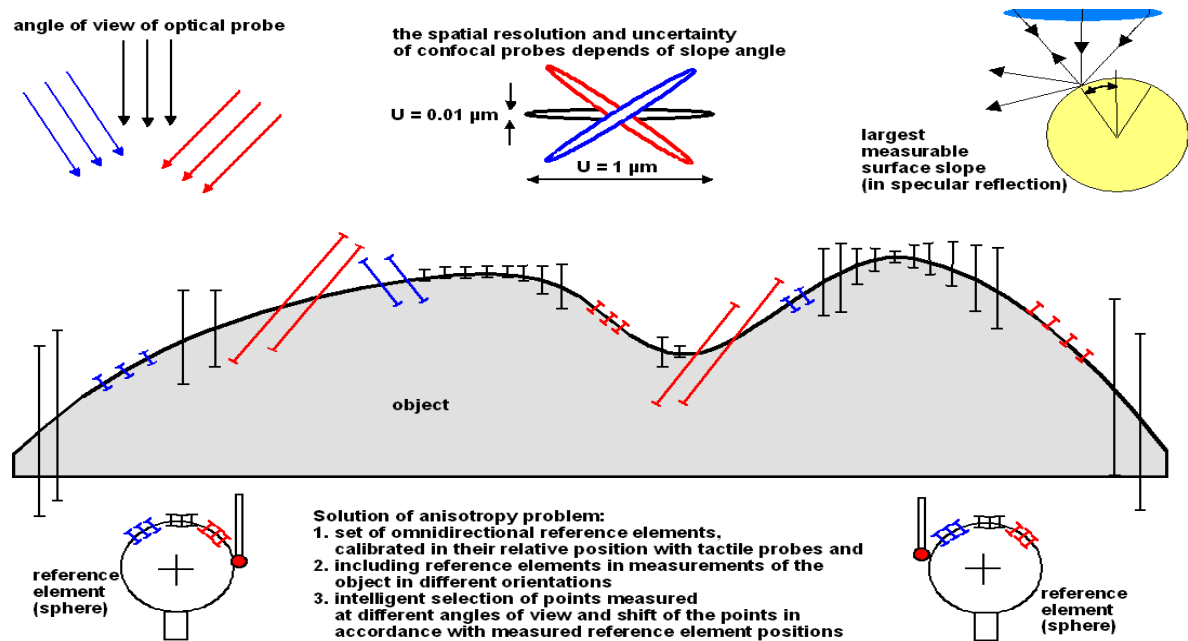
Figure 2.4. Anisotropic uncertainty and limited measurable surface slope and Reference elements as a solution to the anisotropy problem (source: Dr. Eugen Trapet, ISM3D, Gijón, Spain).

2.4.2 Stitching based on workpiece as reference: Best matching software tools

Comparing corresponding areas of different items or on the same object is necessary in a number of cases: *i.e.* stability evaluation of fine manufacturing processes or surface modifications analysis. These applications need precise surface topographies relocation. Automatic software routines can then provide proper tools for an exact and fast solution to the problem whenever relocation inaccuracies smaller than 1-2 μm are needed. In fact best matching position detection can be seen as the result of fitting function maximization. Up to now, different strategies have been proposed and studied. The Table 2.8 gives an overview, with reference to the matching function and the position search criterion.

Matching Function & Base Equation	Advantages/Disadvantages
SAVD Sum of the Absolute Values of Differences $$c_{SAVD} = \sum |z_1 - z_2|_{(x,y)}$$	+ computationally very fast - no distintion made between small and big deviations - no comparable results
SSD Sum of the Squares of Differences $$c_{SSD} = \sqrt{\sum_{(x,y)} (z_1 - z_2)^2_{(x,y)}}$$	+ computationally very good and fast results - no comparable results
CCF Cross-Correlation Function $$cc = \frac{\sum_{x,y}[(z_1 - \overline{z_1}) \cdot (z_2 - \overline{z_2})]_{(x,y)}}{\sqrt{\left[\sum_{x,y}(z_1 - \overline{z_1})^2_{(x,y)}\right] \cdot \left[\sum_{x,y}(z_2 - \overline{z_2})^2_{(x,y)}\right]}}$$	+ well known function, widely used in lot of applications + comparable results - computationally slow
GFF Gradient Field Function $$c_{GGF} = \sum_{(x,y)} \left| \frac{\Delta z_1}{\sqrt{\Delta x_1^2 + \Delta y_1^2}} - \frac{\Delta z_2}{\sqrt{\Delta x_2^2 + \Delta y_2^2}} \right|_{(x,y)}$$	+ not much sensitive to high deformations, when shape is globally kept / unchanged - non comparable results - computationally slow - bad influenced by noise effects

Table 2.8. Main matching functions collected from literature (Vàrady *et al.*, 1997; Weckenmann *et al.*, 2003; Li *et al.*, 2004; Marinello *et al.*, 2005).

2.4.3 The Iterative Closest Point (ICP) algorithm

One of the most widely used stitching techniques is based on the Iterative Closest Point (ICP) algorithm and its modifications (Chen *et al.*, 1992; Vàrady *et al.*, 1997; Weckenmann *et al.*, 2003; Li *et al.*, 2004; Zhu *et al.*, 2007). The ICP algorithm has become the dominant method for aligning three-dimensional models based purely on the geometry. The algorithm is widely used for registering the outputs of 3D scanners, which typically only scan an object from one direction at a time. ICP starts with two meshes and an initial guess for their relative rigid-body transform, and iteratively refines the transformation by repeatedly generating pairs of corresponding points on the meshes and minimizing an error metric (Rusinkiewicz, 2001). This algorithm is also employed to match two clouds of points. This matching is used to reconstruct 3D surfaces from different scans by merging together two or more point clouds. The algorithm is very simple and is commonly used in real-time. It iteratively estimates the transformation (translation, rotation) between two raw scans.

➢ Inputs: two raw scans, initial estimation of the transformation, criteria for stopping the iteration.

➢ Output: refined transformation.

Essentially the algorithm steps are:

1. Associate points by the nearest neighbour criteria;

2. Estimate the parameters using a mean square cost function;

3. Transform the points using the estimated parameters;

4. Iterate (re-associate the points and so on).

More detailed algorithm descriptions and enhancements are given in the above mentioned articles.

2.4.4 Point clouds stitching from 3D-SEM reconstructions

The procedure which leads from two Scanning Electron Microscope (SEM) images of an item to a 3D reconstruction, and to the resulting point cloud, will be described in more details in chapter 3. This technique is called 3D-SEM and it typically leads to point clouds where the uncertainty in the x and y directions is lower than in z-direction. The theoretical and experimental uncertainty of 3D-SEM reconstructions will be discussed in chapter 7, while in this section stitching in the case of SEM point clouds is addressed. As SEM operates in vacuum and at high magnifications, the stitching strategy based on external reference objects is not feasible. One possibility would be, for example, to create indentations on the object to be measured, and to be used later as features enabling software based stitching. Nevertheless this is a destructive procedure which also modifies the shape of the object. Much more convenient would be the use of the features already present on the object such as dust, contaminations or surface topography in the case of rough items. Therefore factors influencing the software performances to stitch together SEM point clouds are the number and the size of features which can be used for the stitching and SEM image quality, since out of focus or blurred features or presence of noise would create some difficulties for the ICP algorithm. Stitching strategies which can be used with SEM point clouds are then ICP algorithms or CAD based alignment. Point clouds stitching can be employed when the following measuring strategies are foreseen:

- Stitch together point clouds from multiple views of the same item starting from SEM images acquired at different magnifications. Object's images taken at low magnifications (*e.g.* 500x) are useful to reconstruct a large part of the item's geometry with low resolution, while high magnification images (*e.g.* 5000x or higher) allow high resolution images of small features which are considered to be relevant;

- Stitch together multiple views of the same item starting from SEM images acquired at high magnification *i.e.* at high resolution. As high magnification results in a small field of view, the complete geometry of an object can be resolved by stitching together the different point clouds of each portion. In this case it is relevant that the different views are acquired by taking images of areas with the presence of recognizable features.

2.5 Algorithms for feature extraction

The logical flow for a tolerance verification process as defined in the Geometrical Product Specification (GPS) project is stated by ISO/TS 17450-1:2005 (2005). It consists of several steps concerning "feature operators":

1. A particular subset of the real surface is identified for each surface to be verified. This feature operation is called <u>partition</u>;

2. A subset of the real feature is approximated using a physical extraction process yielding to a finite set of points. This feature operation is called <u>extraction</u>;

3. The feature <u>filtration</u> operation is then performed, sometimes embedded within the physical extraction process or applied subsequently, reducing the information of the set of points to describe only the frequencies of merit for the verification of the particular surface-tolerance combination;

4. The filtered point set is used to estimate the closest fitting substitute geometry through a process of <u>association</u>;

5. When two or more surfaces are influenced by one tolerance, the <u>collection</u> operation is used to consider all applicable surfaces at the same time;

6. When tolerance specifications depend on features coming from two or more surfaces, the <u>construction</u> operation is used to define these other ideal features.

A chart showing the entire process is presented in Fig.2.5.

A   B   C   D   E   F
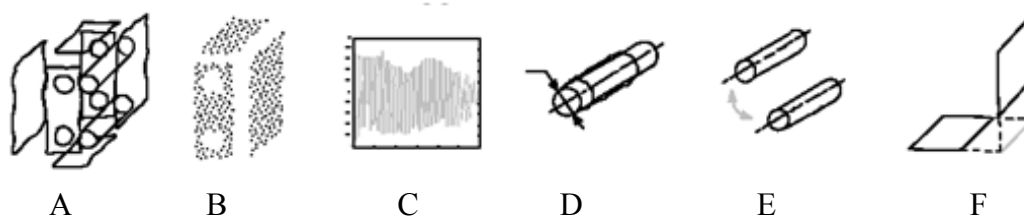
Figure 2.5. Features operations defined in the GPS project; (A) partition, (B) extraction, (C) filtration, (D) association, (E) collection and (F) construction ISO/TS 17450-1:2005 (2005).

The GPS project in ISO/TC213 adopted a classification of three-dimensional surfaces based on their invariance under the action of the Lie group of rigid motions (Srinivasan, 1999). Such a high level framework is extremely concise and powerful but demands a more manageable mathematical formulation.

The classification of Euclidean surfaces according to their invariant properties under the action of rigid motions was introduced in mechanics by Hervé *et al.* (1976) while Clément *et al.* (2004) extended it to tolerance applications in 1994. From a theoretical point of view, the classification descends by the properties of the twelve connected Lie subgroups of T(3)×SO(3) (the group of translations and rotations in $\Re^3$). Seven subgroups leave an invariant proper subset of $\Re^3$, thus giving rise to as many classes of symmetry as illustrated in Table 2.9, which is based on the classification given by ISO/TS 17450-1:2005 (2005). This ISO standard is currently under revision and a newer version will be most likely published in 2011.

No.	Displacements	Group of Symmetry	Dimensions	Surface $S \supseteq \Re^3$	Reference element set
1	Spherical rotations	R(3)	3	Sphere	Point
2	Axial rotations and translations along a fixed axis;	T(1)xR(1)	2	Cylinder	Straight line
3	Planar translations	T(2)xR(1)	3	Plane	Plane
4	Helicoidal displacements (helix pitch: ε)	T(1)xR(1) Pitch ε	2	Helical	Helix
5	Axial rotations	R(1)	1	Revolution	Point, Straight line
6	Translations along a fixed axis	T(1)	1	Prismatic	Straight line, Plane
7	Null	I	0	Complex	Point, Straight line, Plane

Table 2.9. Classes of invariance or symmetry (ISO/TS 17450-1:2005, 2005).

More than in the macro world, interactions between micro fabrication processes and measuring techniques create different scenarios that can hardly be constrained in a general framework. In certain cases standards and tolerance systems developed for macro geometries such as Geometrical Product Specification (GPS) can still be valuable for micro products as well. Functionality requirements in macro world are usually related with mating capabilities.

For this reason it is well known that one of the challenges for the GPS standard is how to manage an object where the form error cannot be separated from the roughness of the surface. In the case of micro products the situation is different: mating capabilities do not generally assure the functionality of the assembly. In some cases the micro-product is monolithic or, more usually in MEMS' application, the distance between one piece and another is of the same order of magnitude of the dimension of the piece itself. In other cases no relative motion between the parts can be assured: the functionality is only related with the geometry and the shape. In these cases actual standards for geometrical specification can be successfully applied. In Fig.2.6 geometries obtained with different machining processes exhibiting typical micro geometries are show.
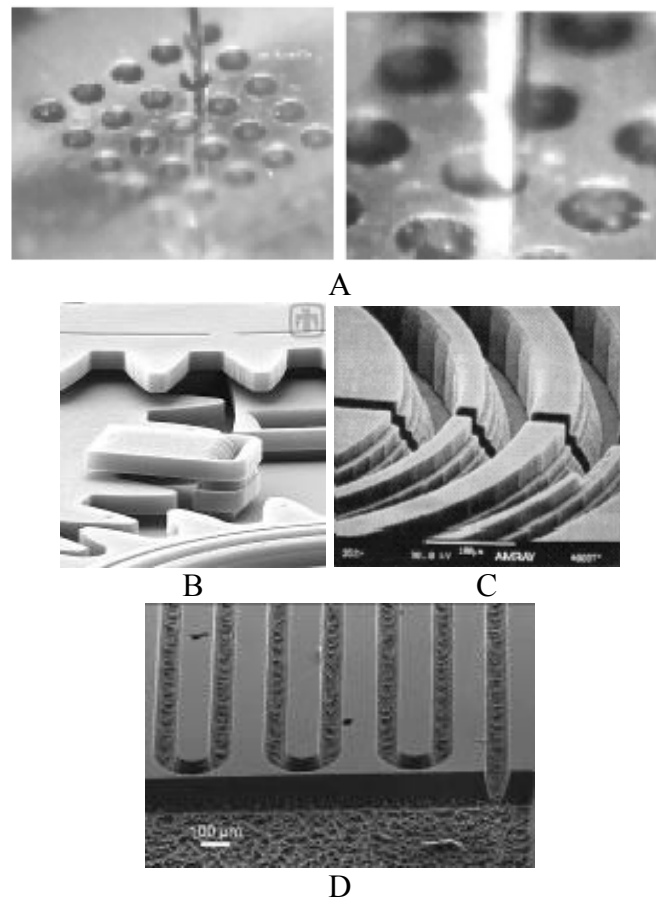
Figure 2.6. Some example of micro structures obtained with different manufacturing processes: micro drilled hole (A); micro gears obtained with photolithography (B); micro-milled channels (C); channels for micro fluidics obtained from Reactive Ion Etching (D) (Hansen *et al.*, 2006).

From Fig.2.6E is possible to observe that MEMS's manufacturing processes lead to clear distinctions between geometry and roughness. In other cases it is possible to distinguish between roughness and form errors. Moreover, it is necessary to take into account the influence of the probing system. As an example the measurement of the circumferences of the micro-milled surface likes those presented in Fig.2.6D by a probe with a ball tip, can lead to a roughness cut off, while if measured with a different probing system (*e.g.* white light interferometry) this will not happen. In the former case it is possible to state that end users are well acquainted to think in terms of substitute features as they are used to do in a macro world. This symmetry is demonstrated by Wilkening *et al.* (2006) which showed that most of the features defined so far, in the case of macro products, are objects of measurement in the micro world as well. This is not to forget that major issues of coordinate metrology related with discrete sampling, anisotropic uncertainty, fitting evaluation, sampling strategy, to cite some of them, are still present. Nevertheless the situation can be complicated due to the capability of small ultra-precision CMMs carrying multiple probing systems: noise factors, usually uncoupled because they affect different probing systems, and can influence the results along the same measurement mission. The to-be-measured and to-be-analyzed object features will differ in type and parameters from classical features (like plane, line, circle, sphere, cylinder, contour, point-deviation-vector from a CAD-given ideal design, form, error and roughness). The measurement of micro- and nano-components requires qualitatively different rules providing feature definitions and measuring procedures. The corresponding algorithms and the first software modules to evaluate measurement data of micro- and nanotechnologies shall be developed.

Starting from this background, in the scientific literature two methods recently appeared that seem to be coherent with the above mentioned requirements. The first one was developed by University of Stanford (Gelfand *et al.*, 2004) while the second was from Politecnico di Torino (Chiabert *et al.*, 2001). They have several interesting characteristics: from a formal point of view they are consistent with the definition of substitute feature presented into the ISO/TS 17450-1:2005 (Li *et al.,* 2004). In fact these algorithms are able to classify a feature as belonging to one of the seven invariant classes defined in ISO/TS 17450-1:2005 (2005). From a practical point of view the algorithms are developed to work with clouds of points and they are able to partition them into features defined by the invariance with respect to the group of rigid motions.

These algorithms are suitable to be implemented in software analyzing data coming from a multiple probing system for the following reasons:

- both of them work with clouds of points;

- both of them do not require any previous information about the shape of the surface;

- both of them have partitioning capabilities;

- they are consistent with GPS framework; enabling these algorithms to be used with new tolerances, specifically designed for microproducts.

- Stanford method is suitable:

  o for high density sampling strategies, like the one performed by optical probing systems and AFM;

  o to be used with data characterized by anisotropic error or resolution.

- Turin method is suitable:

  o for low density sample strategy, like the one performed by contact probing systems like fiber probe;

  o to be used with data with isotropic error like the ones coming from contact probing systems like fiber probe;

  o for the probabilistic estimation of intrinsic parameters leading directly to uncertainty in measurement.

- The characteristics evaluated with the Turin method are probabilistic, therefore it is possible to associate a risk of error in taking a decision based on the measurement results.

A comparison and characterization of both algorithms was found in literature (De Maddis *et al.*, 2007) on macro geometries. A brief description and conclusion are given in order to point out the strong and weak points in the case of a real application. The algorithms present some limitations that can be summarized with the following points:

- The Stanford method can only evaluate relational parameters (*i.e.* direction of the axis of a cylinder but not its radius);

- The Turin method needs a quasi-complete sampling of the surface;

- Accuracy on micro geometries has still not been tested.

While the limitation in the case of the Stanford method involves a key point in the process of product verification and limits the use of this algorithm to position tolerances, limitations of Turin method are less stringent.

Some improvements need to be done in order to achieve complete operability:

- tests on data coming from micro measurements;

- integration with algorithms to collect features and calculate geometrical tolerances.

Positive and negative aspects of these two methods are summarized in Table 2.10.

Stanford Method		Turin Method	
Positive	**Negative**	**Positive**	**Negative**
• Suitable for optical probing systems • able to work with surface's patches • robust w.r.t. noise in the case of high sampling density (>10 pts/cm^2) • robust w.r.t. anisotropic noise • Accurate for high (>10 pts/cm^2) sampling density	• Depends strongly on normal vector estimation in term of accuracy and computational time • normal vector influenced by noise at low sampling density (<1 pts/cm^2) • only relational parameters are recognized; • Accuracy needs to be improved	• Suitable for contact probing systems • Robust to sample size and noise • both relational and intrinsic parameters are recognized • probabilistic description of intrinsic parameters, direct connection with measurement uncertainty	• The surface should be sampled completely • suitable in the case of isotropic noise • accuracy needs to be improved

Table 2.10. Negative and positive characteristics of algorithms for surfaces recognition (Barini *et al.*, 2007).

References

Bariani P. Dimensional metrology for microtechnology. Ph.D. Thesis, Department of Manufacturing Engineering and Management. Technical University of Denmark, 2005.

Barini EM, De Maddis M, Ruffa S, Tosello G. A DOE Approach for Robustness Analysis of Shape Recognition Statistical Method. *Joint ENBIS-DEINDE Conference*, Turin, Italy, 2007.

Binnig G, Quate CF, Gerber CH. Atomic force microscope. *Phys. Rev. Lett.* 1986; **56/9**: 930-933.

Carli, L. Shape and wear of Atomic Force Microscope tips. M.Sc. Thesis, IPL, Technical University of Denmark, 2007.

Chen Y, Medioni G. Object modelling by registration of multiple range images. *Image Vis. Comput.* 1992, **10**: 145-55.

Chiabert P, Costa M, Pasero E. Detection of Continuous Symmetries in 3D Objects from Sparse Measurements through Probabilistic Neural Networks. *Proc. of the IEEE International Workshop on Virtual andIntelligent Measurement Systems*, Budapest, Hungary, 2001.

Clément A, Rivière A, Temmerman M. Cotation Tridimensionnelle des Systemes Mechaniques, Ivry-sur-Seine, PYC Edition, France, 2004.

De Maddis M, Ruffa S., Srinivasan V. Comparison between methods for invariant class partitioning in the ISO framework. *10th CIRP Conference on Computer Aided Tolerancing Specification and Verification for Assemblies*, Erlangen, Germany, 2007.

Gelfand N, Guibas L. Shape Segmentation Using Local Slippage Analysis. *Proc. of Symposium on Geometry Processing* 2004; **71**: 214-223.

Hansen HN, Carneiro K, Haitjema H, De Chiffre L. Dimensional micro and nano metrology. *CIRP Annals* 2006; **55/2**: 721-743.

Hervé J. La géometrie du groupe des déplacements appliquée à l'analyse cinématique des mécanismes. Thèse de Doctorat d'Etat en Sciences Physiques, 1976.

ISO (International Organization for Standardization)-TS 17450-1:2005. Geometrical product specifications (GPS) - General concepts - Part 1: Model for geometrical specification and verification, ISO, 2005.

Li Y, Gu P. Free-form surface inspection techniques state of the art review. *Comp. Aided Design* 2004; **36**: 1395-1417.

Marinello F. Atomic Force Microscopy in nanometrology: modelling and enhancement of the instrument. PhD thesis, University of Padova, Italy and Technical University of Denmark, 2007a.

Marinello F, Bariani P, De Chiffre L, Hansen HN. Development and analysis of a software tool for stitching three dimensional surface topography data sets. *Meas. Sci. Technol.* 2007b; **18/5**: 1404-1412.

Marinello F, Savio E, De Chiffre L. A software tool for sub-pixel surface topography relocation. *Proc. of the 7th AITeM Conference* 2005: 51-52.

Piron L. Dimensional characterization of microtools using optical measuring systems. M.Sc. Thesis, IPL114.03, Technical University of Denmark, 2003.

Rusinkiewicz S, Levoy M. Efficient Variants of the ICP Algorithm. *Third International Conference on 3-D Digital Imaging and Modeling (3DIM '01)* 2001: **145**.

Savio E, Schmitt R, De Chiffre L. Metrology of freeform shaped parts. *CIRP Annals* 2007; **56/2**: 810-835.

Schwenke H, Neuschaefer-Rube U, Pfeifer T, Kunzmann H. Optical methods for dimensional metrology in production engineering. *CIRP Annals* 2002; **51**.

Stedman M. Basis for comparing the performance of surfacemeasuring machines. *Precis. Eng.* 1987; **9**: 149-152.

Srinivasan V. A Geometrical Product Specification Language Based on a Classification of Symmetry Groups. *Comp. Aided Design* 1999; **31/11**: 659-668.

Vàrady T, Martin RR, Cox J. Reverse engineering of geometric models - an introduction. *Comp. Aided Design* 1997; **29/4**: 255–268.

Weckenmann A, Estler T, Peggs G, McMurtry D. Probing Systems in Dimensional Metrology. *CIRP Annals* 2004; **53/2**: 657-710.

Weckenmann A, Ernst R, Velgan R. Local wall thickness measurement of formed sheet metal using fringe projection. *XVII IMEKO World Congress* 2003; Book of Summaries: 205.

Wilkening G, Bosse H. Nano- and micrometrology-State-of-the-art and future challenges. *MAPAN-Journal of Metrology Society of India (MAPAN-JMSI)* 2005; **20/2**:125-151.

Wilkening G, Koenders L. Nanoscale Calibration Satndards and Methods: Dimensional and Related Measurements in the Micro- and Nanometer Range. Wiley 3rd edition, 2006.

Zhu L, Barhak J, Srivatsan V, Zatz R. Efficient registration for precision inspection of freeform surfaces. *Int. J. Adv. Manuf. Technol.* 2007; **32/5-6**: 505-515.

3. Dimensional Metrology using SEM

3.1 Introduction on Electron Microscopy

An electron microscope is an instrument producing an electronically magnified image of a specimen, by using a particle beam of electrons to illuminate it. This physical principle was already proposed by de Broglie in 1925 and the first electron microscope prototype was built by Knoll and E Ruska in 1931, which was capable of four-hundred-power magnification. Although contemporary electron microscopes are capable of a million-power magnification, their working principle is still based upon Ruska's prototype. In 1934 the resolution of an electron microscope better than the light microscope was achieved by Driest & Muller and in 1938 and the first practical commercial TEM by von Borries & Ruska; Siemens in 1939, achieved a 10 nm resolution. The first SEM was built by Zworykin *et al*., in 1942 and in 1945 a resolution of 1 nm was accomplished (Wells, 2006). The resolution can be defined as the ability to discern fine details in an image. This is represented by the minimum distance between two points, such that those points are perceived as separated in the image (Goodhew *et al.*, 2001). According to this definition, electron microscope resolution limit should be ~ 0.001 nm. In any case, the Abbe diffraction limit theory must be considered. This defines the minimum resolvable distance between the images of two point objects using a perfect lens. According to this theory, structures smaller than half a wavelength cannot be resolved (Abbe, 1872). The Abbe equation and a figure illustrating this physical principal are shown in Fig.3.1 where "λ" represents the wavelength, "n" the refractive index, and "α" the aperture angle.

$$d_{min} \approx 0.61 \cdot \frac{\lambda}{n \cdot \sin(\alpha)} \quad (1)$$
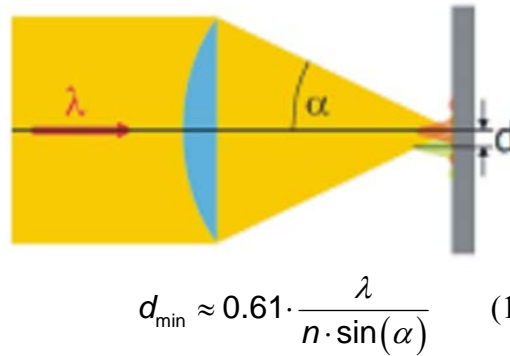
Figure 3.1. Abbe equation and schematic representation of the physical principle (Egerton, 2005). d_{min} is the minimum possible achievable resolution, λ" represents the wavelength, "n" the refractive index, and "α" the aperture angle.

Starting from the Abbe equation (1) it is possible to calculate the minimum theoretical resolution achievable with different techniques, by knowing the physical wavelength. These values are shown in Table 3.1. For the case of light microscopes λ=500 nm, while for SEMs it is theoretically 0.005 nm. Since for a SEM the numerical aperture angle α is ≤ 1 deg. d_{min} results about 1000 times smaller than in the case of light microscopes. Nevertheless, different error sources such as astigmatism, defocus, or non-perfect lenses composing the instrument, yield to resolution values of about 2 nm, which are still 100 times smaller than instruments based on light sources.

Source	**λ/nm**	**d_{min}/nm**
Light	500	~250
X-ray	2	~25
electron	0.005	~0.25

Table 3.1. Theoretical resolution d_{min}, estimated from the physical wavelength λ, achievable from different sources (Egerton, 2005).

3.2 SEM working principle and imaging

Scanning Electron Microscopy (SEM) is a method based on an electron beam scanning a specimen. SEM produces images by detecting low energy secondary electrons, which are emitted from the surface of the specimen due to excitation by the primary electron beam. In the SEM, the electron beam is rastered across the sample, with detectors building up an image by mapping the detected signals to the lateral beam position (Goodhew *et al.*, 2001). Therefore by using a SEM it is possible to obtain topography images of the object under investigation. The general working principle consist in an electron probe focused on a specimen, adjusted using deflector coils and applying detectors in order to collect secondary electrons or other signals to be displayed on a monitor. Thus, an SEM image of the specimen under investigation is obtained. A more detailed description of the main parts and the corresponding components of a SEM is given in Fig.3.2.
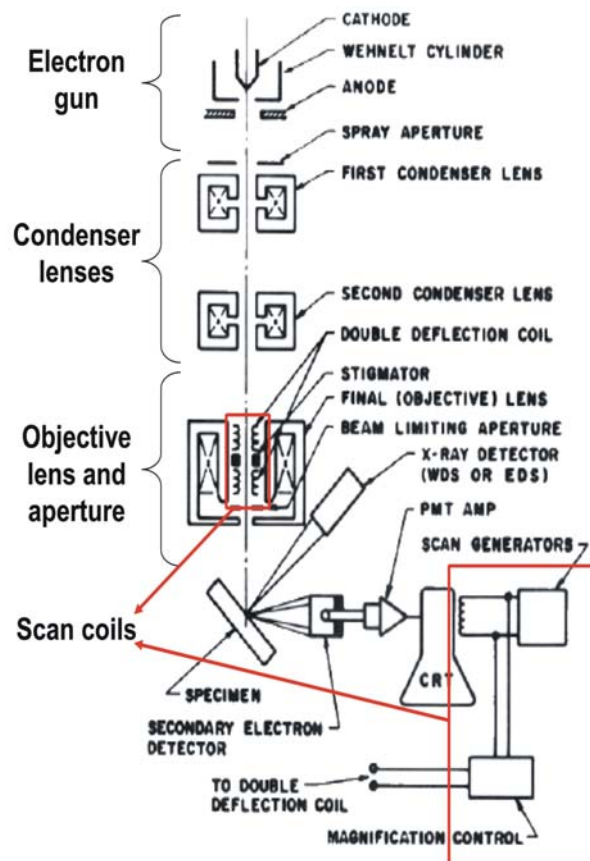
Figure 3.2. Schematic representation main parts and the corresponding components of a SEM (Goodhew *et al.,* 2001).

With reference to Fig.3.2 the main parts composing a SEM are here briefly described:

➢ The electron gun can be in different materials depending on the required capabilities. Its function is to obtain a small spot size with high brightness using different accelerating voltages ranging typically from 1 to 30 kV;

➢ Normally SEMs are composed by two different condenser lenses, the upper one to change the spot size and the lower one to refocus the spot. The stronger the former, the smaller the spot size but also the lower the intensity;

➢ Objective lens determine the final focusing of the beam onto the specimen. For changing the image focus this lens is adjusted and from its quality the microscope resolution is strongly dependent. The role of the numerical aperture, instead, is to determine the beam convergence angle and to change the spot size. The smaller the aperture, in fact, the smaller the spot size but also the lower the beam intensity;

➢ The role of the scan coils is to scan the electron beam across the specimen and also to control the magnification. The higher the magnification the smaller the scan area becomes. Magnifications up to 200,000x are currently achievable using SEM;

➢ The Detectors collect different kind of signals such as secondary electrons, backscattered electrons or x-rays and then they amplify it, feeding a monitor or a computer for data post-processing. Usually secondary electrons are detected when information about the specimen surface is needed. On the other hand, if the specimen is composed by different materials, or more information about the structure are required, backscattered electrons are then collected (see Fig.3.3);
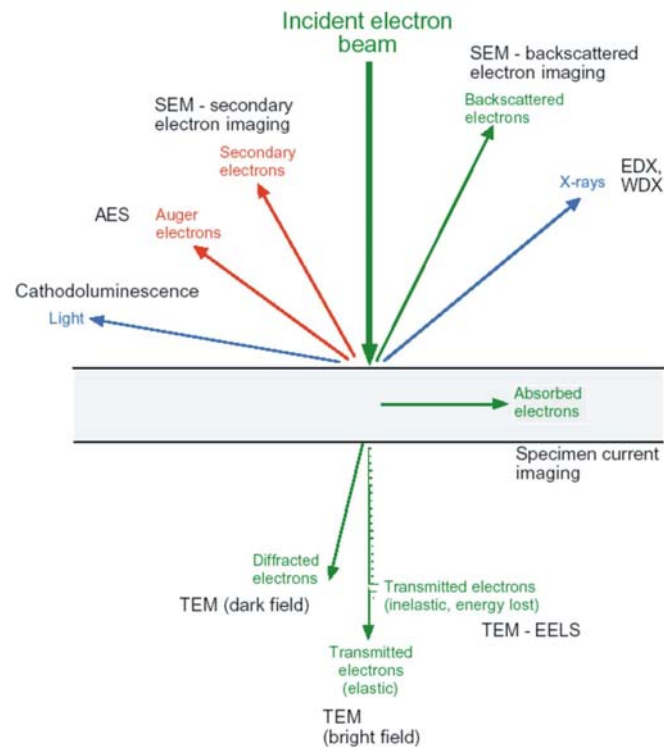
Figure 3.3. Image showing beam-specimen interaction and resulting electron signal (Goodhew *et al.*, 2001).

➢ <u>SEM stage:</u> This part of the microscope has two main functions: to support the specimen holder and to move it inside the SEM chamber (Fig.3.4). The stage allows positioning the specimen, relatively to the electron beam and electron detectors, depending of the measuring task. The stage typically allows, besides x, y and z-axis translations, also specimen tilt and rotation. In particular specimen tilting is performed to enhance the collection of electrons by a particular detector. The combinations of the stage movements permit an accurate location of desired areas of the specimen. Anyhow, as they are liable of affecting magnification, contrast, resolution, and depth of field, the stage should be precisely characterized when accurate SEM measurements are required. Consequently, when poor images are encountered, some improvement may be gained, for instance by the reorientation of the specimen (Bozzola *et al.*, 1992). The metrological characteristics of the stage, of the Inspect 'S' SEM from FEI Company (Europe, The Netherlands) employed in this work, will be discussed in more details in the following sections.
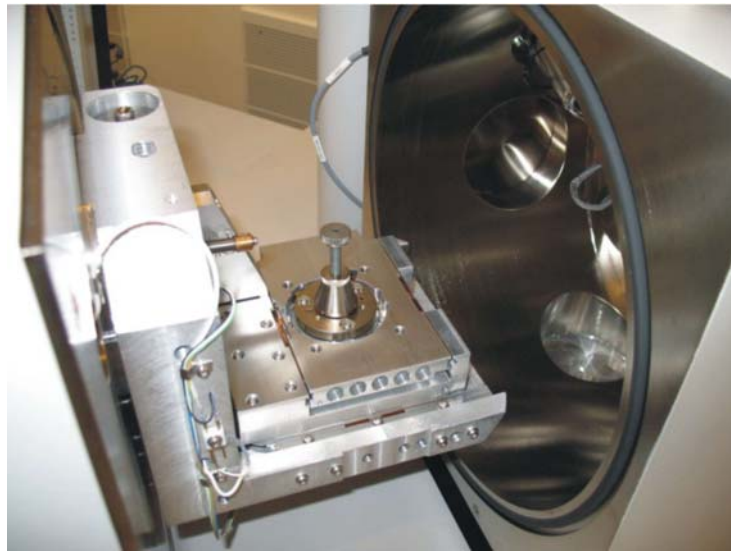
Figure 3.4. Image of the stage supporting the specimen holder, for the Inspect 'S' SEM from FEI Company (Europe, The Netherlands) used in this work.

Some basic definitions related to SEM working principles, taken from (Goodhew *et al.*, 2001), are here reported to facilitate the understanding of the following chapters as they will be extensively used when performing 3D-SEM technique.

➢ Working distance: is defined as the distance between the objective lens and the specimen. The smaller the working distance the smaller the spot size, but also poorer signal collection caused by signal stray. The working distance will be relevant through the whole experimental work also because it is one of the input parameters required by the software performing stereo-pair reconstructions;

➢ Scan rate: It is one of the most influencing factors with regards to image quality. Generally speaking the faster the beam is scanned across the specimen, the faster the image acquisition, but also the noisier the resulting image;

➢ Spot size: It is one of the instrument setting measuring parameters and it can be chosen by the operator. It will be more deeply explained in the next chapter; here just some physical considerations are introduced referring toFig.3.5. The choice of the optimum point size depends also on the line spacing of SEM images, which depends on the magnification and on the number of scan lines per frame. Fig.3.5 A shows the case of a spot size to small, resulting in a poor signal, while the opposite case is represented in Fig.3.5C where a spot size too large causes loss of resolution.

The optimum spot size is represented in Fig.3.5B, where its dimension is proportional to the line spacing. Spot size is determined by the condenser lenses, the objective aperture size, the accelerating voltage and the focus.
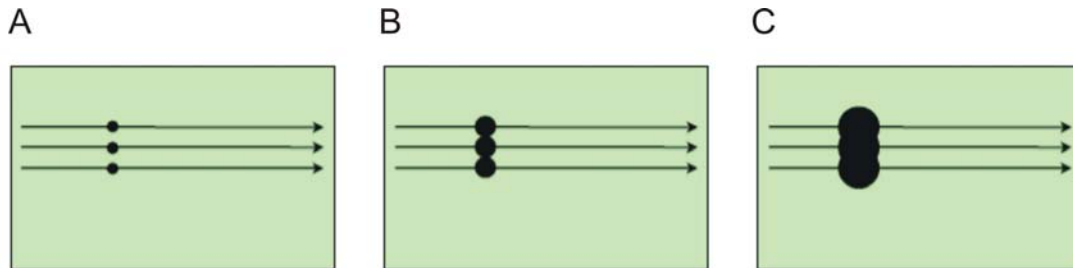
Figure 3.5. Effects of different spot sizes on the resulting image resolution as a function of the line spacing of a SEM image. A) spot size too small causing poor signaling, B) optimum choice of the spot size and C) spot size too large resulting in a loss of resolution (Goodhew *et al., 2001*).

➢ Resolution and pixel size: The image resolution is the smallest spacing visible on the image. It is limited by the line spacing, if the spot size is smaller than optimum (at low magnifications), or by the spot size, if this is larger than optimum (at high magnifications). According to this definition the image resolution results strictly related to the concept of pixel, which can be described as the minimum size of the spot which can be obtained on a cathode ray tube (CRT);

➢ Field of view and depth of field: The field of view (FOV) is defined as the surface region represented on a SEM image and depends on the magnification. The higher the magnification the smaller the field of view. For the Inspect' S SEM used in this work the typical values of the field of view, depending on the chosen magnification, are shown in Table 3.2. The depth of field (DOF) is defined as the portion of a specimen that appears acceptably sharp in the image. One of the great advantages of SEM images is the unusually great depth of focus they exhibit. This makes it possible to examine surfaces much rougher, and at much higher magnifications, than is possible with light microscopes. The DOF is directly proportional to the working distance d and inversely to the magnification M and to the final aperture diameter A. Therefore the depth of field can be increased either by increasing the working distance, either by decreasing the magnification or the final aperture diameter.

As the final aperture diameter is usually ranging from 100 to 600 µm (Goldstein *et al.*, 1992), using a working distance equal to 10 mm at M=3000x would lead to DOF between 10 and 1.5 µm.

Magnification/times	Field of view/µm
700	430.0
1000	300.0
5000	60.4
10000	29.7
20000	15.4

Table 3.2. Typical values of the field of view, depending on the chosen magnification, for the Inspect 'S Scanning Electron Microscope, from FEI Company, used in this work.

3.3 3D-SEM based on stereophotogrammetry

Stereo-photogrammetry technique is commonly employed by acquiring SEM images, composing the stereo-pair, through a stage tilting. This technique has been widely used also at the author's department in the last years (Bariani *et al.*, 2005) and (Marinello *et al.*, 2008a). In the first case an uncertainty evaluation of stereo-pair technique was performed using calibrated gauge-blocks forming steps of different heights, and by the use of two ISO 5436 type C2 roughness standards, while in the second case a newly developed step height was adopted. In both cases, plane items were used for the uncertainty evaluation when measuring different heights using 3D-SEM technique. This measuring procedure remains still valid also in the case of cylindrical items where the object can be positioned and fixed horizontally to the SEM stage to perform eucentric tilting. Multiple views of the item can be acquired, at different tilt angles, to be used later on to form stereo-pairs or stereo-triplets enabling 3D reconstructions using commercial software.

Another possibility is, instead, to position and clamp the cylindrical object vertically on the SEM stage, and then to tilt it by 90 degrees. In this case, the multiple views of the item can be then obtained not through a tilt, but performing rotations along the main axis of the cylinder. The main advantage of this second possibility is the fact that multiple views of the complete geometry of the object can be acquired, while in the case of tilting, only images of a limited portion of the item can be obtained. Fig.3.6 shows the moving stage of the Inspect 'S SEM, from FEI Company, employed in this work where all the possible spatial movements, translations along x, y and z-axis, the xz tilt and the rotation around z-axis are also indicated. Therefore five degrees of freedom are available for positioning the item in the desired position.
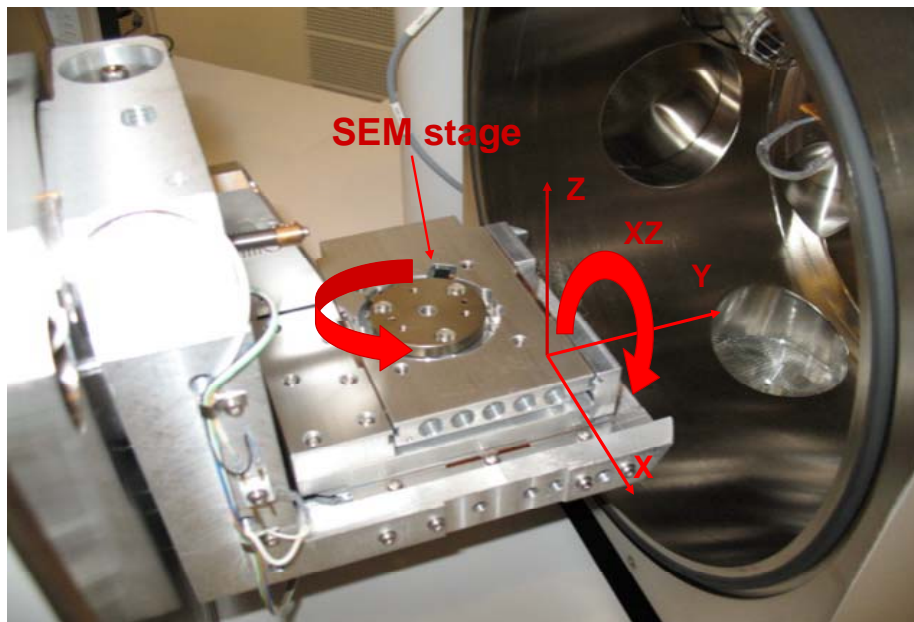
Figure 3.6. Image showing the SEM Inspect ´S stage, from FEI company, enabling translations along x, y and z-axis, xz tilt and rotation around the z-axis, meaning that 5 degrees of freedom are available for positioning the item in the desired position.

3.3.1 Theoretical principles of stereo-pair technique

To produce a stereoscopic reconstruction, a specimen is imaged in the SEM acquiring two images, the stereo-pair, by scanning the same area under two different perspectives, achieved by eucentric tilt of the sample as described in the following section 3.3.2 (see also Fig.3.8). Surface features of different heights on the specimen surface differ in their lateral displacement in the two images.

The disparities between the projections of the surface features in the two images are measured to derive quantitative surface topography. This is the so-called parallax movement, which is the shift of a feature from its location in the first image, to the new location in the second image. For a proper measurement of the parallax it is of paramount importance to be able to successfully calculate the correct matching of single surface features in the two images. The image-matching problem mainly encompasses automatic identification in the stereo-pair of homologous points, representative of corresponding features. Nowadays this procedure is performed using commercial software where the stereo-matching is done using an area-based or a feature-based method (Scharstein *et al.*, 2002). In most SEMs, it is possible to take the two different stereo viewpoints by tilting the specimen about a horizontal axis *x*. Assuming that the surface region on the *x*-axis is brought into focus; the SEM focal plane then coincides with the reference *x*-, *y*-coordinate plane. The stereo-pair technique may be defined using the geometrical definitions given in Fig.3.7.
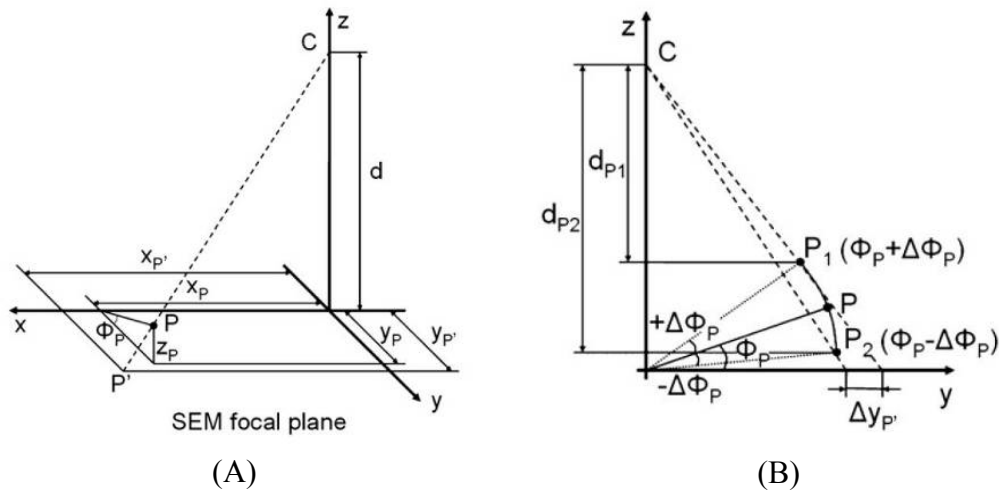
Figure 3.7. Geometrical definitions relative to a point *P* on the specimen surface. The working distance d is not shown to scale (under scaled) for ease of interpretation (Marinello *et al.,* 2008b).

With reference to figure 3.7 (A), *P* is a point elevated with respect to the reference plane by an unknown amount z_P and with unknown lateral coordinates x_P and y_P, the projection of point *P* on the reference plane is denoted as *P'*. A phase angle φ_P describing the surface angular position for the given point *P* and relative to the tilt can be defined as sketched in figure 3.7 (A). The consequences of eucentric tilting are shown in figure 3.7 (B).

50

When rotations of $-\Delta\varphi$ and $+\Delta\varphi$ are imposed on the specimen, point P projections on the reference plane undergo a parallax Δy. A model for deriving surface topography from eucentric stereo-pairs is given by:

$$
\begin{cases}
z = \dfrac{(y_1 - y_2)\cos\Delta\varphi + \dfrac{2 y_1 y_2}{d}\sin\Delta\varphi}{\left(1 + \dfrac{y_1 y_2}{d^2}\right)\sin 2\Delta\varphi + \dfrac{y_1 - y_2}{d}\cos 2\Delta\varphi} \\[4ex]
\xi = \dfrac{2d - 2z\cos\Delta\varphi}{\dfrac{d}{x_1} + \dfrac{d}{x_2}} \\[4ex]
\eta = \dfrac{(y_1 + y_2)(z\cos\Delta\varphi - d)}{(y_1 - y_2)\sin\Delta\varphi - 2d\cos\Delta\varphi}
\end{cases}
\tag{1}
$$

where the indexes 1 and 2 refer to, respectively, the first image (tilted by an amount $-\Delta\varphi$) and the second image (tilted by an amount $+\Delta\varphi$) being used for the calculation. Once introduced the physical P coordinates (ξ, η, z), equation (1) is easily derived from the model provided by Piazzesi (1973) by fixing the constraint $d_1=d_2=d$, meaning constant working distance between the two images (Bariani, 2005). In 3D reconstructions the z coordinate is the most critical one, therefore, starting from the theoretical model of Piazzesi for stereo-pair technique, uncertainty evaluation was performed in chapter 7 according to ISO GUM (JCGM 100:2008).

3.3.2 Stereo-pair reconstructions using MeX[TM]

Among the software packages enabling to perform stereo-pair reconstructions, available on the market, MeX by Alicona Imaging GmbH (MeX[TM], 2007) was adopted in this work. In this section therefore, a short description of the software and its main characteristics is given. The different steps leading from two SEM images to a 3D point cloud are described and main error sources pointed out. Many other tools are available in the software, some of them were used for other purposes, such as dealing with image quality, and therefore they were described in different sections of this thesis. The MeX tool which is used to perform 3D reconstructions is called "creator" and allows obtaining point clouds starting from two images (Stereo Creator for stereo-pair) or from three images (Auto Calibration for stereo-triplet).

Generally speaking it is suggested to use the Stereo-Creator tool, when the tilt angles are accurately known, for instance, through a calibration procedure of the SEM stage. Moreover stereo-pair technique is generally faster than the stereo-triplet function and it can be used also for objects with little structure information. On the other hand, the Auto-Calibration tool is much slower since it is based on an auto-calibration of the tilt angle between the left and center image and between the center and the right one, starting from the nominal values set by the operator. In order to perform this procedure accurately, the software requires the object to have enough height changes and sufficient structure information all over the image. In this case a calibration of the SEM stage is not needed as the software, starting from the nominal input values, performs a refinement, which is crucial when traceable measurements are needed. Generally speaking the stereo-triplet technique cannot be successfully employed for very small tilt angles (e.g. <5 degrees), and for SEM images acquired at too low magnifications and too small working distances.   Anyhow, the stereo-triplet technique is simply based on the averaging of the two stereo-pair reconstructions obtained from the left and middle tilt angle and the middle and right one. For this reason, the uncertainty evaluation of just the stereo-pair technique was performed in this work, hence the Stereo Creator MeX tool was used and tested.

The first step for performing 3D reconstructions, using the Stereo Creator, is to import the two images composing the stereo-pair. The SEM images should be aligned with the eucentric tilt direction and if this condition is not achievable, the software allows image rotations. The operator is then required to input the nominal calibration data which are the relative tilt angle between the two images, the projection distance and the pixel size, here called horizontal measure point size. Therefore the tilt angle, the projection distance and the pixel size are the three main input parameters required by the Stereo Creator to perform stereo-pair reconstructions. It is worth then to briefly analyze each of them separately.

Reference tilt angle (from here on tilt angle): the operator is asked to input the nominal value or the reference one, if a calibration procedure has been performed previously. Angles between 5 and 20 degrees are typically used since angles smaller or larger than these ones would lead to not reasonable reconstructions. As a general fact, smaller tilt angles are chosen with higher specimens yielding a result with steeper slopes, while higher tilt angles are generally used for flat specimens, they provide better vertical resolution, but are difficult to realize for high magnifications;

Projection distance: This parameter is defined as the sum of a ε-value, which depends on the SEM characteristics, and of the working distance, which can be directly read from SEM images. In general ε-values between 5 and 10 provide good measurement result. In this work an ε=6 mm was adopted, as suggested by the SEM manufacturer.

Horizontal Measure Point Size (from here on pixel size): It represents the distance between two consecutive pixels, in a SEM image, along the horizontal direction. MeX provides a tool to calculate this value as shown in Fig.3.12. Starting from a SEM image, the operator is required to draw a line on the image scale bar and then to enter its estimated real world length into the entry field. Multiple measurements are suggested to obtain more accurate results; anyhow it can be easily understood as this procedure itself is highly inaccurate.

To sum up, the operator is asked to set three inputs into the Stereo Creator routine to perform stereophotogrammetry, which are the tilt angle, the working distance (being ε-value constant as described above) and the pixel size calculated from SEM images. These three input parameters are strictly linked to the ones needed for the theoretical calculation of z-coordinate as given by Piazzesi formula described in equation (1). In fact:

> y_1 and y_2 are the lateral coordinates of the same elevated point P in the two SEM images composing the stereo-pair. These lateral coordinates can be calculated by MeX in each image, as the distance of the P point, in pixels, from the reference system of the axis, set in the middle of the SEM image, multiplied by the pixel size;

> d represents the working distance which can be directly input into MeX as previously described;

> $\Delta\Phi$ is the semi-angle of the tilt (or rotation), therefore it is equal to the tilt angle set in MeX divided by two.

The four input parameters y_1, y_2, d and $\Delta\Phi$, introduced in the theoretical model by Piazzesi, can be calculated from SEM images once the three MeX input parameters are given. Nevertheless, it is unknown how MeX operates 3D reconstructions starting from a stereo-pair being the algorithm patented by Alicona (Scherer *et al.,* 1999). It is anyhow possible to determine the MeX working principle based on a number of experimental tests, as it has been done in chapter 7 of this work.

The Global Offset represents the starting point of the MeX algorithm which finds corresponding points in the two images and it is calculated by the software once the two images have been superimposed either automatically or manually by the operator. This Global Offset represents an average value as different spots in the same SEM image undergo different shifts, which are proportional to their height. MeX, in fact, calculates the depth image based on the disparity in the stereo images. In the ideal case of eucentric tilt the offset/shift of the left image with respect to the right one should occur only along the horizontal direction. Anyhow, very often a not ideal tilting is performed due to different causes such as specimen positioning or misalignments. In this case an offset also along the vertical direction is detected, which can be used as an indication of how much the real tilt was close to an eucentric one. A comparison between a correct eucentric tilting and an incorrect one is shown in Fig.3.8.
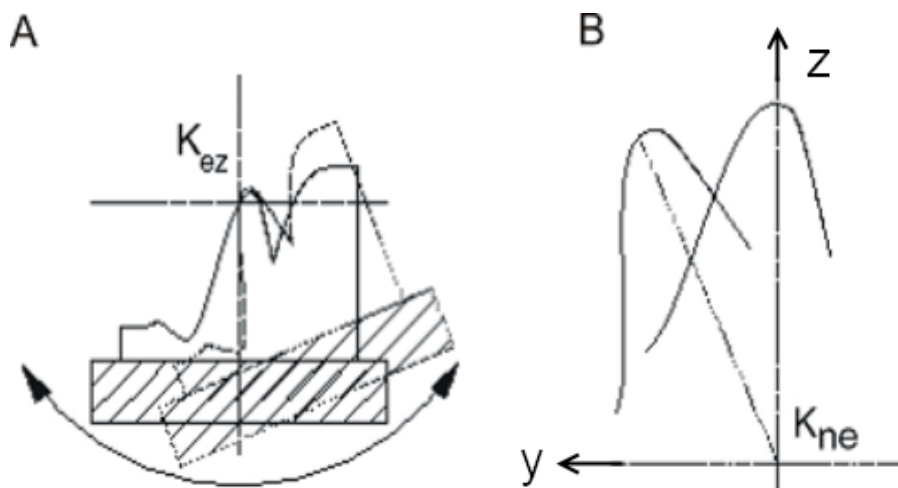
Figure 3.8. A) Correct eucentric tilting. B) Incorrect tilting with the tilt axis being below the specimen's surface (MeX^{TM} Reference manual, 2007).

In the ideal case, the principal axis and the tilt axis intersect at the point K_{ez} on top of the surface. Thus a tilting will result in a static centre point in the image. In the non-ideal case, the principal axis and the tilt axis do not intersect on top of the surface, but below or above (point K_{ne}). A non-ideal tilting results in a migration of the centre point in the image (sideways in the case of vertical tilting and vertically in the case of horizontal tilting). MeX^{TM} Reference manual (2007) prescribes some procedures to be followed by the operator when performing SEM measurements to reduce as much as possible the non-eucentric tilting.

Since, as it was mentioned before, a non-eucentric tilt component is quite often present in SEM images, MeX allows a correction of this non-eucentricity by an option called "Rectification". This option helps the operator to process SEM images even when the assumption of eucentric tilting is violated.

In that case the images composing the stereo-pair are transformed by performing image rotation as well as image warping. An example of this rectification is shown in Fig.3.9.
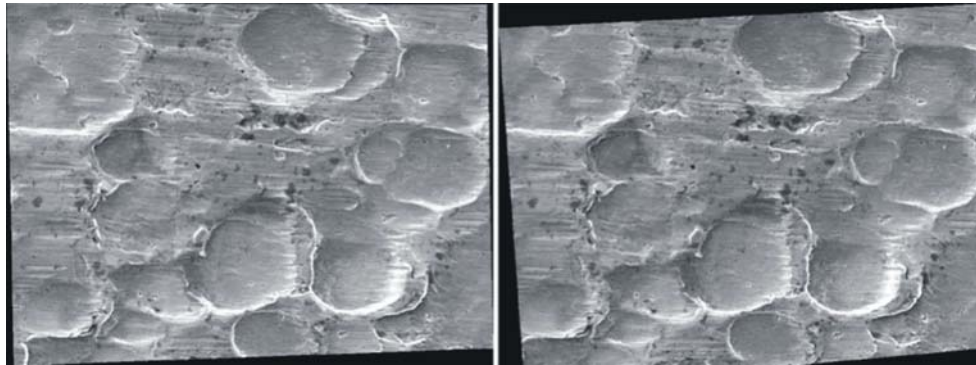
Figure 3.9. Example of MeX rectification performed on a SEM image as a consequence of a not-eucentric tilting. Image on the left is rotated and warped resulting in the image on the right which will be lately used to perform stereophotogrammetry (MeX^{TM} Reference manual, 2007).

The operator is then asked to choose a region of interest (ROI) where the 3D reconstruction is going to be performed. As a consequence a low density Digital Elevation Model (DEM) is created and the operator is asked to confirm if this looks reasonable or if the calculation should be performed again. Once the operator has confirmed that the low density DEM looks reasonable, a final DEM is created and it can be exported as an optical image in different formats or as 3D data as a txt file, representing a point cloud, to be later on post-processed using MeX or another commercial software.

3.4   Main error sources in 2D and 3D-SEM

The measuring procedure, which, starting from an item to be measured using SEM, leads to a 3D reconstruction and lately to a post processed point cloud for feature extraction and measurement, is described in this section. The first step is the identification and the description of every single phase, where possible error sources are also listed distinguishing between the commonly used SEM technique, purely 2D, and the 3D-SEM measurements. A scheme was produced to sum up all the different phases and it is shown in Fig.3.10, where yellow cells indicate the result of a SEM image acquisition process, or of a stereo-pair reconstruction, while light blue cells indicates the steps related to uncertainty sources.
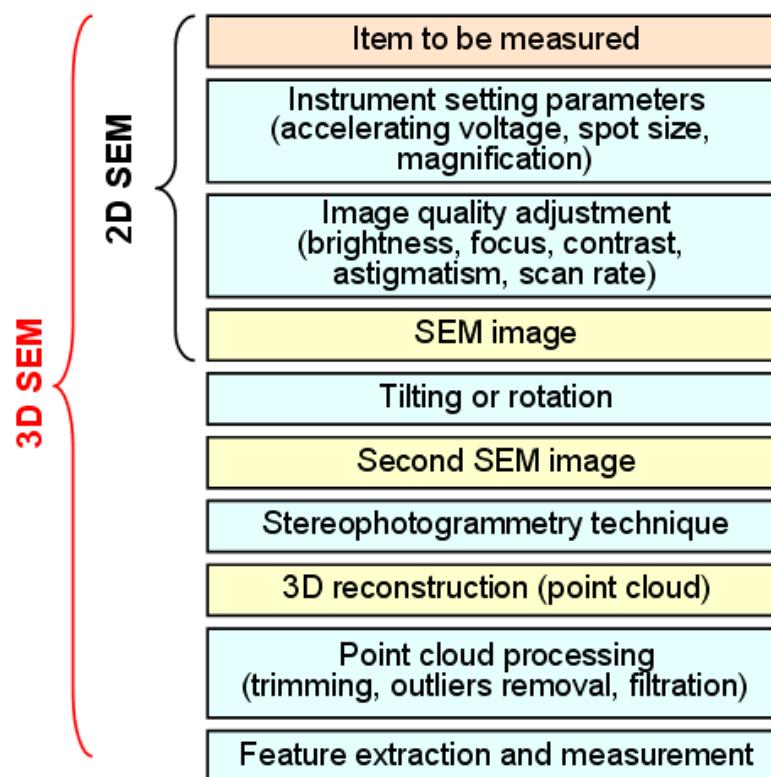
Figure 3.10. Scheme showing all the phases related to 2D and 3D-SEM measurements and reconstructions following the temporal order of the events.

A deep knowledge of the item to be measured, in terms of chemical and physical characteristics, is very important before starting the measuring process. In fact the item size, for instance, influences the choice of magnification and of the working distance, while the item material is affecting the measuring parameter setting, and in particular the proper choice of the accelerating voltage.

It is also relevant to know if multiple materials are involved and which are the measuring tasks in terms of features to be measured and number of reconstructions needed. The optimum tilt angle is typically related to the estimated specimen height. The item has to be then clamped to a fixture to allow tilts or rotations inside the SEM chamber. Moreover an inappropriate clamping might cause non-eucentric tilting leading to a number of problems as discussed before. Once the item has been clamped on the SEM stage, a vacuum is created and the operator is required, as a first step, to set instrument setting measuring parameters such as the accelerating voltage, the spot size and the magnification.

These parameters affect the SEM image quality, noise, and the resolution, mainly through the pixel size and the field of view. Uncertainty evaluation of the instrument measuring parameters is performed in chapter 5, where all these effects are also discussed. After setting the measuring parameters, the operator should adjust image quality to obtain SEM images showing proper conditions of brightness, contrast, focus and astigmatism. This adjustment is also affecting the noise and the ability of the MeX to distinguish between neighbour points when performing stereo-pair reconstructions. The better the image quality, the easier it would be for the software to superimpose the two images composing the stereo-pair in finding corresponding features. Since SEM image quality is supposed to have a relevant effect on stereophotogrammetry, it will be investigated in chapter 6.

From the previous two operations, instrument setting and image quality adjustment, an SEM image of the item can be acquired by choosing the appropriate scan rate. This point terminates the process leading to 2D SEM measurements, as they can be directly performed on the image previously acquired. If instead 3D reconstructions are needed, a second SEM image, which will form the stereo-pair with the previous one, should be acquired by tilting or rotating the item along the main direction, to obtain eucentric tilting. If the tilt angle is relatively small it can be assumed that image quality setting, which was found to be the optimum one for the previous image, remain still the same and that focus adjustment is not needed. Furthermore it is crucial to keep a constant working distance between the two images; otherwise stereo-pair reconstructions can not be performed using MeX. If this assumption is valid, it can be assumed that passing from one view to the following one, the parameter setting and image quality remain the same. Once the two SEM images, one tilted with respect to the other, are obtained, stereophotogrammetry technique can be employed to obtain 3D reconstructions.

The software performing stereo-pair and stereo-triplets was described in the previous section, together with the different input parameters. In this case, the operator would generally set the nominal values for working distance, tilt angle and pixel size, while uncertainty should also be taken into account. The uncertainty evaluation of the stereo-pair technique, under a theoretical and experimental perspective, will be performed in chapter 7.

The result of stereophotogrammetry technique is then a raw point cloud, which needs to be post-processed using commercial software. Usually the following operations are performed: point cloud trimming, outliers' detection and removal and filtration. A post-processed point cloud is obtained which is ready for feature extraction and measurements. The role of the software for point-cloud post-processing and the influence of the single operations are discussed in chapter 4.

Replications should also always be performed, either when performing 3D reconstructions with MeX, or when post-processing the point-cloud, as the operator might strongly influence the results. Therefore, the uncertainty related to measurements repeatability will be also quantified.

In order to quantify the influence of every single phase involved in 3D-SEM reconstructions, uncertainty evaluation can be carried out in accordance with ISO (International organization of Standardization)/TS 213, ISO/TS 14253-2 (1999). This Technical Specification introduces the Procedure for Uncertainty Management (PUMA), which is a practical, iterative procedure based on the GUM for estimating uncertainty of measurement without changing the basic concepts of the GUM. As shown in Fig.3.11 uncertainty management is performed on the basis of a defined measurement task and a given target uncertainty.
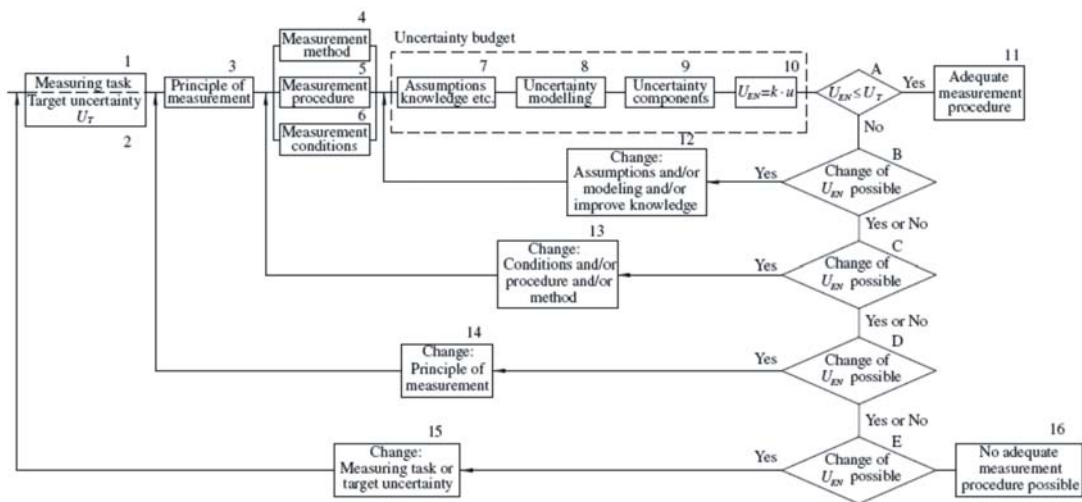
Figure 3.11. Procedure for Uncertainty Management for a measurement process/procedure (ISO/TC 213, ISO/TS 14253-2, 1999).

The idea is to perform a preliminary uncertainty budget leading to the first rough estimate of the expanded uncertainty. If this value proves that the measurement procedure is adequate for the measuring task, then the iteration process stops, otherwise a new iteration has to be performed. Before the new iteration, it is suggested to analyze the relative magnitude of the uncertainty contributors, as in many cases a few uncertainty components pre-dominate the combined standard uncertainty and expanded uncertainty. Therefore, the minor uncertainty contributors can be neglected in the next iterations which will be based on a refinement of the most crucial contributors (Heping *et al.*, 2008). If further iterations are required it could be the case to change the assumptions, the modelling or to increase the knowledge about the uncertainty components to make a more accurate upper bound estimation of the largest (dominant) uncertainty components (BIMP, ISO *et al.*, 2007) and then make the second iteration of the uncertainty budget.

3.5   Case study: 3D-SEM reconstructions of cylindrical items

In this work, an uncertainty evaluation of the main error sources dealing with 3D-SEM reconstructions, as described in the previous section, has been carried out considering a TESA wire gauge, with an external calibrated diameter of 250 ± 0,15 μm as cylindrical item (see Fig.3.12) (Catalogue of TESA Technology, 2007/2008). The case of stereo-pair reconstructions, obtained through item rotations, was considered, although the theoretical uncertainty evaluation of stereo-pair technique, carried out in chapter 7, was performed also considering the case of tilting to allow results comparison. A minor problem arises when the item rotation measuring technique is chosen, as the stage can be tilted up to maximum 78 degrees, meaning that the item can not be perfectly positioned parallel to the stage. This can be seen from Fig.3.13 where an example of cylindrical item clamped to stage and tilted by 78 degrees on the SEM stage is shown.

Figure 3.12.   Image of a TESA wire gauge, with an external calibrated diameter of 250 ± 0,15 μm, clamped and fixed on the SEM stage.
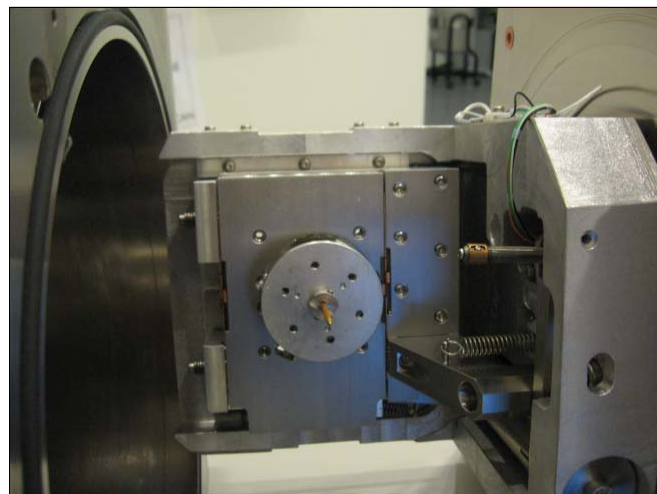
Figure 3.13. Image showing the TESA reference wire gauge, clamped to the stage and tilted to the maximum allowed amount, 78 degrees, on the SEM stage.

This limitation concerning the object tilting, which can not be positioned to exactly 90 degrees to align the item horizontally, may have some practical consequences. For instance, the object's illumination is not uniform and electrons are striking the object' surface not perfectly orthogonal to it, with some consequences on the secondary electrons detection. An example of the effect of a not uniform surface illumination can be seen in Fig.6.3 where the influence of image quality on SEM reconstructions is discussed. This effect is more relevant on the object's side and on features arising from the ideal cylindrical shape. Both the sides and these features are generally trimmed out from the point cloud, as discussed later on in section 4.4.

By knowing the wire gauge external diameter size, which is 250 μm, the optimum magnification, to be used to acquire high resolution SEM images can be calculated, based on the knowledge of the field of view. In this case, M=1000x assures the highest possible resolution, when point cloud stitching is not then considered, allowing also the acquisition of SEM images of the complete geometry of the cylindrical item. The working distance value is not decided a priori by the operator, but it results from the focus adjustment on the cylindrical item surface, which should be positioned as close as possible to the objective lenses. Working distance in the range between 8 and 11 mm, is a realistic estimation in this case. The rotational angle between two images forming the stereo-pair can instead be chosen by the operation based on the required measuring strategy. The MeX "Optimal Tilt Angle Calculator" tool enables the calculation of the optimal angle, starting from the knowledge of the field of view, the image resolution in pixels and estimated specimen height. In the case under consideration, the minimum and the maximum tilt angles suggested by the software are 2 deg. and 13 deg. respectively. For the choice of the optimum value within this range, some considerations should be taken into account. Smaller tilt angles, for instance, yield reconstructions with steeper slopes and they are suitable for higher specimens, while higher tilt angles provides better vertical resolutions and they are generally used with flat specimens (MeX[TM] Reference manual, 2007). In a previous work published by the author (Carli *et al*., 2009), the influence of the rotational angle on the 3D-SEM reconstructions quality was discussed. An example of 3D reconstructions of a cylindrical item, obtained using different rotational angles and starting from the same two SEM images, to perform stereo-pair technique, is shown in Fig.3.14. For the wire gauge under consideration, a trade-off value of 7 deg. was chosen based on the above mentioned considerations.

Moreover, Fig.3.14 demonstrates that good quality stereo-pair reconstructions are obtained by using a rotational angle equal to 7 deg. In conclusion, all the stereo-pair reconstructions of cylindrical items performed in this work were obtained using a rotational angle equal to 7 degree.
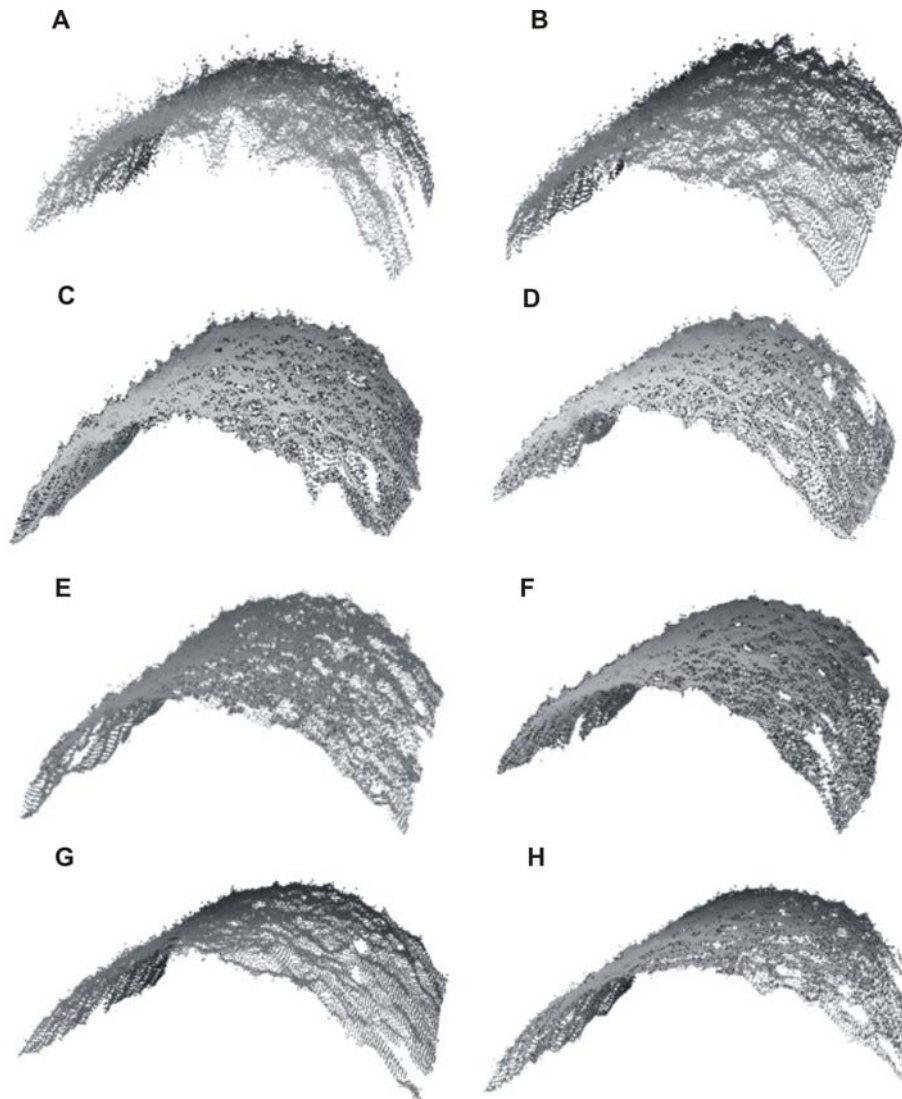
Figure 3.14. Example of 3D reconstructions of a cylindrical item, obtained using different rotational angles, from 3 deg. (A) to 10 deg. (H), in steps of 1 deg., to perform stereo-pair technique. All the 3D reconstructions were obtained starting from the same two SEM images composing the stereo-pair, therefore acquired in the same portion of the item (Carli *et al.*, 2009).

References

Abbe E. Arch. f. mikroskop. *Anat*. 1873; **9**: 413-468.

Bariani P. Dimensional metrology for microtechnology. Ph.D. Thesis, Department of Manufacturing Engineering and management. Technical University of Denmark, 2005.

Bariani P, De Chiffre L, Hansen HN, Horsewell A. Investigation on the traceability of three-dimensional scanning electron microscope measurements based on the stereo-pair technique. *Precis. Eng.* 2005; **29**: 219-228.

BIPM, ISO *et al.* ISO International Vocabulary of Metrology – Basic and General Concepts and Associated Terms (VIM), ISO, 2007.

Bozzola JJ, Russell LD. Electron Microscopy: principles and techniques for biologists. Jones and Bartlett Publishers, 1992.

Catalogue of TESA Technology. Hexagon Metrology, TESA, 2007/2008.

Carli L, De Chiffre L, Horsewell A, Carmignato S, Caroli M, Santin D. Improvement of geometrical measurements from 3D-SEM reconstructions. *11th CIRP Conference on Computer Aided Tolerancing*, Annecy, 2009.

Egerton RF. Physical Principles of Electron Microscopy, 2nd edition. Hardcover, 2005.

Goodhew P, Humphreys J, Beanland R. Electron microscopy and analysis, 3rd edition. Taylor & Francis group, 2001.

Goldstein DE, Newbury P, Echlin DC, Joy AD, Romig Jr, Lyman CE, Fiori C, Lifshin E. Scanning Electron Microscopy and X-ray Microanalysis, 2nd Edition. J. I. Plenum Press, 1992.

Heping P, Xiangqian J. Evaluation and management procedure of measurement uncertainty in new generation geometrical product specification (GPS). *Measurement* 2008; **42**: 653-660.

ISO/TC 213, ISO /TS 14253-2. Geometrical Product Specifications (GPS) – Inspection by Measurement of Workpieces and Measuring Equipment – Part 2: Guide to the Estimation of Uncertainty in GPS Measurement, in Calibration of Measuring Equipment and in Product, ISO, 1999.

JCGM (Joint Committee for Guides in Metrology)100:2008. Evaluation of measurement data - Guide to the expression of uncertainty in measurement (GUM), 2008.

Marinello F, Carmignato S, Savio E, Bariani P, Carli L, Horsewell A, De Chiffre L. Metrological performance of SEM 3D techniques. *Proc. of 18th IMEKO TC 2 Symposium on Photonics in Measurements*, Prague, 2008a.

Marinello F, Bariani P, Savio E, Horsewell A, De Chiffre L. Critical factors in SEM 3D stereo microscopy. *Meas. Sci. Technol*. 2008b; **19***;* 065705.

MeX^{TM} v 5.1. Alicona Imaging, 2007.

MeX^{TM} Reference manual. Alicona Imaging, 2007.

Piazzesi G. Photogrammetry with the scanning electron microscope. *J. Phys. E.* 1973; **6**: 392-396.

Scharstein D, Szeliski R. A taxonomy and evaluation of dense two-frame stereo correspondence algorithms. *Int. J. Comput. Vision. 2002;* **47**: 7-42.

Scherer S, Werth P, Pinz A, Tatschl A, Kolednik O. Automatic surface reconstruction using SEM images based on a new computer vision approach. *Electron. Microsc. Anal.* 1999; **161:** 107-10.

Wells OC, Joy DC. The early history and future of the SEM. *Surf. Interface. Anal.* 2006; **38**: 1738-1742.

4. Point cloud processing and feature extraction
for 3D-SEM metrology

4.1 Point clouds definition and characteristics

A point cloud is the result of an acquisition procedure where the point density depends on the sensor used for the measurement. Typically a contact sensor gives as a result only few points while a non-contact sensor gives an extremely dense point cloud in a few seconds measurement only. However, a single view is usually insufficient to fully measure an object in three dimensions. In this circumstance several digitisations from different orientation are required to fully cover the object. Each single view is assembled to the others by specific algorithms. The assembling accuracy can strongly influence the overall accuracy of the final model. The result of this phase, therefore, is a multiple view model of point clouds. In a second phase, the acquired point clouds are pre-processed in order to prepare the data for the surface features extraction. Points can be filtered in order to reduce the density of clouds and control the distribution over critical areas. During the post-processing phase it is possible to evaluate the deviations existing between reconstructed surfaces and features and the original point clouds. The assessment of such deviations is an essential step of the procedure for the estimation of system accuracy. The surface can be analyzed in terms of deviations against the cloud data (for example *via* colour plots). An example of output data, obtained by measuring the external surface of a hypodermic needle, using optical equipment from Werth and a multi-sensor strategy is shown in Fig.4.1.
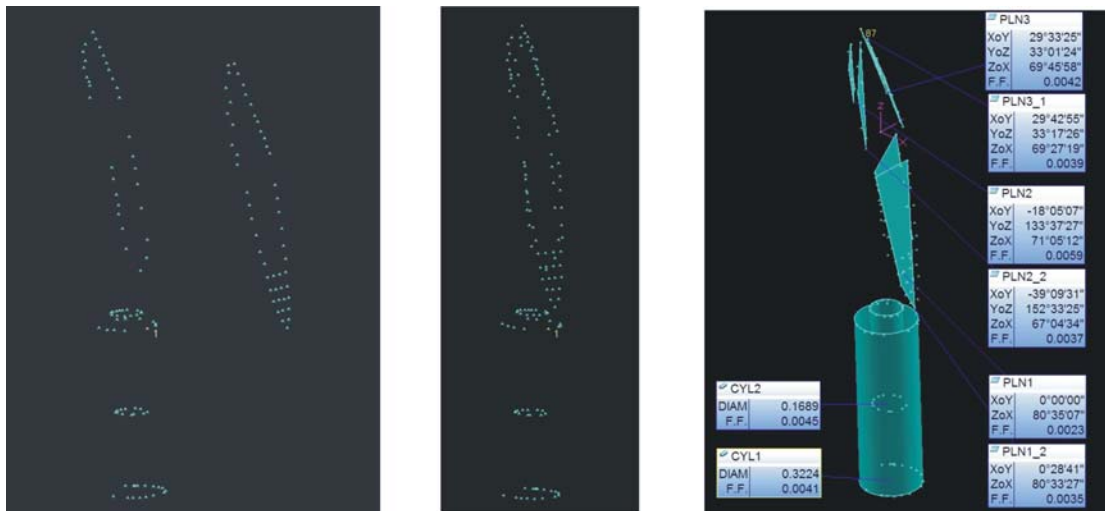
Figure 4.1. Example of multi-sensor technique measuring the external of a hypodermic needle with an optical Werth machine. Image on the left shows the resulting point clouds obtained measuring separately two different parts of the same item. The two point clouds where then assembled together obtaining data structure shown in the center image, while on the right is shown the reconstruction of partial elements with an example of results (Images courtesy of Dr. Vit Zeleny, Czech Metrology Institute, CMI).

Compared to tactile measurements, optical probing systems require many more parameters for describing the data structure. With reference to the general model of error sources for tactile CMMs, optical coordinate metrology introduces a series of additional sources of uncertainty. Therefore, measuring results of optical systems are influenced by many factors. A list of them is represented in Fig.4.2. In particular, many additional error sources take place from the interaction between the optical probe and the object. The number of these additional influence parameters is large and some of them are of a totally different nature than the ones seen in mechanical coordinate metrology. Therefore the operator may not be aware of their presence. The main uncertainty contributor in most applications is the optical characteristic of the work piece surface. For example, in most cases, very smooth surfaces cannot be measured because of insufficiently diffused, reflected light. Controlling the light intensity and the sensitivity of the detector can moderate this effect. For measurements that directly probe the surface of a specimen, often the surface characteristic itself dominantly contributes to the uncertainty of measurement. Depending on the principle applied, surfaces can be entitled cooperative or non-cooperative for a specific metrology.

Other common errors are also induced by: the slope of the surface (which may produce direct reflections to the detector), volume scattering (*e.g.* for plastic material), or an inhomogeneous surface texture. Secondary reflections, specular reflections, volumetric scattering, colour transitions, or ridges left by machining, may lead to gross systematic measuring errors. Typical error sources for measurements based on geometrical optics are lens distortion, spherical aberration, astigmatism and coma on the optical side and non-linearities and geometrical errors of the opto-electronic converters. Further additional uncertainty contributors are environmental illumination and errors in the registration of multiple views (Carmignato, 2005).
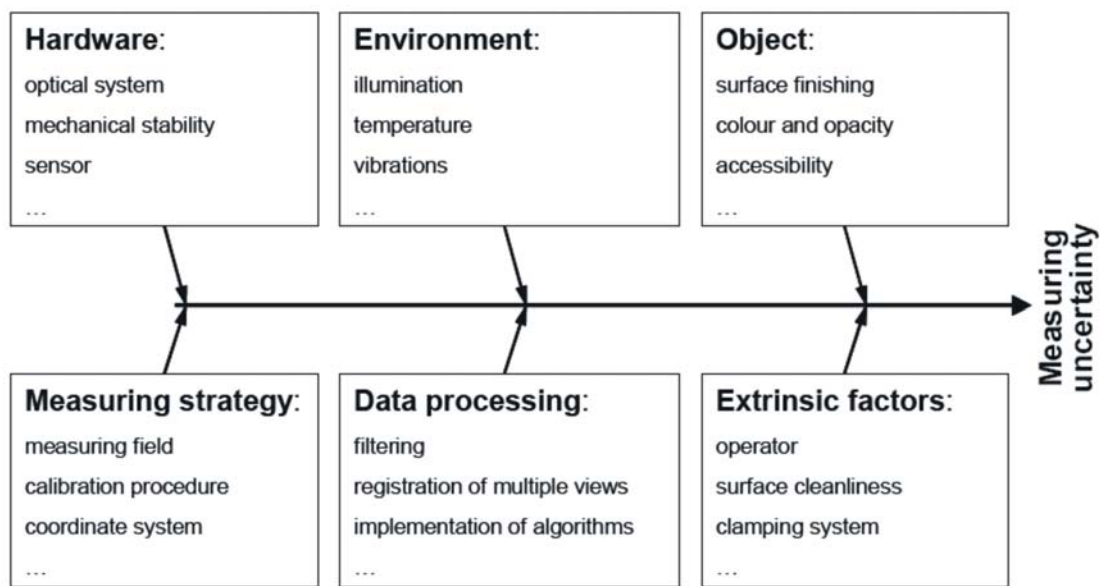
Figure 4.2. Summary of factors influencing the accuracy of optical systems (Carmignato, 2005).

4.2 Point cloud generation in SEM

With reference to the comparison between data structure obtained using tactile or optical probing systems, Scanning Electron Microscopy, which is based on detecting secondary electrons emitted by the object's surface (see section 3.1), has many similarities with the case of optical measurements. Almost all the factors affecting optical measurements uncertainty shown in Fig.4.3 are valid also in the case of SEM measurements, although with some important distinctions. SEM, in fact, is capable of measuring only conducting surfaces even though, in the case of plastic or reflective materials, it is possible to cover them with a thin layer of gold or silver, to allow overcoming such limitations (Cowley, 1987).

Moreover, SEM normally operates in vacuum condition, to avoid surface contamination and to improve performance of the detectors capturing the electrons scattered by the surfaces to be imaged (Cowley, 1987). All the SEM measurements presented in this work were carried out at the Center for Electron Nanoscopy (CEN), at DTU, where the building hosting the equipments was built putting efforts into reducing at the minimum vibrations, noise, external disturbances and temperature and humidity variations. Therefore, in the case of SEM, the effect of the environment on the measuring uncertainty is generally negligible and the main error sources are the ones introduced in section 3.3. In this chapter the uncertainty related to point clouds processing and on feature extraction will be investigated. These operations are generally performed at the very end of the SEM measuring process, but they are always needed in order to obtain consistent post-processed point clouds. For these reasons this investigation was performed at the very beginning to allow uncertainty evaluation of all the other main error sources afterwards. Point clouds are obtained from SEM measurements as a result of stereophotogrammetry technique applications. The software for stereo-pair reconstructions allows exporting data in a plain text format, and lets the operator choose the desired number of points composing the point cloud.

SEM images acquired in this work are composed by 1024x942 pixel in the x and y direction respectively, meaning that almost 1 million pixels are available to perform the 3D reconstructions. Among these about 100.000 pixels are used to visualize the measuring conditions information panel on SEM images and some others are excluded while choosing the desired Region of Interest (ROI) (see section 3.2.2). In the case of the wire gauge item under consideration (Catalogue of TESA Technology, 2007/2008), the region of interest is equal to the effective dimension of the item to be reconstructed, *i.e.* about 900x884 pixel (Fig.4.3). This situation still corresponds to a huge amount of data to be calculated by MeX^{TM} (2007) when performing the low and high-density digital elevation model (DEM), strongly influencing computational time. Moreover such a huge amount of data would make it difficult and very time consuming for the point cloud post-processing operations to be performed afterwards. For this reason, in this work clouds of about 60.000 points were considered when performing post-processing and feature extraction operations. The result of applying the stereo-pair reconstruction technique, to the item under consideration, yield then, as a result, to a raw point cloud which requires then a number of post-processing operations as described in the following section.
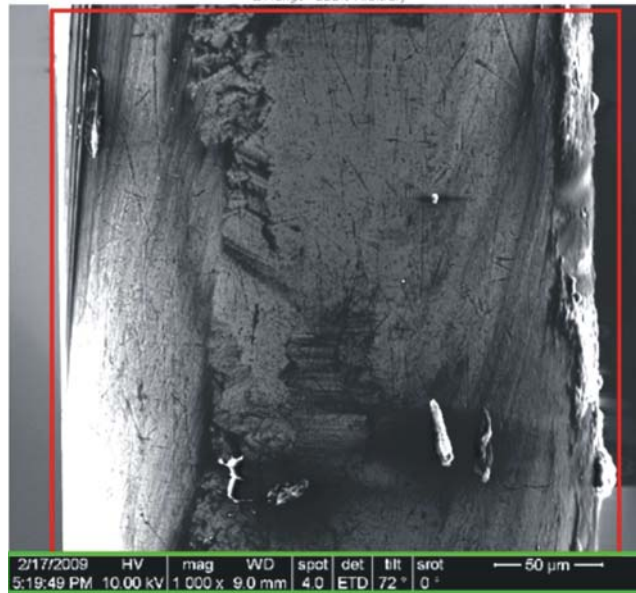
Figure 4.3. Example of SEM image of the wire gauge having an external diameter of 250 μm showing the whole amount of pixels in the x and y direction. Red squared area represent the typical Region of Interest (ROI), while the area marked in green represent SEM image information panel which consists usually in about 10^5 pixel.

4.3 Point cloud processing

Generally speaking, a number of post-processing operations can be performed on a given point cloud, among which some are more relevant than others from a metrological point of view. These actions are listed in Table 4.1 where it is also described whether they are performed manually by the operator or automatically by the software. Moreover the expected influence of these actions on the resulting post-processing point cloud is given. The trimming operation and the filtering are considered to be crucial since they are both modifying the shape of the raw point cloud. In order to better understand the influence of the different actions described in the Table 4.1, an example of point cloud processing is given where the different steps are described in more detail. Two point clouds were considered, both obtained from stereo-pair reconstructions performed using MeX, starting from three SEM images of a wire gauge with a reference diameter of 250 μm. Images taken at -7 and 0 degrees composed the stereo-pair named -7&0, while images acquired at 0 and +7 degrees formed a stereo-pair named 0&+7. The software used in this work, for point cloud processing, is a demo version of Geomagic Studio 10 (2008).

Action	Type	Expected influence	Section
Trimming	Manual	High	4.4.1
Outliers removal	Automatic	Medium	4.4.1
Filtering	Automatic	High	4.4.2
Sampling	Automatic	Medium	4.4.3
Meshing	Automatic	Low	4.4.3
Mesh trimming	Manual	Medium	4.4.3
Feature extraction and measurement	Automatic	Medium	4.4.4

Table 4.1. Example of post-processing operations which can be typically performed on a given point cloud. For every action it is specified whether they are performed manually by the operator or automatically and their expected influence on the final post-processed point cloud.

4.3.1 Point cloud trimming and outliers removal

A point cloud, obtained from stereo-pair reconstructions of a cylindrical object, looks typically as shown in Fig.4.4A. The SEM electrons scatter, on the sides of the item, generates a sort of "bat-wings effect" meaning that the shape of the cylinder cannot be precisely reconstructed at the extremities. This effect was observed in all the reconstructions performed by 3D-SEM technique of cylindrical shapes. A point cloud trimming is therefore needed, before performing a feature extraction of such geometry, to avoid cylindrical shapes extraction of points not directly belonging to the feature itself. This operation is typically performed manually by the operator, choosing the points to be trimmed out. As it will be demonstrated afterwards, this trimming operation is crucial as different operators might choose different points to be trimmed out. Furthermore the same operator might trim in different ways the same point cloud when repeated measurements are required.

Thus, this reproducibility error is mainly due to the manual points selection by the operator. In order to reduce as much as possible the variability introduced by this trimming operation, a stable procedure must be then developed to allow performing similar point cloud trims on different views of the same object or on the same view in the case if repeated measurements are required. In this work the following procedure was developed and applied to all the stereo-pairs to be later on analyzed and inspected:

1. Choose a "bottom view" of the item, which will be visualized, aligned with the yz plane. This allows the operator to recognize easily the points at the extremes of the cylinder not following a cylindrical shape. These points, which are marked in red in Fig.4.4B, can be later on removed;

2. Choose a "front view" of the item, which this time is visualized, aligned with the xz plane. With reference to Fig.4.4C the points selected at the previous step can be seen. Moreover, it is possible to see that some other points must be trimmed out not belonging to the cylindrical shape. These points could not be visualized at the previous step, thus this further step is always needed;

3. A trimming operation at the sides of the cylinder is then performed based on the two previous views and leading to a trimmed point cloud as shown in Fig.4.5.
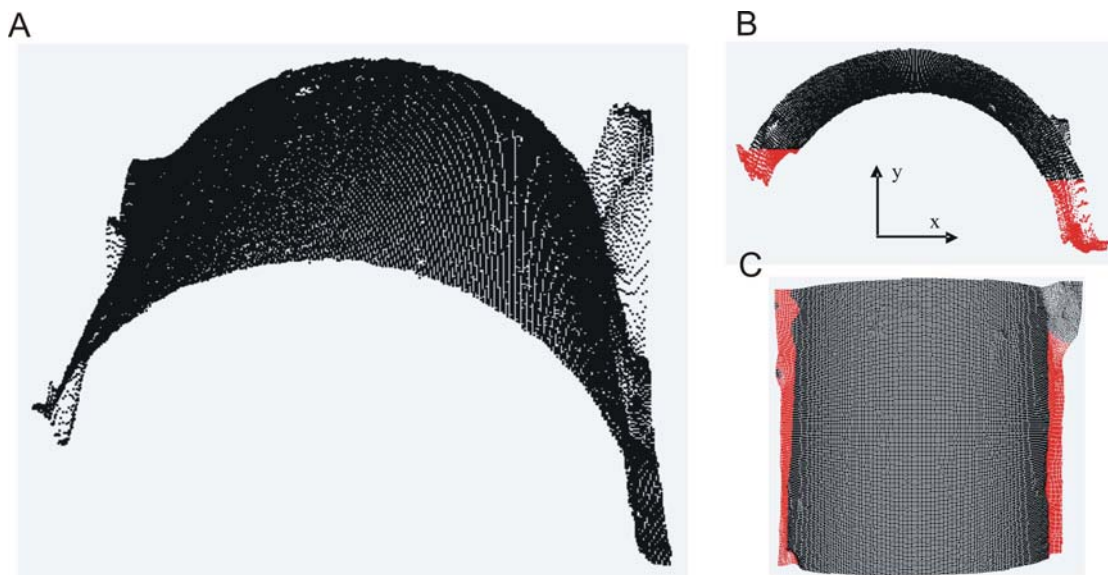
Figure 4.4. Example of point cloud resulting from stereo-pair reconstructions (A) and trimming operation performed considering first a bottom view of the item (B) and a then front view (C).
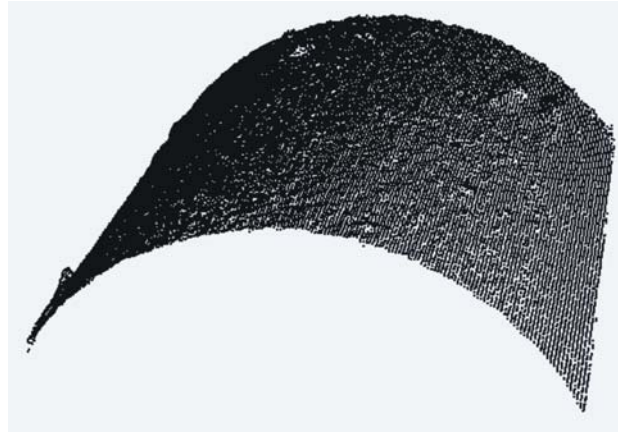
Figure 4.5. Resulting point cloud after trimming operation.

The point cloud obtained after the trimming operation described above, looks generally as shown in Fig.4.5. The "bat-wings effect" has been removed, but the presence of some "artefacts" on the cylindrical shape can still be noticed. Apart of the noise, which is supposed to be uniformly distributed, the presence for instance of dust, contamination or defects on the item's surface affect the cylindrical shape, creating some undesired "features" as it can be seen from Fig.4.5. The next post-processing operation, which can optionally be performed by the operator, is the outliers removal. According to Grubbs (1969), outliers are defined as follows: "An outlying observation, or outlier, is one that appears to deviate markedly from other members of the sample in which it occurs".

Based on this definition it can be concluded that an outlier, within a point cloud, is a point, which deviates remarkably from the overall shape of the surrounding points.

Different software for point cloud processing might implement diverse algorithms for outlier detection and removal. In this case, among all the different possibilities, Geomagic was chosen for its availability as demo version and for it's easy of use. Thus, its working principle will be described through an example based on the two stereo-pairs previously introduced. Concerning outlier detection, the software includes an user-friendly routine, which allows the operator to perform this operation just by choosing a "sensitivity level" ranging from 0 to 100 where a lower value limits selection to the farthest points, while a higher value includes a wider range of outliers. An experimental investigation was therefore performed to determine the sensitivity level setting leading to a proper outlier removal operation. Different levels were selected and the number of outliers detected by the software was recorded.

They can also be directly visualized in red colour on the trimmed point cloud as shown in Fig.4.6.

Figure 4.6. Example of a trimmed point cloud showing in red the points suggested being outliers from the Geomagic routine Select Outliers.

The experimental investigation allowed the calculation of the percentage of outliers removed with respect to the overall number of points composing the point cloud. The results for two stereo-pairs, -7&0 and 0&+7 is shown in Fig.4.7.

◆ stereo-pair -7&0   ● stereo-pair 0&+7
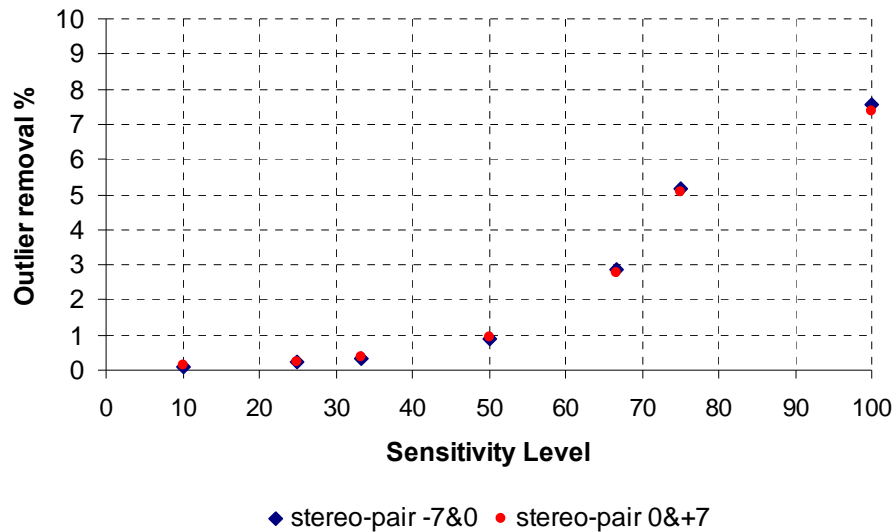
Figure 4.7. Graph showing the outliers removal rate, as a percentage of the original number of points composing the cloud, as a function of the chosen Sensitivity Level for two stereo-pairs named -7&0 and 0&+7. An exponential trend-line could be fit for Sensitivity Levels below 80.

The application of different sensitivity levels, on two different stereo-pairs, as shown in Fig.4.7, led to the following conclusions:

- As the sensitivity level increases the number of detected outliers also increases for both stereo-pairs;

- The increase rate follows an almost perfect exponential trend for sensitivity level lower than 80, then, even if the sensitivity level is set to higher values, an asymptotic trend can be observed;

- Small differences regarding the number of outliers detected on the two different stereo-pairs can be noticed, as probably both the raw point clouds were composed by the same number of points (*i.e.* 37500);

- Approximately 7.5% of the points composing the cloud are considered to be liable of being outliers when the sensitivity level is set to the maximum value *i.e.* 100 and about 3% for the default value of 66.6.

Based on the previous consideration a sensitivity level equal to 66.6 was chosen to be used for all the following experimental activities described in the next chapters. This choice is based on the fact that, by selecting this value, the operator can still remove a consistent number of outliers, which is approx. 3% (*e.g.* 1071 outliers) of the original number of points, still within the exponential trend working area of the routine. A different tool can also be used to investigate the influence of the sensitivity level on the point cloud shape. Being the item to be measured a cylinder, it is possible to calculate a radius, for each point composing the point cloud, starting from the x, y and z coordinates. Thus, the radii distribution can be plotted in a histogram showing the frequencies for each class of intervals of the given variable. Choosing intervals corresponding to 100 nm, a graph is then obtained where the radii distribution of the original trimmed point cloud is compared with the one obtained after setting the sensitivity level equal to 66.6 (Fig.4.8) and with the one at 99.9 (Fig.4.9). These two graphs provide also a better understanding of the outlier removal mechanism, by observing the difference in the distribution between the original point cloud and the one resulting from outlier's removal. The distribution shape, in fact, is changing on the sides, but it remains constant in the central part where the radii frequencies are higher. This effect becomes even more relevant when the sensitivity level is increasing.
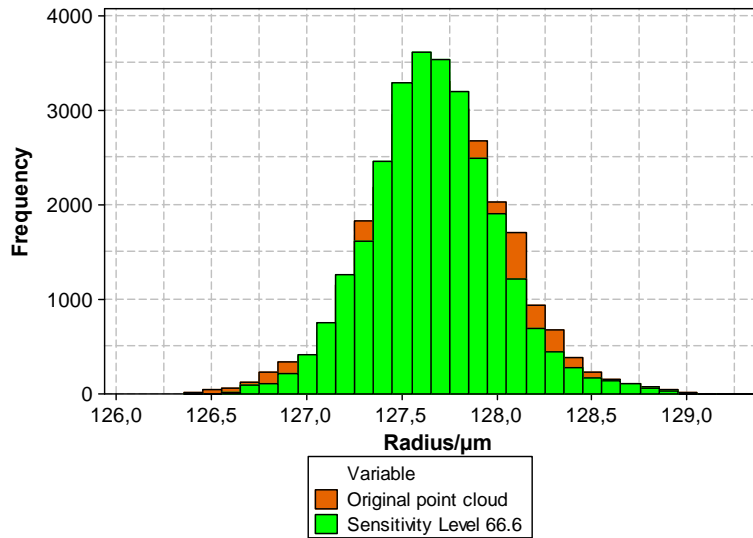
Figure 4.8. Histogram showing the frequency of radii distributions for a point cloud obtained by measuring a cylindrical item. The distribution of the original point cloud is compared with the one resulting from the application of a Sensitivity Level equal to 66.6. The number of intervals was chosen to achieve an interval range of 100 nm.
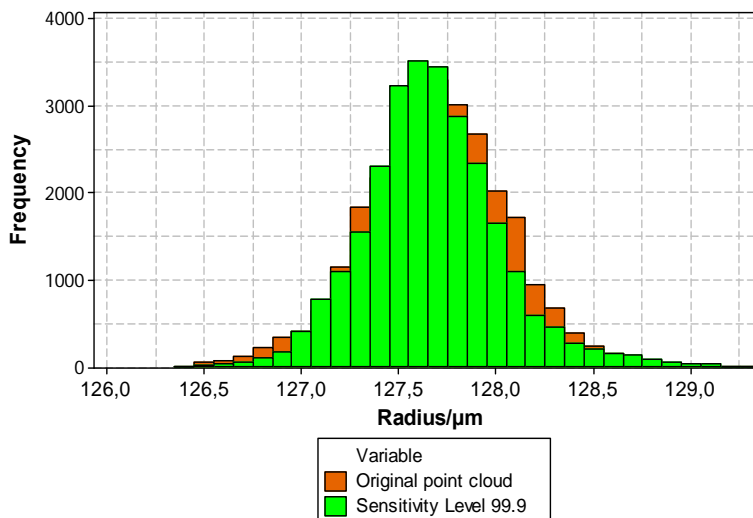
Figure 4.9. Histogram showing the frequency of radii distributions for a point cloud obtained by measuring a cylindrical item. The distribution of the original point cloud is compared with the one resulting from the application of a Sensitivity Level equal to 99.9. The number of intervals was chosen to achieve an interval range of 100 nm.

4.3.2 Point cloud filtering

The result of the previous two operations, trimming and outlier detection and removal, is a point cloud having a cylindrical shape and exhibiting some holes deriving from the outliers removed. Nevertheless there is always a certain amount of noise in SEM images, coming from different sources such as vibrations, charge-up of specimen surface and improper setting of instrument parameters. These noise sources will be discussed in more details in chapter 6, anyhow as a general rule the noisier the SEM image the noisier the resulting 3D reconstruction. Four classes of filters have been proposed by the recent ISO/TS 16610-1:2006 (2006) series of standards and they were described in (Savio, 2007):

• <u>Linear Filters:</u> replace every point of the measured data with a weighted average of points in its neighbourhoods. An example is the Gaussian or the Spline filter (Krystek, 1996);

• <u>Morphological Filters:</u> based on mathematical Minkowski operations, where dilation and erosion are the two fundamental morphological operations (Muralikrishnan, 2005);

• <u>Robust filters:</u> are tolerant to outliers, *i.e.* they are insensitive to extreme points. These are effective in particular when measurements are affected by localized disturbances, or when external features interfere with measurement operations;

• <u>Segmentation filters:</u> are useful for dividing a surface into its constituent homogeneous sub-regions.

Among the four classes of filters described above, linear filters are the only ones adopted for noise reduction. In this section, point cloud filtering, aimed to remove or to reduce the presence of noise, is discussed with an exampled based on the application of the Geomagic routine called Reduce Noise. This routine first asks the operator to choose between two different point cloud shapes, free form or prismatic, and then it allows the operator to set two different input parameters named Smoothness Level and Iterations. In particular, the smoothness can be set at 5 different levels from None (0) to Max (4), while the iterations can range from 1 to 5. The Smoothness Level slider specifies the degree of noise reduction *e.g.* the aggressiveness of point detection. The software recommends using typically the lowest setting that gives acceptable results. By selecting the desired values for both the input parameters described above, a number of outputs are available for the operator such as a display showing the deviations from the unfiltered point cloud, the maximum and the average distance of the filtered points and their standard deviation.

Among all the possible available outputs, an useful information is represented by the average distance, which is an indication of the amount of noise being suppressed in the point cloud. This can be defined as the mean distance of each point from a fitted mean line. A graph was therefore produced plotting the resulting average distance as a function of the four available Smoothness Levels and of the iterations number (Fig.4.10).
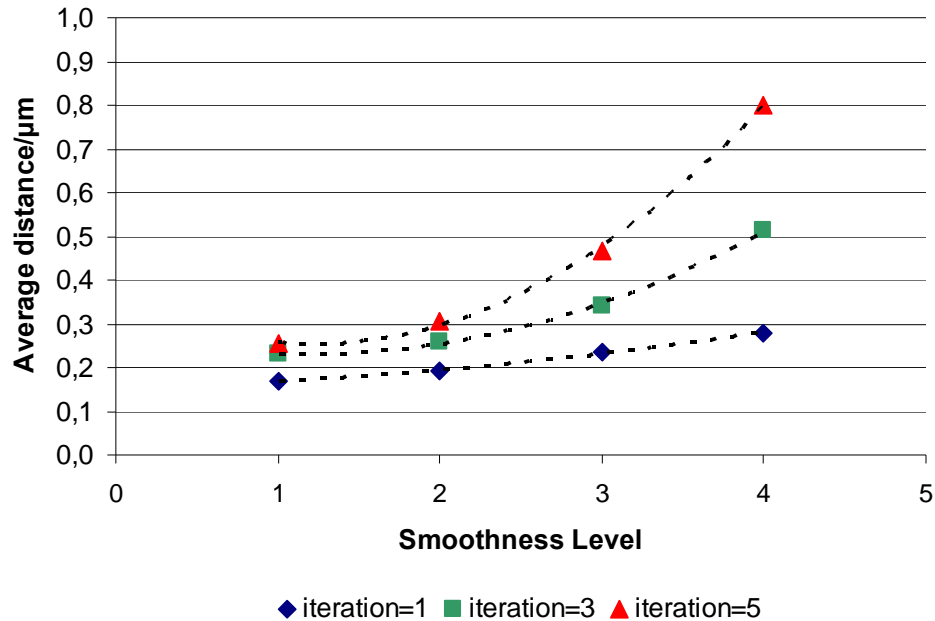
Figure 4.10. Graph showing the average distance as a function of the Smoothness Level and the iterations number. The correlation between the average distance and the Smoothness level was found to follow a second order-fitting trend (dotted line) at any iteration number.

It was found that, as the Smoothness Level is increasing, also the average distance is increasing, following a second order-fitting trend at any choice of the iteration number. Moreover, the influence of the iterations becomes relevant only for Smoothness Levels equal to 3 or 4. Similarly to the outlier's removal case, a graph was produced showing the change in the radii distribution frequency, compared to trimmed and unfiltered point cloud, as a consequence of setting different values of the Smoothness Level (SL) choosing iteration (it) equal to 1 (Fig.4.11) or iteration (it) equal to 5 (Fig.4.12).
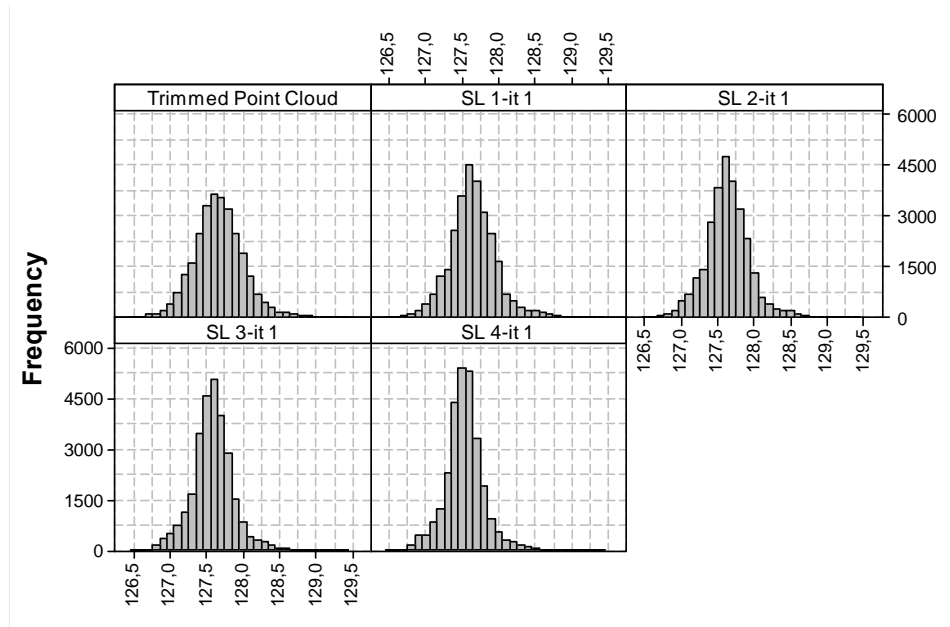
Figure 4.11. Graph showing the change in the radii distribution frequency, compared to trimmed and unfiltered point cloud, as a consequence of setting different values of the Smoothness Level (SL) choosing iteration (it) equal to 1. The number of intervals was chosen to achieve an interval range of 100 nm.
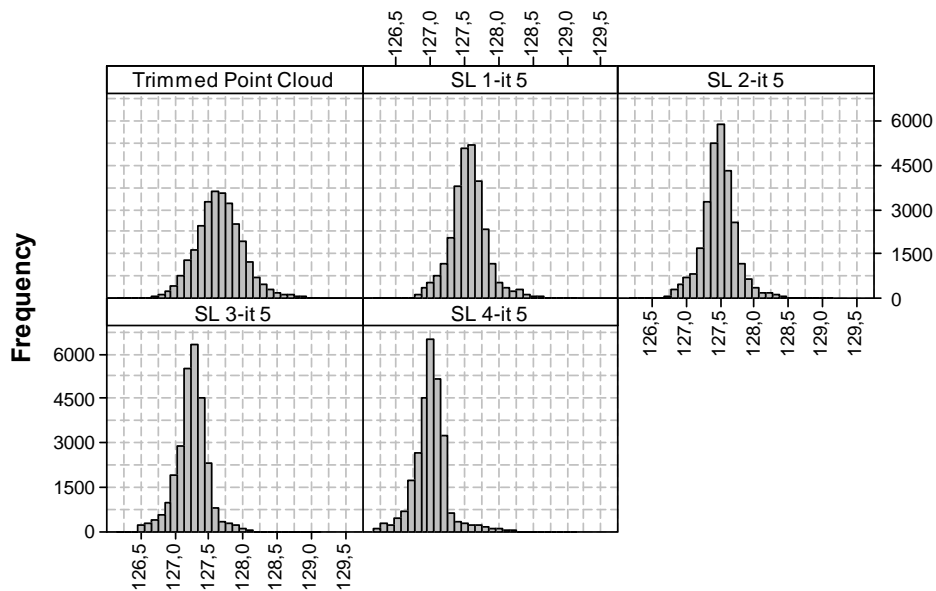
Figure 4.12. Graph showing the change in the radii distribution frequency, compared to trimmed and unfiltered point cloud, as a consequence of setting different values of the Smoothness Level (SL) choosing iteration (it) equal to 5. The number of intervals was chosen to achieve an interval range of 100 nm.

Considering the previous results, it can be concluded that an inappropriate choice of Smoothness Level and the number of iterations might lead to changes in the point cloud shape. This fact can be observed from the radii distribution frequency, which is getting narrower (*i.e.* with a reduced standard deviation), compared to the case without filtration. This effect is becoming more relevant for iterations equal to 5, while is much more limited in the case for iteration equal to 1. Therefore, as the aim is to obtain a filtered point cloud without changing its original shape, setting the iteration number to 1 would reduce the chances of getting a shape modification. Moreover, the graph of Fig.4.11 shows that a shape modification in the radii distribution frequency starts to occur for a Smoothness Level equal to 3. As a conclusion, in this work, all the point cloud, requiring filtration process, were filtered, after outliers were removed, by setting the Smoothness Level=2 and iteration=1. As a result of the filtration process a point cloud, as the one shown in Fig.4.13, is then obtained with the colour plot showing deviations from the mean nominal value calculated by the software. Areas represented in red or orange exhibit deviations above 500 nm, corresponding to portions of the item contaminated by dust or affected by the presence of defects on the structure.
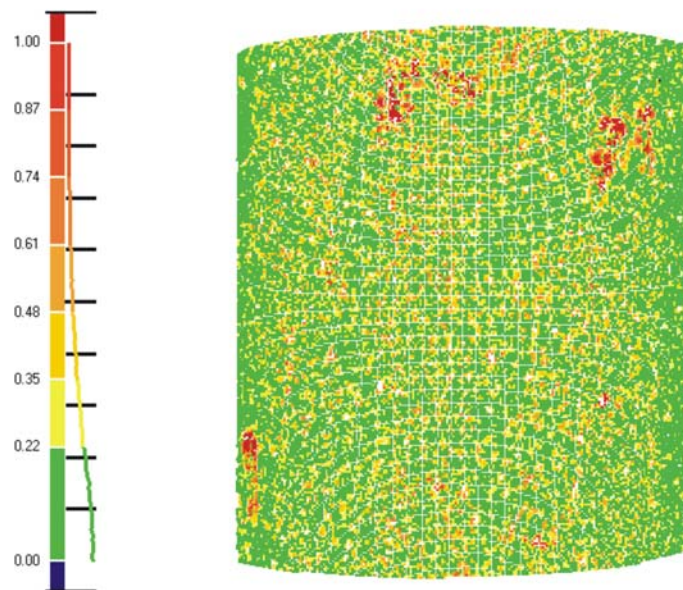
Figure 4.13. Example of a point cloud resulting from the filtration process. The colour plot shows deviations from the mean nominal value calculated from the software. Areas represented in red or orange exhibit deviations above 500 nm, corresponding to portions of the item contaminated by dust or affected by the presence of defects on the structure.

4.3.3 Point cloud sampling, meshing and mesh trimming

Software for point clouds processing can usually handle a large amount of data. Anyhow, if for instance multi-orientation strategy, performing point cloud stitching, is lately foreseen, a too large amount of data may cause too long computational time. Therefore the operator could decide to reduce the number of points composing the cloud by performing a uniform sampling, which could be random or feature based, following for example the curvature. This option is implemented in the Geomagic version tested in this work, which allows choosing the desired number of points composing the cloud to be obtained after sampling also enabling an optimization based on curvature priority. The uniform sampling routine was not used in this work, since the trimmed point cloud consists of about 37000 elements. Nevertheless, a quantitative analysis of the effects of point cloud sampling on the final diameter estimation has been performed in the following sections. Much more relevant, in the case under consideration, is the point cloud meshing performed by "wrapping" the point cloud by selecting the desired number of target triangles. An example of a mesh operation on the point cloud under consideration is shown in Fig.4.14 where two wrapped point clouds are reported. The relevance of a point cloud filtering operation before wrapping appears clearly from the two images comparison. From images reported in the previous figure, the presence of some bumps deviating from the ideal cylindrical shape can be observed. If then the operator is performing a feature extraction operation on such a wrap, these "defects" can affect the ability of the software to perform properly the, least square, algorithm to determine the cylinder diameter. These defects might be due to the presence of dust on the external surface of the wire gauge prior to the SEM measurements, or to imperfections coming to the manufacturing process, as this reference item is not usually intended for optical measurements, but for tactile ones.
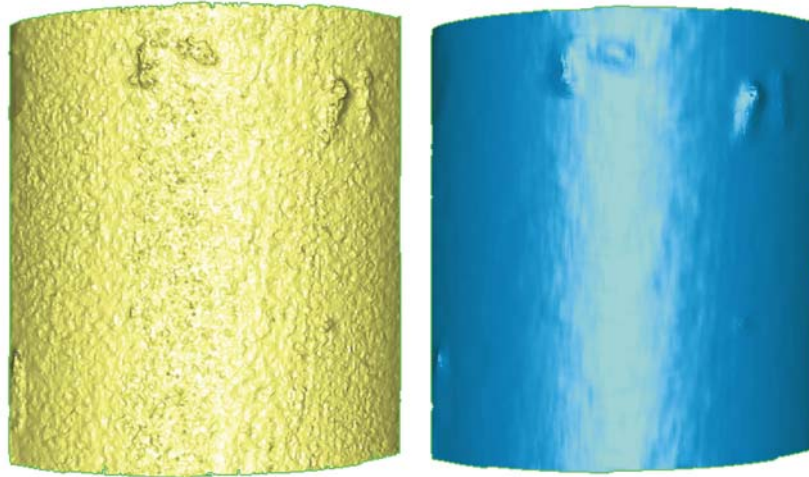
Figure 4.14. Examples of wrapped point cloud resulting from meshing operations. The effect of performing a noise reduction operation before wrapping, results clearly from the comparison of the unfiltered (left) and filtered (right) image.

Thus, it could be relevant to remove these spots from the wrap before performing a feature extraction operation and calculating the diameter. This operation is facilitated by a deviation plot routine implemented in the feature extraction tool in Geomagic, therefore it is described in the following section.

4.3.4 Feature extraction and diameter evaluation

Generally speaking, commercial software allow the operator to choose among different kinds of features, to be extracted from a given point cloud. For instance, the Geomagic "Create Feature tool" allows choosing one of the following four ones: plane, sphere, cylinder and cone. Having chosen the desired geometry a best fit algorithm, based on the least square method, is then implemented leading, for instance, to a best fit cylinder in the case under consideration. A panel shows the base points of the cylinder and the direction with respect to x, y and z-axis in the space, together with a height and diameter estimation. Moreover, the operator can decide to visualize the deviations of the given point cloud to the best fit cylinder. As a general rule, it is relevant to visualize these deviations to establish whether the reconstructed cylinder is fitting the point cloud properly. Furthermore a colour plot bar is given enabling quantitative and qualitative comparisons of these deviations.

In Fig.4.15 an example of deviation plot, in the case of a point cloud resulting from 3D-SEM, when measuring the wire gauge with a reference diameter of 250 μm, is shown. The colour bar scale allows distinguishing points with a distance within ±0.15 μm range, corresponding to the provided accuracy of the reference item, from points showing higher deviations.
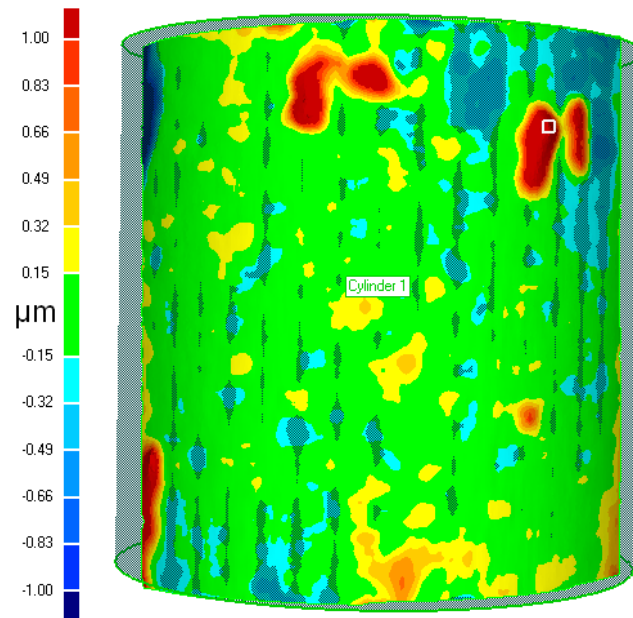
Figure 4.15. Example of deviation plot, in the case of a point cloud resulting from 3D-SEM technique when measuring the wire gauge with a reference diameter of 250 μm.

In the case in hand it can be seen as the largest amount of points showing a distance within the item accuracy range, represented in green, while few others lay within the range of about ±0.60 μm (yellow and light orange if positives, light blue and turquoise if negatives). On the other hand, spots coloured in red and in dark blue show much higher deviations. Taking a deeper look to these surface portions it can be noticed that they correspond to the item defects or bumps previously described, in the case of high positive deviations, and to improper stereo-pair reconstructions, in the case of highly negative deviations. The latter are probably due to bad SEM image quality in the area of interest. In both cases, as these areas might affect the diameter estimation through the best fit algorithm, the operator could decide to trim those spots out of the wrapped point cloud in order to allow a more accurate feature extraction and diameter estimation as shown in Fig.4.16.
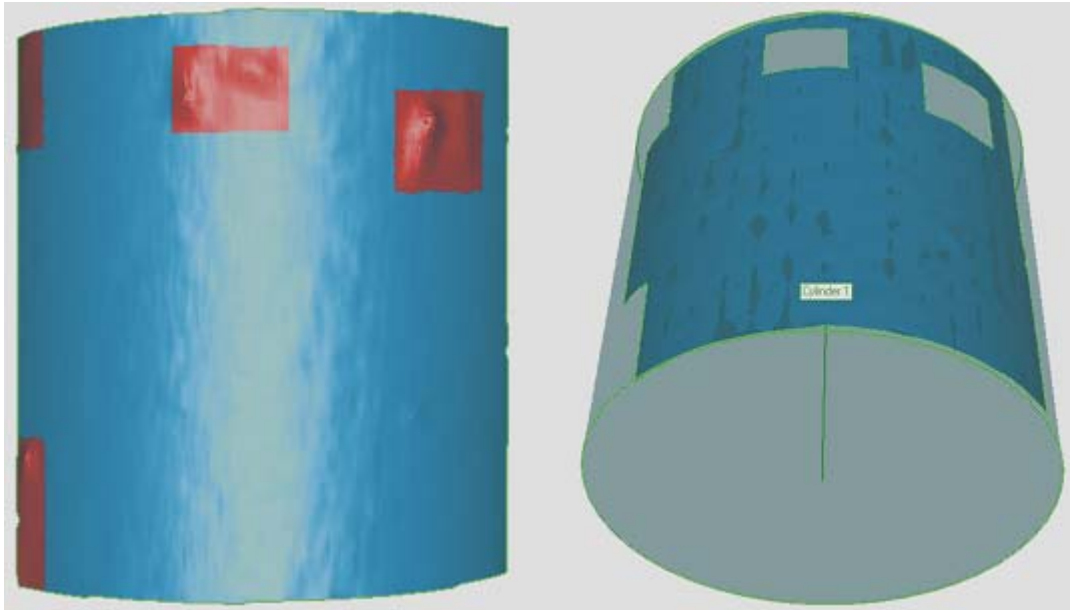
Figure 4.16. Example of wrapped point cloud trimming (left) to exclude portions of the item not belonging to the cylindrical shapes deriving from presence of dust during SEM measurements or to imperfections of the item under consideration. The resulting feature extraction operation performed on this trimmed wrap is shown in the right image.

4.4 Experimental investigation on the effects of point cloud processing on diameter calculation

Among the operations described in Table 4.1 to be performed on point clouds, some are more relevant than others both from a qualitative and a quantitative perspective. A point cloud resulting from stereo-pair reconstructions needs, in fact, to be trimmed to remove the so called "bat-wings effects", moreover outliers removal and filtering are desirable operations to improve point cloud quality before feature extraction. On the other hand, the sampling, the meshing and the mesh trimming are operations that might not always be needed, although they could be necessary time by time. Based on these considerations an experimental investigation was carried out to determine the influence of every single point cloud processing operation on the resulting feature extraction procedure and in diameter estimation.

It is relevant to determine the influence of choosing different sensitivity levels (for outliers reduction) or filtering smoothness in the diameter estimation. For this reason an analysis of variance (Montgomery, 2008) was performed considering two influencing factors, the outliers sensitivity and levels and the reduced noise smoothness, each one set at different values as shown in Table 4.2.

The experimental investigation was carried out starting always from the same trimmed point cloud, to not take into account the error source introduced by the trimming operation, and considering only the stereo pair -7&0. The results are summarized in Table 4.3 where DF indicates the degrees of freedom (*i.e.* number of levels minus one), the *p*-value (P) and the percentage sum of squares (SQ%).

Error source	Factor	Levels				
Point cloud processing	Outliers Sensitivity	0	66.6	100		
	Reduce Noise Smoothness	0	1	2	3	4

Table 4.2. List of factors and levels considered for testing the influence of point cloud processing, performed by the operator, on the resulting diameter estimation, by performing an analysis of variance.

Source	DF	P	SQ%
Outliers Sensitivity	2	0.080	0.3
Reduce Noise Smoothness	4	0.000	99.3
Error	8		
Total	14		99.6

Table 4.3. Results of the analysis of variance considering outliers sensitivity and reduce noise smoothness as factors set at different levels. Degrees of freedom (DF), *p*-value (P) and percentage sum of squares (SQ%) are indicated. The two factors under consideration account for 99.6% of the overall results variability, and outlier sensitivity was found not to be significant (*p*-value >0.05).

From the experimental results the outliers sensitivity is shown not to be significant, being p-value >0.05. Furthermore, the reduce noise smoothness is highly significant accounting for 99.3% of the overall variability. The results for diameter calculation are shown in Fig.4.17 where the graph shows the calculated diameter of the cylindrical item under consideration, as a function of the different levels tested for reduce noise smoothness and outliers sensitivity. From data analysis it can be concluded that the presence of a large amount of noise, in the case of unfiltered point cloud, is leading to a difference of 0.4 μm in the resulting diameter compared to the case of point cloud filtered with the highest possible smoothness. Moreover, as the reduce noise smoothness is increasing, the diameter value is also decreasing although with variations in the sub-micron order. This is due to the fact that high smoothness values lead to a slight modification of the point cloud shape as demonstrated in Fig.4.11 and Fig.4.12. The outlier removal results not to be relevant since its effect on the diameter is of the same order of magnitude as the software resolution which is 0.1 μm. Therefore the operator can perform an outliers removal operation without affecting the diameter calculation. Moreover, a reduce noise smoothness equal to 2 was shown to be the optimum trade off, among the different levels tested, with respect to its ability to filter noise without modifying consistently the shape and distribution of the points composing the cloud.
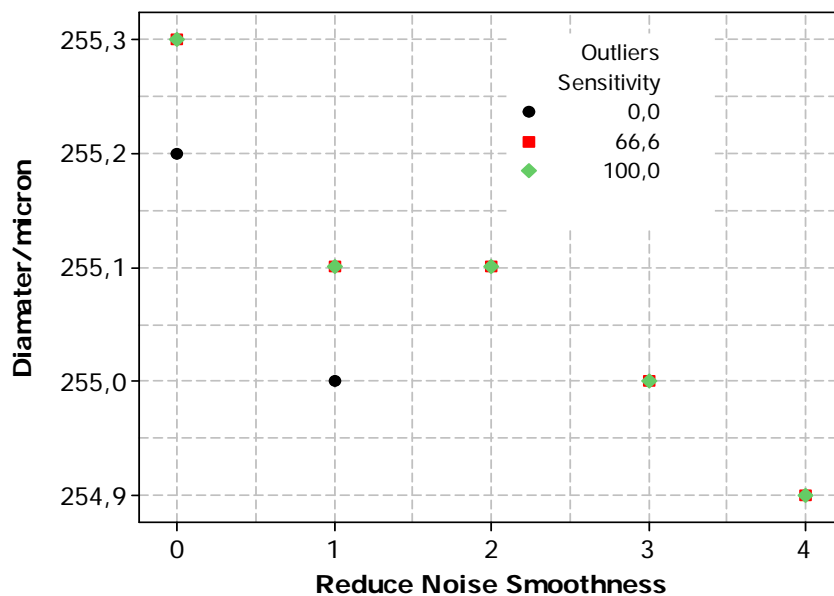
Figure 4.17. The graph shows the calculated diameter values as a function of the different levels tested for the reduce noise smoothness and the outliers sensitivity.

Having tested the quantitative effects of setting different values of outlier reduction and noise reduction, it is also relevant to test the efficacy of the feature extraction and diameter estimation tool. When a point cloud stitching operation is for instance, foreseen, or the utilization or another software for data analysis is needed, it might be necessary to reduce the number of points composing the cloud to decrease the computational time and to simplify the data handling process. For this reason a feature extraction and diameter calculation operations were performed on the original point cloud, composed of 36604 points, and on the point clouds resulting from a curvature based or a random sampling process. For instance, the application of a 75% sampling, on the original point cloud, results in a 25% points reduction. From the results reported in Fig.4.18 it can be concluded that the feature extraction operation is very efficient also when performed on a limited amount of data, as the calculated diameter is not significantly changing even for a sampling equal to 5%. Difference between the curvature base and the random sampling is below 0.1 μm for sampling higher than 50%, and then it starts to increase up to a maximum of 0.4 μm. This could be explained by the fact that, as the number of points is significantly reduced, a sampling performed on the curvature base and not on a random one should lead to more consistent results as the shape of the point cloud is maintained.
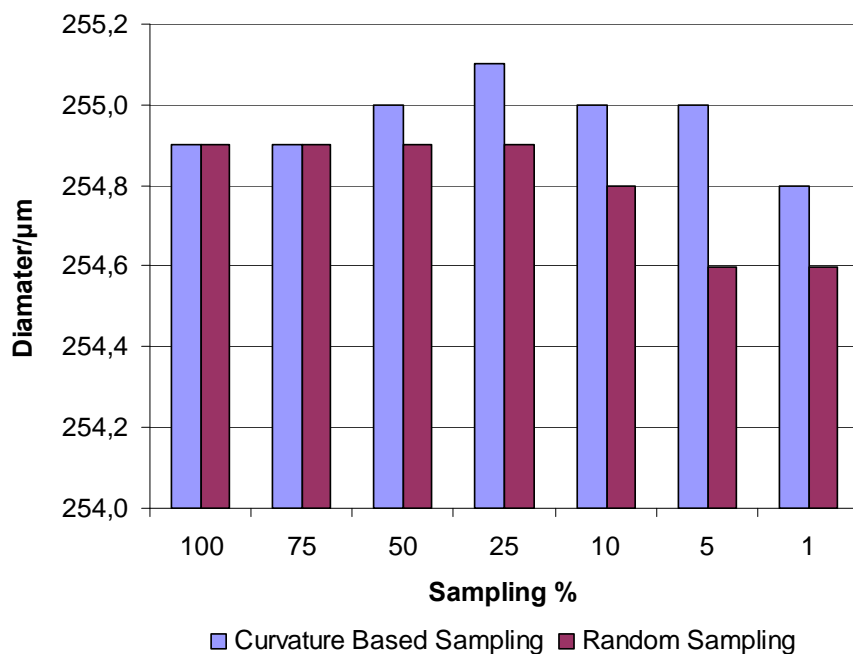
Figure 4.18. Graph showing the diameter estimation as a function of a sampling operation performed on a curvature based or on a random manner.

In all the previous experimental investigations the trimming operation was assumed to be constant, meaning that the outliers removal and the filtering operations, for instance, were always performed starting from the same trimmed point cloud. By doing this it was possible to estimate the influence of the different operations dealing with point cloud processing, on the resulting diameter calculation. Considering again Table 4.1, it could be seen that the only operations to be manually performed by the operator are the point cloud trimming and the mesh trimming, meaning that a further error source is then introduced.

In fact, as every point cloud, resulting from a different stereo-pair, requires a different kind of trimming based on the raw point cloud shape, this operation might be relevant when aiming to perform a proper uncertainty evaluation. Moreover, performing a trimming operation on the same point cloud, with the same operator, would generally result in small differences, which anyhow might be relevant for the diameter calculation. For this reason a trimming operation was performed 15 times on two different stereo-pairs, -7&0 and 0&+7, by the same operator, keeping constant the outliers removal sensitivity=66.6 and the reduce noise smoothness=2 with 1 iteration.

This investigation allows evaluating the uncertainty of the trimming operation, in terms of measurement repeatability, deriving from the standard deviation of the 15 replicated experiments for both the stereo-pairs under consideration. The experimental results are illustrated in Fig.4.19, while the mean value and the standard deviation of the 15 replicated experiments, for the two point clouds under considerations are shown in Table 4.4.
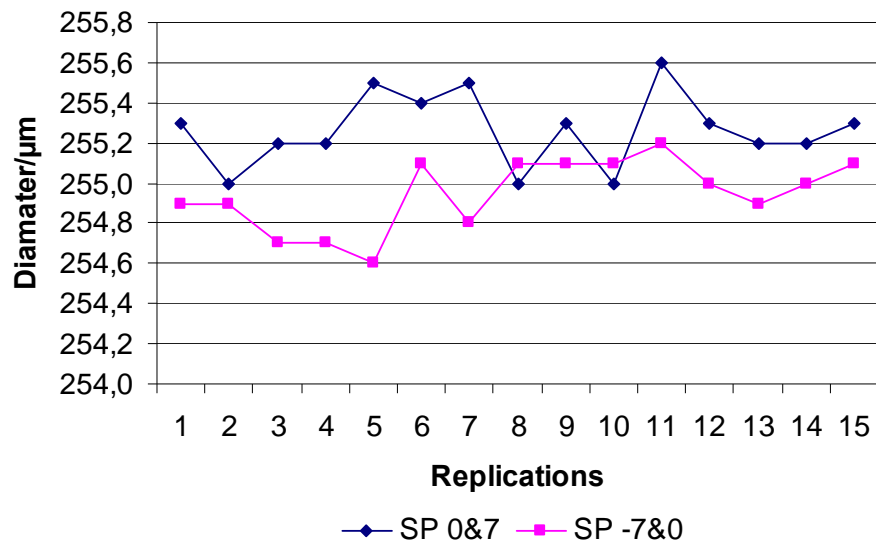
Figure 4.19. Results of 15 replicated experiments carried out to evaluate the influence of the trimming operation on the calculated diameter for two different stereo-pairs. Outliers removal sensitivity and reduce noise smoothness were kept constants and equal to 66.6 and 2 respectively.

	Diameter/µm	
	SP -7&0	**SP 0&+7**
Mean value	254.9	255.3
Standard deviation	0.2	0.2

Table 4.4. Mean value and standard deviation for the diameter calculated from the 15 replicated trimming operations performed on two stereo-pairs: -7&0 and 0&+7.

From results shown in Table 4.4 it can be concluded that the standard deviation (k=2) of 15 replicated trimming operations, is equal to 0.4 µm for both the stereo-pairs under consideration. This error source is by far higher than the uncertainty related to the Geomagic resolution. In fact, being the resolution equal to 0.1 µm, the related uncertainty can be evaluated, according to ISO GUM (JCGM 100:2008), as $R/2\sqrt{3}$ therefore resulting equal to 0.03 µm.

4.5 Development of a Matlab routine for point cloud processing

A Matlab® 7.4 (R2007a) routine was developed in collaboration with Ph.D. student Gianfranco Genta from Politecnico di Torino, Italy. The aim was to establish an automatic procedure for point cloud processing, starting from a trimmed point cloud and obtaining a number of different outputs providing relevant information about the point cloud under investigation. A list of the more relevant operations, performed by the Matlab code, is here given. These operations are described through an example based on the point cloud resulting from the stereo-pair -7&0 analyzed in the previous sections.

1. Open the Matlab routine and upload the point cloud dataset;

2. Dataset reduction, down to the desired number of points, performed using a random point selection from the original dataset. The size of the resulting dataset is linked to the computational capabilities of the computer processor used for running Matlab. A commercial pc nowadays available is typically capable of handling dataset with 15000 points without crashing;

3. Saving of a txt file with the new dataset to allow further analysis;

4. Application of the Least Mean Square (LMS) algorithm, through the *lscylinder.m* routine (developed by the National Physical Laboratory (UK) and available online), to determine some preliminary cylinder parameters such as: coordinates of the center ($x0_n$), vector representing the spatial directions of the three main axis (a_n), and an first estimation of the cylinder diameter (r_n);

5. Estimation of the angular size and of the axial length of the point cloud;

6. Creation of a virtual cylinder, through the routine *cyl3d.m,* having the same characteristics estimated at step 5 for the point cloud under processing, but oriented along (0, -1, 0) vector in the space;

7. Application of an ICP algorithm (routine *icp.m*) for calculating the relative roto-translation matrix between the real and the virtual point cloud to perform a spatial alignment (Fig.4.20). This procedure is necessary in order to make the point cloud to be oriented along (0, -1, 0) vector in the space, otherwise the outliers removal operation would not be feasible;

8. Angular (θ) and radial (r) outliers identification and removal. The outlier detection on angular position eliminates angular portions of the point cloud at the extremes, not removed by the trimming operation. The outlier detection on radial distance (from the centre of least-squares cylinder) is aimed to eliminate residual anomalies. It exploits a modified version of IQR (Interquartile Range) method (Barbato, 2010). In general, the number of outliers detected on angular position is small, whereas the number of outlier on radius is significant, as it can be seen in Fig.4.21;

9. Saving of the point cloud dataset after outliers removal and plot in a Matlab window;

10. Evaluation of cylindrical item geometrical parameters by means of least squares and statistical analysis (Matlab® 7.4, R2007a). In order to evaluate object form error, the Absolute frequency histogram of radius (radial distance of each point from the centre of least-squares cylinder) has been evaluated, together with the relevant normal probability plot. An example related to stereo-pair -7&0 is shown in Fig.4.22;

11. Creation of a final matrix containing the radius values after dataset reduction, after angular outliers removal and after radial outliers removal, *i.e.* the final estimated radius.
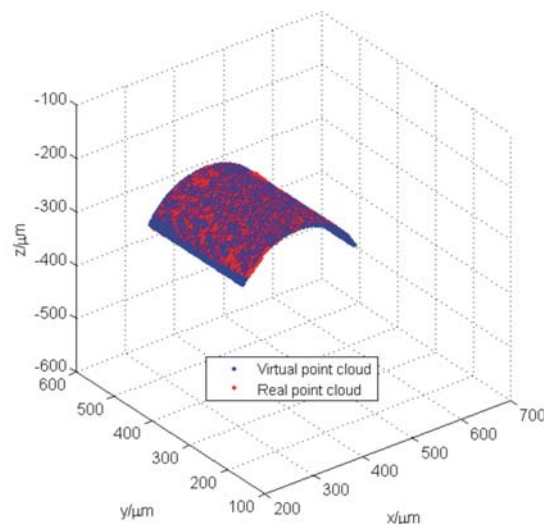
Figure 4.20. Result of a roto-translation performed by ICP routine in Matlab, to align the point cloud under investigation to a virtual point cloud oriented along (0, -1, 0) vector in the space, to allow outliers removal operations.
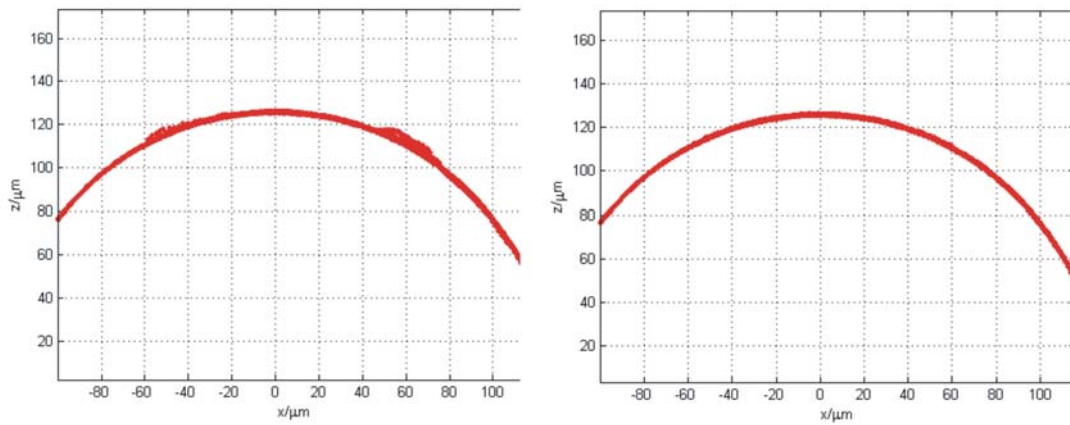
Figure 4.21. Image showing the 2D profile of the cylinder after angular outliers removal (left) and after radius outlier removal (right). In this case only 1 outlier was detected performing angular removal while approx. 300 were removed along the radius.
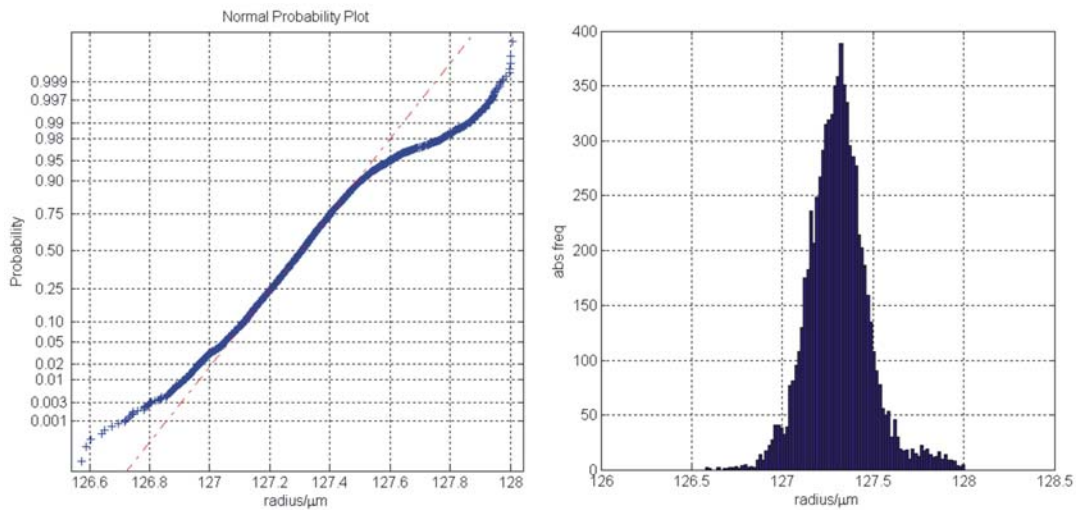
Figure 4.22. Matlab creation of the normal probability plot (left) and of the absolute frequency histogram (right) of the radius distribution for the stereo-pair -7&0 under consideration.

From the previous description of the Matlab routine for point cloud processing, aimed to determine the radius of the cylinder measured using 3D-SEM methodology, it can be deduced that the weak point of this operation is the dataset reduction. Nevertheless this procedure is always necessary as the computational capabilities of the computer are often limited.

The random reduction of points might influence the accuracy of the Least Square Method implemented in Matlab, thus leading to higher uncertainties, with regards to diameter estimation. For this reason an experimental investigation was carried out, similarly to the case described in section 4.5, to determine the influence of the dataset reduction procedure on the estimated diameter value. The investigation was performed considering six repeated calculations, using Matlab, of the wire gauge diameter for the case of the stereo-pair -7&0, performed by varying the number of points composing the cloud, *i.e.* by performing different dataset reductions. Values from 25000 down to 5000 were tested for the analysis, where values around 10.000 points were usually the upper limit for the case of the computer used in this work, while higher dataset were available when the DTU *"G-bar super-computer"* was employed. This computer provides much higher computational power, therefore enabling the Matlab routine to run also for clouds consisting of 25000 points. The mean value and the standard deviation of the diameter values, for six replicated experiments, performed at a different number of points, are shown in Table 4.5.

Calibrated Value= 250 ± 0,15 μm					
Number of Points	**25000**	**20000**	**15000**	**10000**	**5000**
Mean value/μm	254.65	254.65	254.66	254.62	254.64
St.Dev./μm	0.01	0.03	0.03	0.04	0.07
St. Dev./μm (k=2)	0.02	0.06	0.06	0.08	0.14

Table 4.5. Results of the experimental investigation on the influence of dataset reduction of diameter evaluation performed using the developed Matlab routine. Mean value and standard deviation for six replicated experiments are shown for different number of points composing the cloud, considering the stereo-pair -7&0 as dataset.

From the experimental investigation results that, even though a relevant dataset reduction is performed, for instance from 25000 to 5000 points, the calculated mean value of the diameter is showing variations in the order of 10 nm. On the other hand a significant difference can be seen for the standard deviation values that result in being 7 times higher when a dataset reduction is performed down to 5000 points in relation to a 25000 points total.

Nevertheless for the case considered in this work, a Matlab dataset of 10000 points, the uncertainty deriving from Matlab replications is in the order of 80 nm, and therefore negligible with respect to other effects such as the point cloud trimming performed using Geomagic as described in section 4.5. To conclude with, it is worth mentioning that bigger datasets lead to higher computational time, which is influenced by the power of the processor employed for running the Matlab routine as it can be seen in Fig.4.23.
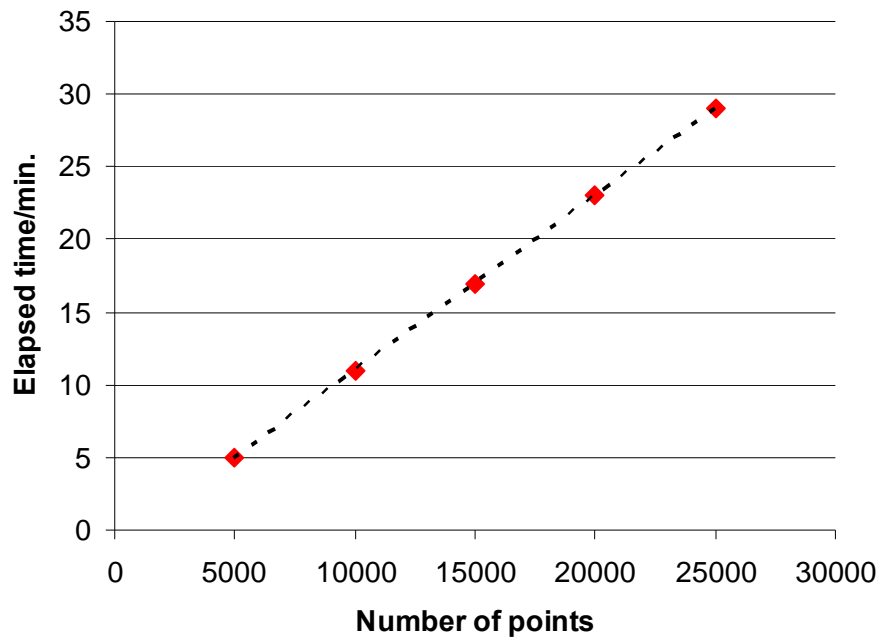
Figure 4.23. Matlab elapsed time, for the diameter estimation using Matlab, as a function of the number of points to be analyzed. Results were obtained by using an Intel Core 2.00 GHz processor.

4.6 Summary and conclusions

In this chapter factors influencing the accuracy of optical systems were discussed and compared to the case of measurements performed using Scanning Electron Microscopy technique. Having defined a point cloud as the result of an acquisition procedure, where the point density depends on the sensor used for the measurement, its main characteristic were also described. In particular point clouds, obtained when performing stereo-pair reconstructions, result to be relevant for the case of 3D-SEM technique. For this reason the point cloud generation, employing SEM, was described with the main focus put on the process leading from a raw point cloud to a post-processed one, ready for feature extraction and measurement operations. This procedure, which is typically described as point cloud processing could be more or less complicated depending on the raw point cloud quality. The case of point clouds, deriving from stereo-pair reconstruction, obtained from SEM measurements on a cylindrical item, a wire gauge with a reference diameter of 250 μm, was discussed, pointing out the sequential operations to be performed and the related error sources. In this work a demo version of Geomagic was employed as software for performing the different operations needed to analyze and inspect the point clouds. A series of experimental investigations were carried out to determine the role and the influence of the different actions performed on a raw point cloud. The main results were the following:

 ➢ Choosing different Sensitivity Levels, ranging from 0 to 100, can perform the outliers removal. The number of outliers detected and removed is following an exponential trend for values <80, moreover the influence of outliers removal on the diameter calculation was found to be negligible and a value equal to 66.6, corresponding to the one given by default from the software, was chosen for the further investigations carried out in this work;

 ➢ The effect of filtering was tested from a qualitative and quantitative point of view, considering also the frequency chart of radii distribution. Two parameters must be set for performing iteration in Geomagic: the Reduce Noise Smoothness and the number of iterations. It was proven that the second modifies the point cloud shape when set to values higher than 1, therefore this value was chosen in the following analysis. Moreover, differences of about 0.4 μm in the diameter calculation were determined from the case of unfiltered data points compared to the filtered ones.

Anyhow Reduce Noise Smoothness=2 was chosen, enabling proper data filtration without affecting the shape of the point cloud and of the radii distribution;

➢ Meshing operation was also considered where from a given point cloud a wrap is obtained. If defects or bumps are visible on the surface, due for instance to the presence of dust during SEM measurements, these can be discarded by trimming the mesh;

➢ A point cloud sampling could be optionally performed, to reduce the number of points, when, for instance, stitching operations are required. The sampling could be carried randomly or curvature based and experimental results demonstrated that the calculated diameter is not influenced by this operation for sampling down to 10% (*i.e.* when reducing by 90% the number of points composing the original point cloud);

➢ Point cloud trimming was found to be the most relevant operation to be performed, among the ones considered, when point cloud processing is carried out. In fact, a standard deviation (k=2) equal to 0.4 μm, for the diameter calculation, was calculated from 15 replicated experiments on two different point clouds, -7&0 and 0&+7;

➢ The contribution of Geomagic resolution, which is equal to 0.1 μm when estimating the diameter value, was calculated to be equal to 0.03 μm by performing an uncertainty evaluation of this error source according to ISO GUM (JCGM 100:2008).

References

Grubbs F E. Procedures for detecting outlying observations in samples. *Technometrics* 1969; **11**: 1–21

Barbato G, Barini EM, Genta G, Levi R. Features and Performances of Some Outlier Detection Methods. Unpublished Report, Deparment of Production System and Business Economics (DSPEA), Politecnico di Torino, 2010.

Catalogue of TESA Technology. Hexagon Metrology, TESA, 2007/2008.

Carmignato S. Traceability of coordinate measurements on complex surfaces. Ph.D. Thesis, DIMEG – Università di Padova, IPL – Technical University of Denmark, 2005.

Cowley JM. High Resolution Electron Microscopy. *Annual Review of Physical Chemistry* 1987; **38**: 57-88.

Geomagic Studio 10. Geomagic Inc., 2008.

ISO/TS 16610-1:2006. Geometrical product specifications (GPS) - Filtration - Part 1: Overview and basic concepts, ISO, 2006.

JCGM (Joint Committee for Guides in Metrology) 100:2008. Evaluation of measurement data - Guide to the expression of uncertainty in measurement (GUM), 2008.

Krystek M. Form filtering by splines. *Measurement* 1996; **18**: 9-15.

Matlab® 7.4 (R2007a). MathWorks, 2007.

MeX™ v 5.1. Alicona Imaging, 2007.

Montgomery DC. Design and analysis of experiments, 7th edition. John Wiley, 2008.

Muralikrishnan B, Raja J. Functional Filtering and Performance Correlation of Plateau Honed Surface Profiles. *J. Manuf. Sci. Eng.-Trans. ASME* 2005; **127**: 193-197.

Savio E, De Chiffre L, Schmitt R. Metrology of freeform shaped parts. *CIRP Annals* 2007; **56/2**: 810-835.

5. Uncertainty evaluation of instrument setting parameters for 3D-SEM metrology

5.1 Introduction

Scanning Electron Microscope (SEM) image resolution depends on the area covered by the beam or spot size, but it is also linked to the magnification and to the acceleration voltage. A proper parameter adjustment is therefore of paramount importance to perform traceable 2D-SEM measurements, as well as when stereophotogrammetry techniques are employed to perform 3D-SEM reconstructions. In this chapter an experimental investigation was carried out to perform an uncertainty evaluation of instrument setting parameters at a 2D and 3D level. SEM images of an ultrasharp silicon grating TGT1 from NT-MDT (Europe, The Netherlands), usually intended for SPM calibration, were acquired, to evaluate the different effects in the 2D case. Similarly, stereo-pair reconstructions of a cylindrical item, a TESA wire gauge, were considered to estimate the role of instrument setting parameters, accelerating voltage (HV), spot size (SS) and magnification (M) at a 3D level.

5.2 Influence of instrument setting on SEM image formation

SEM's electron beam is thermionically emitted from a heated filament with an energy typically ranging from a few hundreds to 40 keV and then focused to a spot with few nanometers in diameter. The beam is then deflected in the x and y-axes scanning in a raster mode over a rectangular area on the sample (Watt, 1997; Bhushan, 2006). Thus, SEM image quality and resolution depend on the scanning area, related to the magnification, and on beam characteristics linked to the spot size and the accelerating voltage. A high accelerating voltage leads to a better image resolution, but also to more unclear surface structures, more edge effect and more sample damage. A decrease in the spot size results in a higher image resolution although a grainy and noisy image is obtained. The magnification is also strictly related to the resolution since the higher the former, the smaller is the pixel size, but this setting results in a smaller field of view (JEOL USA, 2006).

The Inspect 'S' Scanning Electron Microscope, from FEI Company, was employed in this experimental investigation. The microscope, owned by the Center of Electron Nanoscopy (CEN), at DTU, is shown in Fig.5.1. In this work two different investigations were performed, one related to 2D SEM images and one to 3D-SEM reconstructions, both aimed to quantify the influence of three factors; accelerating voltage HV, spot size SS and magnification M.

Figure 5.1. The Inspect 'S' Scanning Electron Microscope (SEM), from FEI Company, with a tungsten filament electron source.

5.3 Influence of instrument setting on pixel size and nonlinearity in SEM image formation

An experimental investigation was carried out concerning the influence of SEM instrument settings on the image formation process in terms of pixel size and nonlinearity, which are related to image quality and resolution. The relevance of three main influencing factors, accelerating voltage HV, spot size SS and magnification M, was investigated qualitatively and quantitatively using an ultrasharp silicon grating TGT1 from NT-MDT (Europe, The Netherlands) as calibrated artefact, usually intended for SPM calibration. This consists in an array of sharp tips with a top curvature radius of 10 nm, a period of 3 μm and a diagonal period of 2.12 μm (Fig.5.2). The calibration certificate states an uncertainty of 0.05 μm for the period, which corresponds to approx. 1.7 % of the nominal value. In Fig.5.3 an example of two SEM images of the artefact, acquired under different experimental conditions, is reported. The effects of accelerating voltage and spot size at a constant magnification are clearly visible.

In particular, as the accelerating voltage (HV) is increasing (from the left to the right) and the spot size (SS) is decreasing (from the bottom to the top), a better resolution is achieved and also a clearer structure details (with less noise).
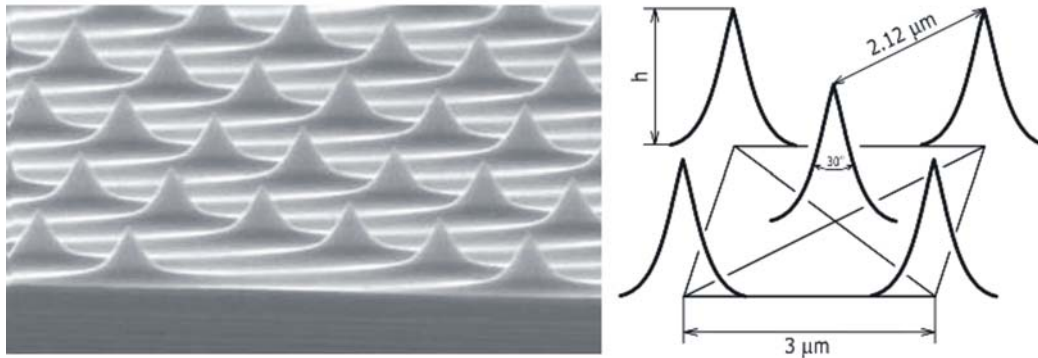
Figure 5.2. SEM image of the ultrasharp silicon grating TGT1 from NT-MDT (left) used as calibrated artefact to calculate pixel size and pixel nonlinearity. The artefact consists of an array of sharp tips with a period of 3 µm and a diagonal period of 2.12 µm as shown on the right (source: NT-MDT website).
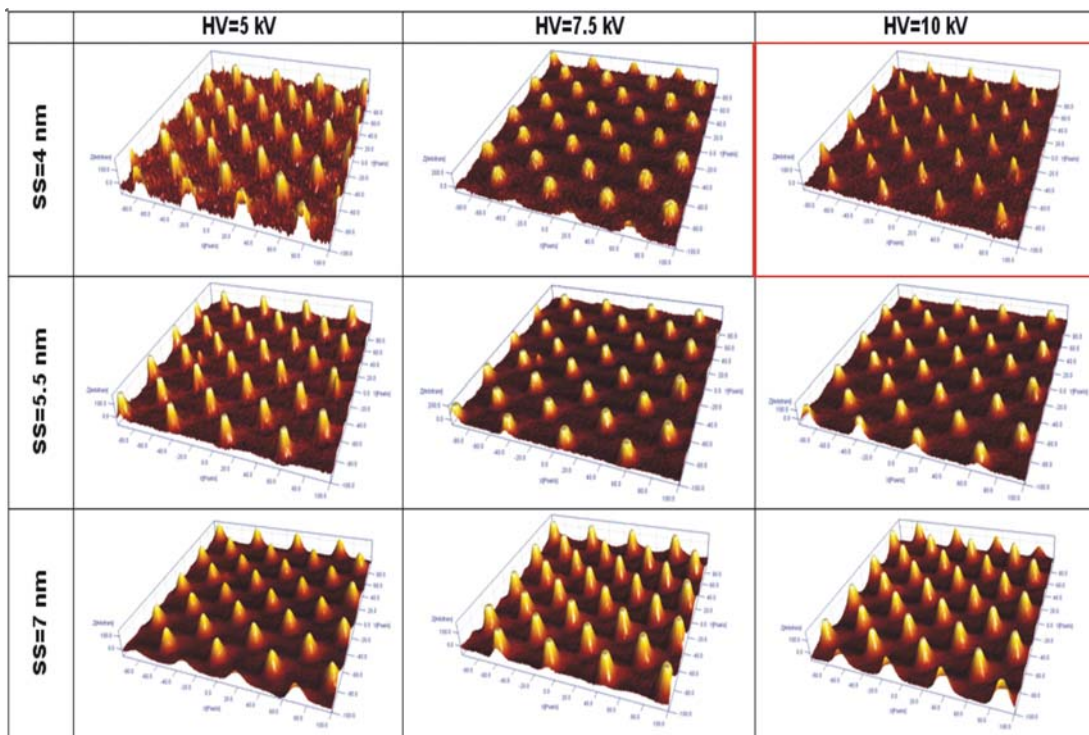
Figure 5.3: 3D rendering of the calibrated artefact from SEM images performed at same M=5000x but at different spot size and accelerating voltage levels. Qualitatively, the optimum parameter setting results HV=10.0 kV and SS=4.0 nm (red mark). Only a zoom of 300x300 pixels is shown to facilitate the comparison.

Starting from SEM images of the artefact, which is a calibrated grating, it is possible to calculate the period. This could be automatically done by using, for instance, Scanning Probe Image Processor software (SPIP[TM], 2010) and the related routine called Unit Cell Detection allowing also nonlinearity evaluation. This routine first calculates *a* and *b* vectors, these being the main directions of the spikes in the image, and then the average distance, in pixels, between two consecutive spikes in both these directions (Fig.5.4). The diagonal pitch, which is the calibrated value of the grating, is calculated from the average distance in pixels in the two orthogonal directions, *i.e.* the pitch. Thus, the pixel size of the SEM image is calculated as the ratio between the calibrated distance of the diagonal pitch and the number of pixels estimated through the SPIP routine. A similar procedure, on the same type of calibrated artefact, was also applied by (Bariani, 2005).
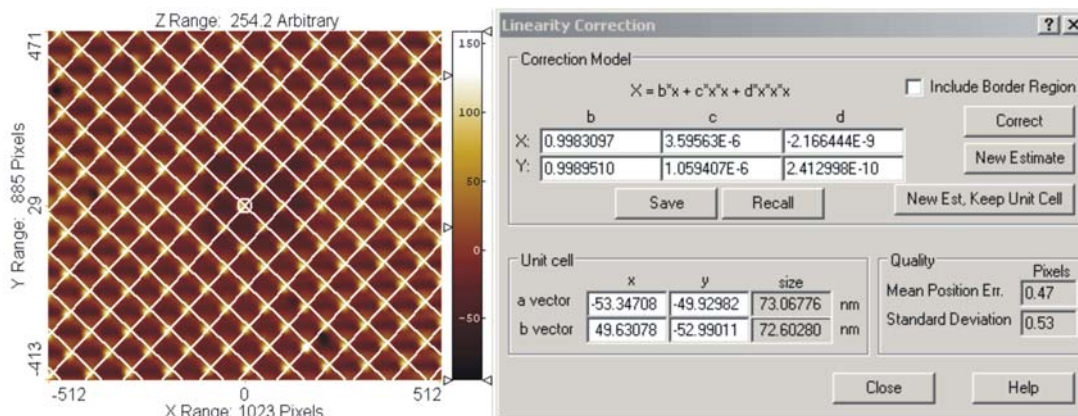
Figure 5.4. Example of Unit Cell and nonlinearity calculation performed using Scanning Probe Image Processor (SPIP[TM]) software, starting from a SEM image of the TGT1 silicon grating for SPM calibration. Determination of two main vectors a and b, representing spikes position in the image is show on the left, while on the right the average distance, in pixels, for the spikes laying on both vectors is shown, together with mean position error calculation.

Three factors were selected for investigation among those influencing SEM image formation, namely; accelerating voltage (HV), spot size (SS) and magnification (M). Pixel size and pixel nonlinearity, in terms of mean positioning error, were identified as the main parameters in image formation, and accordingly considered as response variables. Since the factors are considered as being liable to have nonlinear effects on both responses, three levels were chosen for each factor covering as much as possible, the sample space. Hence, it has been realized the 3^3 factorial plans, described in Table 5.1, are a result of a preliminary screening as shown in Fig.5.5.
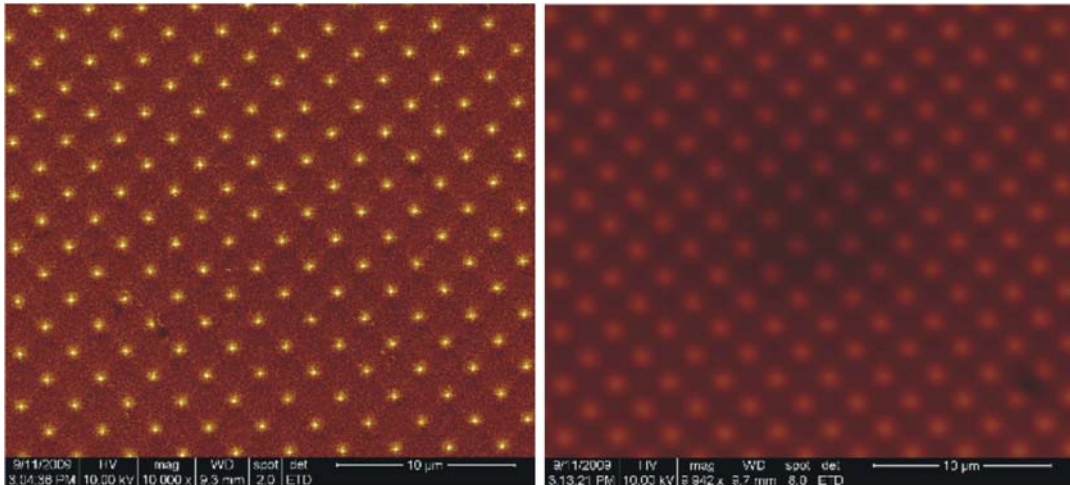
Figure 5.5. Preliminary screening of instrument settings with both SEM images acquired with M=10000x and HV=10 kV, and with a spot size too small (2 nm, left) and too large (8 nm, right).

Factors and Levels	0	1	2
HV/kV	5.0	7.5	10.0
SS/nm	4.0	5.5	7.0
M/times	2500	5000	10000

Table 5.1. Summary of factors and related levels for the Design of Experiment analysis to investigate the role of measuring parameter setting on SEM images.

No replications were performed since continue changes in the accelerating voltage may cause filament blow up and result in severe damage of the calibrated artefact as shown in Fig.5.6. However, the experimental design permits "hidden replications" (Fischer, 1935); some of the effects of the factors can be safely ignored, thus determining replications in remaining factors. Hidden replication is a commonly used practice in "screening" experiments. Analysis of variance was therefore performed considering pixel size and pixel nonlinearity as outputs. In particular the nonlinearity was quantified through pixel mean position error and related standard deviation. An example of mean position error output, calculated through the Unit Cell Detection routine in SPIP is shown in Fig.5.7.
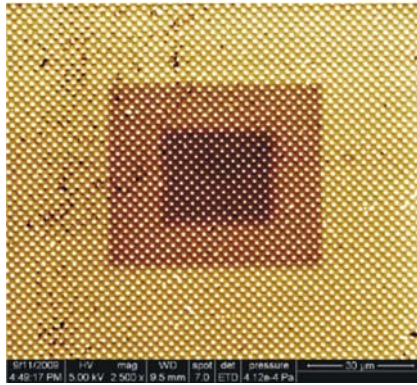
Figure 5.6. Example of sample damage as a consequence of different HV levels. The three areas correspond to the different levels of magnification.
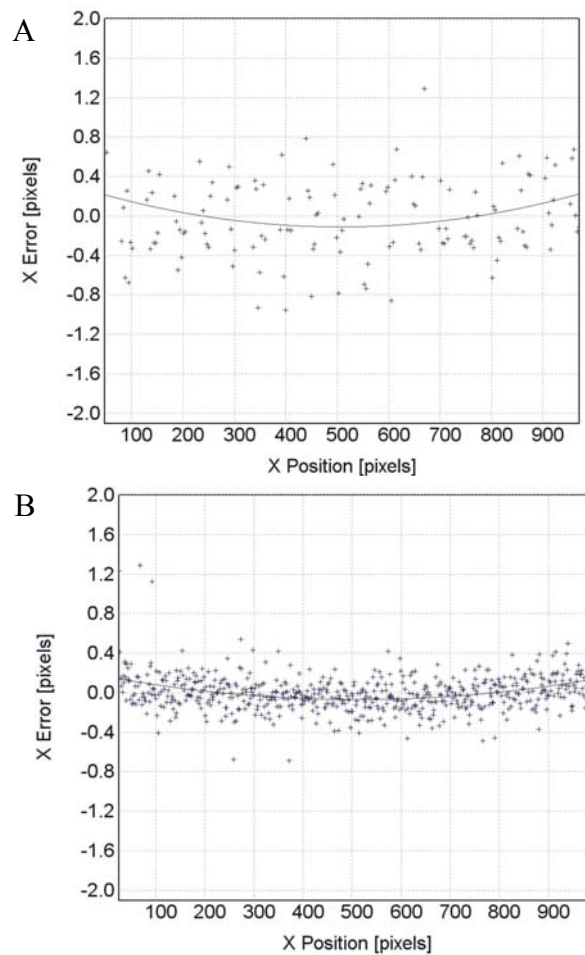
Figure 5.7. Examples of outputs of the Unit Cell Detection routine showing a standard deviation of position error of 0.61 pixels (A) and 0.20 pixels (B). Measuring parameters were set as follows: M=10,000x, HV=5 kV, SS=7 nm for image on the left and M=5000x, HV=10 kV and SS=4 nm for the one on the right.

5.3.1. Experimental investigation results

As a result of the SEM measurements described in the previous sections, 27 SEM images were obtained from the three factors, HV, SS and M set at three levels as shown in Table 5.1. All these SEM images were analyzed using SPIP to determine the pixel size and the nonlinearity in terms of mean position error of the pixels. Being the working distance slightly changing between the different experiments, due to focus adjustments, it was considered as a covariate, meaning a factor which is not under control of the operator, but which could have some effects on the responses. Here the main results are summarized and commented upon. In order to perform the Design of Experiments analysis (Montgomery, 2008), a demo version of Minitab$^®$ 14.1 statistical software (2003) was employed. This allowed obtaining information about the influence of the three factors under investigation in terms of the main effects and their interactions considering the man position error, representing nonlinearity and the pixel size "p" as responses. Main results of the analysis are shown in Table 5.2. Considering pixel size as response, analysis of variance pointed out a high significance of Magnification, while Acceleration Voltage and Spot Size are barely significant. This was proven by the p-value, being the one related to M, way lower 0.05 and the ones dealing with HV and SS, way higher than 0.05. The effects of interactions is negligible, therefore they could be discarded from the analyses to obtain more degrees of freedom, meaning a finer estimation of the main effects. This test was also carried out obtaining results very similar to the ones shown in table 5.2, with Magnification accounting for 99.3% of the whole response and HV, SS and the working distance, considered as a covariate, accounting for only 0.7%, being nevertheless not significant. Accelerating voltage HV is neither significant also in the case of mean position error considered as a response, as well as the three interaction being p-value >0.05. Anyhow, in this case, SS was shown to have an influence accounting for approx. 21% of the final response, being the magnification M responsible of 32.4%. In this case, all the contributes lead to a model fitting 81.7% meaning that some effects, not being under control, are responsible for about 20% of the mean position error estimation. This could be due to the uncertainty of the software SPIP in calculating the mean position error. Moreover, since the experiments could not be replicated as explained in the previous section, the testing of repeatability was not feasible. The main effects plot for both responses under consideration is shown in figure 5.8, while the interaction plots were not posted here because interactions were demonstrated not to be relevant.

Source	DF	Pixel Size "p"/(μm/pixel)		Mean position error/pixel	
		p-value	SQ %	*p*-value	SQ %
HV/kV	2	0.900	0.0	0.104	8.1
SS/nm	2	0.363	0.4	0.033	20.7
M/times	2	0.000	99.3	0.005	32.4
Main Effects	6		99.7		61.2
HV/kV·SS/nm	4	0.197	0.0	0.286	7.8
HV/kV·M/times	4	0.193	0.0	0.329	7.2
SS/nm·M/times	4	0.621	0.0	0.464	5.2
Interactions	12		0.0		20.2
d/mm	1	0.163	0.3	0.227	9.6
Covariates	1		0.3		0.3
Error	7				
Total	26		100.0		81.7

Table 5.2. Summary of the degrees of freedom (DF), *p*-value and percentage sum of squares (SQ %) for the three factors under investigation considering pixel size s and mean position error as responses. Results were obtained from a DOE analysis performed using Minitab.
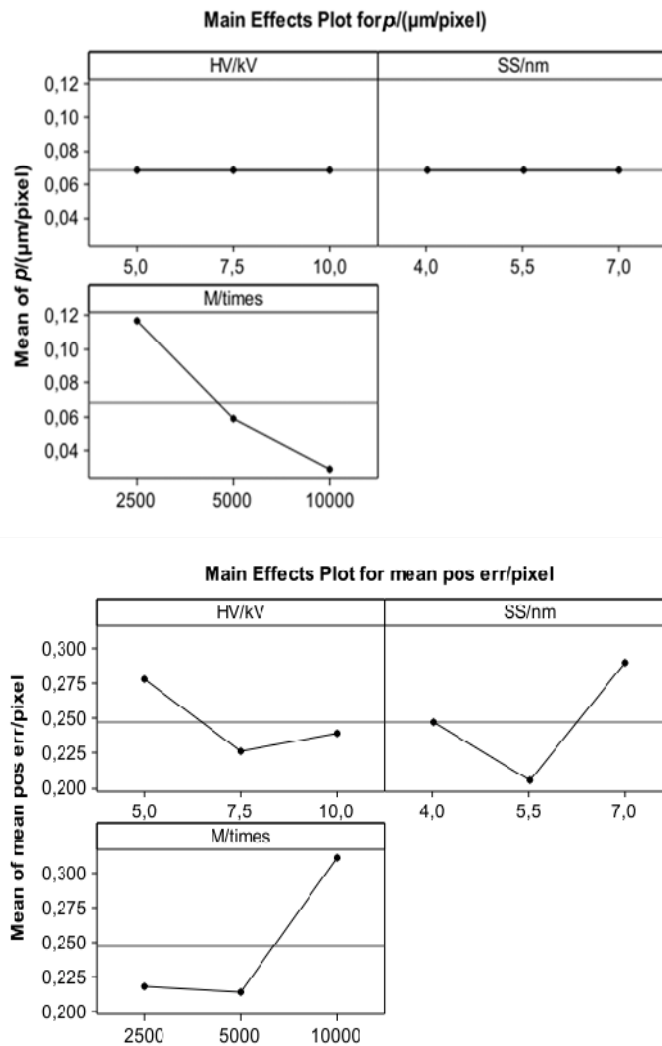
Figure 5.8. Main effects plot considering pixel size "p" (left) and mean position error (right) as responses and HV, SS and M as influencing factors.

Fig.5.8 is a further confirmation of the results shown in table 5.2, where M was found to be the only factor influencing the pixel size. Considering mean position error as a response, it can be noticed that the higher the magnification, the higher the error. This is due to the fact that, the smaller the pixel size, the more difficult for the software to distinguish between two neighbouring pixels. The effect of SS is also relevant and SS=5.5 nm is the setting providing the lowest mean position errors, while the HV was demonstrated not to be significant. These results were presented in a paper by the author (Carli *et al.*, 2010), where similar results were obtained also by applying two other well-established techniques, *i.e.* Best Subset Regression (Hocking, 1976) and an extension of the classic Yates algorithm (Davies, 1954).

The former identifies the best-fitting empirical regression models up to quadratic order, among all possible combinations of predictor variables. The latter enables a detailed estimation of all 26 (orthogonal) factorial effects, and evaluation of the relevant levels of significance (irrespective of order). These techniques jointly offer a number of advantages, Best Subset Regression leading to the identification of parsimonious models, and Yates algorithm offering an overall picture of all effects estimated in terms of the factorial design adopted; a minor constraint being represented by even spacing of levels. As far as pixel size is concerned, Best Subset Regression identifies a second order model including M and M^2; the model accounts for almost the whole variability. Similarly, the application of Yates algorithm shows that log M covers 96% of the total sum of squares and (log M^2) covers the remaining 4%; the other effects are negligible. As far as nonlinearity is concerned, Best Subset Regression identifies a second order model including SS, HV 2, SS 2, M 2 and the interaction HV-SS; the model accounts for 58% of variability. On the other hand, the application of the Yates algorithm shows that log M covers 27% of the total sum of squares, followed by SS 2 (11%), the interaction HV-SS-log M (10%) and the interaction SS 2–log M (10%); therefore, these effects cover 58% of total sum of squares and the others, the remaining 42% (each one with a percentage less than 10%). Differences between two methods depend on the fact that Yates algorithm considers a logarithm of Magnification and effects of an order greater than two. However, the main effect of Magnification is a common result between the different statistical techniques employed for the data analysis.

5.4 Influence of instrument setting on 3D-SEM reconstructions

The main conclusion arising from the previous section is that HV, SS and M influence the SEM image formation process. In particular, while the pixel size is mainly influenced just by the magnification, the pixel nonlinearity, estimated as the pixels mean position error, depends also on the accelerating voltage and on the spot size. In this section a similar analysis was carried out considering the influence of the same parameters on 3D-SEM reconstructions. The experimental investigation was based on 3D-SEM measurements performed on the TESA wire gauge having a reference diameter of 250 μm (Catalogue of TESA Technology, 2007/2008) described in chapter 3.

Three influencing factors, related to the SEM instrument setting, were considered for the analysis, accelerating voltage HV, spot size SS and magnification M. Three levels were considered for HV and SS, and two for the magnification as shown in Table 5.3.

Error source	Factor	Symbol	Unit	Levels		
SEM instrument setting	accelerating voltage	HV	kV	5.0	7.5	10.0
	spot size	SS	nm	2	3	4
	magnification	M	times	900	1000	

Table 5.3. Summary of all the factors and levels tested for investigating main error sources related to the SEM instrument setting, considering pixel size and mean position error as responses.

The choice of the levels of magnification is justified by the considerations made in the following pages, while considering HV and SS the levels were chosen after some preliminary SEM measurements aimed to identify the optimum ranges. The result of this investigation is shown in Fig.5.9 where SEM images, acquired at different levels from the one chosen for the experimental plan, are shown to result in bad quality images and poor resolution of the details. Differently from the 2D case, which allows the calculation of the pixel nonlinearity using a suitable calibrated artefact, for the 3D reconstructions different outputs should be considered, as pixel nonlinearity evaluation is not directly feasible in this case. The average noise of the point cloud, obtained from the stereo-pair reconstructions, was considered as response assuming it to be proportional to the noise of the images composing the stereo-pair. Moreover, together, the wire gauge diameter was also calculated. When performing measurements on a point cloud, obtained from reconstructions based on the stereo-pair technique, it is not usually possible to distinguish the influence of the instrument setting from the other main contributors affecting the uncertainty of 3D-SEM described in chapter 3. In this case, while some of these factors could be kept constant through all the experiments, a few others were varying in a non-directly, controllable way. All these factors are summarized in the following Table 5.4.
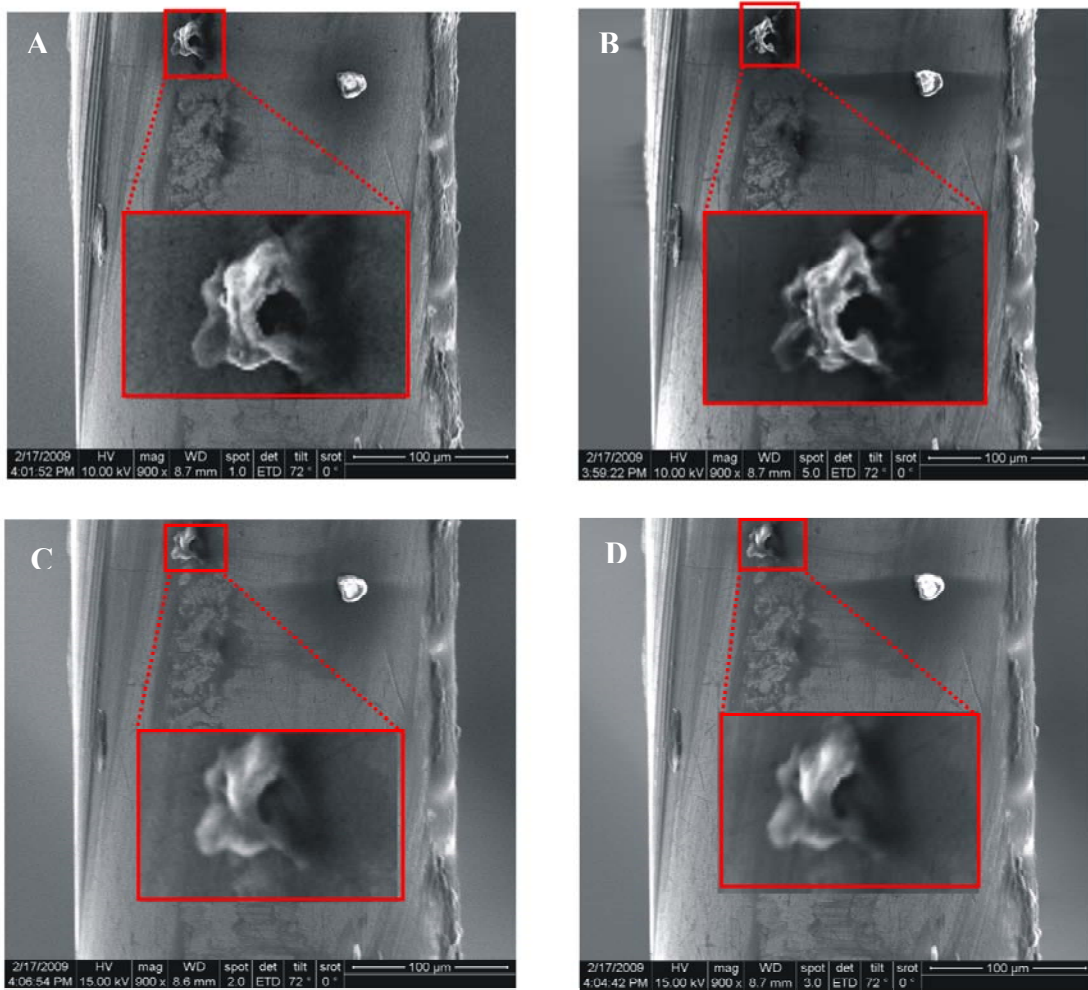
Figure 5.9. Examples of SEM images acquired at M=1000x and different levels of HV and SS. Images A and B were obtained at SS=1 nm and SS= 5 nm respectively at HV=10 kV, while both images C and D show the effect of setting HV=15 kV at SS=2 nm and SS=3 nm. A zoomed part is shown on each image, where the same feature is enlarged to facilitate the understanding of the qualitative effects of setting different values of HV and SS.

Main uncertainty sources	Influencing factors	
	Under control	**Not under control**
Image quality adjustment	Same scan rate for all the SEM images acquired.	Brightness, contrast and focus adjusted time by time to obtain optimum SEM image quality.
Software for stereo-pair reconstructions	MeX input parameters were the same for all the cases under consideration: working distance 9.0 mm, rotational angle 7 degrees and pixel size equal to 0.329 for M=900x and to 0.299 for M=1000.	Stereo-pair superimposition was performed automatically by MeX to reduce influence of operator. Not eucentric rotations result in different X and Y offsets of the images composing the stereo-pair.
		Stereo-creator repeatability.
Software for point clouds inspection and feature extraction	Same procedure for outliers removal and filtration for all the point clouds.	Point clouds trimming reproducibility

Table 5.4. Description of 3D-SEM main uncertainty sources, with respect to the instrument setting analysis. Influencing factors are divided into factors under operator control and not under control and a short list is provided for each of them.

As shown in the previous table a number of parameters, not directly controllable by the operator, is playing an important role for the analysis. For these reasons, two different stereo-pairs were considered deriving from three SEM images of the reference wire gauge.

The item was rotated at -7 and 0 degrees, obtaining stereo-pair named -7&0 and then the one obtained rotating the item to 0 deg. and the +7 deg. was named 0&+7. Therefore the central image, representing the item in the 0 deg. rotation position, is common for both views. Moreover stereo-pair reconstructions were performed 5 times to allow the estimation of the experimental error due to variability introduced by MeX^{TM} (2007) and by the software for point clouds inspection and feature extraction. The effect of different image qualities setting was not considered, as it will be investigated in the next chapter, while the effect of the uncertainty related to MeX input parameters will be investigated in chapter 7. For this work only the nominal input values were considered. The whole experimental investigation consists then in a large number of factors and levels, which would make it, too time consuming and the estimation of the different effects too complicated.

For this reason some assumptions were made before performing the experiments.

> ➢ The pixel size, which calculated from SEM images as described in chapter 3, was found to depend only on the magnification resulting therefore equal for all the SEM images acquired for this investigation. Furthermore the magnification *i.e.* the pixel size, affects not only the image resolution, but it is also one of the input parameters required from MeX to perform the 3D reconstructions. In addition to that, the higher the magnification the smaller the pixel size and also the field of view, therefore the operator usually chose the highest possible magnification which also allows obtaining measurements of the whole item or features under consideration. In the case of the wire gauge, since the reference diameter is 250 μm, setting the magnification to 1000x allows the operator to obtain a field of view equal to 300 μm and a pixel size equal to 0.299 μm. All the experiments were then carried out at 1000x, while only a few others were performed at 900x to allow a final comparison of the results. An updated table with all the influencing parameters considered for this investigation was produced based on the above-mentioned considerations, for an easier understanding.

Error source	Factor	Symbol	Unit	Levels		
SEM instrument setting	accelerating voltage	HV	kV	5.0	7.5	10.0
	spot size	SS	nm	2	3	4
MeX	stereo-pair	SP	-	-7&0	0&+7	
	Replications	REP	-	1st, 2nd, 3rd, 4th, 5th		

Table 5.5. Summary of the main factors and levels considered for the experimental investigation, divided into different error sources. The role of these factors on the average point cloud noise and the wire gauge diameter was tested together with their influence on the two responses.

The wire gauge diameter and the average point cloud noise were considered as output parameters, while stereo-pair offsets X and Y, automatically calculated by MeX, when performing SEM images superimposition, were considered as covariates, meaning parameters supposed to influence the result were not directly under control of the operator. A design of the experiments approach was employed to be able to determine the influence of the main effects and of the interactions of the influencing factors on the outputs. The main results are here discussed. The first important conclusion is that replications were found not to be relevant for estimating either the average noise or the diameter. This means that the experimental investigation is consistent, since the variability of stereo-pair creation process and of the trimming operation with Geomagic Studio 10 (2008) has a negligible effect on the responses under consideration. Therefore, by not considering the replications as an influencing factor, but just as a process variability parameter, the results of table 5.6 were obtained. Considering average noise as response, the spot size SS accounts alone for 63% of the total variability, followed by the accelerating voltage HV accounting for 19.0%. Their interaction HV-SS is responsible for 6.3 of the overall variability; therefore HV, SS and their interaction are responsible for an overall variability of 88.4%. Both the covariates, offset X and offset Y results were significant (p-value <0.05), while the effect of the stereo-pair and its interaction with HV and SS, although being significant, are responsible for just 0.5% of the whole variability. In order to obtain more quantitative information on these effects, the main effect plot for average noise is shown (Fig.5.10) together with the interaction plot (Fig.5.11).

		Avg. Noise		Diameter	
Source	**DF**	*p*-value	**SQ %**	*p*-value	**SQ %**
offset X/pixel	1	0.002	2.6	0.285	
offset Y/pixel	1	0.000	8.2	0.000	0.5
HV/kV	2	0.000	19.0	0.000	10.1
SS/nm	2	0.000	63.0	0.000	14.3
Stereo-pair	1	0.000	0.3	0.000	49.2
Main Effects	7		93.1		74.1
HV/kV·SS/nm	4	0.000	6.3	0.000	11.2
HV/kV·Stereo-pair	2	0.000	0.1	0.000	0.7
SS/nm·Stereo-pair	2	0.000	0.1	0.000	8.6
Interactions	8		6.5		20.5
Error	74				
Total	89		99.6		94.6

Table 5.6. Summary of the degrees of freedom (DF), *p*-value and percentage sum of squares (SQ %) for the three factors under investigation considering pixel size s and mean position error as responses and X and Y offsets as covariates. Results were obtained from a DOE analysis performed using Minitab.
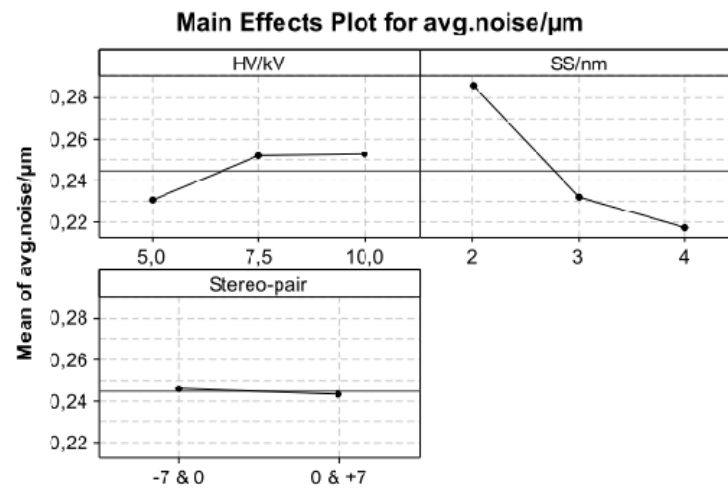
Figure 5.10. Main effects plot of for the average noise resulting from the analysis of variance considering HV, SS and the stereo-pair as factors.
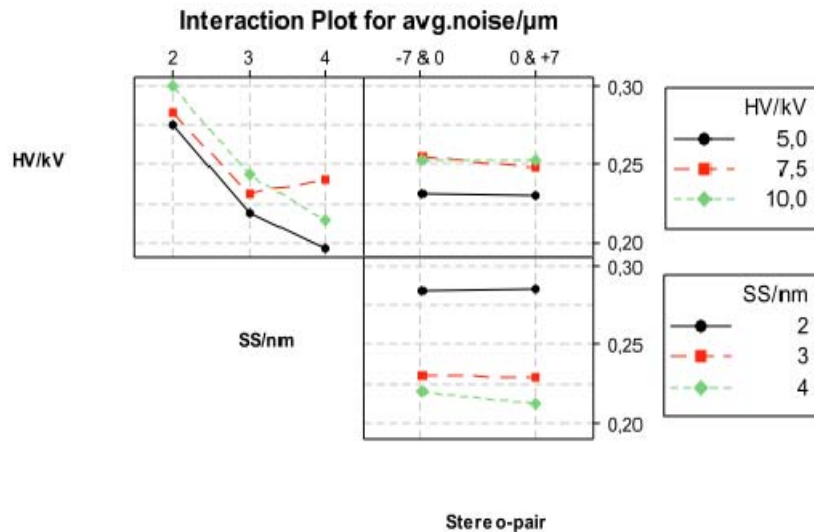
Figure 5.11. Interaction plot of for the average noise resulting from the analysis of variance considering HV, SS and the stereo-pair as factors.

From the previous two graphs it can be noticed that choosing SS=4 nm leads to a lower average noise of the point cloud, regardless of the HV value. An exception is represented by the case HV=7.5 kV and SS=4 nm which makes the interaction HV-SS relevant. These results are generally valid for both the point clouds under investigation. The average noise of the resulting point clouds is an indication of the noise of the SEM images, therefore we can assume that acquiring images of the wire gauge at HV=10 kV and SS=4 nm leads to minimize the noise in the range of values under consideration.

The noise can still be filtered afterwards, but it would still affect the shape of the point cloud as shown in the image below (Fig.5.12).
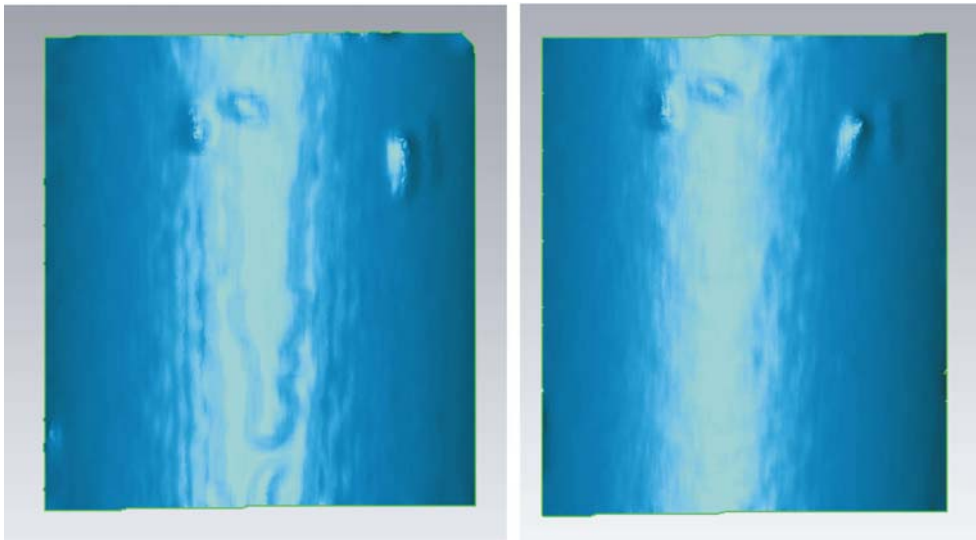
Figure 5.12. Example of two point clouds (-7&0) acquired with the same SS=4 nm and with HV=7.5 kV (left) and HV=10 kV (right) after trimming procedure, outliers removal and filtration. Although noise was removed by filtration it can be seen that the image on the right exhibits a smoother surface.

Considering then the diameter as a response, DOE results, reported in Table 5.6 above, showed that the effect of the stereo-pair is highly significant being responsible for almost 50% of the overall variability. HV, SS and their interaction HV-SS accounts for only about 36%. Some relevant considerations arise from these results:

➢ Stereo-pair 0&+7 shows an higher diameter values compared to the -7&0 one. The image at 0 degree in common for the two stereo-pair, differences in image quality, therefore, can not be highly responsible for this difference in the mean values, nor in the X and Y offset between the images composing the two stereo-pair;

➢ A systematic overestimation of approx. 2% compared to the reference diameter value can be noticed. This is most likely due to the uncertainty of MeX input parameters, which will be investigated in chapter 7.

Main effects and interaction plots for the diameter are shown in Fig.5.13 and Fig.5.14.
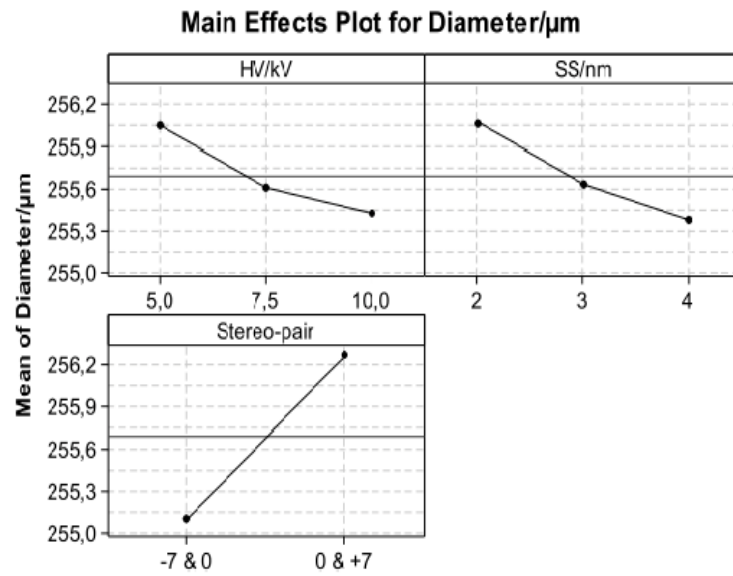
Figure 5.13. Main effects plot for the diameter resulting from the analysis of variance considering HV, SS and the stereo-pair as factors.
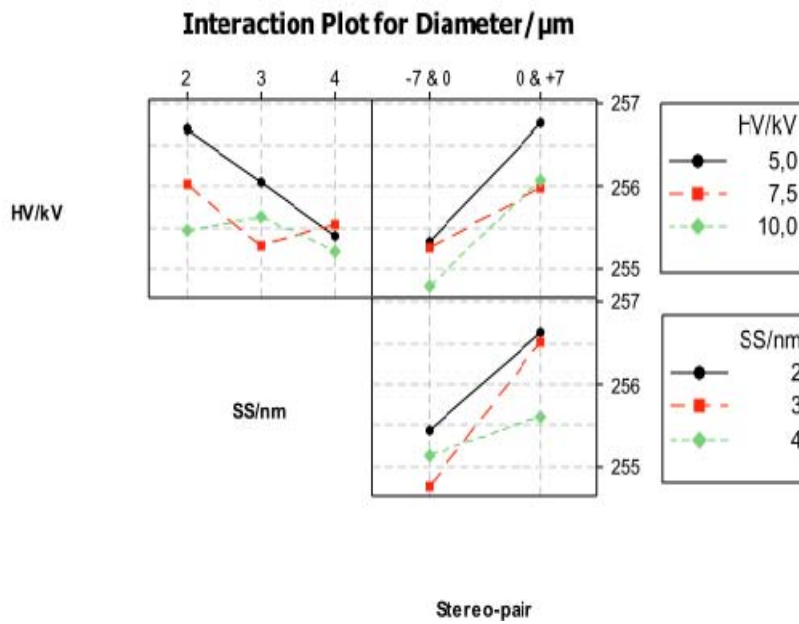
Figure 5.14. Interaction plot for the diameter resulting from the analysis of variance considering HV, SS and the stereo-pair as factors.

The effect of the different setting of HV keeping fixed SS=4 nm, is shown in the Fig.5.15 where the mean value and the expanded uncertainty (k=2) for five replicated experiments are indicated. Moreover, Table 5.7 reports the experimental results in terms of mean values and the expanded uncertainty (k=2) of diameter value and the average noise of the five replicated experiments at SS=4 nm and HV=10 kV for both stereo-pairs.

■ stereo-pair -7 & 0 ■ stereo-pair 0 &+7
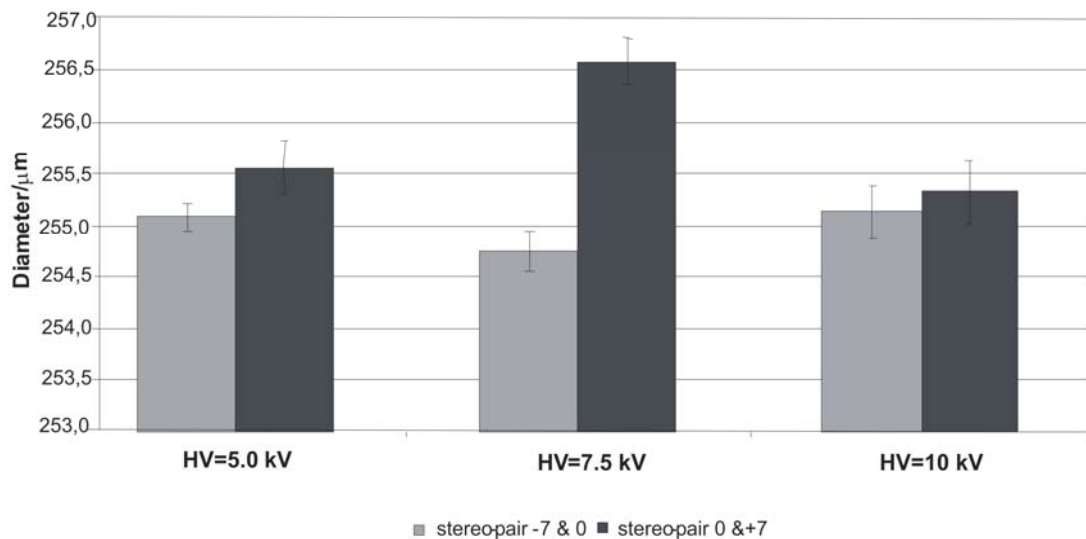
Figure 5.15. Graph showing the effect of the different HV setting, at a constant SS=4 nm and M=1000x, for the two stereo-pairs under investigation. Mean value and expanded uncertainty (k=2) for five replicated experiments are shown.

Stereo-pair	Avg.noise/µm		Diameter/µm	
	mean	U (k=2)	mean	U (k=2)
-7&0	0.214	0.003	255.1	0.3
0&7	0.211	0.004	255.3	0.3

Table 5.7. Mean value and expanded uncertainty (k=2) of the average noise and the wire gauge diameter estimated on five replicated experiments at SS=4 nm and HV=10 kV for two different stereo-pairs,-7&0 and 0&+7.

As previously described in the chapter, the magnification might also be a relevant factor when investigating the effects of HV and SS. In fact, different magnification levels give different pixel sizes *i.e.* the higher M the smaller the pixel size. For this purpose, five replicated experiments were performed at the optimum parameter setting identified earlier, HV=10 kV and SS=4 nm and at M=900x for the two stereo-pair under investigation. Results obtained at M=1000x and M=900x were then compared to test the effect of the magnification on the estimated wire gauge diameter and average point cloud noise. Results are shown in Table 5.8 where it can be noticed that, while the average noise is not significantly changing from measurements at M=900x to the ones at 1000x, the wire gauge diameter is increasing as the magnification becomes bigger. For an easier interpretation of these results, a graph was produced (Fig.5.16) showing the effect of the magnification on the estimated diameter.

		Avg.noise/µm		Diameter/µm	
	Stereo-pair	**mean**	**U (k=2)**	**mean**	**U (k=2)**
M=900x	**-7&0**	0.230	0.001	251.5	0.2
	0&+7	0.222	0.003	252.1	0.3
M=1000x	**-7&0**	0.214	0.003	255.1	0.3
	0&+7	0.211	0.004	255.3	0.3

Table 5.8. Effect of two different magnification levels on the average noise and diameter estimated for both stereo-pair under investigation. The mean value and expanded uncertainty (k=2) for five replicated experiments is shown.
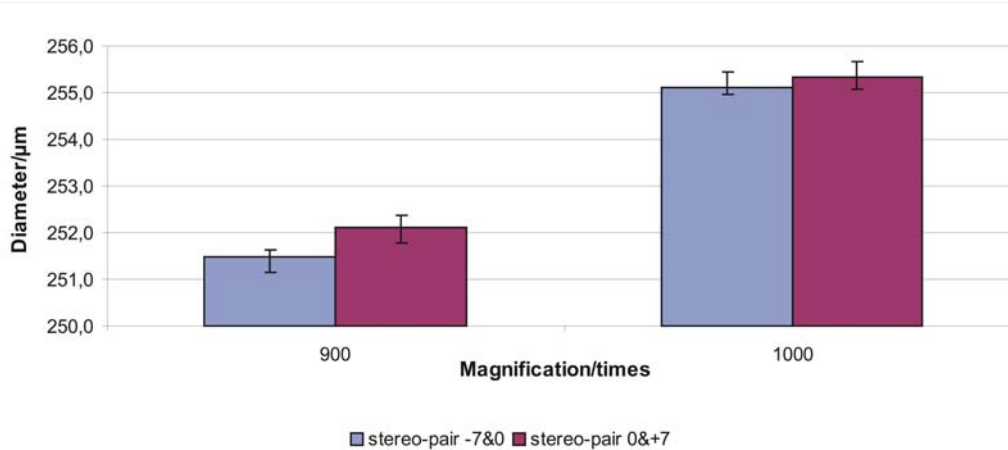
Figure 5.16. Mean value and expanded uncertainty (k=2) of the wire gauge diameter for five replicated measurements at M=900x and M=1000x and for the two different stereo-pairs under investigation,-7&0 and 0&+7.

Before commenting on the previous results, it is worth repeating how the two magnification values were chosen. The wire gauge has a reference diameter value of 250 μm, therefore SEM images must contain the whole object to be measured. It is possible to calculate the optimum magnification value considering the desired field of view, which was already defined previously in the chapter, and the smallest resolution. The choice of the magnification is therefore a trade-off between the field of view and the resolution. In this case both the magnification under test, 900x and 1000x, provide a feasible field of view, which is equal to 336 μm and 306 μm, respectively. This means that the reference item to be measured covers 74% and 82% of the whole SEM image area, where a certain part of the image is left for the background, usually suggested as a "thumb" rule for optimum SEM measurements as shown in Fig.5.17. The magnification is therefore capable of providing different fields of views, but its main influence regards the pixel size, which is known to depend mainly on the magnification, as it was also demonstrated in this work. Pixel size was calculated to be equal to 0.329 μm/pixel for M=900x and to 0.299 μm/pixel for M=1000x. Smaller pixel sizes should provide smaller resolution and therefore finer details in the image can be visualized and later on measured. 3D-SEM reconstructions, even though performed at different magnifications, should provide similar results when the evaluating the wire gauge diameter, which is the reference value.

Thus, results shown in Fig.5.15, clearly exhibit a trend in diameter values, estimated at different magnification levels, which was unexpected from a theoretical perspective. In fact, diameter values at 1000x, for the two stereo-pairs -7&0 and 0&+7, are respectively 1.6% and 1.2% higher than at M=900x. This difference is most likely due the uncertainty associated to pixel size nominal values, set when performing 3D reconstructions using MeX. Further investigations on the effect of pixel size uncertainty on 3D-SEM reconstruction have been carried out in chapter 7.
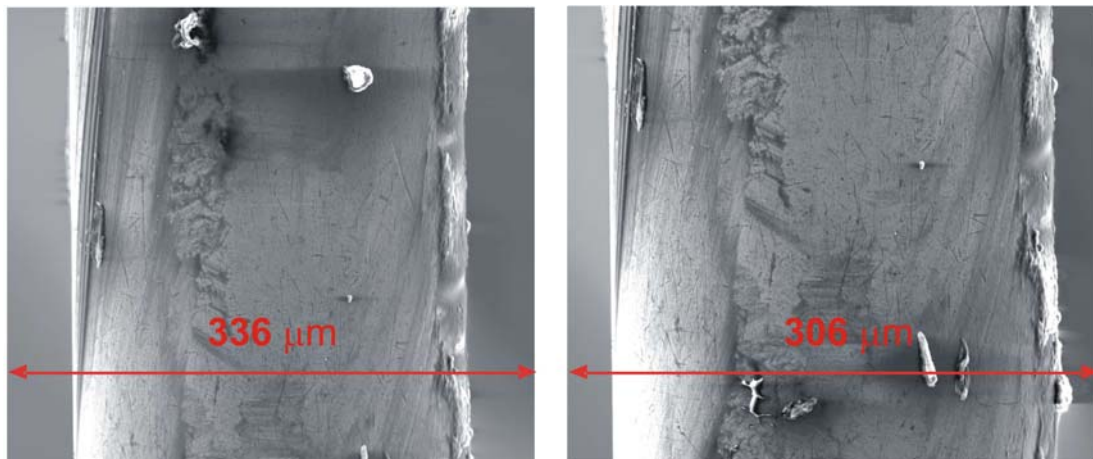
Figure 5.17. Comparison of SEM images of the wire gauge acquired at M=900x (left) and M=1000x (right) and at different rotational angles. Field of view was calculated to be equal at 336 μm for M=900x and 306 μm for M=1000x, meaning that the reference wire gauge covers 74% and 82% of the SEM image respectively.

5.5 Summary and Conclusions

In this chapter, uncertainty of SEM instrument setting parameters was evaluated. For this purpose, SEM images of an ultrasharp silicon grating TGT1, employed as calibrated artefact, were acquired to evaluate uncertainty in the 2D case. Similarly, stereo-pair reconstructions of a cylindrical item, a wire gauge with a known reference diameter, were considered to perform an uncertainty evaluation of 3D-SEM technique.

Influence of instrument setting on 2D SEM images: The influence of the three main SEM parameter settings, accelerating voltage (HV), spot size (SS) and magnification (M) on SEM image formation was investigated considering pixel size and pixel nonlinearity as outputs. A design of experiment approach was adopted to account for the different main effects or interactions among the factors. Considering the pixel size as response, it was demonstrated that this depends mainly on the magnification level, which accounts for about 99.3% of the whole results variability. In the case of mean position error, the spot size starts to become a relevant factor being its p-value <0.05, even though the magnification is still the main influencing factor accounting for 32.4% of the whole variability, while SS accounts for about 21% and HV for 8.1%. Interactions, although being not relevant in general (p-values >0.05), account for about 20% of the whole results variability, while they were negligible in the case of pixel size estimation.

Similar results were obtained by applying other two well-established techniques, *i.e.* Best Subset Regression and an extension of classic Yates algorithm. The magnification resulted to be the most influencing factor, among the one considered, from all the different statistical techniques employed for the data analysis.

Influence of instrument setting on 3D-SEM reconstructions: Three SEM images of a wire gauge, with a reference diameter of 250 μm, were coupled to form two stereo-pairs. Similarly to the previous case, SEM instrument setting HV, SS and M were set each at three different levels to evaluate their influence on the stereophotogrammetry technique considering average noise of the resulting point cloud and the diameter as responses. A design of experiment approach was employed, at a fixed magnification M=1000x, to reduce the total number of reconstructions. Five replications were also performed to account for the experimental error. This error was found to be negligible compared with other effects considering both responses. In fact the model fitting was calculated to be equal to 99.6% for the average noise and 94.6% for the diameter. In the case of average noise all the main effects and interactions were found to be significant (p-value <0.05) and among them SS accounts for 63% of the whole experimental variability, followed by HV (19.0%) and the HV-SS interaction (6.3%). Different instrument settings determine also a change in the X and Y offset between the two images composing the stereo-pair. The software performing the 3D reconstructions calculates this offset, automatically. These shifts in the X and Y direction, although not being factors in the analysis, but covariates, were found to account for about 11% of the overall variability.

The knowledge of the effect of different instrument settings on the resulting average noise is crucial. In fact, even though the operator can eventually post-process the point cloud afterwards by filtering, the presence of high average noise causes the wrapped point cloud to be rougher.

From the 2D-SEM images investigation it can be concluded that, among the three different instrument settings tested in this work, the magnification is the only responsible factor for variations of the image pixel size, accounting for 99.3% of its variability. Moreover, different settings of, accelerating voltage and spot size, although not influencing the image pixel size, are responsible for changes in the pixel nonlinearity. This effect can be quantified through mean position error of the pixels. The Magnification was found again to be the most influencing factor, since 32.4% of the mean position error result depends on the magnification level, followed by the spot size (21%) and the accelerating voltage (8.1%).

Considering the stereo-pair reconstructions of the wire gauge, different results were obtained considering the calculated diameter as a response of the experimental investigation.

➢ A difference in the calculated diameter was observed for the two stereo-pairs under consideration meaning that different stereo-pairs, although reconstructed using the same MeX nominal input parameters, may lead to different results. This difference covered about 50% of the results variability;

➢ Keeping constant M=1000x and setting HV and SS at different levels, leads to changes in the average noise, but not significant changes in the diameter calculation. From this chapter, all the SEM images have been acquired setting HV=10 kV and SS=4 nm to minimize the noise in the range of values under consideration;

➢ The effect of magnification was investigated by performing five replicated reconstructions at the optimum values for HV and SS and at M=900x. An overestimation of the wire gauge diameter (about 1.5%) for both stereo-pairs was found in the case of higher magnification *i.e.* lower pixel size. This experimental result underlines as MeX input parameters, have a strong influence on 3D reconstructions.

References

Carli L, Genta G, Cantatore A, Barbato G, De Chiffre L, Levi R. Experimental investigation on the influence of instrument settings on pixel size and nonlinearity in SEM image formation. *Proc. at 10th euspen Int. Conference*, Delft, 2010; **1**: 51-55.

Catalogue of TESA Technology. Hexagon Metrology, TESA, 2007/2008.

Bhushan B. Springer Handbook of Nanotechnology, 2nd edition. Springer-Verlag, 2006.

Davies OL. The design and analysis of industrial experiments. Oliver & Boyd, 1954

Fisher RA. The design of experiments, 1st edition. Oliver and Boyd, 1935.

Geomagic Studio 10. Geomagic Inc., 2008.

Hocking RR. The analysis and selection of variables in linear regression. *Biometrics* 1976; **32**: 1-49.

JEOL USA. A Guide to Scanning Electron Microscope Observation, JEOL, 2006.

Minitab$^{®}$ 14.1 statistical software (demo version). Minitab Ldt., 2003.

MeX^{TM} v 5.1. Alicona Imaging, 2007

Montgomery DC. Design and analysis of experiments, 7th edition. John Wiley, 2008.

Scanning Probe Image Processor (SPIP^{TM}) v 5.1.3. Image Metrology, 2010.

Watt IM. The principles and practice of Electron Microscope, 2nd edition. U. Cambridge Press, 1997.

6. Uncertainty evaluation of image quality
in 3D-SEM metrology

6.1 Introduction

A good quality SEM image should be sharp, noiseless and show an optimum combination of contrast and brightness. Nevertheless this is true only in an ideal case, since a number of image disturbances are often present in images. These, besides being attributed to defects in the instrument itself, are occasionally caused by the operator's lack of experience, improper specimen preparation and external influences such as the installation room conditions. Image disturbances, though diverse in types, can be classified by the following expressions (JEOL USA, 2006):

1) Images lacking sharpness and contrast;

2) Unstable images;

3) Generally poor-quality images;

4) Noisy images;

5) Images showing jagged edges;

6) Unusual-contrast images;

7) Distorted or deformed images.

The above-listed image disturbances and their causes are summarized in Fig.6.1.

Lack of sharpness	• Improper accelerating voltage setting. • Instability of gun emission caused by insufficient heating of filament. • Improper electron probe diameter. • Improper setting and incorrect centering of objective aperture. • Insufficient astigmatism correction • Improper focal depth • Too large magnification • Specimen charge-up and magnetization • Defocus of camera system
Low image quality	• Improper accelerating voltage setting • Improper probe current setting • Incorrect astigmatism correction • Noise caused by excessive photomultiplier (PMT) gain • Improper contrast and brightness • Improper specimen preparation process • Improper photographic material • Improper positional relation between specimen and detector • No specimen tilting
Noises	• Instability of accelerating voltage anci gun emission • Discharge of detector • Charge-up of specimen surface • Burnt CRT or dusty CRT screen • External stray magnetic field • Mechanical vibration
Image distortion and deformation	• Specimen charge-up • External stray magnetic field • Electron beam damage • Deformation of specimen itself during its preparation • Image drift caused by column interior charge-up • Specimen drift on heating and cooling stages

Figure 6.1. Image disturbances and their causes (JEOL USA, 2006).

As already described in chapter 5, there is a strict link between SEM instrument setting parameters and the resulting image quality. A SEM images lack of sharpness, for instance, could be due to improper accelerating voltage or spot size setting, as shown in Fig.6.1. Assuming that this setting is properly carried out, the operator should also correct the astigmatism, responsible for lack of sharpness and low image quality, and the three main image parameters: brightness, contrast and focus. In commercial SEMs optimum contrast and brightness can usually be adjusted automatically or by the operator. In the second case, the operator could use a helpful tool, belonging to the SEM employed in this experimental work, which consists of a histogram, overlapped in the specimen under investigation, showing the grey-scale of the pixels composing the SEM image as shown in Fig.6.2. After having properly adjusted the focus, it is in fact possible to adjust brightness and contrast using the tool shown in Fig.6.2, where the upper yellow line represents the grey-level 255 (white) and the lower one the grey-level 0 (black).
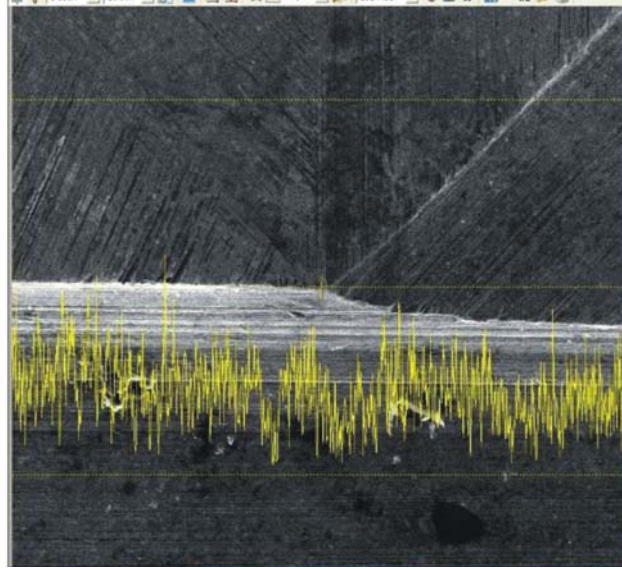
Figure 6.2. Example of the SEM tool assisting the operator to set the proper values of brightness and contrast for the image to be acquired. The upper yellow line represents the grey-level 255 and the lower one the grey-level 0.

A change in the levels of these two parameters, results in a different shape of the grey-levels histogram. In fact, changes of the contrast level result into a "stretch" of the grey-scale histogram, which becomes wider or narrower, while setting different values of the brightness cause simply a shift of the grey-scale histogram. The optimum adjustment would be the one having the mean value set at the central line and the spikes ranging from the bottom to the upper line. This configuration would provide SEM images having pixels distributed in the range of 0-255 *i.e.* in the whole grey-scale. This can be defined as a series of grey tones ranging from white to pure black. The more shades or levels of grey, the more accurately an image will look like a full-toned black-and-white photograph (Bonnet, 2004). SEM allows scans up to 256 grey tones. Problems may arise if a portion of the item under investigation is saturated. This would result in a totally white area in the image with grey-levels all set to 255. In Fig.6.3 an example of a saturated SEM image area is reported together with the related grey-scale histogram.
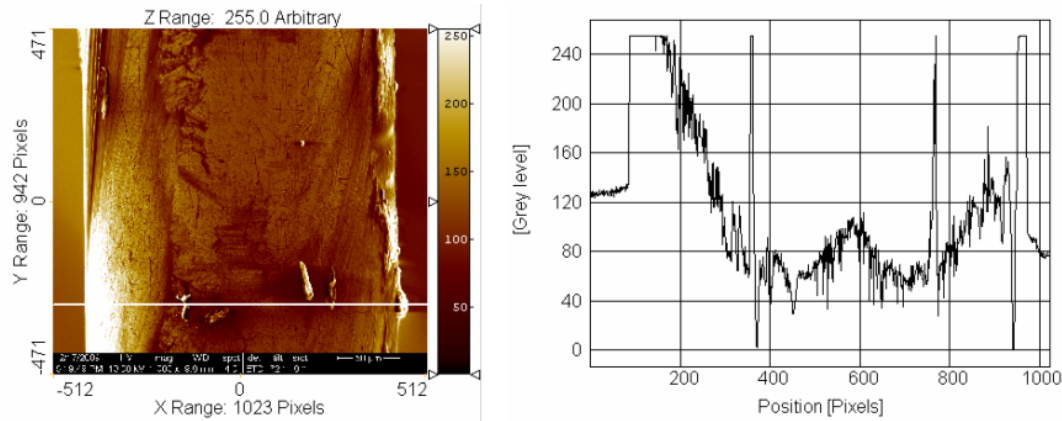
Figure 6.3. Example of SEM image of the wire gauge under investigation (on the left) where a 2D profile was plotted using Scanning Probe Image Processor software (SPIP^{TM}, 2010). The profile results in a graph (on the right) showing the grey-scale of the pixels. Saturated areas are represented by a "plateau" of pixels all set at the maximum grey-level equal to 255.

6.2 Experimental investigation on SEM image quality

In the previous section it was ascertained a number of factors influence SEM image quality. Among the factors responsible for low image quality, accelerating voltage, spot size, astigmatism, focus, brightness and contrast are the ones that can be more easily adjusted by the operator. Different settings or combinations of these parameters correspond to different image quality and different noise levels. The qualitative and quantitative effects of accelerating voltage and spot size were already investigated in chapter 5, while here an investigation on the role of brightness and contrast has been carried out, similarly to was previously done by the author in Marinello *et al.* (2008a) and by Marinello *et al.* (2008b). In particular, the effect of setting these two factors at different levels was tested. For this reason an experimental investigation was carried out starting from SEM images at HV=10 kV and SS=4 nm, and varying brightness and contrast to five different levels where level 0, 0 corresponds to the original image. Two stereo-pairs were also considered, -7&0 and 0&7, to be able to establish more general conclusions. As output parameters, the estimated diameter of the wire gauge and the average noise of the point cloud were considered. Changing the levels of brightness and contrast would change the ability of the MeX^{TM} (2007) to distinguish among neighbour points in the sub-pixelling phase. The clearer are the structures, the easier it would be for the software to match correspondent features in the two images composing the stereo-pair.

However, the blurrier the image, the more difficult it would be for the matching algorithm of the software to superimpose the two images to perform the stereo-photogrammetry. The experimental plan for the experiments is summarized in Table 6.1.

Error source	Factor	Symbol	Unit	Levels				
Image quality	brightness	B	-	-20	-10	0	10	20
	contrast	C	-	-20	-10	0	10	20
Stereo-pair reconstruction	stereo-pair	SP	-	-7&0	0&+7			

Table 6.1. Experimental plan for testing the influence of setting different levels of brightness and contrast on the estimated wire gauge diameter and point cloud noise. Effect of two different stereo-pairs was also taken into account.

The different levels of brightness and contrast were set offline starting from the same SEM image and using a freeware software available online (PAINT.NET, 2010). This allows manual adjustments of brightness and contrast level, by applying variations in the range ± 100%, anyhow. Nevertheless, too high or too low levels for both brightness and contrast would result in some unrealistic SEM images. For this reason, the range under investigation was set to be ± 20%, corresponding to the case of realistic variations due to the operator.

A design of experiments (DOE) approach was adopted to be able to evaluate not only the effects of the single factors but also their interactions which are supposed to be relevant. More information about this technique, based on analysis of variance, can be found in Montgomery (2008). A demo version of Minitab® 14.1 statistical software (2003) was employed. Having two factors and five levels, 25 combinations were obtained for each stereo-pair, meaning that a total of fifty 3D reconstructions were performed. Images where then imported into MeX to perform stereo-pair reconstructions leading to point clouds to be later post processed using a demo version of Geomagic Studio 10 (2008). The point clouds were all treated and analyzed using the same procedure consisting of trimming, outliers removal and filtering as described in chapter 4. This was done to reduce the variability due to the software for post processing.

Due to the large amount of data to be post-processed, six replications were performed only for three combinations: the B=C=0 one, corresponding to the original SEM image and the ones at the design corners, B=C=-20 and B=C=20. Therefore 40 combinations for each stereo-pair were obtained in total for testing. In Table 6.2 results obtained from the DOE analysis are shown and summarized to facilitate the comparison and in Fig.6.4 the main effects plot for the diameter and the average noise are shown.

		Avg.Noise		Diameter	
Source	**DF**	*p*-value	SQ%	*p*-value	SQ%
Brightness	4	0.000	7.8	0.442	3.9
Contrast	4	0.000	80.8	0.004	13.1
Stereo-pair	1	0.000	4.1	0.000	40.2
Main Effects	9		92.7		57.1
Brightness·Contrast	16	0.000	5.5	0.306	11.4
Brightness·Stereo-pair	4	0.310	0.2	0.537	2.0
Contrast·Stereo-pair	4	0.027	0.3	0.509	2.0
Interactions	24		6.0		15.4
Error	46				
Total	79		98.7		72.5

Table 6.2. Summary of the design of experiments results showing, for each main effect and interaction, the degrees of freedom (DF), the *p*-value (relevant if <0.05) and the percentage sum of squares (SQ%) considering average noise and diameter as responses.
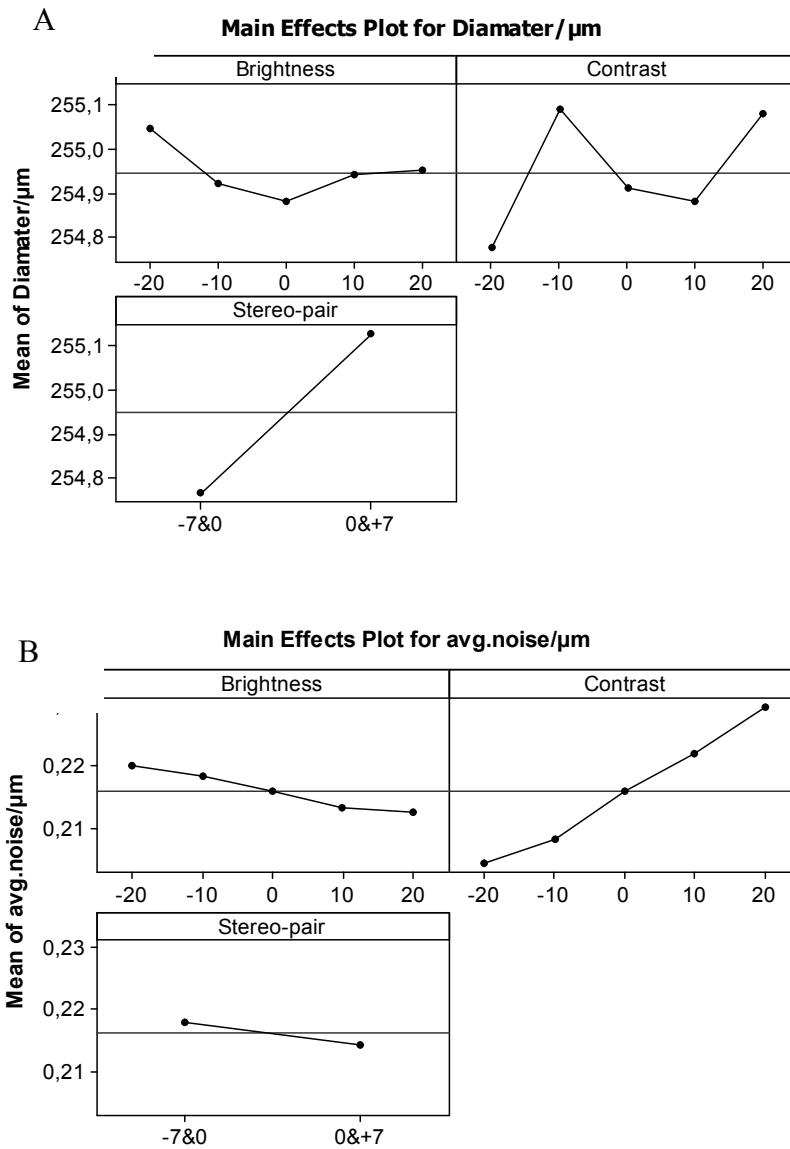
Figure 6.4. Main effects plot resulting from the design of experiments analysis considering wire gauge diameter (A) and average noise (B) of the point cloud as responses.

From the results shown in Table 6.2 and the Fig.6.4 the following conclusions can be drawn:

- Considering the <u>average noise</u> as response:

  o Main effects are all significant being the *p*-value <0.05, brightness-contrast interaction is also significant as well as contrast-stereo-pair;

  o Image contrast is the most influencing factor by far, accounting for almost 81% of the overall response variability followed by the brightness (7.8%) and the interaction brightness·contrast (5.5%). This result was expected as contrast is responsible for modifying the grey-scale histogram shape, thus producing noise variations;

  o Main effects account for about 93% of the whole variability, therefore the interactions could be neglected;

  o There is a slight influence of the stereo-pair (4.1%), meaning that the average noise is almost non sensitive to the uncertainty of MeX input parameters set to perform the 3D reconstructions.

- Considering the <u>diameter</u> as response:

  o A key role on the overall variability is played by the stereo-pair. This means that analyzing different portions of the same object results in a difference on the diameter value. This difference could be due to the influence of MeX input parameters, working distance, rotational angle and pixel size on the 3D reconstructions;

  o Considering the *p*-value, only the stereo-pair and the contrast are significant with regards to their influence on the diameter estimation;

  o Generally speaking, the effect of repeatability on the estimated diameter is higher than the effect of setting different levels of brightness and contrast.

In Table 6.3 mean values, standard deviation, maximum and minimum values and variability ranges for all the 40 reconstructions are shown for each stereo-pair under investigation. Moreover in figure 6.5 mean value and expanded standard deviation (k=2) of the six replicated experiments are shown for the three cases under consideration: B=C=-20, B=C=0, and B=C=20. The systematic overestimation of stereo-pair 0&+7 with respect the other one is clearly visible, while uncertainties due to the repeatability of 3D reconstructions are ranging from 0.3 μm to 0.6 μm.

Variations due to setting brightness and contrast at different levels are in the order of approx. 0.5 μm, therefore in the same order of magnitude of the uncertainty related to the replications.

| | Stereo-pair | | | |
| | -7&0 | | 0&+7 | |
	Avg.noise/μm	Diamater/μm	Avg.noise/μm	Diamater/μm
Mean value	0.219	254.7	0.215	255.1
Standard Deviation	0.009	0.3	0.010	0.2
Max. value	0.234	255.2	0.231	255.5
Min. value	0.200	254.3	0.193	254.6
Variability range	0.034	0.9	0.038	0.9

Table 6.3. Summary of the results showing mean value, standard deviation, max and min value and variability range for the 40 experiments considering average noise and diameter as responses and the two stereo-pair -7&0 and 0&+7.
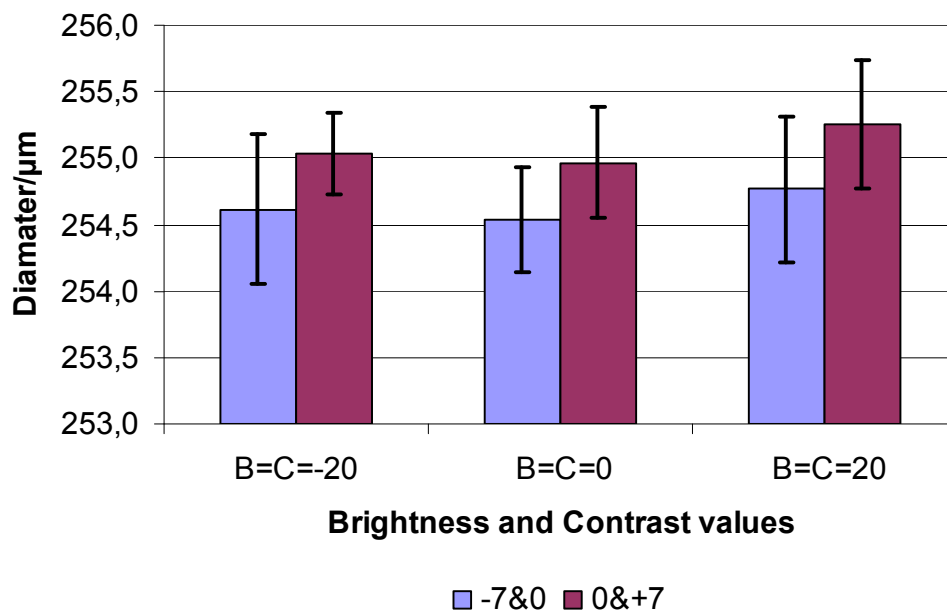
Figure 6.5. Mean value and expanded standard deviation (k=2) for the six replicated experiments for the three cases under consideration: B=C=-20, B=C=0, and B=C=20. Effect of the two stereo-pair, -7&0 and 0&+7 was also tested.

From Fig.6.5 it can be concluded that, considering the wire gauge diameter as response, different levels of brightness and contrast have a slight influence on the diameter estimation. This means that the MeX algorithm, performing stereo-pair reconstructions, is consistent and stable and that image quality, although playing a role in the overall uncertainty, has an influence considerably smaller, compared to other error sources such as, for example, the one to be further investigated, leading to wire gauge diameter overestimation of about 2%. In fact, mean values of the diameter for the two stereo-pair were 254.7 μm for -7&0 and 255.1 μm for 0&+7, which are respectively 1.9 and 2.0% higher than the reference value equal to 250 μm. A further experimental investigation was subsequently carried out concerning the effect of noise, affecting SEM images, on 3D reconstructions. A certain amount of noise is always present in SEM images due to the sources shown in table 6.1 and to the scan rate select by the operator defined as the number of lines scanned per second in a SEM. Faster scan rates result in quicker image acquisition, but also noisier images are obtained.

The effect of setting different scan rates in SEM images was investigated in (Marinello *et al.*, 2008b). Images of the wire gauge acquired at -7, 0 and 7 rotational degrees were considered for the experimental analysis. An automatic adjustment of brightness and contrast was performed using the same commercial software previously employed for image analysis. It must be noticed that saturated areas can not be improved qualitatively, as they will remain always saturated (*i.e.* grey-level equal to 255) even though brightness and contrast are changed manually or automatically.

After this operation, using same commercial software, it was possible to add, offline, 4 different levels of noise, 10, 20, 30 and 40 to the original images to simulate experimental conditions of noisy images. Nevertheless these values provide just a rough indication of the noise, as they are not related to any measurement unit. The two SEM Images were superimposed using MeX and 3D reconstructions. These were performed to obtain point clouds to be post processed. Six replicated experiments were performed for a total of 30 point clouds (six for five levels). Wire gauge diameter and average point cloud noise were considered as responses to test the effect of different levels of noises. The first relevant result is shown in Fig.6.6 where the mean value and expanded standard deviation (k=2) of the diameter for the six replicated experiments at the five noise levels are represented.

As a clear trend in the results can not be seen, it can be concluded that that by post-processing the point clouds, removing outliers and filtering, the effect of noise can be reduced. Moreover the least square method for diameter estimation on cylindrical items is most likely not too sensitive to presence of noise in the point cloud.
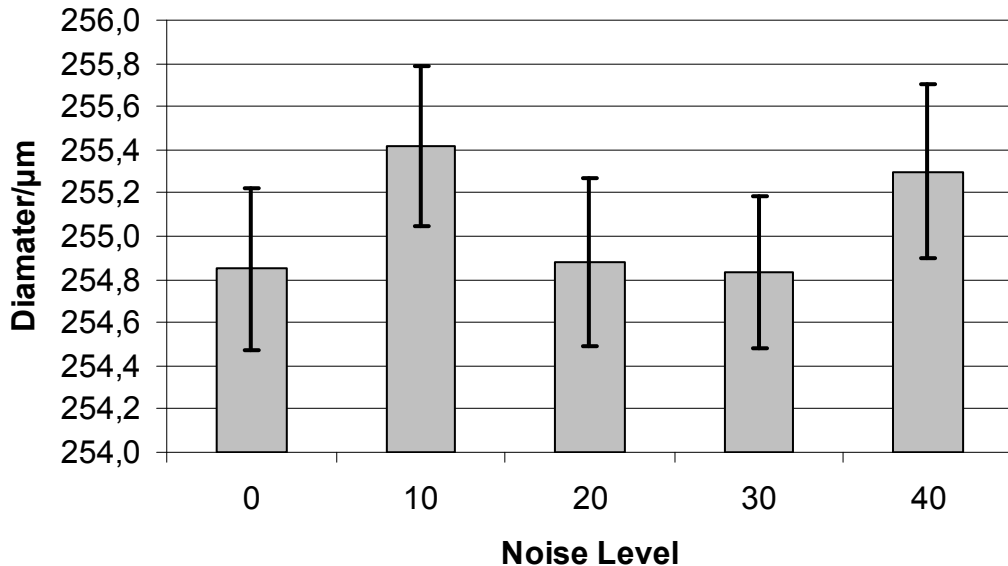
Figure 6.6. Mean value and expanded uncertainty (k=2) of the estimated diameter, for six replicated experiments, performed at different noise levels.

A graph showing the average noise of the point cloud as a function of the different noise levels was also produced (Fig.6.7). In this case, differently from the diameter estimation, there is a clear trend in the relationship between average noise and noise level of the SEM images. In fact, as this is increasing, the average noise is increasing following a third order *i.e.* the cubic fitting line. This is probably due to the fact that noise variations at a 2D level, results in 3D variations when stereo-pair technique is employed. Slight changes of the noise level in SEM images result in differences in the average noise, affecting the point cloud, ranging from 100 nm to about 600 nm. Therefore outliers removal and filtering become necessary operations to be performed although rougher surfaces are obtained as shown in Fig.6.8.
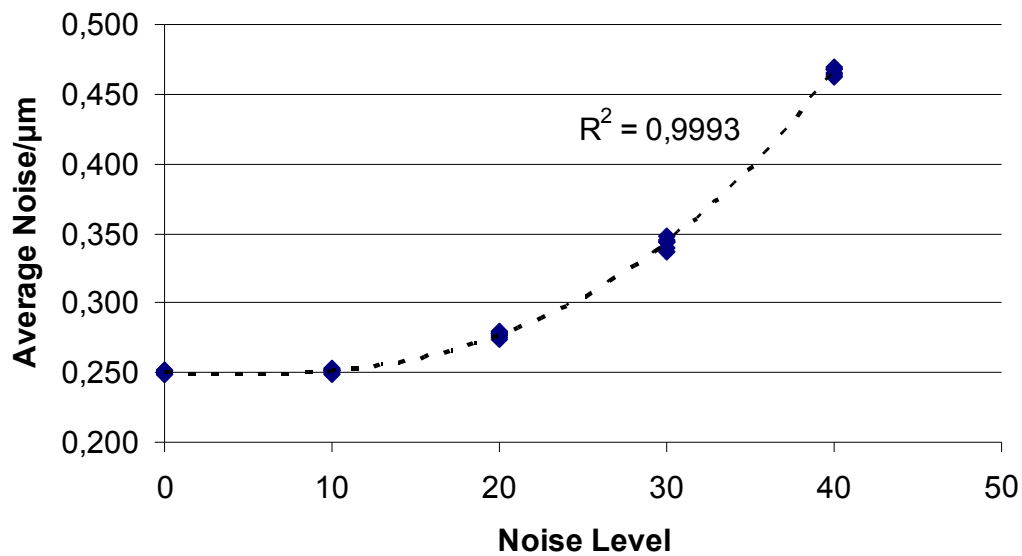
Figure 6.7. Graph showing the effect of different noise levels on the average noise estimated from the resulting point clouds. A cubic trend was obtained by plotting the regression line (dotted line).

Figure 6.8. Example of three wrapped point clouds obtained from SEM images exhibiting noise levels equal to 0 (left), 20 (center) and 40 (right). All the three point clouds were post processed by removing outliers and filtering, nevertheless rougher surfaces are obtained when starting from noisier SEM images, while smoother surfaces are obtained when SEM images are less noisy, as it can be seen in the left image.

The last test performed concerning effects of noise was the 3D comparison of the wrapped point cloud obtained from 0 noise SEM images and the one from noise level 40 (Fig.6.9). The colour scale indicates the difference in micron of the different areas of the wrapped point cloud using the one obtained from noise level 40 as reference and subtracting the noise level 0 one from it. Green areas represent portions of the item where the mean difference lies in the area belonging to the uncertainty dealing with repeatability uncertainty of diameter estimation (approx. ± 0.3 μm). Areas showing the highest deviations, dark blue and red colours, corresponds to the borders or to the feature affecting the cylindrical shape.
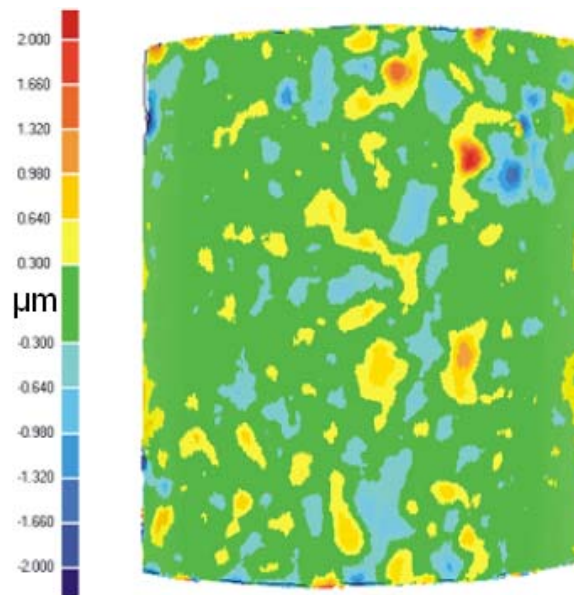
Figure 6.9. Deviation ranges in micron of the point cloud at noise 0 compared with the one at noise 40. Deviations represented in green, cover the standard deviation of six replicated measurements (±0.3 μm at k=2). Highest deviations correspond to the features on the wire gauge, which are used by MeX to superimpose the two images composing the stereo-pair.

From all the previous experiments it can be concluded that higher levels of noise in the SEM images composing the stereo-pair generate a noisier point cloud, resulting then in a rougher wrapped surface. Moreover, performing an anova statistical analysis, on the influence of noise level on diameter estimation, it was found it to be significant being *p* value <0.001 giving a R-squared value of about 68%, meaning that the variability due to MeX repeatability in performing 3D reconstructions and due to the operator performing the trimming, accounts for about 32%.

With reference to Fig.6.6, smaller variations of the noise level *e.g.* 10, are more critical than higher variations *e.g.* 20 or 30. In this second case, the presence of noise starts to be visible in the image, therefore the operator might decide to perform the measurements again. On the contrary, smaller levels of noise are not easily visible and, as it was demonstrated, they are responsible for an increase of about 0.6 μm in the mean value of the six replicated experiments at noise level equal to 10.

Another relevant effect of different noise levels on stereo-photogrammetry technique was also observed. In fact, it was proven as different levels of noise in SEM images can modify the ability of MeX to superimpose the two images composing the stereo-pair by finding same spots on the two images. The main conclusion is that different noise levels may cause a shift in the horizontal-offset (X), while they have a random effect on the vertical one (Y). In Fig.6.10 the resulting X-offset (horizontal) as a function of the different noise levels is shown.
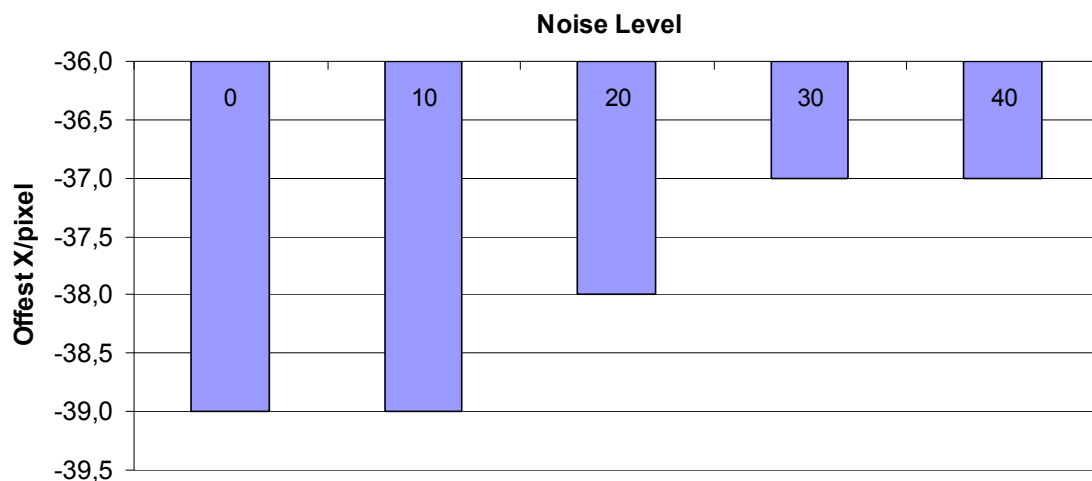
Figure 6.10. Effect of different noise levels on the ability of MeX to find correspondent features in the two SEM images composing the stereo-pair, in terms of horizontal-offset (X).

It has been therefore proven that the presence of noise in SEM images is affecting the MeX ability to find correspondent features in the two images composing the stereo-pair. In fact, as the noise level is increasing the X-offset, which is the shift, in pixels, of a feature from the first image to the second one, is changing. In particular within the noise level range tested, variations of 2 pixels were observed for the X-offset.

A similar X-offset shifting effect can be caused also by a slight out of focus of SEM images, as in this case the contours of the features present in the image becomes blurry and this affects the MeX ability to find exact correspondences between same features in the two images. An experimental investigation was therefore carried out to investigate the effects of a X-offset shifting, on 3D-SEM reconstructions similarly to what previously done by Marinello *et al.* (2008b). Stereo-pair named -7&0 was considered and a horizontal X-offset equal to -37 pixels was calculated using MeX. This value was then manually varied, within the range ±25 pixels, by the operator to simulate the conditions of presence of noise or slight image out of focus. Each time a Δoffset X quantity was calculated, which represents the different, in pixels, between the original X-offset and the one set by the operator. A series of 3D reconstructions were then performed, starting from the same stereo-pair -7&0 and from different Δoffset X values, and the external diameter of the cylinder was calculated for each reconstruction. The graph in Fig.6.11 shows the calculated external diameter as a function of the different Δoffset X values. In order to determine whether these offsets are statistically relevant, the resulting values should be compared with the diameter calculated for Δoffset X=0 pixel also taking into account the diameter calculation uncertainty, due to the point cloud trimming replicated operations σ (see section 4.5), which is equal to 0.4 μm (k=2).
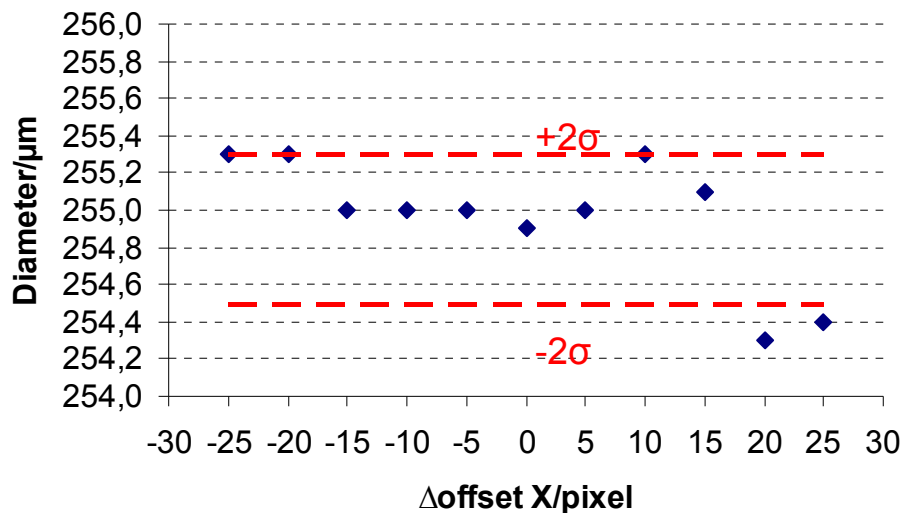
Figure 6.11. Calculated values of the external diameter as a function of the different Δoffset X values. 3D reconstructions were performed from stereo-pair -7&0. Values must be compared to the one obtained for Δoffset X=0 and considering the uncertainty due to the point cloud trimming replicated operations σ=0.2 μm (k=2).

From the results shown in Fig.6.11 it can be concluded that a Δoffset X, applied to the original offset X value equal to -37 calculated automatically by MeX, does not lead to any significative influence on the diameter evaluation, considering also the uncertainty related to the point cloud trimming operation for Δoffset X within the range -25 to +15 pixels. For Δoffset X higher than +15 pixels the shift starts to become relevant for diameter calculation, leading to differences in the order of -0.6 μm compared to the original value of 254,9 μm obtained for Δoffset X=0. In the case of measurements performed at M=1000x, where the pixel size is about 0.295 μm/pixel, an offset equal to 25 pixels corresponds to a drift of about 7,4 μm between the two images composing the stereo-pair. Moreover, in the case of not perfect eucentric tilting, or object misalignment, a drift in the Y direction can also occur. For the case under consideration, the stereo-pair -7&0, an offset Y equal to -4 pixels was automatically calculated by MeX. In this case, the effect of a Δoffset Y on 3D reconstructions was also estimated through an experimental investigation, similarly what was already done for the case of Δoffset X. The procedure in this case was exactly the same as before, and Δoffset Y=±25 pixels were tested. The results are shown in Fig.6.12.
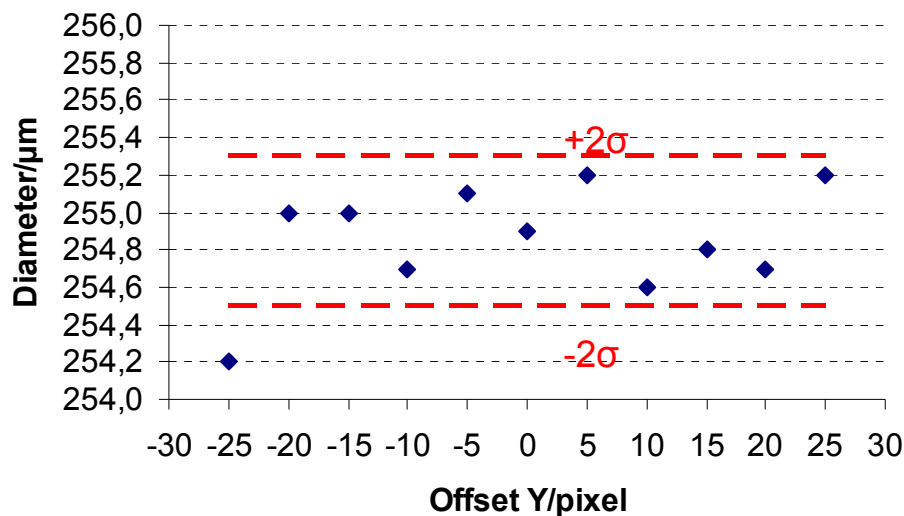
Figure 6.12. Calculated values of the external diameter as a function of the different Δoffset Y values. 3D reconstructions were performed from stereo-pair -7&0. Values must be compared to the one obtained for Δoffset Y=0 and considering the uncertainty due to the point cloud trimming replicated operations σ=0.2 μm (k=2).

From the analysis of the results shown in Fig.6.12 it can be concluded that also a Δoffset Y, applied to the original offset Y value equal to -4 calculated automatically by MeX, does not lead to any significative influence on the diameter evaluation, considering also the uncertainty related to the point cloud trimming operation for Δoffset Y within the range -20 to +25 pixels. For Δoffset Y lower than -20 pixels the shift starts to become relevant for diameter calculation, leading to differences in the order of 0.7 μm compared to the original value of 254,9 μm obtained for Δoffset Y=0.

6.3 Summary and conclusions

The quantitative effect of SEM image quality on 3D-SEM reconstructions was tested in this chapter. Contrast, brightness, focus, astigmatism, saturation and noise were the factors identified as characteristics of a SEM image. Nevertheless, in this work, optimum focus and astigmatism settings were assumed and only the effects of brightness, contrast and noise were tested through an experimental investigation. As a case study, three SEM images of a cylindrical item, a wire gauge with a reference diameter of 250 μm, were considered. Those three images allow performing two stereo-pair reconstructions, named after the rotational angle -7&0 and 0&+7. 80 reconstructions were performed using MeX and the automatic superimposition technique, considering the two different stereo-pairs and five levels of brightness and contrast, which were adjusted offline using commercial software ranging in a realistic range of SEM image qualities that could be considered acceptable by the operator. Six replications were also performed only at the design corners to be able to evaluate uncertainty related to repeatability. A design of the experiment approach was adopted to account for main influencing factors considering average point cloud noise and estimated diameter as responses. The following conclusions were obtained:

➢ Brightness and contrast were found to significantly affect the average noise, calculated from stereo-pair reconstructions, being p-values <0.05;

➢ The contrast is responsible for about 81% of the whole results variability. This result was expected as contrast is responsible for modifying the grey-scale histogram shape, thus producing noise variations;

➢ Brightness was found not to be a significant factor affecting the wire gauge diameter estimation, while contrast and stereo-pair were found to have a strong influence. In particular a systematic overestimation of point cloud 0&+7 with respect to the -7&0, one was found. Nevertheless it was not possible to calculate a clear trend of the diameter as a response considering contrast and stereo-pair as factors, being this effect was most likely random. The variability range of the 40 reconstruction for each stereo-pair was estimated equal to 0.9 μm with a standard deviation of 0.3 μm. It can be therefore be concluded that image quality determines a variation in the wire gauge diameter estimation. Nevertheless this variation is not so large as to explain the systematic overestimation of both stereo-pairs which was about 2% with respect to the reference value of the diameter equal to 250 μm.

Some tests were also performed, concerning the influence of the presence of noise in SEM images, on the resulting 3D-SEM reconstructions. Five different noise levels were tested for their influence on average point cloud noise and diameter estimation. It was found that, although noise levels slightly influence the diameter estimation, they strongly affect the average noise, being the relationship represented by a cubic trend. Moreover the presence of noise in SEM images affects the ability of MeX of superimposing the two images composing the stereo-pair, by making it more difficult to recognize the correspondent features in the two images.

The effects of an inaccurate automatic Horizontal (X) and Vertical (Y) offset calculation by MeX, for two images composing the stereo-pair, were tested with regards to their influence on the diameter estimation. Through an experimental investigation it was demonstrated that varying manually both the horizontal and vertical offsets in a range of $\pm$ 25 pixels does not lead to any significative difference in the diameter calculation also taking into account the uncertainty due to the point cloud trimming replicated operations $\sigma = \pm$ 0.2 μm (k=2). In particular, Δoffset X becomes relevant only for values higher than +20 pixels, when a difference of about -0.6 μm can be observed in the diameter calculation. Concerning Δoffset Y it was proven to influence the diameter calculation, leading to a variation of about 0.7 μm, compared to the original value of 254,9 μm obtained for Δoffset Y=0, for Δoffset Y lower than -20 pixels.

References

Bonnet N. Some trends in microscope image processing. *Micron. 2004;* **35:** 635-53.

Geomagic Studio 10. Geomagic Inc., 2008.

JEOL USA. A Guide to Scanning Electron Microscope Observation. JEOL, 2006.

Marinello F, Carmignato S, Savio E, Bariani P, Carli L, Horsewell A, De Chiffre L. Metrological performance of SEM 3D techniques. *Proc. of 18th IMEKO TC 2 Symposium on Photonics in Measurements*, Prague, 2008a.

Marinello F, Bariani P, Savio E, Horsewell A, De Chiffre L. Critical factors in SEM 3D stereo microscopy. *Meas. Sci. Technol.* 2008b; *19;* 065705.

MeX^{TM} v 5.1. Alicona Imaging, 2007.

Minitab$^{®}$ 14.1 statistical software (demo version). Minitab Ldt., 2003.

Montgomery DC. Design and analysis of experiments, 7th edition. John Wiley, 2008.

PAINT.NET v 3.5.5. Getpaint, 2010.

Scanning Probe Image Processor (SPIP^{TM}) v 5.1.3. Image Metrology, 2010.

7. Uncertainty evaluation of stereo-pair technique

7.1 Introduction

3D-SEM, based on a stereophotogrammetry technique, is a method for obtaining three dimensional topographic reconstructions of an item starting from two SEM images called the stereo-pair. The theoretical basis of this methodology was already discussed in section 3.3, together with the model function introduced by Piazzesi (1973), adapted for eucentrically tilted stereo-pairs. For a more practical implementation of this technique many software programs are nowadays available on the market including MeX by Alicona Imaging GmbH (MeX^{TM}, 2007) which is the one used in this work. The aim of this chapter is to perform a theoretical and an experimental uncertainty evaluation of stereo-pair technique, according to ISO GUM (JCGM 100:2008), and to compare these two approaches. As a case study, 3D-SEM reconstructions, performed on a wire gauge with a 250 μm reference diameter and using the multi-view strategy through item rotations, were considered.

Some problems may arise when the multi-view technique is performed using rotations, due to the limitation concerning the object tilting, which can not be positioned to exactly 90 degrees to align the item horizontally. Among the factors involved in stereo-pair reconstructions, the inclination of the item, with respect to the horizontal direction, leads, in particular, to slight variations of the working distance along the longitudinal direction of the cylinder (Fig.7.1). This effect was quantified, with reference to Fig.7.2, where L is the longitudinal length of the cylinder, d the nominal working distance and θ the object tilting with respect to the vertical direction y.
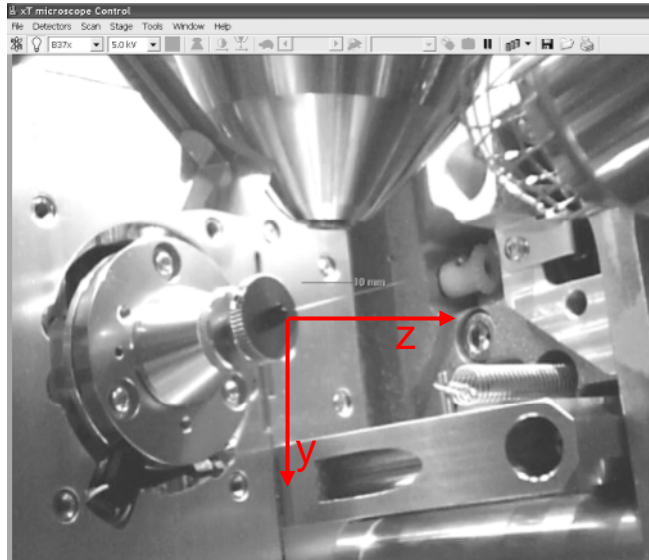
Figure 7.1. Example of a cylindrical item, fixed to the stage inside the SEM chamber, tilted to 78 degrees to allow rotations along its main axis. The y and z-axis direction, with respect to the degrees of freedom of the SEM stage are also shown (Caroli, 2009).
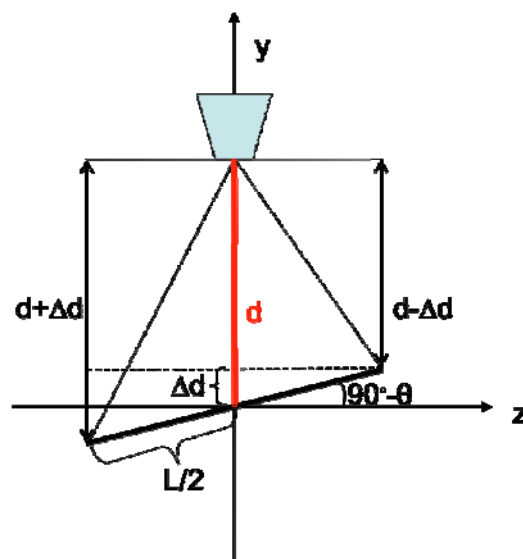
Figure 7.2. Geometrical definition of working distance variation Δd, deriving from a cylindrical item, with a longitudinal length L, being tilted by an amount θ inside the SEM chamber to perform rotations. The working distance d is under scaled for ease of interpretation.

Therefore, it is possible to calculate the working distance variation, named Δd as follows:

$$\Delta d = L/2 \cdot \sin(90 - \theta) = L/2 \cdot \cos(\theta) \qquad (1)$$

It follows that, being the estimated valued of L, resulting from stereo-pair reconstructions, equal to approx. 250 μm, and assuming a working distance d=10.0 mm, the result from the equation (1) is Δd=26 μm, that is about 0.3% of the nominal d value. Nevertheless, since the quantitative influence of the working distance, on the stereo-pair reconstructions, which will be calculated performing a theoretical and experimental uncertainty evaluation, was found to be negligible, the Δd contribution can be considered negligible.

7.2 Theoretical uncertainty evaluation of stereo-pair technique

The theoretical model of Piazzesi, for deriving surface topography from eucentric stereo-pairs, was described in section 3.3 and an equation for calculating the z-coordinate was provided. The same equation can be written in a different form, based on the following considerations. The distance between two points in a digital picture is given by the number of pixels n counted between the two points multiplied by the single pixel dimension (pixel size) p, therefore it holds that $y_1 = n_1 p$ and $y_2 = n_2 p$. It follows that Piazzesi equation for the z-coordinate becomes:

$$z = \frac{p(n_1 - n_2)\cos\Delta\varphi + \dfrac{2p^2 n_1 n_2}{d}\sin\Delta\varphi}{\left(1 + \dfrac{p^2 n_1 n_2}{d^2}\right)\sin 2\Delta\varphi + p\dfrac{n_1 - n_2}{d}\cos 2\Delta\varphi} \qquad (2)$$

A theoretical uncertainty evaluation according to GUM (JCGM 100:2008) has been performed starting from equation (2), thus considering p, n_1, n_2, d and $\Delta\varphi$ as independent variables. It is subsequent to a preliminary evaluation given in Genta (2010). It has been checked that a linear approximation of the measurement function is acceptable within the range of variation of input quantities. On the other hand, the hypothesis of non-correlation among input quantities is supported by the following considerations. Pixel size p and working distance d are instrument parameters which can be reasonably assumed constant, while tilt angle $\Delta\varphi$ is a process parameter, therefore these variables are not correlated. In the measurement process $\Delta\varphi$ is also constant; so, for a given value of z, pixel numbers n_1 and n_2 remain constant. Moreover, each of mentioned variables is affected by random effects.

145

In conclusion, the presence of correlation among variables seems to be unlikely. In particular, the tilt angle (or, similarly, rotational angle) $\Delta\varphi$ is chosen a priori before performing the reconstructions, while the working distance d can be read on the screen when SEM images are acquired. The pixel size p is linked to instrument settings, mainly in relation to magnification level as described in chapter 3. Pixel numbers n_1 and n_2 are instead directly read on the images composing the stereo-pair as previously described.

Metrological characteristics of each input variable (p, n_1, n_2, d and $\Delta\varphi$) have to be taken into account. In fact, ISO/IEC 17025:2005, which deals with the concept of "measurement complex", stresses the important effects of measuring instrument, operators, working conditions and measurand on measurement results. Note that instrument influence is usually described by bias, repeatability and resolution, while measurement complex performances are described by reproducibility (JCGM 200:2008).

Therefore, in principle, reproducibility comprises repeatability and resolution; however, in a few cases, resolution is the worst characteristic. It can be reasonably neglected when it is lower than 50% of reproducibility.

The theoretical uncertainty evaluation was carried out in two cases, tilt and rotation, to allow a comparison between these two measuring strategies. Moreover, some calibration operations were necessary, since no calibration certificate or any other information were available stating SEM stage performances.

7.2.1 Evaluation of main uncertainty contributions

A) Pixel size

> ### *Bias evaluation*

The pixel size p has been calibrated through a TGT1 silicon grating from NT-MDT (Europe, The Netherlands), intended for SPM calibration, already exploited for the uncertainty evaluation of instrument settings (section 5.3). . The grating consists of an array of sharp tips with a period of 3.00±0.05 μm and a diagonal period of 2.12 μm as declared by the producer. This calibration procedure was carried out at fixed values of the main instrument settings (*i.e.* accelerating voltage HV=10 kV and spot size SS=4 nm) and the working distance. The whole range of magnification M in the measurement conditions has been explored.

146

In particular 24 SEM images of the calibrated artefact were acquired to allow pixel size calculation as described in section 5.3. Among these 24 experiments, 5 replications were performed at M=1000x and M=10.000x to enable reproducibility evaluation. A graph was produced (see Fig.7.3), where the empirical relation (regression dotted curve) between pixel size *p* and magnification M calculated from the 24 experiments carried out. The correctness of fit of the empirical relation is confirmed by the standard deviation of residuals, which is then equal to 5·10-4 μm/pixel. It means, also, that the uncertainty of the model is negligible. The empirical relation can also reasonably be approximated by the hyperbola p=293.2/M. The bias to be considered in this case is the one deriving from the calibrated artefact. In this evaluation, just to be on the safe side, the period is totally attributed to bias error (that is the most severe condition); a relative bias of 1.6% has thus been considered. For magnifications equal to 800x and 1000x, pixel size results equally respectively to 0.366 μm/pixel and 0.293 μm/pixel. Therefore, the bias is equal to about $5.9 \cdot 10^{-3}$ μm/pixel and $4.7 \cdot 10^{-3}$ μm/pixel, respectively.
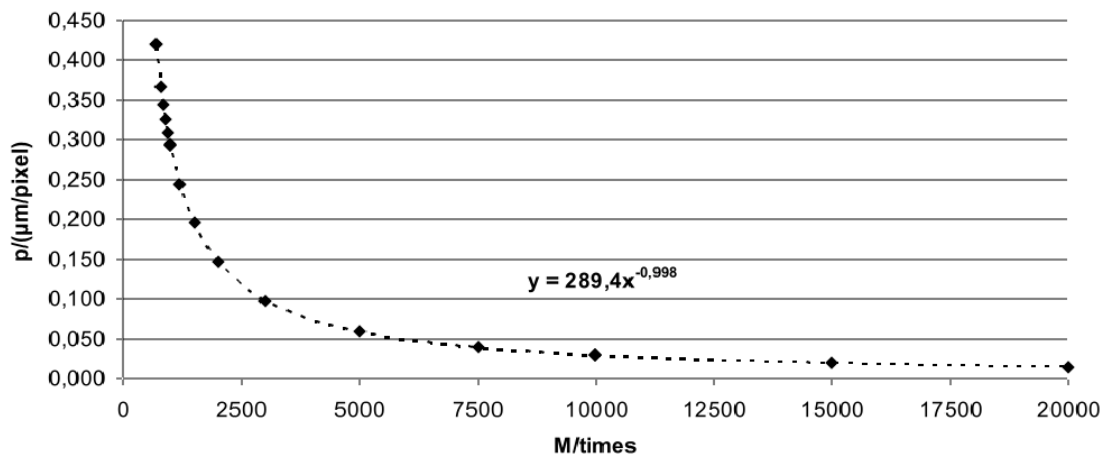
Figure 7.3. Empirical relation (regression dotted curve) between pixel size p and magnification M calculated from 24 experiments.

> *Reproducibility evaluation*

Fixing the magnification to 1000x, the standard deviation of five replicated measurements is equal to $6.2 \cdot 10^{-4}$ μm/pixel, corresponding to about 2% of the calibrated pixel size value. For magnification equal to 800x, that is near to the lower bound of M in the measurement conditions, one half of variability range equal to $1 \cdot 10^{-3}$ μm/pixel can reasonably be assumed.

> *Resolution*

It can be estimated by dividing pixel size *p* that is variability in the evaluation of diagonal period of the grating by the square root of number of cells considered in the measurement conditions. The number of cells can be easily calculated when the field of view at a given magnification is known and by the grating' size. For magnification equal to 800x and 1000x, a total of 27081 and 17324 cells are respectively considered. Therefore, the resolution is equal to about $2.2 \cdot 10^{-3}$ μm/pixel. Note that it is a unique value depending on grating diagonal period and SEM digital resolution (*i.e.* 1024x884 pixels). This contribution has to be considered, since the value is greater than the reproducibility for both values of magnification tested.

B) Number of pixels

The same considerations, made for the case of the pixel size, apply to the numbers of pixels n_1 and n_2 relevant to coordinates y_1 and y_2, respectively

> *Bias*

Since the variable is a count, this contribution is not considered.

> *Reproducibility evaluation*

The reproducibility in the identification of homologous points has been considered. It depends on the quality of the image and how the image is handled by the software. It is possible to evaluate the reproducibility for classes of images (well-defined details, visible details, blurry image). Rough values of reproducibility from 0.1 to 5 pixels were considered, basing also on the available literature (Scharstein, 2002).

> *Resolution*

It is not considered, since it is contained in reproducibility.

C) Working distance

> *Bias evaluation*

The calibration of the working distance d is problematic, since this quantity is not directly controllable. However this calibration can be omitted, as the contribution of working distance in terms of overall uncertainty is negligible (see section 7.2.3).

➢ *Reproducibility evaluation*

In order to evaluate the reproducibility of the working distance d, its relation with z-coordinate has been empirically derived. The z-axis was previously calibrated (Caroli, 2009) with reference to ISO 230-2:2006 (see Fig.7.4). Fixing main instrument settings (*i.e.* accelerating voltage, spot size and magnification), a total of 18 measurements of d were performed along the lines of ISO 230-2:2006 (two backward and one forward series). The whole z-coordinate range has been explored in the measurement conditions (see Fig.7.5).
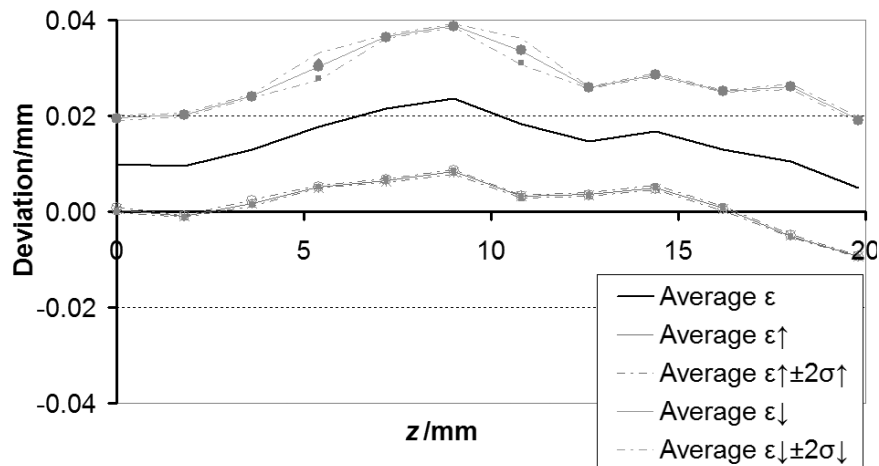
Figure 7.4. Z-axis bi-directional accuracy of positioning. Dark grey symbols represent runs taken when moving forwards, while light grey runs are taken moving backwards (Caroli, 2009).
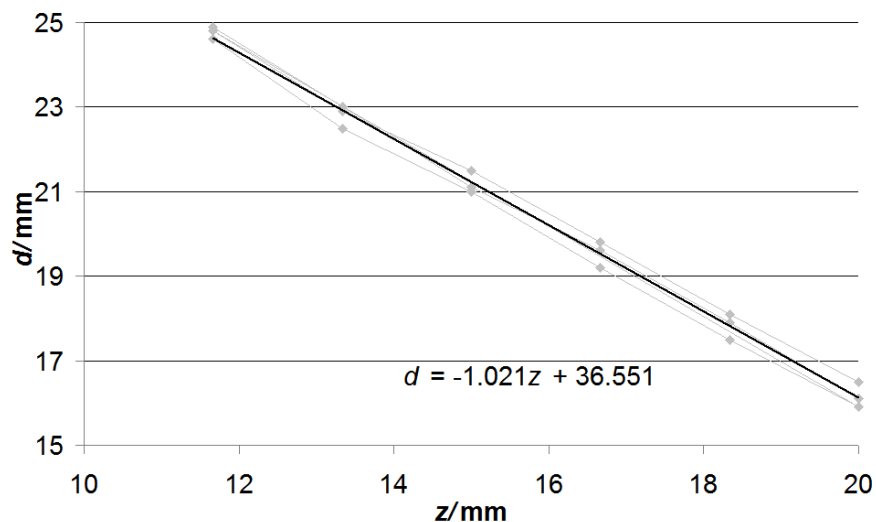
Figure 7.5. Empirical relation (regression line) between working distance d and coordinate-z (Genta, 2010).

The reproducibility of the working distance d can be assessed as a deviation from a hypothetical model, that is the regression equation d=az+b. In particular, it has been evaluated as a standard deviation of regression residuals, which is equal to 0.25 mm.

Looking at the empirical relation (Fig.7.5) an absolute value of slope different from unity implies that varying z (*i.e.* changing focus), also changes the focal length.

> *Resolution*

The resolution is equal to 0.1 mm, as it can be read from the SEM controller. Since this value is lower than 50% of reproducibility, it can be neglected.

D) Rotational angle

The rotary table was calibrated for rotational angles φ between 0° and 360°.

> *Bias evaluation*

The SPM calibration grating pitch, previously used for pixel size calibration, may also be adopted for calibration of rotational angle φ. This calibration was performed along the lines of ISO 230-2:2006 (two forward and one backward series). The whole range of rotations of the rotary table was explored performing a total of 93 measurements (see Fig.7.6).
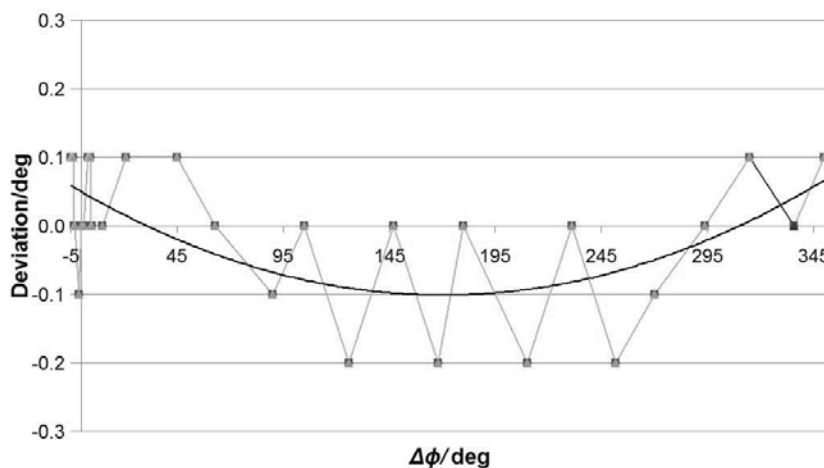
Figure 7.6. Rotational angle φ bi-directional accuracy of positioning. The deviation is modelled by a regression curve. Differences between run taken moving forwards and backwards are negligible (Genta, 2010).

A systematic effect due to the resolution (saw tooth trend in Fig.7.6) and one due to the characteristic of the rotary table may be observed, the deviation e of the latter being reasonably modelled by the parabola,

$$e = a\varphi^2 + b\varphi + c \tag{3}$$

Where $a=3.0 \cdot 10^{-4}$ rad^{-1}, $b=-1.8 \cdot 10^{-3}$ and $c=8.7\ 10^{-4}$ rad. The systematic effect for any value of φ may thus be corrected. The parabolic correction is significant on the definition of the direction of view, while for the angle between two images is negligible against the variation given by the saw tooth effect.

In fact, in this case, assuming stereo-pair angle $\Delta\varphi$ equal to $6.11 \cdot 10^{-2}$ rad, the correction is found to be $9.8 \cdot 10^{-4}$ rad in the worst case. When necessary, uncertainty of the model (3) can be considered, and approximated as;

$$u_e^2 = \left(\varphi^2\right)^2 u_a^2 + \varphi^2 u_b^2 + u_c^2 \tag{4}$$

Terms u_a, u_b and u_c are known from regression, while $\Delta\varphi$ is the rotational angle adopted. Concluding, in the case at hand, the bias u_e to be considered is 0.011°, *i.e.* $2.0 \cdot 10^{-4}$ rad.

As far as the saw tooth effect is concerned, a mathematical model may not be implemented owing to lack of information (pattern in the interval between any couple of experimental points being unknown), therefore it is taken into account by the reproducibility evaluation.

➢ *Reproducibility evaluation*

It can be evaluated as the standard deviation of regression residuals against the parabolic pattern (see Figure 5), which is equal to 0.077°, *i.e.* $1.3 \cdot 10^{-3}$ rad.

➢ *Resolution*

The resolution is equal to 0.1°, *i.e.* $1.7 \cdot 10^{-3}$ rad. It has to be considered, since it is greater than reproducibility.

E) Tilt angle

> ➢ *Bias evaluation*

The tilt angle φ was previously calibrated (Caroli, 2009) with reference to ISO 230-2:2006 by tilting the stage from -5 deg. to +5 deg. and acquiring data points at each target several times to test the machine's repeatability. The target points were also approached from the two opposite directions to verify the backlash error of the stage (i.e. the bi-directional accuracy).
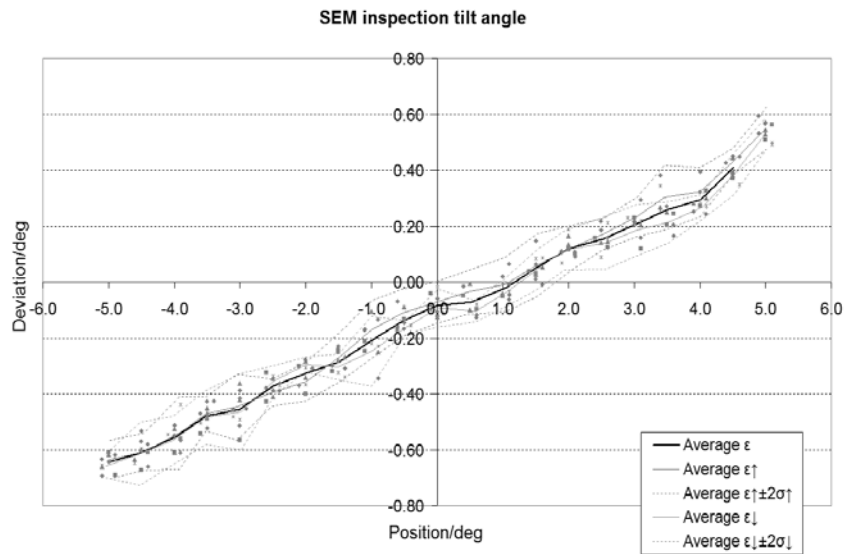
Figure 7.7. Tilt Angle bi-directional accuracy of positioning. Dark grey symbols represent runs taken moving forwards, while light grey runs are taken moving backwards (Caroli, 2009).

Looking at the Fig.7.7, the deviation *e* is reasonably modelled by the regression line

$$e = a\varphi + b \qquad (5)$$

Where $a=1.1\cdot10^{-1}$, $b=-1.9\cdot10^{-3}$ rad. The systematic effect for any value of φ may thus be corrected. The correction, more significant than the case of the rotational angle, can lead to a different management of the model (5). The stereo-pair angle Δφ can be represented by

$$\Delta\varphi = \frac{\varphi_{dx} - \varphi_{sx}}{2} \qquad (6)$$

Where φ_{sx} is relevant to the first image (negative tilt angle), while φ_{dx} is relevant to the second image (positive tilt angle). These two angles can respectively be corrected by

$$\varphi_{sx} = \varphi_1 + a\varphi_1 + b \qquad (7)$$

And

$$\varphi_{dx} = \varphi_2 + a\varphi_2 + b \qquad (8)$$

Where φ_1 and φ_2 are the two angles which, have been set.

In this way, the stereo-pair angle $\Delta\varphi$ can be modelled by

$$\Delta\varphi = \frac{\varphi_2 - \varphi_1 + a(\varphi_2 - \varphi_1)}{2} \qquad (9)$$

In the case under consideration, assuming φ_1 equal to $-6.11 \cdot 10^{-2}$ rad and φ_2 equal to $6.11 \cdot 10^{-2}$ rad, the corrected angles φ_{sx} and φ_{dx} resulted in, respectively, $-6.97 \cdot 10^{-2}$ rad and $6.60 \cdot 10^{-2}$ rad. The correction is not the same because the model has an intercept. The corrected value of stereo-pair angle $\Delta\varphi$ results in $6.79 \cdot 10^{-2}$ rad. Once the systematic effect has been corrected, the uncertainty of the models (7) and (8) has to be considered. It is taken into account in terms of reproducibility.

The standard deviation of coefficient a, that is equal to $1.2 \cdot 10^{-3}$, has also to be taken into account. It is a bias contribution for both tilt angles φ_1 and φ_2, because it applies to both corrections.

➢ *Reproducibility evaluation*

It can be evaluated as uncertainty of the models (7) and (8). In particular, for both tilt angles φ_1 and φ_2, the reproducibility can be assessed as the standard deviation of regression residuals against the line (9), which is equal to $9.1 \cdot 10^{-4}$ rad.

➢ *Resolution*

The resolution is equal to $0.1°$, *i.e.* $1.7 \cdot 10^{-3}$ rad. It has to be considered, since it is greater than reproducibility for both tilt angles φ_1 and φ_2.

7.2.2 Uncertainty budget

The aim is to refer the uncertainty evaluation to the measurement of a wire gauge with nominal radius equal to 125 μm, already subject of a previous analysis (Carli *et al.,* 2009).

Two possible movements of rotary table have been considered, *i.e.* rotation and tilt. First of all, uncertainty evaluation through the uncertainty table is briefly described (section 7.2.2a), and then uncertainty assessment is performed in case of rotation (section 7.2.2b) and tilt (section 7.2.2c) of the rotary table.

7.2.2a Uncertainty table

The uncertainty evaluation according to GUM may be properly organized in a tabular format, referring to EA-4/02:1999. A small modification from this format has been introduced by substituting standard deviations with variances; it has the advantage to manage additive quantities which can be compared more easily. In this way, the table shows individual contribution to the variance of output quantity Y (Barbato *et al.,* 2005). Therefore, following the PUMA method (ISO 14253-2:1999), it is clear which uncertainty components are more important (Table 7.1). Symbols of independent variables appearing in the mathematical model, their value and, if necessary, notes, are written down in column x_j. Entries in column s_j are standard deviations for contributions of Type A (GUM 4.2); and in column a_j one half of the range for contributions of Type B, as well as k_a factors of 2, 3 or 6 respectively, correspond to U-shaped, uniform or triangular distribution (GUM 4.3). Taking into account these considerations, one may evaluate for every contribution the relevant variance as s_j^2, or dividing a_j^2 by k_a factor, as proper for Type B contributions. Coefficients of sensitivity may then be evaluated either by partial derivation, or numerically, and eventually contributions $u_j^2(y)$ of variance of dependent variable y can be calculated.

x_j			s_j	a_j	k_{aj}	$u^2(x_j)$	c_j	$u_j^2(y)$	v_j	$u_j^4(y)/v_j$
Symb.	**Value**	**Note**								
X_1		Bias								
		Res.								
		Repr.								
…										
X_j										
…										
X_n										
Y			Variance of y						Σ	
			Standard deviation of y						v_y	
			Confidence level							
			Coverage factor							
			Expanded uncertainty							

Table 7.1. Uncertainty table as suggested by EA-4/02:1999

Degrees of freedom (d.o.f.) v_j of independent variables should be evaluated according to the following considerations (Barbato *et al.,* 2005):

- For Type A contributions data numbers are known, and so is the relevant d.o.f.

- For Type B contributions information is usually fairly robust, therefore the number of d.o.f. may be considered infinite (from a practical point of view 100 is large enough). The value of d.o.f. may also be taken as a figure of merit of the relevant variability information: if almost certain one can take *e.g.* 100 d.o.f. if it is of medium level one can put 30 d.o.f., if of low level 15 d.o.f. or less. Further details are given in Genta (2010).

7.2.2b Uncertainty in case of rotation

Expected values of independent variables are theoretically evaluated in the measurement conditions. The rotational angle $\Delta\varphi$ is an, a priori set, based on past experience (Carli *et al.,* 2009); in this case $\Delta\varphi$ is assumed equal to 3.5°, *i.e.* $6.11 \cdot 10^{-2}$ rad. The value of working distance d is read on SEM screen during the measurement; it is closely related to measure and dimension and a set level of magnification. The latter has also a large influence on the value of pixel size (Carli *et al.,* 2010). In the case at hand, for a magnification equal to 1000x, the working distance is 8.6 mm, while the pixel size is 0.293 μm/pixels.

Referring to a point on the surface of the wire gauge, considered as an ideal cylinder, it is assumed $y_1=125$ μm. Looking at Fig.3.7, it is noticeable that y_2 depends on the vertical elevation z; therefore, inverting the first relation of (1), the coordinate y_2 can be expressed as a function of the input variables y_1, d, $\Delta\varphi$ and the output variable *z* as

$$y_2 = \frac{d^2 z \sin\left(2\Delta\varphi\right) - d^2 y_1 \cos\left(\Delta\varphi\right) + dzy_1 \cos\left(2\Delta\varphi\right)}{-d^2 \cos\left(\Delta\varphi\right) + dz \cos\left(2\Delta\varphi\right) + 2dy_1 \sin\left(\Delta\varphi\right) - zy_1 \sin\left(2\Delta\varphi\right)} \tag{10}$$

For the adopted operational conditions, the coordinate y_2 results equal to about 110 μm. Finally, numbers of pixels $n_1 \approx 426$ and $n_2 \approx 375$ are immediately derived from y_1 and y_2, respectively.

Referring to these preliminary considerations and to the detailed description of uncertainty contributions given in the previous section, the preparation of Table 7.2 is straightforward. SI units are adopted, without any multiples or submultiples.

The calculation of sensitivity coefficients is quite complex, therefore these are numerically approximated. A detailed analysis of sensitivity coefficients has been performed in Bariani (2005), to which reference is made to validate numerical approximations.

x_j			s_j	a_j	k_{aj}	$u^2(x_j)$	c_j	$u_j^2(y)$	v_j	$u_j^4(y)/v_j$
Symb	**Value**	**Note**								
p	$2.93 \cdot 10^{-7}$	Bias		$4.7 \cdot 10^{-9}$	3	$7.3 \cdot 10^{-18}$	$4.2 \cdot 10^2$	$1.3 \cdot 10^{-12}$	30	$5.8 \cdot 10^{-26}$
		Res		$1.1 \cdot 10^{-9}$	3	$4.1 \cdot 10^{-19}$	$4.2 \cdot 10^2$	$7.4 \cdot 10^{-14}$	100	$5.5 \cdot 10^{-29}$
		Repr	$6.2 \cdot 10^{-10}$			$3.8 \cdot 10^{-19}$	$4.2 \cdot 10^2$	$6.9 \cdot 10^{-14}$	4	$1.2 \cdot 10^{-27}$
n_1	$4.26 \cdot 10^2$	Repr		$5.0 \cdot 10^{-1}$	3	$8.3 \cdot 10^{-2}$	$2.4 \cdot 10^{-6}$	$4.7 \cdot 10^{-13}$	30	$7.4 \cdot 10^{-27}$
n_2	$3.75 \cdot 10^2$	Repr		$5.0 \cdot 10^{-1}$	3	$8.3 \cdot 10^{-2}$	$-2.4 \cdot 10^{-6}$	$4.7 \cdot 10^{-13}$	30	$7.3 \cdot 10^{-27}$
$\Delta\varphi$	$6.01 \cdot 10^{-2}$	Bias	$2.0 \cdot 10^{-4}$			$3.9 \cdot 10^{-8}$	$-2.0 \cdot 10^{-3}$	$1.6 \cdot 10^{-13}$	90	$2.8 \cdot 10^{-28}$
		Res		$8.7 \cdot 10^{-4}$	3	$2.5 \cdot 10^{-7}$	$-2.0 \cdot 10^{-3}$	$1.0 \cdot 10^{-12}$	100	$1.0 \cdot 10^{-26}$
		Repr	$1.3 \cdot 10^{-3}$			$1.8 \cdot 10^{-6}$	$-2.0 \cdot 10^{-3}$	$7.2 \cdot 10^{-12}$	90	$5.8 \cdot 10^{-25}$
d	$8.60 \cdot 10^{-3}$	Repr	$2.5 \cdot 10^{-4}$			$6.2 \cdot 10^{-8}$	$2.8 \cdot 10^{-5}$	$4.9 \cdot 10^{-17}$	16	$1.5 \cdot 10^{-34}$
z	$1.25 \cdot 10^{-4}$		— Variance of y (z)					$1.1 \cdot 10^{-11}$	Σ	$6.6 \cdot 10^{-25}$
			— Standard deviation of y (z)					$3.3 \cdot 10^{-6}$	v_y	175
			— Confidence level					95%		
			— Coverage factor					2.0		
			— Expanded uncertainty					$6.5 \cdot 10^{-6}$		

Table 7.2. Uncertainty table in case of rotation.

7.2.2c Uncertainty in case of tilt

The tilt angle $\Delta\varphi$ is set equal to 3.5°, that is $6.11\cdot10^{-2}$ rad, similarly to rotational angle. The model (9) for the stereo-pair angle $\Delta\varphi$ is directly inserted in (2). In the measurement conditions, magnification level is equal to 800x, therefore pixel size is 0.366 µm/pixel. The value of working distance d, read on SEM screen, results in being 16.0 mm.

Referring to a point on the surface of the wire gauge, it is again assumed y_1=125 µm, and therefore, through (10), the coordinate y_2 results in being equal to about 108 µm. Finally, numbers of pixels $n_1\approx341$ and $n_2\approx295$ are immediately derived.

x_j			s_j	a_j	k_{aj}	$u^2(x_j)$	c_j	$u_j^2(y)$	v_j	$u_j^4(y)/v_j$
Symb	Value	Note								
p	$3.66\cdot10^{-7}$	Bias		$5.9\cdot10^{-9}$	3	$1.1\cdot10^{-17}$	$3.4\cdot10^2$	$1.3\cdot10^{-12}$	30	$5.9\cdot10^{-26}$
		Res		$1.1\cdot10^{-9}$	3	$4.1\cdot10^{-19}$	$3.4\cdot10^2$	$4.8\cdot10^{-14}$	100	$2.3\cdot10^{-29}$
		Repr		$1.0\cdot10^{-9}$	3	$3.3\cdot10^{-19}$	$3.4\cdot10^2$	$3.9\cdot10^{-14}$	30	$5.0\cdot10^{-29}$
n_1	$3.41\cdot10^2$	Repr		$5.0\cdot10^{-1}$	3	$8.3\cdot10^{-2}$	$2.7\cdot10^{-6}$	$5.9\cdot10^{-13}$	30	$1.2\cdot10^{-26}$
n_2	$2.95\cdot10^2$	Repr		$5.0\cdot10^{-1}$	3	$8.3\cdot10^{-2}$	$-2.7\cdot10^{-6}$	$5.9\cdot10^{-13}$	30	$1.2\cdot10^{-26}$
φ_1	$-6.11\cdot10^{-2}$	Res		$8.7\cdot10^{-4}$	3	$2.5\cdot10^{-7}$	$1.0\cdot10^{-3}$	$2.6\cdot10^{-13}$	100	$6.7\cdot10^{-28}$
		Repr	$9.1\cdot10^{-4}$			$8.3\cdot10^{-7}$	$1.0\cdot10^{-3}$	$8.5\cdot10^{-13}$	100	$7.1\cdot10^{-27}$
a_1	$1.1\cdot10^{-1}$	Bias	$1.2\cdot10^{-3}$			$1.4\cdot10^{-6}$	$-5.5\cdot10^{-5}$	$4.3\cdot10^{-15}$	100	$1.8\cdot10^{-31}$
φ_2	$6.11\cdot10^{-2}$	Res		$8.7\cdot10^{-4}$	3	$2.5\cdot10^{-7}$	$-1.0\cdot10^{-3}$	$2.6\cdot10^{-13}$	100	$6.5\cdot10^{-28}$
		Repr	$9.1\cdot10^{-4}$			$8.3\cdot10^{-7}$	$-1.0\cdot10^{-3}$	$8.3\cdot10^{-13}$	100	$6.9\cdot10^{-27}$
a_2	$1.1\cdot10^{-1}$	Bias	$1.2\cdot10^{-3}$			$1.4\cdot10^{-6}$	$-5.5\cdot10^{-5}$	$4.3\cdot10^{-15}$	100	$1.8\cdot10^{-31}$
d	$1.60\cdot10^{-2}$	Repr	$2.5\cdot10^{-4}$			$6.2\cdot10^{-8}$	$8.6\cdot10^{-6}$	$4.6\cdot10^{-18}$	16	$1.3\cdot10^{-36}$
z	$1.25\cdot10^{-4}$	Variance of y (z)						$4.8\cdot10^{-12}$	Σ	$9.8\cdot10^{-26}$
		Standard deviation of y (z)						$2.2\cdot10^{-6}$	v_y	235
		Confidence level						95%		
		Coverage factor						2.0		
		Expanded uncertainty						$4.3\cdot10^{-6}$		

Table 7.3. Uncertainty table in case of tilt.

7.2.3 Discussion

As previously mentioned, regarding the reproducibility evaluation of the number of pixels, it is possible to make an uncertainty assessment for classes of images, associating their quality to the reproducibility in the identification of homologous points. Tables 7.4 and 7.5 indicate percentages of influence of each contribution on expanded uncertainty $U(z)$, the value of $U(z)$ and the value of relative expanded uncertainty $U(z)/z$, varying reproducibility of n_1 and n_2 from 0.1 to 5 pixels, in case of rotation and tilt. The contribution of working distance d is omitted because is negligible. Comparing the results obtained for the case of rotation (Table 7.4) and tilting (Table 7.5), the following conclusions can be drawn:

> ➢ The expanded uncertainty $U(z)$ ($k=2$) does not significantly change for the number of pixels reproducibility values ranging from 0.1 to 1 pixel, as the differences are in the order of 200 nm, for the case of rotation, and 500 nm, for the case of tilting;

> ➢ Considering the different values of the number of pixels reproducibility, the percentage influence of the pixel size is about 2.5 times smaller in the case of rotation compared to the case of tilt. This difference is due to the fact that a much higher influence of $\Delta\varphi$ can be noticed in the case of rotations compared to the case of tilt. In fact, the systematic error compensation was possible just in the case of the tilt angle and not for the case of the rotational one.

> ➢ The systematic error compensation, in the case of tilt, led to smaller expanded uncertainties *(i.e.* 3.9 μm) compared to the case of rotations *(i.e.* 6.3 μm) for the case of number of pixels reproducibility equal to 0.5 pixels.

Repr. n_1 and n_2/ pixel	Percentage influence on U(z)			U(z)/m	(U(z)/z)/%
	p	n_1 and n_2	$\Delta\varphi$		
0.1	15	0	85	$6.2\cdot10^{-6}$	5.0
0.5	15	2	83	$6.3\cdot10^{-6}$	5.0
1	14	9	78	$6.5\cdot10^{-6}$	5.2
5	4	70	25	$1.1\cdot10^{-5}$	9.2

Table 7.4. Percentage influences on U(z), the value of U(z) and the value of U(z)/z, varying reproducibility of n_1 and n_2, in case of rotation.

Repr. n_1 and n_2/ pixel	Percentage influence on U(z)			U(z)/m	(U(z)/z)/%
	p	n_1 and n_2	$\Delta\varphi$		
0.1	39	0	61	$3.8\cdot10^{-6}$	3.0
0.5	36	8	56	$3.9\cdot10^{-6}$	3.1
1	30	25	46	$4.3\cdot10^{-6}$	3.5
5	4	89	7	$1.1\cdot10^{-6}$	9.2

Table 7.5. Percentage influences on U(z), value of U(z) and value of U(z)/z, varying reproducibility of n_1 and n_2, in case of tilt.

Figure 7.8 shows the trends of percentage influence on U(z) and of n_1 and n_2 with the increase of their reproducibility in case of rotation and tilt, while Figure 7.9 reports the trends of relative expanded uncertainty U(z)/z.
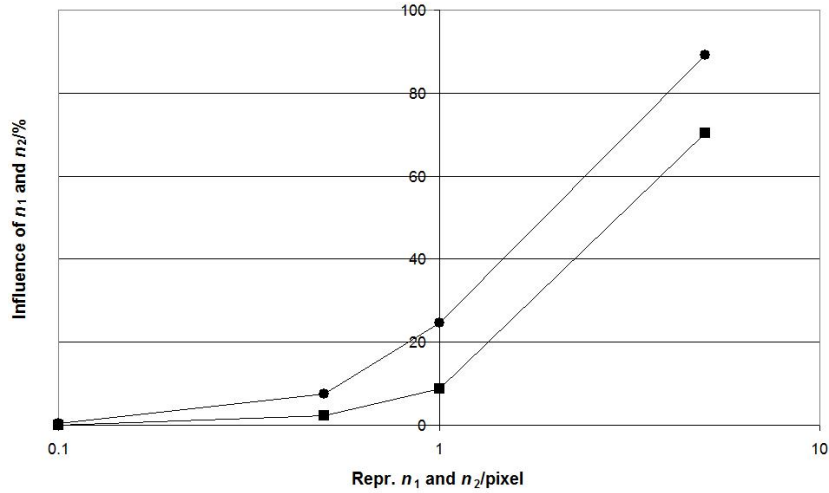
Figure 7.8. Trends of percentage influence on U(z) of n_1 and n_2 with the increase of their reproducibility in case of rotation (squares) and tilt (circles).
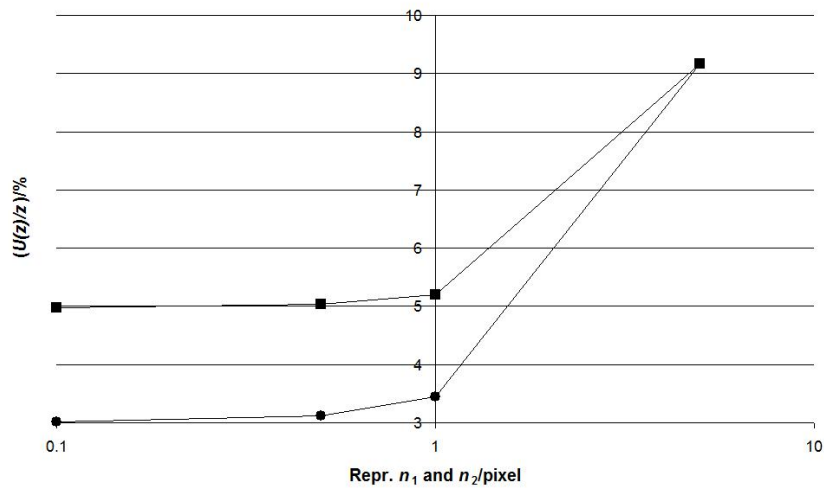
Figure 7.9. Trends of relative expanded uncertainty U(z)/z with the increase of reproducibility of n_1 and n_2 in case of rotation (squares) and tilt (circles).

Based on experimental evidence, a value of 1 pixel has been chosen as typical reproducibility. For the case of <u>rotations</u>, by examining Table 7.2, the largest contribution is due to reproducibility of the rotational angle, $\Delta\varphi$, followed by a bias of pixel size p. Therefore, in order to reduce the uncertainty in 3D-SEM reconstructions, performances of the rotary table should above all, be improved. As the main contribution in rotational angle's reproducibility is due to the saw tooth trend, a more refined calibration is needed, in order to produce a correction table. Thereafter, one can check whether the parabolic correction of φ bias reaches significance. Moreover, after these corrections, the contribution of p bias may rise near to the first place, therefore dictating a better calibration of the artefact.

In the case of <u>tilting</u>, with reference to Table 7.3, the largest contribution is due to the bias of pixel size p, followed by the reproducibility of the tilt angle $\Delta\varphi$. Therefore, in order to reduce the uncertainty in 3D-SEM reconstructions when performing tilting, a calibrated artefact, with a lower uncertainty, should be adopted to refine pixel size bias calculations. Moreover, the high uncertainty associated to tilt reproducibility, is due to the fact that the stage can be tilted manually by the operator, while, for instance, rotations are controlled by the piezo-motor of the stage. Therefore, since this uncertainty contribution can not be improved by further calibrations, another positioning system allowing item tilting should be adopted to improve the performances.

7.3 Experimental uncertainty evaluation of stereo-pair technique

The uncertainty evaluation performed on the influence of SEM instrument setting parameters (chapter 5) and of SEM image quality (chapter 6) pointed out that, although these error sources are relevant, an overestimation in the diameter evaluation of about 2%, compared to the reference one, was still observed. The theoretical uncertainty evaluation of stereo-pair technique revealed a high influence of pixel size and of the tilt (rotational) angle on the results. As it was already underlined in chapter 3, MeX input parameters, required to perform stereo-photogrammetry, can be directly linked to the factors considered in the Piazzesi equation. Working distance d and tilt (rotation) angle $\Delta\varphi$ (from here on Dphi) remain the same, while the other contributors, the lateral coordinate y_1 and the parallax Δy where considered as a function of the number of pixels n multiplied for the pixel size p being $y_1 = n_1 \cdot p$ and $\Delta y = y_1 - y_2 = p \cdot (n_1 - n_2)$. The main difference is that the theoretical investigation allowed performing an uncertainty evaluation of the z coordinate, while in the case of 3D reconstructions this has to be performed considering the diameter as a response. The z-coordinate and the diameter are linked through the least-square algorithm implemented in the software for point cloud analysis and inspection, as the uncertainty of the estimated diameter is linked to the uncertainties of the single z-coordinates of the points composing the cloud. 3D-SEM reconstructions were therefore performed using MeX, starting from SEM images of a wire gauge with a reference diameter of 250 μm. The item was tilted inside the SEM chamber to allow rotations along its central axis enabling measurements on different portions of the object. The same three SEM images, used for uncertainty evaluation of the other error sources, as described in the previous chapters, were hereby considered leading to two different stereo-pairs, named after the rotational angles, -7&0 and 0&+7. For each stereo-pair three different values of MeX input parameters, working distance, rotational angle and pixel size, were chosen to perform stereophotogrammetry. This allowed a Design of Experiment (DOE) analysis (Montgomery, 2008) considering the three MeX input parameters as factors, each one set at three different levels, being level 0 the nominal input value and levels -1 and +1 the nominal value including its uncertainty. The uncertainty ranges of the three factors were chosen based on the results of the theoretical uncertainty evaluation which were slightly overestimated to cover a higher variability range. A preliminary investigation was also carried out, using the so-called one-factor-at-the-time method, to determine whether the relationship between each factor and the response can be assumed to be linear or not.

The results are summarized in Fig.7.10 where, from the R^2 results analysis, it can be concluded that the relationship between Dphi and p and the calculated diameter is linear (R^2=0.999), while in the case of the working distance d, being R^2=0.909 for a linear fitting, the response can be assumed to be linear although a second order polynomial fitting would be more appropriate.
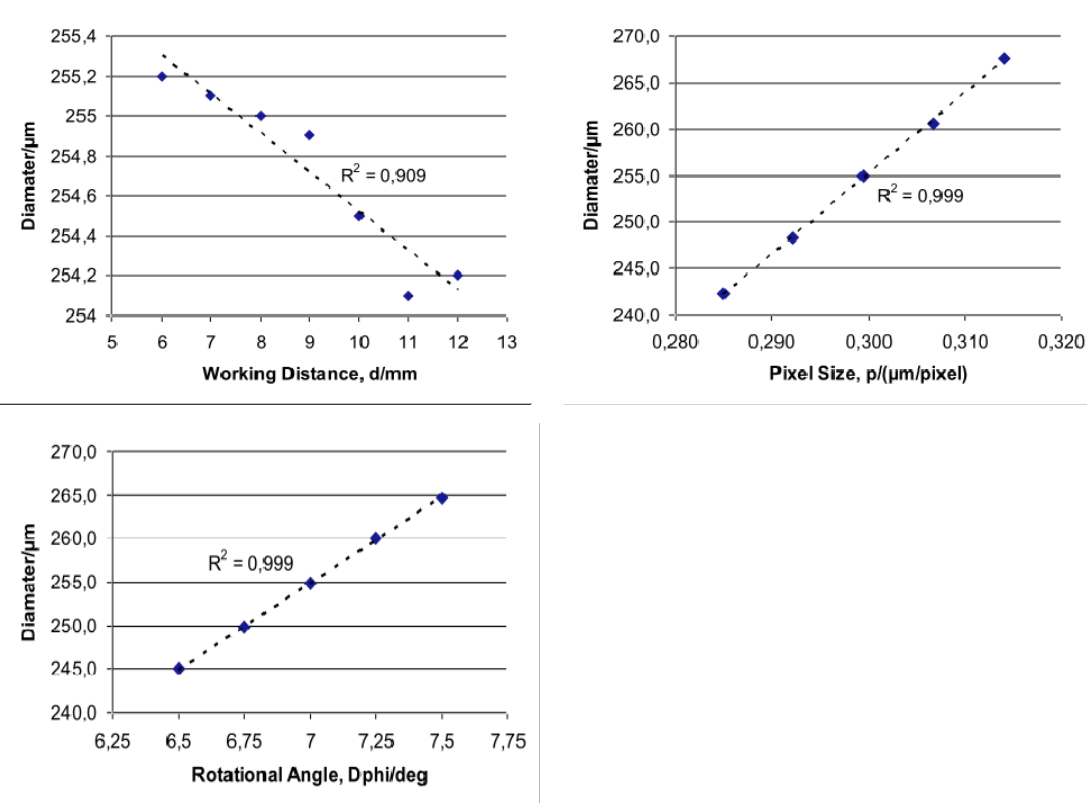
Figure 7.10. Results of the preliminary investigation on the influence of MeX input parameters, working distance d, rotational angle Dphi and pixel size p, on the wire gauge diameter calculation. A fitting curve (dotted line) was calculated to determine whether the relationship between the different input values and the diameter can be assumed to be linear.

164

As a general rule, if a linear relationship can be assumed for a factor included in the analysis, two levels would be enough for determining its effect on the response. On the other hand, if the relationship is estimated not to be linear, more levels should be tested to allow a more accurate estimation of the effects (Montgomery, 2008). However, in this case three levels for each factor were considered to achieve more detailed information on the response. For the experimental investigation, two different stereo-pair were considered to obtain more reliable results. The point clouds obtained after stereo-pair reconstructions were analyzed and inspected using a demo version of Geomagic Studio 10 (2008) and the procedure described in chapter 4. Three replications were also performed to enable the estimation of the experimental error. This is linked to the measuring uncertainty deriving from replication capability of MeX, when performing 3D reconstructions from the same stereo-pair, and to the operators influence when inspecting the point clouds for diameter estimation. All the factors and the levels are summarized in Table 7.6. Having a $2 \cdot 3^3$ factorial design, considering two stereo-pairs, replicated three times, a total number of 162 point clouds were obtained from MeX reconstructions, in order to estimate wire gauge diameter. A summary of the main results is here provided to allow drawing the main conclusions.

Error source	Factor	Symbol	Unit	Levels		
MeX Input parameters	Working distance	d	mm	6	9	12
	Rotational angle	Dphi	deg	6.5	7.0	7.5
	Pixel size	p	μm/pixel	0.2850	0.2994	0.3140
	Stereo-pair	SP	-	-7&0	0&+7	

Table 7.6. Summary of all the factors and the respective levels chosen for performing an uncertainty evaluation of the influence of MeX input parameters on the estimated wire gauge diameter.

Analysis of variance was carried out using a demo version of Minitab® 14.1 statistical software (2003), considering the diameter as a response and interactions up to the third order. Results are shown in Table 7.7.

Source	DF	*p*-value	SQ%
Dphi/deg	2	0.000	39.4
d/mm	2	0.000	0.3
p/(µm/pixel)	2	0.000	60.3
SP	1	0.000	0.0
Main effects	7		**99.9**
Dphi/deg·d/mm	4	0.000	0.0
Dphi/deg·p/(µm/pixel)	4	0.000	0.1
Dphi/deg·SP	2	0.178	0.0
d/mm·p/(µm/pixel)	4	0.000	0.0
d/mm·SP	2	0.000	0.0
p/(µm/pixel)·SP	2	0.012	0.0
Interactions -2nd order	18		**0.1**
Dphi/deg·d/mm·p/(µm/pixel)	8	0.084	0.0
Dphi/deg·d/mm·SP	4	0.813	0.0
Dphi/deg·p/(µm/pixel)·SP	4	0.241	0.0
d/mm·p/(µm/pixel)·SP	4	0.253	0.0
Interactions -3rd order	38		**0.0**
Error	116		
Total	161		**100.0**

Table 7.7. Analysis of variance performed using a demo version of Minitab considering the diameter as a response and interactions up to the third order for the three factors considered in the experimental work: working distance d, pixel size p and rotational angle Dphi. For each source are indicated the degrees of freedom (DF), the *p*-value and the percentage sum of squares (SQ %). Effects being not significant (*i.e. p*-value >0.05) are represented in red.

The results obtained from analysis of variance, including 3rd order interactions, showed that these 4 interactions are not all significant being the related *p*-values >0.05. Therefore the fitting model can be refined discarding 3rd order interaction and furthermore adding more degrees of freedom from calculating the experimental error.

As a result of this model refining operation another table was produced with the updated results, considering interactions up to the 2nd order (Table 7.8).

Source	DF	*p*-value	SQ%
Dphi/deg	2	0.000	39.4
d/mm	2	0.000	0.3
p/(μm/pixel)	2	0.000	60.3
SP	1	0.000	0.0
Main effects	7		**99.9**
Dphi/deg·d/mm	4	0.000	0.0
Dphi/deg·p/(μm/pixel)	4	0.000	0.1
Dphi/deg·SP	2	0.193	0.0
d/mm·p/(μm/pixel)	4	0.000	0.0
d/mm·SP	2	0.000	0.0
p/(μm/pixel)·SP	2	0.014	0.0
Interactions -2nd order	18		**0.1**
Error	136		
Total	161		**100.0**

Table 7.8. Analysis of variance performed using a demo version of Minitab considering the diameter as a response and interactions up to the second order for the three factors considered in the experimental work: working distance d, pixel size p and rotational angle DPhi. For each source are indicated the degrees of freedom (DF), the *p*-value and the percentage sum of squares (SQ%). Effects being not significant (*i.e.* *p*-value >0.05) are represented in red.

From the analysis of variance results, summarized in Table 7.8, the following considerations can be drawn:

➢ Main effects are all significant and accounts for 99.9% of the overall results variability.

➢ Among the main effects the pixel size p is the most influencing one accounting for 60.3% of the overall results variability, followed by the rotational angle Dphi having a SQ% equal to 39.4%. The working distance d, although being significant from a statistical point of view, accounts for only 0.3% of the overall results variability and the effect of the stereo-pairs "SP" is negligible.

➢ Among the 2nd order interactions, only the Dphi-SP one results not to be significant. Nevertheless, from a fitting point of view, only the interaction Dphi-p resulted to be significant being SQ%=0.1, while the effects of all the others is negligible.

➢ The overall model fitting was calculated to be equal to 99.98%, meaning that the statistical analysis is significant and that the experimental error, mainly related to the diameter calculation variability, is negligible. This usually happens when the model is consistent, as it was proven to be also in this case.

Main effects (Fig.7.11) and interaction (Fig.7.12) plots were produced to allow the visualization of the quantitative effects, of the factors under consideration, on the diameter calculation.
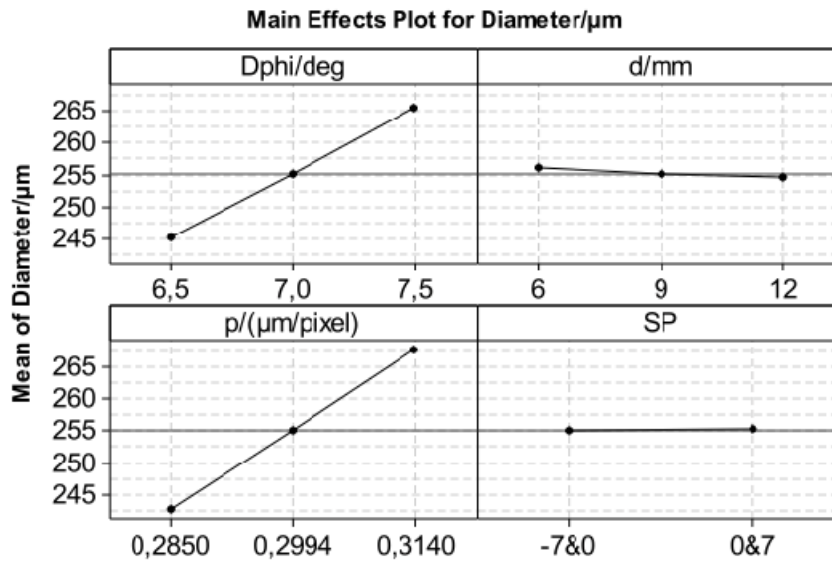
Figure 7.11. Main effects plot of the mean values of the diameter, resulting from the analysis of variance, considering four influencing factors: the rotational angle Dphi, the working distance d, the pixel size p and the stereo-pair SP.
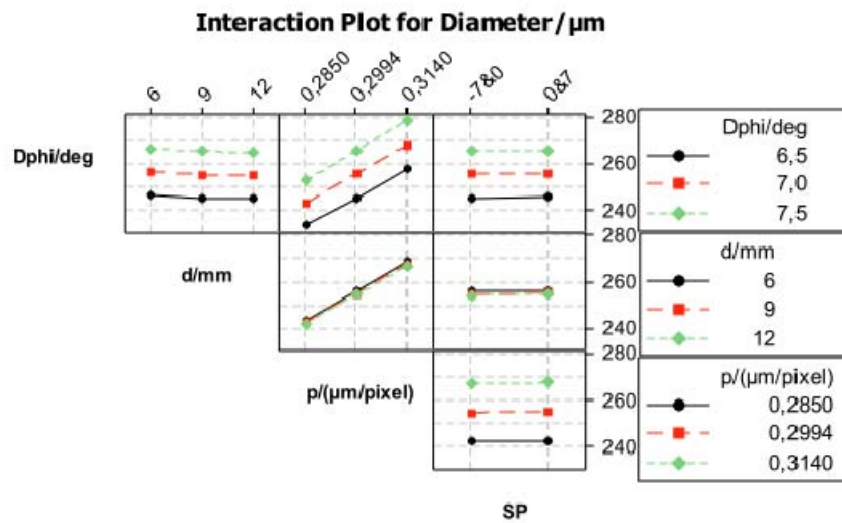
Figure 7.12. Interaction plot of the mean values of the diameter, resulting from the analysis of variance, considering four influencing factors: the rotational angle Dphi, the working distance d, the pixel size p and the stereo-pair SP.

From the analysis of the main effects plot it can be concluded as follows:

- ➢ Setting a variability range of ± 0.5 deg for the rotational angle Dphi leads to an overall diameter calculation variability of about 20 μm. Moreover the relationship between Dphi and the calculated diameter was found to be linear.

- ➢ Setting a variability range of about ± 0.015 μm/pixel for the pixel size p leads to an overall diameter calculation variability of about 25 μm. Furthermore, also the relationship between p and the calculated diameter was found to be linear.

- ➢ Considering the effect of the stereo-pair SP, the experimental results shown as the SP 0&+7 exhibits diameters which are, on average, always 0.3 μm higher than for SP -7&0. This fact could be explained by assuming a small variability in the uncertainty range for the factors considered in the analysis for one stereo-pair compared to the other.

- ➢ Setting a variability range of about ± 3 mm for the working distance d yields to an overall diameter calculation variability of about 2 μm. In this case, differently from the case of Dphi and p, the relationship between the working distance and the calculated diameter was found not to be exactly linear, but parabolic.

In order to perform an uncertainty evaluation according to ISO GUM (JCGM 100:2008) a fitting model should be calculated considering the main effects and the interactions described before. For this purpose, a response surface methodology (RSM) (Montgomery, 2008) was employed through a demo version of Minitab® 14.1 (2003). Being the stereo-pair SP the only factor qualitative and not quantitative, it could not be included in the analysis. Nevertheless the applied methodology remains still valid as SP plays a minor role in the overall model fitting. Moreover, although SP 0&+7 showed higher diameter values, compared to the other one, for the purpose of estimating a model fitting, it could be relevant to not include the effect of the stereo-pair. In this case the resulting fitting equation is averaging the effects of the stereo-pairs. The residual plots, resulting from the application of the response surface methodology are shown in Fig.7.13.
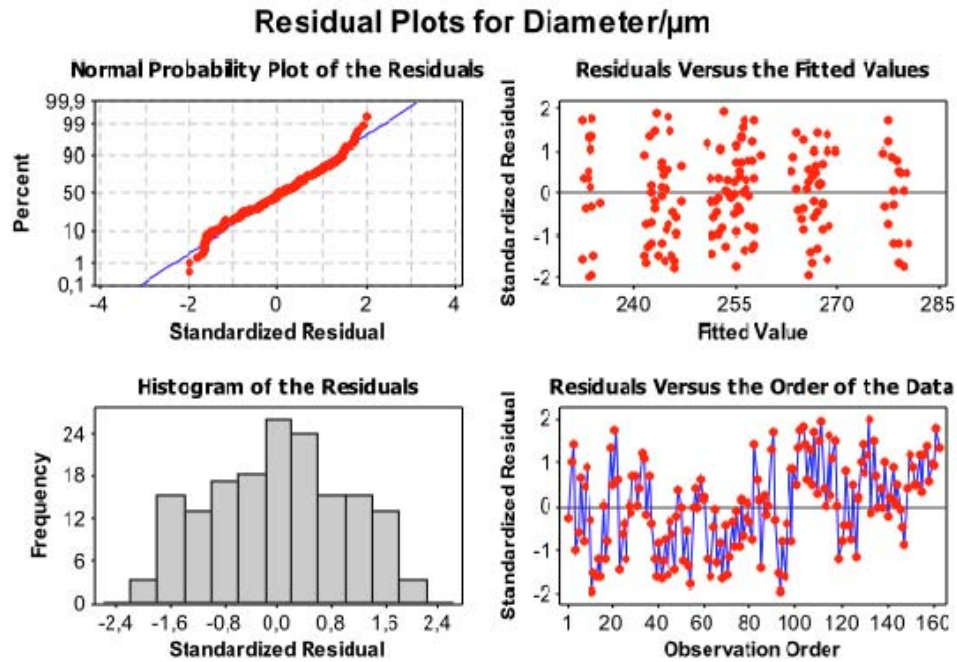
Figure 7.13. Residual plots obtained from the response surface methodology, performed using a demo version of Minitab, considering main effects and 2nd order interactions for the modelling.

From the analysis of the graphs shown in Fig.7.13 it can be concluded that the modelling is consistent, as not any significant trend can be seen for the standardize residuals and for the fitted values. Moreover, by observing the residuals versus the order of the data an increment in the standardized residuals can be observed for observation orders higher than 81. This is due to the fact that those observations correspond to the SP 0&+7, which was demonstrated to have, on average, higher values for the diameter compared to stereo-pair -7&0. This difference can be ascribed to the presence of a systematic error, which was not compensated. Once the model consistency has been validated, a regression curve can be calculated based on the 162 experimental values of the diameter considered for the analysis. In this case, the regression curve was calculated by taking into account the main effects and the 2nd order interactions. Therefore the resulting regression equation will have this form:

Diameter/μm= A_0+A_1·Dphi+A_2·d +A_3·p+A_4·Dphi·d+ A_5·Dphi·p+A_6·d·p (11)

The regression coefficients were estimated through the surface response analysis and the results in Table 7.9 were obtained.

Term	Coef.	SE Coef.	p-value
Constant	-6.449	8.681	0.459
Dphi/deg	0.337	1.211	0.781
d/mm	0.367	0.241	0.130
p/(μm/pixel)	401.887	28.679	0.000
Dphi/deg·d/mm	-0.034	0.019	0.078
Dphi/deg·p/(μm/pixel)	67.399	4.000	0.000
d/mm·p/(μm/pixel)	-1.311	0.667	0.051
R^2 = 100,0% R^2 (adj) = 100,0%			

Table 7.9. Regression coefficients (Coef.) for the main effects and 2nd order interactions estimated from the response surface methodology. Standard error (SE) for the coefficients and *p*-values are also shown, together with the R^2 value of the fitting model.

The goodness of the fitting model can be proven by the R^2 value which is 100, 0%. Another relevant consideration arising from Table 7.9 is that the *p*-value of the regression coefficients of Dphi and d is not statistically significant (*e.g.* *p*-value >0.05), meaning that the model could be refined by discarding this two factors. In fact, it resulted that their interaction with the pixel size is more relevant than their main effect alone. Anyhow, surface response methodology does not generally permit estimating regression curves including interactions involving factors whose main effects were not considered, this being not relevant. If the coefficients reported in Table 7.9 are substituted to the ones of the equation (11), the following fitting model is then obtained:

$$\text{Diameter}/\mu m = -6.449 + 0.337 \cdot \text{Dphi} + 0.367 \cdot d + 401.887 \cdot p - 0.034 \cdot \text{Dphi} \cdot d + 67.399 \cdot \text{Dphi} \cdot s$$
$$-1.311 \cdot d \cdot s \qquad\qquad (12)$$

Note that equation (12) is valid within the variability range tested for the input parameters *i.e.* 6.50 deg<Dphi<7.50 deg, 6.0 mm<d<12.0 mm and 0.290 μm/pixel<p<0.310 μm/pixel. An useful tool allowing an easier results visualization is the contour plot (Minitab® 14.1, 2003) of the diameter values, estimated from the fitting equation (12), as a function of the three factors considered for the analysis: working distance d, rotational angle Dphi and pixel size p. The resulting contour plot is shown in Fig.7.14.

As the influence of the working distance was found to be negligible on the diameter calculation, only the contour plot showing the effects of the rotational angle Dphi and the pixel size p was produced, holding working distance d at the nominal input value of 9 mm, to underline their effects on the diameter estimation (Fig.7.15).
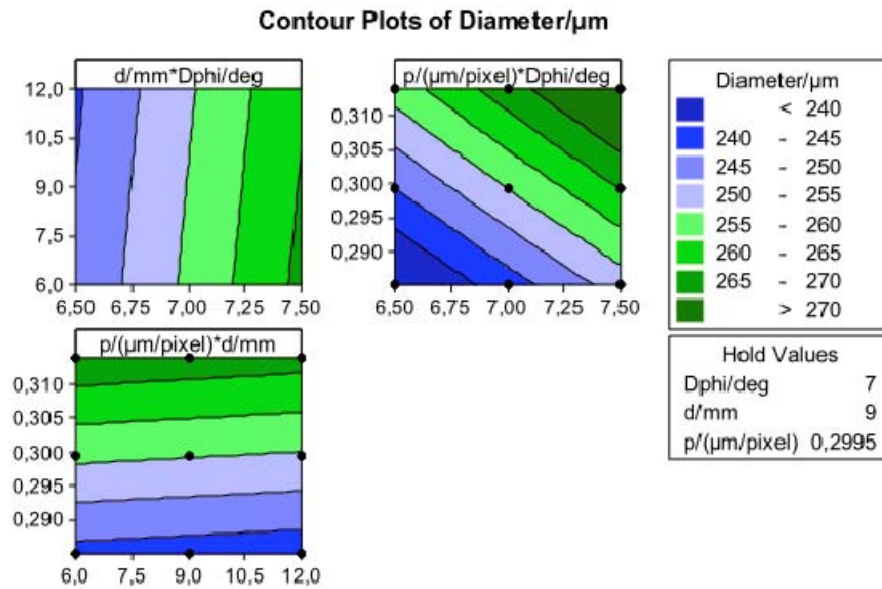
Figure 7.14. Contour plots of the diameter as a function of the MeX input parameter values working distance d, rotational angle Dphi and pixel size p.
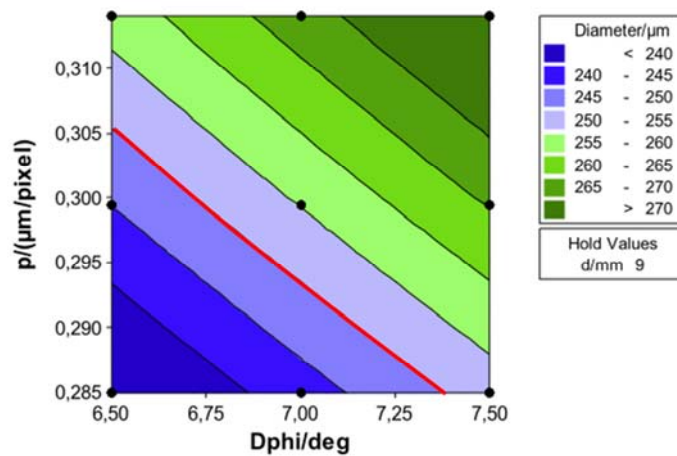
Figure 7.15. Contour plot of the diameter as a function of the MeX input parameter values rotational angle Dphi and pixel size p. The red line represents the reference diameter equal to 250 μm.

The contour plot of Fig.7.15 shows the resulting diameter values as a function of the MeX input parameter values rotational angle Dphi and pixel size p. The red line represents the reference wire gauge diameter value which is equal to 250 μm. As it can be noticed by the graph, the reference value can be obtained through an infinite number of combinations of the rotational angle Dphi and pixel size p values. The Minitab application named Response Optimizer (Minitab$^{®}$ 14.1 statistical software, 2003), allows one to determine the optimum setting of the input parameters to achieve a desired value of the output. By using this tool it was possible to determine, for instance, the values of d (7.8 mm) and p (0.299 μm/pixel) leading to a diameter of 250 μm, by setting the Dphi at the nominal value of 7 deg. This was done for all the three nominal input values of the parameters under consideration and results are shown in Table 7.10. Among the three proposed input parameters combinations, the second one, *i.e.* the one with p=0.293 μm/pixel, corresponds to the case where a systematic correction of the pixel size is applied. In fact, for the given value of magnification M=1000x, the pixel size calibration curve (see Fig.7.3) yields p=0.2934 μm/pixel. If then this systematic correction of the pixel size input value is applied, the calculated wire gauge diameter would result equal to the reference one (*i.e.* 250 μm). This conclusion was proven by means of six replicated reconstructions, performed using MeX and setting Dphi=7.0 deg, d=9.0 mm and p=0.2934 μm/pixel. The mean diameter value of these confirmation experiments resulted to be 250.1 μm, with an expanded standard deviation (k=2) equal to 0.4 μm, mainly due to the point cloud post-processing operation.

Dphi/deg	d/mm	p/(μm/pixel)	Diameter/μm
6.75	7.8	0.299	250.1
7.00	7.4	0.293	250.0
6.85	9.0	0.297	250.0

Table 7.10. Example of three MeX input parameters combinations leading to an estimated value of the diameter equal to the reference one (*i.e* 250 μm). The values were obtained using the Minitab tool called "Response Optimizer" (Minitab$^{®}$ 14.1 statistical software, 2003).

As it was previously mentioned, using response surface methodology, it is not possible to estimate interactions by not including the correspondent main effects in the model (Montgomery, 2008). In the case under consideration, for instance, the regression coefficient estimated for the main effect Dphi, was not significant (*i.e. p*-value >0.05), while the coefficient for the interaction Dphi-p was highly significant as shown in Table 7.9. Therefore, another possible methodology to be employed, called Best Subset Regression, was also employed and described in chapter 5. A short description of this methodology is here given as taken from the Minitab Manual (2003). Best Subsets Regression is a method used to help determine which predictor (independent) variables should be included in a multiple regression model. This method involves examining all of the models created from all possible combinations of predictor variables. Best Subsets Regression uses R^2 to check for the best model. It generates regression models using maximum R^2 criterion by first examining all one-predictor regression models and then selecting the two models giving the largest R^2. Minitab displays information on these models, examines all two-predictor models, selects the two models with the largest R, and displays information on these two models. This process continues until the model contains all predictors. This methodology was applied to the 162 data used as inputs also for the DOE analysis, and the results are shown in Table 7.11. From results reported in Table 7.11 it derives that all the regression models containing three or more predictors lead to R^2 values equal to 100, meaning that the model fitting is fully consistent. In order to choose one of these combinations the Mallows' Cp has to be then considered. This is generally used to compare the full model to a model with a subset of predictors. In general, a model should be chosen where Mallows' C_p is small and close to p, where p is the number of predictors in the model, including the constant. A small C_p value indicates that the model is relatively precise in estimating the true regression coefficients and predicting future responses (Statistics Dictionary, 2008). Hence, as the lowest Mallows' Cp is obtained for the case highlighted in Table 7.11, the regression model containing those 5 predictors was chosen. Thus, the simplified resulting regression equation is as follows:

$$\text{Diameter}/\mu m = -2.79 + 395.4 \cdot p + 0.026 d^2 - 0.0382 \cdot \text{Dphi} \cdot d + 68.6\ \text{Dphi} \cdot p - 1.55 \cdot d \cdot p \quad (13)$$

Where the estimated coefficients, with the related standard errors and *p*-values are shown in Table 7.12.

			Main effects			Squares			Interactions		
Vars	R^2	Mallows C-p	Dphi	d	p	$Dphi^2$	d^2	p^2	Dphi·d	Dphi·p	d·p
1	91.3	5058.5								X	
1	60.3	23137.7			X						
2	99.7	147.0			X					X	
2	99.7	148.1						X		X	
3	100.0	45.7			X					X	X
3	100.0	46.3			X				X	X	
4	100.0	7.5			X		X			X	X
4	100.0	9.0		X	X		X			X	
5	100.0	2.5			X		X		X	X	X
5	100.0	6.1		X	X		X			X	X
6	100.0	4.3		X	X		X		X	X	X
6	100.0	4.4			X		X	X	X	X	X
7	100.0	6.1		X	X		X	X	X	X	X
7	100.0	6.2	X	X	X		X		X	X	X
8	100.0	8.0	X	X	X		X	X	X	X	X
8	100.0	8.1		X	X	X	X	X	X	X	X
9	100.0	10.0	X	X	X	X	X	X	X	X	X

Table 7.11. Results of the application of Best Subset Regression methodology to the 162 experimental diameter values, considering main effects, squares and interactions for the three MeX input parameter under consideration: working distance d, rotational angle Dphi and pixel size p. The grey row indicates the case providing the lowest Mallows' Cp.

Predictor	Coef.	SE Coef.	*p*-value
Constant	-2.794	0.991	0.005
p	395.375	6.186	0.000
d^2	0.026	0.004	0.000
Dphi·d	-0.0382	0.014	0.009
Dphi·p	68.641	0.4518	0.000
d·p	-1.553	0.363	0.000
R^2 = 100,0% R^2 (adj) = 100,0%			

Table 7.12. Regression coefficients (Coef.) for the model estimated using the Best Subset Regression methodology. Standard error (SE) for the coefficients and *p*-values are also shown, together with the R^2 value of the fitting model.

As it is proven by the *p*-values and the R^2 this model is very consistent in estimating the diameter as a function of the predictors shown in table 7.12.

Starting from the modelling equation (13) it is possible to carry out an uncertainty evaluation according to ISO GUM. The sensitivity coefficients c_d, c_p and c_{Dphi} can be directly calculated from the equation, whereas, in order to estimate the expanded uncertainty of the diameter, different uncertainty values for the pixel sixe and the rotational angle were tested. These were chosen as a fraction of the values reported in Table 7.6, *i.e.* u_p=0.007 µm/pixel and u_{Dphi}=0.25 deg and assuming u_d=0.250 mm and constant. A graph was produced were the expanded uncertainty of the diameter U(D) is plotted as a function of the different uncertainty values for the pixel size and the rotational angle (see Fig.7.16). It can be seen that an uncertainty increment of about 1 nm for the pixel size results in about 1 µm increment in the expanded uncertainty of the diameter. If the values shown in Table 7.2., for the theoretical uncertainty evaluation in the case of rotations, are assumed, an expanded uncertainty of the diameter equal to approx. 9 µm derives.
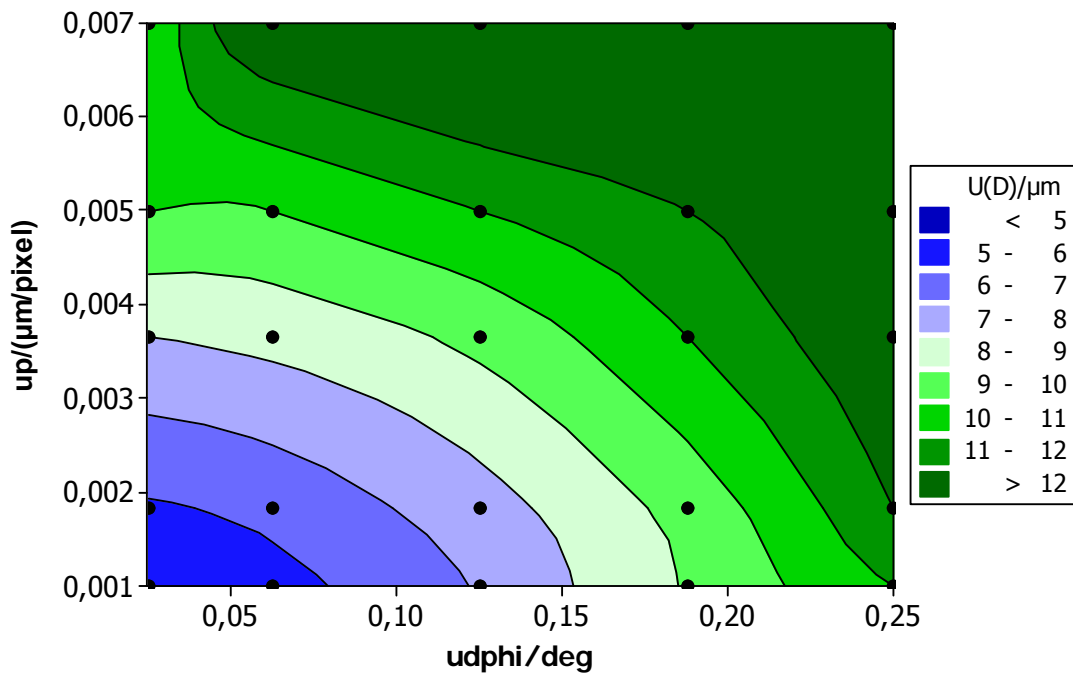
Figure 7.16. Graph showing the expanded uncertainty of the diameter U(D) as a function of different uncertainty values for the pixel size (u_p) and for the rotational angle (u_{Dphi}). Black dots represent the experimentally calculated values.

7.4 Comparison of theoretical and experimental uncertainty evaluation of stereo-pair technique in the case of rotations

A comparison of the results obtained from the theoretical and the experimental uncertainty evaluation is not directly feasible. In fact, while the former enables the estimation of uncertainty of the z-coordinate, the other is related to diameter estimation through the implementation of a least square algorithm.

Nevertheless some considerations can be drawn from the analysis of the results:

> ➢ If the nominal values for p, d and Dphi, used for the theoretical uncertainty evaluation, leading to a radius equal to 125.0 µm according to Piazzesi formulation, are set as inputs in the equation (13), a radius equal to 125.7 µm is obtained. This means that a difference in the two approaches can be quantified as 0.7 µm.

➤ Considering the theoretical uncertainty evaluation, if the reproducibility of n1 and n2 is set to be equal to 1 pixel, the rotational angle Dphi accounts for 78% of the overall uncertainty, followed by the pixel size accounting for 14%. The contribution of the working distance was found to be negligible. This conclusion was proven also through the experimental investigation, where the main difference deals with the weight of p and Dphi on the estimated uncertainty. In this case in fact, the contribution of the rotational angle Dphi is of about 39.4%, while pixel size accounts for 60.3% of the response variability. This probably means that the uncertainty contributors in terms of bias, resolution and reproducibility, calculated for the rotational angle in the theoretical case, were probably overestimated, leading to a consistent underestimation of the effects of the uncertainty related to the pixel size. Since the rotational angle reproducibility was found to be the most dominant uncertainty contributor, an improvement of the SEM stage rotary table calibration procedure may lead to a systematic reduction of this uncertainty component.

➤ The theoretical uncertainty evaluation, performed considering a cylindrical item with a radius of 125 μm, led to an expanded uncertainty of 6.5 μm. Moreover, by performing 3D-SEM reconstructions, starting from SEM images acquired on the reference wire gauge and using the nominal input parameters, a 2% diameter overestimation was observed. This difference can be significantly reduced by correcting the systematic error due to the pixel size.

➤ Finally it has to be remarked that, while Piazzesi equation considered Dphi/2 as input value, the experimental investigation was carried out considering the real MeX input value which is equal to Dphi (*i.e.* 7 degree in the case under consideration). Therefore the uncertainty related to the rotational angle, obtained in the experimental case, should be divided by a factor of 2 if a comparison with the one obtained from the theoretical investigation is foreseen.

As the rotary table uncertainty was found to be the weak point by the theoretical uncertainty evaluation (see Table 7.2), a different calibration procedure could be carried to reduce this uncertainty contributor. For instance the same calibration procedure could be applied by using a different artefact such as a unidirectional TGTZ grating intended for SPM calibration from NT-MDT (Europe, The Netherlands).

Another possibility for reducing the uncertainty in the case of rotations, would be to purchase a new rotary table to perform item rotations inside the SEM chamber. Many different solutions are available on the market with different prices depending on the required performances. It would be therefore interesting to model the uncertainty dealing with rotations, considering the different characteristics of the rotary table, and to investigate the resulting expanded uncertainty of the z-coordinate. Concerning rotary tables, the bias is generally the higher uncertainty contributor, the reproducibility is fractional value of the bias and the resolution can typically be neglected. An uncertainty modelling was then carried out taking into account different values for the bias and setting the reproducibility to 1/5th of that value and the resolution to negligible. The different values were set as inputs in the uncertainty Table 7.2, considering outputs as the combined Dphi uncertainty ($u(\Delta\Phi)$), the percentage influence of Dphi ($\Delta\Phi\%$) and p ($p\%$), the resulting expanded uncertainty for the z-coordinate ($U(z)$) and the percentage relative expanded uncertainty ($U(z)/z\%$). The results are shown in table 7.13. from which it can be concluded that the combined uncertainty of the rotational angle remains the limiting factor, when estimating the expanded uncertainty of the z-coordinate, until the bias is set to be equal to 0.050 deg. For lower bias values the influence of the pixel size combined uncertainty starts to become predominant. The $U(z)/z\%$ values suggest that, whenever aiming to obtain a relative uncertainty of the z-coordinate below 3% a rotary table with a bias equal to 0.025 deg should be purchased. Further reduction of the bias value does not lead to any significant improvement in the performances, as the uncertainty related to the pixel size then becomes the limiting factor. A graph was also produced showing the $U(z)/z\%$ value as a function of the combined uncertainty of the rotational angle $u(\Delta\Phi)/\text{deg}$ (Fig.7.17).

Bias $\Delta\Phi$/deg	u($\Delta\Phi$)/deg	$\Delta\Phi$%	p%	U(z)/µm	U(z)/z%
0.500	0.511	99.0	0.6	30.0	24.0
0.400	0.409	98.5	0.9	25.0	20.0
0.300	0.306	97.5	1.5	19.0	15.2
0.200	0.204	94.5	3.1	13.0	10.4
0.100	0.102	83.1	10.3	7.3	5.8
0.050	0.051	55.8	26.5	4.5	3.6
0.025	0.026	24.3	46.2	3.5	2.8
0.012	0.013	7.5	56.4	3.2	2.6

Table 7.13. Theoretical uncertainty modelling, considering different values for the rotational angle bias (Bias $\Delta\Phi$), and setting the reproducibility to be 1/5th of that value and the resolution negligible. The following outputs were considered as calculated from uncertainty table 7.2: the combined Dphi uncertainty (u($\Delta\Phi$)), the percentage influence of Dphi ($\Delta\Phi$%) and p (p%), the resulting expanded uncertainty for the z-coordinate (U(z)) and the percentage relative expanded uncertainty (U(z)/z%).
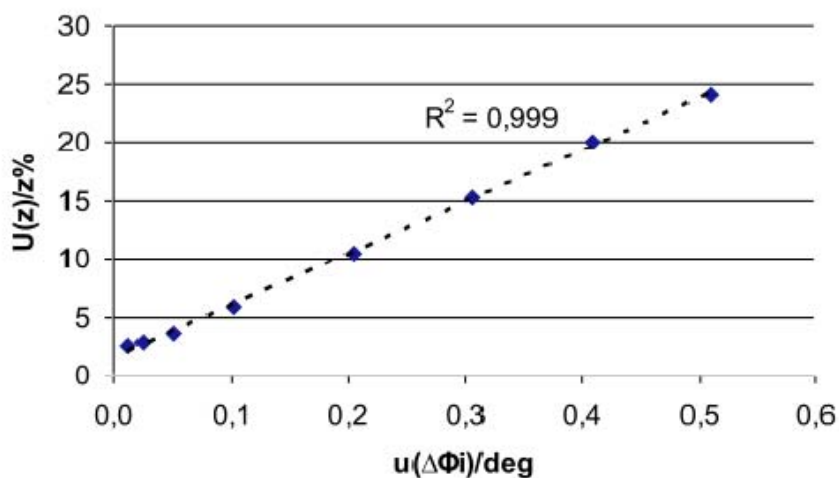

Figure 7.17. Graph showing the U(z)/z percentage value as a function of the combined uncertainty of the rotational angle u($\Delta\Phi$)/deg as resulting from the uncertainty modelling performed considering different rotary table capabilities. The dotted line represents the linear fitting of the results.

7.5 Summary and conclusions

In this chapter a theoretical and an experimental uncertainty evaluation of stereo-pair technique, according to ISO GUM (JCGM 100:2008), was carried out. As a case study, 3D-SEM reconstructions, performed on a wire gauge with reference diameter of 250 μm, were considered. Starting from the most commonly used tilting strategy, performed to obtain images composing the stereo-pair, a multi-view strategy through item rotations was also considered for the uncertainty evaluation. This methodology obtains 3D reconstructions of the complete geometry of the cylindrical item, by acquiring SEM images rotating the item along its main axis.

The theoretical uncertainty evaluation was performed starting from a modified version of Piazzesi's equation, enabling the calculation of the z-coordinate from a given stereo-pair. The pixel size p, the number of pixels n_1 and n_2, the working distance d and the tilt (or rotation) angle $\Delta\varphi$ were considered as independent variables. Metrological characteristics of each input variable (p, n_1, n_2, d and $\Delta\varphi$) were taken into account, and the uncertainty, in terms of bias, resolution and reproducibility for each variable, was calculated. An uncertainty table, for the case of tilt and rotation, was then produced leading to the calculation of the final expanded uncertainty value.

The main conclusions of this theoretical uncertainty evaluation were the following:

> ➢ For the case of rotations, the largest uncertainty contribution is due to reproducibility of rotational angle, $\Delta\varphi$, followed by bias of pixel size p. Therefore, in order to reduce the uncertainty in 3D-SEM reconstructions, performances of the rotary table should be improved and/or a different calibration procedure could be, for instance, considered by employing a different artefact.

> ➢ For the case of tilting, the largest uncertainty contribution is due to the bias of pixel size p, followed by the reproducibility of the tilt angle $\Delta\varphi$. Therefore, in order to reduce the uncertainty in 3D-SEM reconstructions when performing tilting, a calibrated artefact, with a lower uncertainty, should be adopted to refine pixel size bias calculation. Moreover, the high uncertainty associated to tilt reproducibility, is due to the fact that the stage can be tilted just manually by the operator. Therefore, since this uncertainty contribution can not be improved by further calibrations, another positioning system allowing item tilting should be adopted to improve the performances.

The <u>experimental uncertainty evaluation</u> was carried out considering 3D-SEM reconstructions of a wire gauge, with a reference diameter of 250, obtained using software MeX from Alicona. Three SEM images of the wire gauge, were considered leading to two different stereo-pairs, named after the rotational angles, -7&0 and 0&+7. For each stereo-pair three different values of MeX input parameters, working distance, rotational angle and pixel size, were chosen to perform stereophotogrammetry. This allowed a Design of Experiment (DOE) analysis, considering the three MeX input parameters as factors, each one set at three different levels, being level 0, the nominal input value, and levels -1 and +1, the nominal value including its uncertainty. The uncertainty ranges of the three factors were chosen based on the results of the theoretical uncertainty evaluation which were slightly overestimated to cover a higher variability range. Three replications were performed leading to a total number of 162 point clouds obtained from MeX reconstructions.

The main conclusions of this <u>experimental uncertainty evaluation were the following</u>:

> A fitting model was calculated, including main effects and interactions, leading to a $R^2 = 99.98\%$, meaning that the statistical analysis is significant and that the experimental error, mainly related to the diameter calculation variability, is negligible.

> Among the main effects the pixel size p is the most significant influence, accounting for 60.3% of the overall results variability, followed by the rotational angle Dphi which accounts for 39.4%. The working distance d, although being significant from a statistical point of view, accounts for only 0.3% of the overall results variability and the effect of the stereo-pairs "SP" was found to be negligible.

A response surface methodology (RSM) was also employed to calculate a fitting model equation allowing it to perform uncertainty evaluation in accordance with ISO GUM. A regression curve was calculated from the 162 responses, considering the main effects and their interactions as input variables. This methodology enables one to obtain a contour plot of the diameter as a function of the MeX input parameter value and allows it to determine the optimum setting of the input parameters to achieve a desired value of the output. By knowing the theoretical uncertainty values associated to the MeX input parameters, the resulting expanded uncertainty related to the diameter calculation can then be calculated. An improvement of the fitting model was obtained employing a Best Subset Regression method leading to $R^2 = 100.0$.

It was proven that the best possible fitting model is the one including the pixel size p, as the only main effect, the three interactions Dphi-d, Dphi-p and d-p and d^2.

A comparison of the theoretical and experimental uncertainty evaluation of stereo-pair technique in the case of rotations was also carried out including a modelling of rotary table capabilities. The results enables choosing the desired capabilities of a rotary table, in terms of combined uncertainty, to obtained a target percentage expanded uncertainty (U(z)/z%).

References

Barbato G, Germak A, D'Agostino D. Misurare per Decidere, Progetto Leonardo, 2005.

Bariani P. Investigation on Traceability of 3D SEM based on the stereo-pair technique. Internal Report, IPL DTU, 2003

Bariani P, De Chiffre L, Hansen HN, Horsewell A. Investigation on the traceability of three-dimensional scanning electron microscope measurements based on the stereo-pair technique. *Precis. Eng.* 2005; **29**: 219-228.

Carli L, De Chiffre L, Horsewell A, Carmignato S, Caroli M, Santin D. Improvement of geometrical measurements from 3D-SEM reconstructions. *Proc. of 11th CIRP International Conference on Computer Aided Tolerancing,* Annecy, 2009.

Carli L, Genta G, Cantatore A, Barbato G, De Chiffre L, Levi R. Experimental investigation on the influence of instrument settings on pixel size and nonlinearity in SEM image formation. *Proc. of 10th EUSPEN International Conference,* Delft, 2010.

Caroli M. Traceability of 3D-SEM-Uncertainty estimation. M.Sc Thesis, Department of Manufacturing Engineering and management. Technical University of Denmark, 2009.

EA-4/02:1999. Expressions of the Uncertainty of Measurements in Calibration, European co-operation for Accreditation, 1999.

Genta G. Methods for uncertainty evaluation in measurement. Ph.D. Thesis, Deparment of Production System and Business Economics (DSPEA), Politecnico di Torino, 2010.

Geomagic Studio 10. Geomagic Inc., 2008.

Goodhew PJ, Humphreys J, Beanland R. Electron Microscopy and Analysis, 3rd edition. Taylor and Francis, 2001.

ISO 230-2:2006. Test code for machine tools - Part 2: Determination of accuracy and repeatability of positioning numerically controlled axes, International Organization for Standardization, 2006.

ISO 14253-2:1999. Geometrical Product Specifications (GPS) - Inspection by measurement of workpieces and measuring equipment -- Part 2: Guide to the estimation of uncertainty in GPS measurement, in calibration of measuring equipment and in product verification, International Organization for Standardization, 1999.

ISO/IEC 17025:2005. General requirements for the competence of testing and calibration laboratories, International Organization for Standardization, 2005.

JCGM (Joint Committee for Guides in Metrology)100:2008. Evaluation of measurement data - Guide to the expression of uncertainty in measurement (GUM), 2008.

JCGM (Joint Committee for Guides in Metrology)100:2008. Evaluation of measurement data - Guide to the expression of uncertainty in measurement (GUM), 2008.

JCGM (Joint Committee for Guides in Metrology)200:2008- International Vocabulary of Metrology – Basic and General Concepts and Associated Terms (VIM), 2008.

Lawrence P. The Dualbeam (FIB/SEM) and its Applications - Nanoscale Sample Preparation and Modification. *Proc. of the Vacuum Nanoelectronics Conference* 2006; 127-128.

Lonardo PM, Lucca D, De Chiffre L. Emerging Trends in Surface Metrology. *CIRP Annals* 2002; **51**: 701-723.

Marinello F, Carmignato S, Savio E, Bariani P, Carli L, Horsewell A, De Chiffre L. Metrological performance of SEM 3D techniques. *Proc. of 18th IMEKO TC 2 Symposium on Photonics in Measurements*, Prague, 2008a.

Marinello F, Bariani P, Savio E, Horsewell A, De Chiffre L. Critical factors in SEM 3D stereo microscopy. *Meas. Sci. Technol.* 2008b; *19;* 065705.

MeX™ v 5.1. Alicona Imaging, 2007.

Minitab® 14.1 statistical software (demo version). Minitab Ldt., 2003.

Montgomery DC. Design and analysis of experiments, 7th edition. John Wiley, 2008.

Piazzesi G. Photogrammetry with the scanning electron microscope. *J. Phys. E.* 1973; **6**: 392-396.

Sato H. A way to measurement for submicron meter: surface profile by scanning electron microscope. *Proc. of manufacturing international 90* 1990; H0580C: 63-73.,

Scharstein D, Szeliski R. A taxonomy and evaluation of dense two-frame stereo correspondence algorithms. *Int. J. Comput. Vision. 2002;* **47**: 7-42.

Statistics Dictionary. A Dictionary of Statistics, 2nd edition. Oxford University Press, 2008.

8. Uncertainty budget for 3D-SEM reconstructions
of cylindrical items

8.1 Introduction

In the previous chapters of this work, the different error sources affecting 3D-SEM reconstructions were discussed and the uncertainty of the different contributors was evaluated. In particular, the effects of point cloud processing and feature extraction, the instrument setting parameters, the image quality and the stereo-pair technique on 3D reconstructions, were investigated. In this chapter the resulting expanded uncertainty, deriving from the above mentioned error sources, has been evaluated considering three cylindrical items as case studies: two wire gauges (WG) with a reference diameter of 250 µm and 260 µm and a hypodermic needle (HN) with a nominal external diameter of 260 µm. SEM images of the three items were acquired at the optimum measuring conditions through a multi-view strategy via item rotations in order to enable the overall cylindrical shape reconstruction. 3D-SEM reconstructions were then performed starting from those 2D images and the diameter of each resulting point cloud was calculated. From the analysis of the experimental results it will be possible to determine the resulting 3D reconstructions uncertainty, for both the WG and for the HN, and to compare it with the uncertainty budget performed taking into account all the different error sources listed above.

8.2 3D-SEM reconstructions of two reference wire gauges (WG) and a hypodermic needle (HN)

In order to carry out an uncertainty evaluation of 3D-SEM reconstructions performed on cylindrical objects, three items were considered for the experimental investigation.

1) A TESA reference wire gauge (WG), with an external diameter value of 250 ± 0,15 µm (Catalogue of TESA Technology, 2007/2008) which was already described and employed previously in this work.

2) A TESA reference wire gauge (WG), with an external diameter value of 260 ± 0,15 µm (Catalogue of TESA Technology, 2007/2008).

3) A Hypodermic needle (HN) with an external nominal diameter value of 260 µm.

A 1-D length measuring machine was preliminarily used to perform reference measurements of the HN external diameter as described in (Carli *et al.*, 2009). From the reference measurements a mean value for the reference diameter equal to 259.7 µm was calculated with a standard deviation of 0.2 µm.

The three cylindrical items were measured on the same Scanning Electron Microscope, the Inspect 'S owned by DTU CEN, under the same experimental conditions, and following the same procedure. Each object was mounted vertically inside the SEM chamber and clamped to the stage in order to keep it fixed during rotations as shown in Fig.8.1.
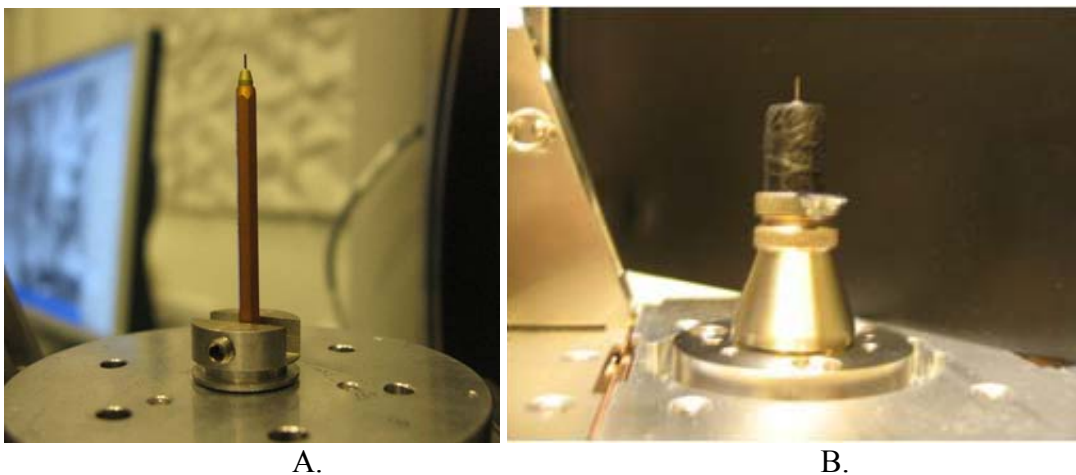

| A. | B. |

Figure 8.1. (A) Wire gauge and (B) hypodermic needle clamped and fixed on the SEM stage to allow rotation strategy.

After a vacuum had been created inside the SEM chamber, some minutes were required to achieve the thermal stability of the whole system. A room temperature of 22.1°C was measured; therefore linear thermal expansion was estimated to be negligible, due to the small diameter of the cylindrical items. The moving stage was tilted to 77 degrees, which was the maximum tilting permitted inside the microscope, to perform item rotations as the measuring strategy described in section 3.5 of this work. The cylindrical items were eucentrically rotated around their main axis to acquire images in different sections of the same object The measuring strategy used to acquire images of the cylindrical shape with the highest possible quality and with the highest number of pixels, then results in a more accurate stereo-reconstruction *i.e.* in a high-point density point cloud which leads to a more accurate diameter estimation. For this reason SEM instrument setting parameters and image quality were set to the optimal values in accordance with the item's geometrical characteristics and surface topography as well as the magnification and the working distance. The rotational angle between the two SEM images composing the stereo-pair at each portion of the item was always set equal to 7 degrees. This choice obtained a 3D reconstruction of a sufficiently large portion of the objects, leading to a good quality point cloud (*i.e.* exhibiting low noise). The measuring settings for the two wire gauges and for the hypodermic needle are shown in table 8.1 were all the experimental conditions are summarized. SEM images of a wire gauge were previously shown in this work, whereas one of the hypodermic needle is shown in Fig.8.2.

Item	Diamater/μm	HV/kV	SS/nm	M/times	Rep.	SEM images
WG	250.0	10	4.0	900	3	30
WG	260.0	10	4.0	1000	1	14
HN	259.7	5	3.5	837	1	20

Table 8.1. Summary of the experimental measuring settings for the SEM measurements performed on three cylindrical items. Three replications (rep) were carried out for the wire gauge (WG) with a reference diameter of 250 μm and one for the wire gauge with a reference diameter of 250 μm and for the hypodermic needle (HN) with a calibrated diameter of 259.7 μm. For each item the setting for the following parameters are indicated: accelerating voltage (HV), spot size (SS) and magnification (M).
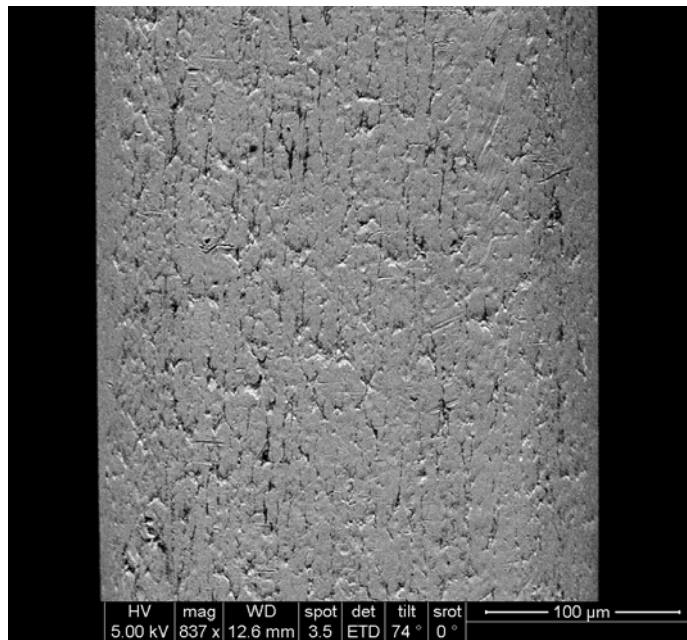
Figure 8.2. SEM image of a hypodermic needle with a calibrated diameter equal to 259.7 μm. The image was acquired using HV=5 kV, SS=3.5 nm and M=837x.

Starting from the SEM images, acquired in different views of the three cylindrical items, 3D reconstructions were performed employing the stereo-pair technique using MeX by Alicona Imaging GmbH (MeX^{TM}, 2007). The theoretical principles of this technique and the procedure for obtaining 3D reconstructions using MeX were already described in chapter 3. Basically MeX requires the operator to set the following input parameters in order to carry out stereo-pair reconstructions: the working distance (d), the rotational angle (Dphi) and the pixel size (p). The choice of the nominal input values for these parameters depends on the measuring strategy and on the geometrical characteristics of the item. The pixel size is directly linked to the magnification which should be chosen considering the desired field of view. The rotational angle was chosen equal to 7 deg. for all the 3D reconstructions based as described above. The pixel size and the rotational angle input parameters are constant for all the 3D reconstructions performed, starting from the SEM images of the same cylindrical items, whereas the working distance varies from one stereo-pair to the other in the sub-mm range. The nominal values for these three input parameters and for the three different cylindrical items considered in this work are shown in Table 8.2.

Item	Diameter/μm	p/(μm/pixel)	d/mm	Dphi/deg
WG	250.0	0.329	8.1 to 8.6	7.0
WG	260.0	0.295	11.7 to 11.9	7 .0
HN	259.7	0.350	11.4 to 12.6	7.0

Table 8.2. Summary of the nominal input parameters for the 3D-SEM reconstructions performed on three cylindrical items using MeX. The values of pixel size (p), working distance (d), and rotational angle (Dphi) are shown for the two wire gauges (WG) and for the hypodermic needle (HN).

8.2.1 3D-SEM reconstructions of a wire gauge with a 250 μm diameter

Three series of measurements were carried out acquiring SEM images of a reference wire gauge with a diameter equal to 250 μm, to test measuring reproducibility. A multi-orientation strategy was adopted performing 3D reconstructions of two portions of the item, by rotating it along its main axis from -14 to 14 deg. and from 36 to 64 deg. in steps of 7 degrees. This gives 5 SEM images per rotational range (*e.g.* -14, -7, 0, +7 and +14). From these 5 images always two successive ones are used to form the stereo-pairs enabling 3D-SEM reconstructions. Therefore 8 stereo-pair reconstructions were carried out for each measuring series, starting from the 10 SEM images acquired. The 24 resulting point clouds were processed using Geomagic Studio 10 (2008), following the procedure described in chapter 4, and the external diameter was calculated, after the feature extraction procedure. The experimental results for the three series of measurements (series) are shown in Fig.8.3 where the calculated external diameter is plotted as a function of the central rotational angle. This is calculated as the mean value of the rotational angles, set to acquire the SEM images forming the stereo-pair. From the graph it can be concluded that there is no systematic trend in the diameter value as a function of the rotational angle, meaning that the effect of the uncertainty related to the rotary table, when performing rotations, is randomly distributed. Moreover, the replicated measurements show differences in the calculated diameter values, for the same rotational angle, ranging from 1.8 to 4.7 μm.

191
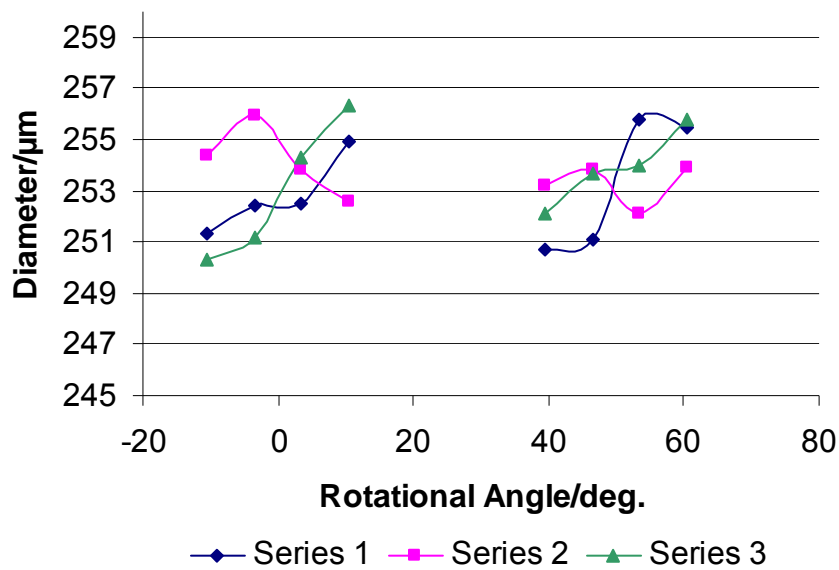
Figure 8.3. Experimental results showing the calculated diameter values for three runs of measurements performed on a wire gauge with a reference diameter equal to 250 μm. The diameter values, calculated from 3D-SEM reconstructions, using a Geomagic Studio 10 (2008), are plotted as a function of the central rotational angle.

The 24 experimental results were then plotted in another graph, without being specifically linked to the measuring series, to investigate the overall spread of the calculated values (Fig.8.4). A correction of the systematic error, related to the pixel size, which is set as input value to carry out stereo-pair reconstructions, was performed. According to the pixel size calibration curve, shown in chapter 7, setting M=900x a pixel size equal to 0.326 μm/pixel is obtained. This systematic error correction allows evaluating the uncertainty related to 3D-SEM measurements, performed on a wire gauge with a reference diameter of 250 μm. In particular the mean value resulted to be 251.1 μm and a 95% confidence interval equal to ± 3.8 μm was estimated to contain all the diameter values. This was calculated from the standard deviation of the 24 reconstructions, using a coverage factor of k_p=2.12 as calculated from ISO GUM (JCGM 100:2008), by taking into account the number of degrees of freedom. Therefore a relative percentage uncertainty equal to 1.4% was estimated from the previous values for the case of 3D-SEM reconstructions performed on a cylindrical item having a reference diameter equal to 250 μm. Moreover, an overestimation of about 0.6% was calculated from the mean value compared to the reference one.

Figure 8.4. Experimental results of the diameter calculation performed on 24 3D-SEM reconstructions of a wire gauge with a reference diameter of 250 μm. The central red dotted line represents the mean value equal to 251.1 μm, while the upper and the lower dotted lines represents the interval that contains 95% of the diameter values, calculated from the standard deviation of the results using a coverage factor k_p=2.12. Nominal values of the rotational angle and of the working distance were used as input parameters to perform 3D-SEM reconstructions, while the pixel size was set equal to the calibrated value obtained for M=900x, to correct the systematic error.

8.2.2 3D-SEM reconstructions of a wire gauge with a 260 μm diameter

3D reconstructions were carried out starting from SEM images of a wire gauge with a reference diameter equal to 260 μm. One series of measurements was performed using the measuring settings described in Table 8.1 and the MeX nominal input values reported in Table 8.2. From the 14 SEM images, acquired on three different portions of the item, 10 stereo-pairs were carried out. In particular the following areas were considered by rotating the wire gauge along its axis: from -10.5 to 10.5 deg., from 180 to 201 deg. and from 262.5 to 283.5 deg. in steps of 7 degrees as described in the previous section. The resulting point clouds were again processed using a demo version of Geomagic to carry out trimming, outliers removal, filtering and meshing in order to perform feature extraction and the diameter calculation.

3D-SEM reconstructions were performed using the pixel size value equal to 0.295 μm/pixel, calculated with MeX, and the calibrated one resulting in 0.293 μm/pixel for M=1000x. The experimental results for the 10 reconstructions, considering the nominal and the calibrated of the pixel size, are shown in Fig.8.5, where the calculated diameters, as a function of the different rotational angle, are shown. From the graph in Fig.8.5, it can be seen that 3D reconstruction performed using the nominal pixel size value leads to calculated diameters systematically higher than the ones obtained considering the calibrated pixel size. In particular the mean diameter value, calculated from the 10 reconstructions, is equal to 263.1 μm in the first case and to 261.7 μm in the second case. Therefore the diameter overestimation, obtained comparing the mean values with the reference one (*i.e.* 260 μm), was calculated to be approx. 1.2% and 0.6% respectively. Moreover, considering the reconstructions performed using the pixel size calibrated value, a ±4.1μm interval was estimated, containing 95% of the diameter values. This was calculated using a coverage factor of k_p=2.32, for the case of standard deviation calculated from 10 values (*e.g.* 9 degrees of freedom), calculated from ISO GUM (JCGM 100:2008).
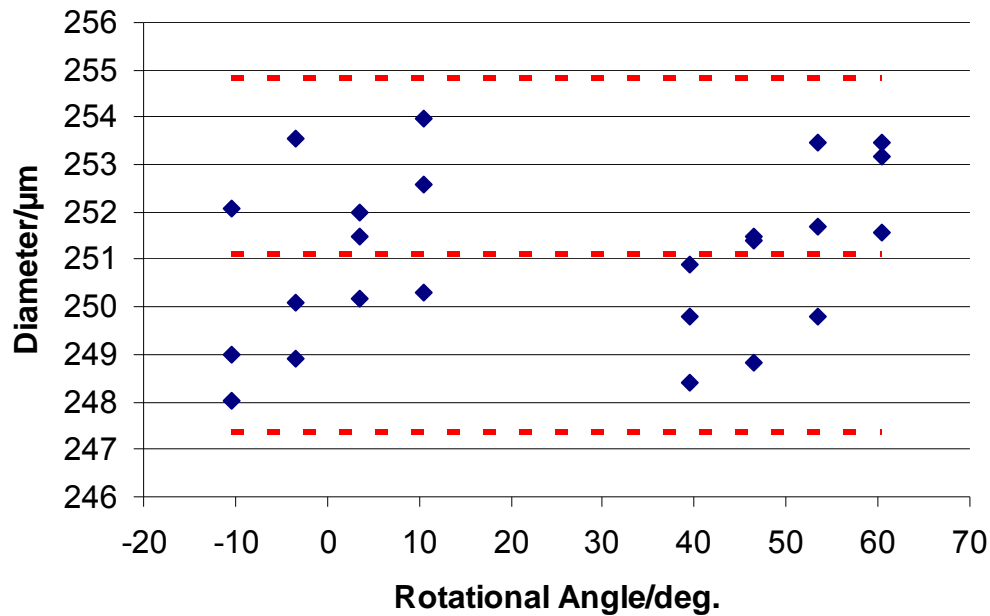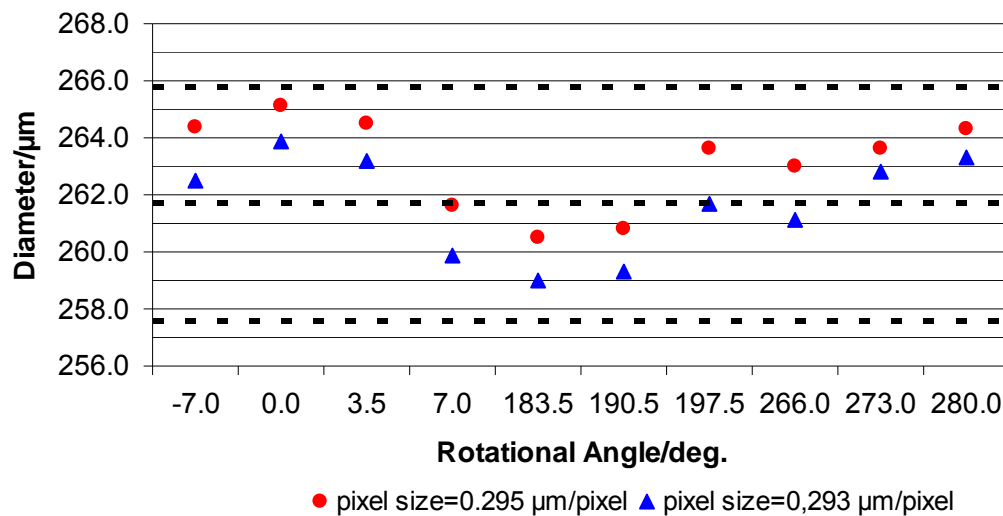

Figure 8.5. Experimental results of the diameter calculation performed on 10 3D-SEM reconstructions of a wire gauge with a reference diameter of 260 μm. The reconstructions were performed using MeX considering the nominal pixel size value (red dots) and the calibrated one (blue triangles). The central dotted line represents the mean value equal to 261.7 μm for the case of pixel sizes equal to the calibrated value, while the upper and the lower dotted lines represents the interval that contains 95% of the diameter values, calculated from the standard deviation of the results using coverage factor k_p=2.32.

8.2.3 3D-SEM reconstructions of a hypodermic needle with a 260 μm diameter

A series of 3D-SEM reconstructions were carried out, starting from SEM images acquired by measuring a hypodermic needle (HN) with a nominal diameter of 260 μm, similarly to that, which was previously done in Carli *et al.*, 2009. The item was clamped and fixed on the SEM stage as previously described and the measuring settings were the ones described in Table 8.1. A total of 20 SEM image were acquired by rotating the cylindrical item along its main axis leading to 16 stereo-pair reconstructions. In particular four different portions of the item were investigated by rotating the stage of 7 deg. each time. Thus, 5 images were acquired in each of these areas: from 31 to 59 deg., from 116 to 144 deg, 176 to 204 deg. and from 276 to 304 deg., in steps of 7 degrees, in order to enable multi-orientation measuring strategy. Stereo-pair reconstructions were performed using MeX, considering the nominal input values as shown in Table 8.2. In particular, the calibrated pixel size value, determined for M=837x, was considered to compensate for the systematic effect due to this input parameter, which was previously shown to affect 3D-SEM reconstructions. The external diameter, for the 16 resulting point clouds, was calculated using a demo version of Geomagic and the results are shown in Fig.8.6. A mean diameter value equal to 262 μm was calculated from the 20 experimental data together with the standard deviation of the results which was 3.2 μm. Thus, as these values were calculated based on 19 degrees of freedom, a coverage factor of k_p=2.17 derived in accordance to ISO GUM (JCGM 100:2008) and leading to a ±6.9 μm interval, containing 95% of the diameter values. This value leads to a percentage error of approx. 2.7%. Comparing the mean diameter value with the one obtained from the reference measurements previously performed in Carli *et al.,* (2009) which resulted to be equal to 259.7 μm, a 0.9% overestimation in the diameter calculation was estimated.
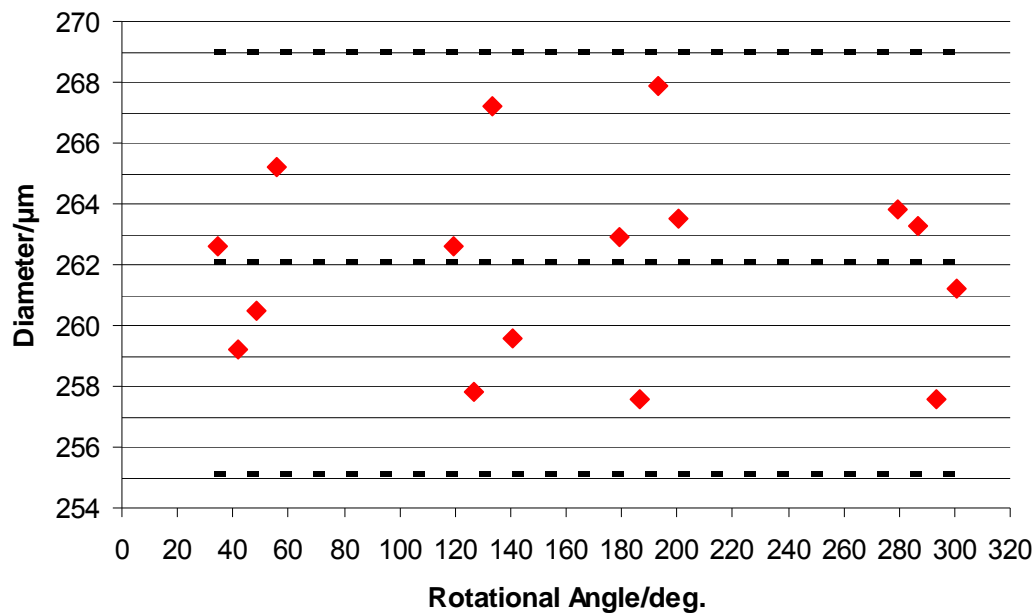
Figure 8.6. Experimental results of the diameter calculation measured on 20 3D-SEM reconstructions of a hypodermic needle with a calibrated diameter of 259.7 μm. The reconstructions were performed using MeX, considering the nominal input values for the rotational angle, the working distance and the calibrated value of the pixel size. The central dotted line represents the mean value equal to 262.0 μm, while the upper and the lower dotted lines represents the interval that contains 95% of the diameter values, calculated from the standard deviation of the results using a coverage factor of k_p=2.17.

8.3 Uncertainty budget for 3D-SEM reconstructions of cylindrical items

In section 3.4 of this work, the main phases related to 3D-SEM reconstructions were described. The different error sources linked to the single steps were underlined and an uncertainty evaluation on the influence of these error sources, with regards to 3D-SEM technique, was carried out in chapters 4, 5, 6 and 7 to quantify all the effects. Table 8.3 summarizes the different sources of uncertainty, related to 3D-SEM reconstructions, divided into the main categories suggested by ISO/TS 14253-2 (1999). For each uncertainty source a number of influencing factors is listed and a reference to the chapters, where they were investigated, is also provided.

Category	Sources of uncertainty	Influencing factors	Chapter
Reference	Reference wire gauge		3
Instrument	Instrument setting parameters	accelerating voltage, spot size, magnification	5
	Image quality	brightness, contrast, out of focus, saturation, noise	6
	Moving stage	eucentricity	3 and 6
Object	Physical and geometrical characteristics	Roughness, form error, material, presence of undesired features and dust	
Environment	Environmental conditions	temperature, humidity, noise, vibrations	
Procedure	Stereo-pair reconstructions	pixel size, working distance, tilt (rotation) angle	3 and 7
	Point cloud processing	trimming, outliers reduction, filtering, meshing	4
	Feature extraction	least squares algorithm	4
	Repeatability of measurements	operator	4

Table 8.3. List of uncertainty sources related to 3D-SEM reconstructions divided into the categories suggested by ISO/TS 14253-2 (1999). The main influencing factors are also listed together with a reference to the chapters where they were investigated.

With reference to the 3D-SEM reconstructions, performed on the three cylindrical items, described in the previous sections, the following preliminary considerations can be drawn:

- Among the instrument setting parameters, accelerating voltage and spot size were demonstrated not significantly influence the pixel size, although they affect the pixel nonlinearity. In particular, the setting of these parameters modifies the resulting SEM image quality. Therefore their effect on 3D-SEM reconstructions is partially confounded with the one of image quality;

- The magnification is typically set depending on the desired field of view, linked to the geometrical characteristic of the object to be measured. The magnification was proven to be strictly linked to the resulting pixel size. Therefore, as the uncertainty of the pixel size influences stereo-pair reconstructions, this contribution was considered just once, when evaluating uncertainty of stereophotogrammetry technique performed using MeX;

- The effect of a non-eucentric tilting, when carrying out stereo-pair reconstructions, was discussed from a theoretical point of view in chapter 3. From a practical point of view, the presence of non-eucentricity influences the horizontal shift of the features in the image. This effect was proven to be negligible in chapter 6, when performing stereo-pair reconstructions, compared to other error sources;

- The form error is already considered into the uncertainty of the reference item. The presence of dust should be avoided as SEM is usually operating in high vacuum environments. Defects on the surface topography (*e.g.* features) can not be always avoided, anyhow they are suitable when performing stereo-pairs superimposition and furthermore they were always trimmed out from the resulting point cloud. The wire gauge roughness was estimated in terms of Rz to be approx. equal to 250 nm, meaning the same order of magnitude of the point cloud noise. At this micro-level it is generally difficult to distinguish these two contributors;

- SEM measurements were performed at DTU CEN, where the building hosting the Inspect 'S' SEM, from FEI Company, used in this work, was build to almost perfectly insulate the environment from external noise and vibrations. The effect of temperature on the wire gauge diameter was calculated to be negligible in a previous paper from the author Carli *et al.*, (2009);

- The measuring procedure encompasses the use of software for stereo-pair reconstructions and one for point clouds processing and feature extraction. The uncertainty related to these two error sources was extensively investigated in chapters from 3 to 7, and the experimental results will be taken into account in the uncertainty budget;

- When executing repeatability tests on the diameter calculation, it is not generally possible to distinguish between the effect of the software for stereo-pair reconstructions and the one for point cloud processing. In fact, MeX obtains a 3D reconstruction but does not calculate the diameter of the cylindrical shape by means of a least square algorithm. One possibility is, for example, to perform a series of stereo-pair reconstructions, starting always from the same two SEM images, and, once the cylindrical shape has been obtained, fit a circle to the resulting mean 2D profile. This investigation was carried out considering 16 reconstructions of the wire gauge with a reference diameter of 250 μm, which resulted in a standard deviation, of the 2D diameter calculation, equal to 0.105 μm.

Starting from the above listed considerations it is then possible to carry out an uncertainty budget for 3D-SEM reconstructions in accordance with the PUMA method (ISO/TS 14253-2, 1999), *i.e.* discarding the contributions which were found to be negligible and taking into account only the most relevant ones. For this reason a table was produced where the main influencing factors, considered for the uncertainty budget, were listed together with their resulting uncertainty as calculated in the previous chapters of this work (see Table 8.4).

Sources of uncertainty	Evaluation Type	Value/μm	Distribution type	u_i/μm	DOF
Reference wire gauge	A	0.150	Normal	0.075	100
SEM Image quality	A	0.263	Normal	0.263	39
Repeatability of point cloud trimming	A	0.361	Normal	0.361	15
Diameter value resolution	B	0.100	Rectangular	0.029	100
Stereo-pair recontructions repeatability	A	0.105	Normal	0.105	15

Table 8.4. Main influencing factors, considered for the uncertainty budget, were listed together with their resulting uncertainty as calculated in the previous chapters of this work. Degrees of freedom (DOF) were assumed equal to 100 when the information is considered to be highly reliable.

The values reported in Table 8.4 were calculated from experimental investigations performed considering the wire gauge with a reference diameter equal to 250 μm. Nevertheless, it can be assumed that, whenever calculating these effects for the case of a cylindrical item with a different diameter value (within for instance a small variation range of 10%), a linear correction applies. With reference to the wire gauge with a 260 μm diameter, for example, a correction factor equal to (260/250) could be used for the type A values shown in Table 8.4. Moreover, it can be noticed that the uncertainty dealing with stereo-pair reconstructions was not taken into account in Table 8.4. This effect is assumed to be the most influencing one when performing the uncertainty evaluation; therefore it will now be discussed in more details. The uncertainty related to stereo-pair reconstructions is directly linked to the uncertainty of MeX input parameters as it was proven in chapter 7. In particular, the uncertainty related to the nominal input values of the rotational angle and the pixel size should be taken into account, while the effect of the working distance was demonstrated to be negligible. An example of stereo-pair uncertainty modelling, based on the uncertainty of the MeX input parameters, was calculated in chapter 7 for the case of 3D-SEM reconstructions carried out on the wire gauge with a diameter of 250 μm. When performing stereo-pair reconstructions of the other two cylindrical items considered in this work, different values of working distance and magnification (*i.e.* pixel size) where chose as shown in Table 8.2. Besides the uncertainty related to the stereo-pair technique, the surface topography of the item to be measured is different for SEM images acquired at different rotational angles. Moreover, the number and the size of the different features on the surface topography, to be used by MeX when superimposing the images forming the stereo-pair, are typically different from one view to another. On top of that, a non-eucentricity error is always present, which could be considered negligible for a single-stereo-pair, but could become relevant when the cylindrical item is rotated by the SEM stage. The quantification of these effects, which are considered to be strongly affecting the 3D-SEM reconstructions, is not normally easy to perform. One possible way to quantify the uncertainty contributor due to the stereo-pair technique, the object' s surface topography (in terms of roughness and number and size of features) and the non-eucentricity, is to consider the standard deviation of the experimental results, obtained by performing 3D-SEM reconstructions on the three cylindrical objects under consideration.

Thus, when making the uncertainty budget, the standard deviation of the multi-view reconstructions performed for the two wire gauges and for the hypodermic needle was considered, as representative of the uncertainty due to the sources described above. This uncertainty contribution was divided by the square root of the number of experiments as prescribed by the ISO GUM.

A preliminary uncertainty evaluation, for the case of a wire gauge with a diameter of 250 μm, was carried out considering the uncertainty sources listed in Table 8.4, and the considerations just mentioned, in accordance with ISO /TS 213, ISO/TS 14253-2 (1999). The results are shown in Table 8.5, where the effective degrees of freedom v_{eff}, where calculated with the Welch-Satterwaite formula described in ISO GUM (JCGM 100:2008).

Sources of uncertainty	Evaluation Type	Value/ μm	Distribution type	u_i/μm	DOF	U(D)/D
Reference wire gauge	A	0.150	Normal	0.075	100	1.6 %
SEM Image quality	A	0.263	Normal	0.263	39	19.8 %
Repeatability of point cloud trimming	A	0.361	Normal	0.361	15	37.4 %
Diamater value resolution	B	0.100	Rectangular	0.029	100	0.2 %
Stereo-pair recontructions repeatability	A	0.105	Normal	0.105	15	3.2 %
Topography, stereo-pair technique and non-eucentricity	A	1,781	Normal	0,364	23	37.8 %
Combined standard uncertainty/μm				0.591		
v_{eff}				60		
k_p				2.04		
Expanded Uncertainty/μm				1.206		

Table 8.5. Summary table of the uncertainty budget carried out considering the main uncertainty sources related to 3D-SEM reconstructions performed on a wire gauge with a reference diameter equal to 250 μm.

The uncertainty due to the surface topography, the stereo-pair technique, and the non-eucentricity was evaluated from the experimental standard uncertainty, calculated from the values shown in Fig.8.3. Moreover, the uncertainty sources described in table 8.4 were taken into account. For a coverage factor k_p=2.04, the expanded uncertainty in the case of 3D-SEM reconstructions performed on a wire gauge with a reference diameter value equal to 250 μm, resulted to be 1.206 μm. The percentage influence of the different uncertainty sources was also calculated, and it can be concluded that the uncertainty due to the stereo-pair technique, the surface topography and the non-eucentricity, accounts for 37.8% of the combined standard uncertainty, followed by the repeatability of the point cloud trimming procedure which accounts for 37.4% and the SEM image quality for about 20%. Therefore, in order to reduce the 3D-SEM reconstructions uncertainty, efforts should be made to decrease the uncertainty related to the non-eucentricity, although this task is not always simple to fulfill, or to the stereo-pair technique. The latter practically means that the uncertainty of the nominal input parameters, when performing stereo-pair reconstructions using MeX, should be reduced. Since the pixel size depends mainly upon the chosen value of magnification, which is linked to the lenses composing the SEM in use, it would be much easier to operate on the SEM stage responsible for performing the rotations. The SEM stage calibration procedure, aimed at the rotational angle uncertainty evaluation, could be for instance refined leading to a decrease in the resulting uncertainty. Another possibility, in the case where much more accurate 3D-SEM reconstructions are needed, a different rotary table could be then purchased to be installed in the SEM used to perform stereophotogrammetry. Issues related to point cloud trimming procedure should be also addressed in order to establish a more consistent procedure, leading to a decrease of this uncertainty source. Two other tables were also produced stating the expanded uncertainty obtained from 3D-SEM reconstructions performed on the wire gauge with a 260 μm reference diameter value and for the hypodermic needle with a calibrated diameter equal to 259.7 μm. The results are shown in Table 8.6 and Table 8.7.

Sources of uncertainty	Evaluation Type	Value/μm	Distribution type	u_i/μm	DOF	U(D)/D
Reference wire gauge	A	0.150	Normal	0.075	100	1.0 %
SEM Image quality	A	0.274	Normal	0.274	39	13.7 %
Repeatability of point cloud trimming	A	0.376	Normal	0.376	15	25.8 %
Diamater value resolution	B	0.100	Rectangular	0.029	100	0.2 %
Stereo-pair recontructions repeatability	A	0.109	Normal	0.109	15	2.2 %
Topography, stereo-pair technique and non-eucentricity	A	1.768	Normal	0.559	9	57.1 %
Combined standard uncertainty/μm				0.740		
v_{eff}				24		
k_p				2.11		
Expanded Uncertainty/μm				1.561		

Table 8.6. Summary table of the uncertainty budget carried out considering the main uncertainty sources related to 3D-SEM reconstructions performed on a wire gauge with a reference diameter equal to 260 μm.

Sources of uncertainty	Evaluation Type	Value/μm	Distribution type	u_i/μm	DOF	U(D)/D
HN diameter calibration	A	2.3E-04	Normal	0.075	9	0.0
SEM Image quality	A	0.274	Normal	0.274	39	8.6
Repeatability of point cloud trimming	A	0.376	Normal	0.376	15	16.3
Diamater value resolution	B	0.100	Rectangular	0.029	100	0.1
Stereo-pair recontructions repeatability	A	0.109	Normal	0.109	15	1.4
Topography, stereo-pair technique and non-eucentricity	A	3.200	Normal	0.800	15	73.6
Combined standard uncertainty/μm				0.932		
v_{eff}				26		
k_p				2.11		
Expanded Uncertainty/μm				1.967		

Table 8.7. Summary table of the uncertainty budget carried out considering the main uncertainty sources related to 3D-SEM reconstructions performed on a hypodermic needle with a calibrated diameter equal to 259.7 μm.

203

From the results shown in Table 8.6 and Table 8.7 the following conclusions can be drawn:

- The combined standard uncertainty, for the case of 3D-SEM reconstructions of a wire gauge with a reference diameter of 260 μm, it is equal to 0.740 μm, meaning about 150 nm more than in the case of WG with a reference diameter of 250 μm. This difference is due to the fact that a linear trend was assumed for the uncertainty related to the SEM image quality, point cloud trimming procedure and stereo-pair reconstructions repeatability. Moreover, the uncertainty due to the surface topography, stereo-pair reconstruction and non-eucentricity was in this case calculated based only on 10 stereo-pair reconstructions, while 24 were performed for the WG with a smaller reference diameter.

- The uncertainty budget carried out for the case of 3D-SEM reconstructions of a hypodermic needle, with a reference diameter equal to 259.7 μm, lead to an expanded uncertainty equal to 1.967 μm, meaning about 400 nm higher than in the case of WG with a similar diameter value. This is mainly due to the uncertainty related to the stereo-pair technique, the surface topography and the non-eucentricity, which in this case accounts for about 74% of the combined expanded uncertainty. The uncertainty related to the rotational angle nominal value, set into MeX, can be assumed to be the same as for the 3D-SEM reconstructions performed for the other two cylindrical items. Therefore the increase in the stereo-pair technique uncertainty is then probably due to the uncertainty of the pixel size. In fact, in this case, a lower magnification was adopted for acquiring SEM images of the HN (*i.e.* 837x against 900x and 1000x of the previous two cases). This choice of the magnification, results in a higher value of the pixel size which was calibrated in chapter 7. Higher values of the pixel size results in higher values of the related uncertainty in terms of bias and reproducibility. This is also proven by the fact that, as it was demonstrated in chapter 7, the pixel size uncertainty strongly affects the resulting diameter of a cylindrical item. For this reason the stereo-pair uncertainty in the case of HN can be reduced by performing 3D-SEM reconstructions from SEM images acquired at higher magnifications, *i.e.* at 1000x.

To allow an easier uncertainty budget results comparison, a graph was produced where the reference or calibrated diameter values, for the three cylindrical items under consideration, is shown together with the calculated expanded uncertainty (Fig.8.7). In this case a 0.025 deg. correction of the rotational angle systematic error was also applied, leading to a decrease in the mean calculated diameter values. This value was estimated from the rotational angle calibration performed in chapter 7.
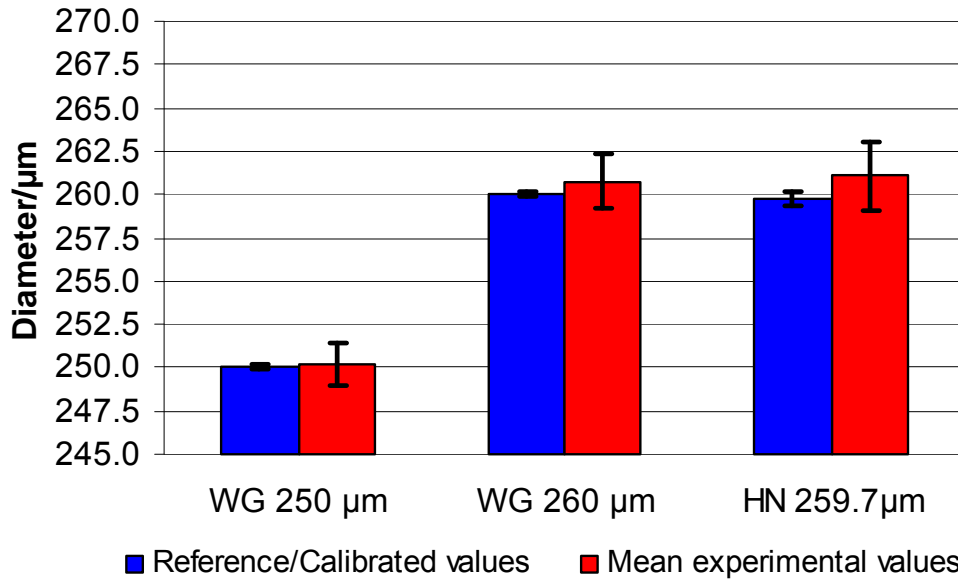
Figure 8.7. The graph shows the mean experimental diameter values and the expanded uncertainty calculated from 3D-SEM reconstructions performed on the two wire gauges (WG) and on the hypodermic needle (HN).The values are compared to the reference diameter value, in the case of WG, and to the calibrated value in the case of HN. The systematic error, due to the pixel size and to the rotational angle, was corrected before setting the input values into MeX to perform the stereo-pair reconstructions.

8.4 Comparison of software algorithms for feature extraction

In this work the external diameter of the cylindrical items was calculated performing a feature extraction on the point cloud resulting from MeX stereo-pair reconstructions. In particular, the point cloud processing and feature extraction were performed using a demo version of Geomagic. This software performs feature extraction based on the Least Squares Method (LSM) as it was described in chapter 4. In order to test the performances of this algorithm, a comparison was carried out considering the feature extraction capabilities of two other pieces of software: Polyworks v.10 (2007; license valid until 2009 by Università degli Studi di Padova) and the Matlab® 7.4 (R2007a) developed by the author and described in chapter 3 of this work.

The experimental investigation was performed considering point clouds obtained by MeX, from three different stereo-pairs of the wire gauge (WG) with a reference diameter of 260 μm and three of the hypodermic needles (HN) with a calibrated diameter equal to 259.7 μm. Six replications were performed for each stereo-pair under consideration, to test the uncertainty of the feature extraction algorithm of the different software. The point clouds where processed only, using Geomagic, performing trimming, outliers removal and filtration, in order to allow testing of the feature extraction algorithm. Thus, the resulting expanded uncertainty, calculated using a coverage factor of k=2, comprises not only the uncertainty related to the feature extraction process, but also to the other error sources described and investigated in the previous section. The mean value and the expanded uncertainty (k=2), resulting from six replicated experiments, for three different pieces of software, Geomagic, Polyworks and Matlab, are shown in Fig.8.8 for the case of WG and in Fig. 8.9 for the HN.
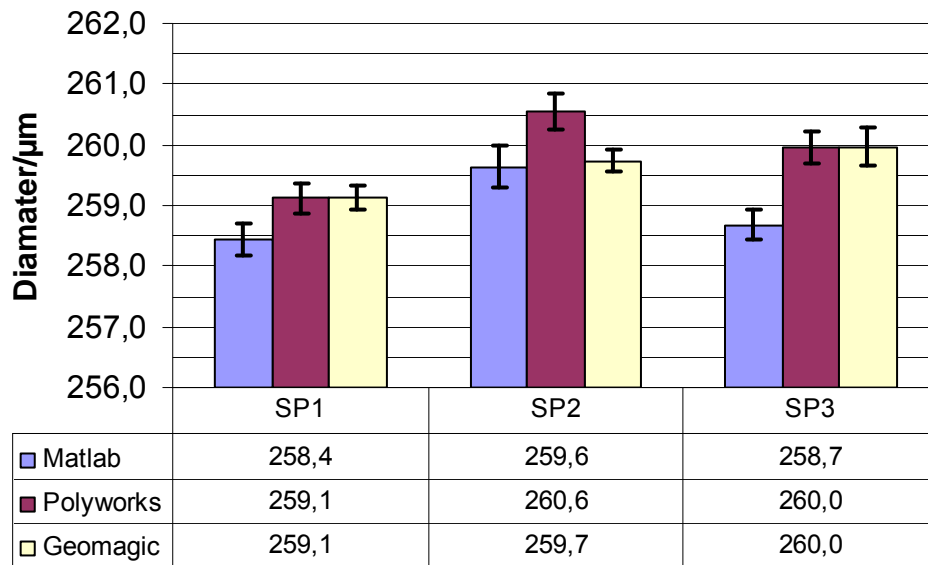
	SP1	SP2	SP3
☐ Matlab	258,4	259,6	258,7
■ Polyworks	259,1	260,6	260,0
☐ Geomagic	259,1	259,7	260,0

Figure 8.8. Experimental results of testing the feature extraction algorithm performances of three different pieces of software: Geomagic, Polyworks and Matlab. Mean value and expanded uncertainty (k=2), for six replicated experiments are shown for three different stereo-pairs (SP) obtained from SEM images of a wire gauge with a reference diameter of 260 μm.

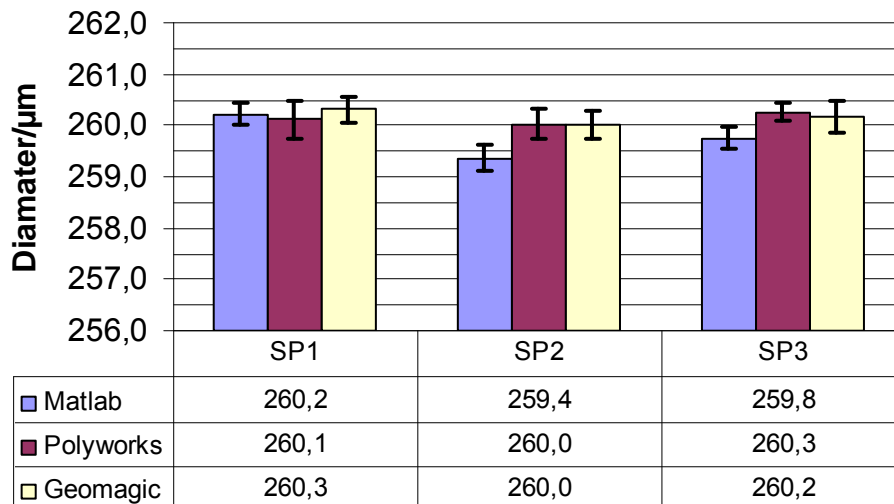|	SP1	SP2	SP3
☐ Matlab	260,2	259,4	259,8
■ Polyworks	260,1	260,0	260,3
☐ Geomagic	260,3	260,0	260,2

Figure 8.9. Experimental results of testing the feature extraction algorithm performances of three different pieces of software: Geomagic, Polyworks and Matlab. Mean value and expanded uncertainty (k=2), for six replicated experiments are shown for three different stereo-pairs (SP) obtained from SEM images of a hypodermic needle with a calibrated diameter of 259.7 μm.

The comparison of the feature extraction algorithm of the software should be based on the mean values rather then on the resulting expanded uncertainty, as this is related only to Geomagic as described above. The following conclusion can be drawn:

- The feature extraction algorithm, performed using Geomagic, leads to lower diameter values, compared to Polyworks and Matlab, for five stereo-pairs among the six considered. This difference is ranging from 0.3 to 0.6 μm;

- The feature extraction algorithm, performed using Polyworks and Matlab, provides very similar results for five stereo-pairs among the six considered. The maximum difference in the diameter calculation was in the order of 0.2 μm;

- Performing feature extraction, on the same point cloud, but with different software, leads to differences in the resulting diameter calculation, which in some cases could be consistent (*e.g.* 1 μm for the case of SP2 of the WG).

The data considered, for the algorithms for feature extraction performances comparison, does not allow determining which software, among the ones considered, leads to the most accurate results. In order to solve this issue, some test should be performed considering synthetic data, meaning point clouds artificially created by the operator with a known diameter value. A first attempt was done in a previous work at the author's department (Trevisan, 2010), but it is should be followed by a more consistent experimental investigation.

8.5 Summary and conclusions

In this chapter an uncertainty evaluation of 3D-SEM reconstructions was carried out considering measurements on three cylindrical items: two wire gauges (WG) with a reference diameter of 250 μm and 260 μm and a hypodermic needle (HN) with a nominal external diameter of 260 μm. The HN diameter was calibrated by means of a 1-D length measuring machine leading to a value of 259.7 μm. SEM images of the three items were acquired at the optimum measuring conditions performing a multi-view strategy through item rotations in order to be able to reconstruct the overall cylindrical shape. 3D-SEM reconstructions were then performed using MeX Alicona starting from those 2D images and the diameter of each resulting point cloud was calculated.

The resulting point clouds were processed using a demo version of Geomagic and the cylindrical shape was extracted to calculate the external diameter. In particular, three series of measurements were performed with the WG with a reference diameter of 250 μm and one for the other wire gauge and for the hypodermic needle. An uncertainty budget was then carried out taking into account the experimental results and considering the main uncertainty sources and influencing factors, described in the previous chapters. Following the approach suggested by the PUMA method, the following uncertainty sources were determined to be the most relevant ones in the case of 3D-SEM reconstructions: the uncertainty stated in the calibration certificate or obtained through a calibration procedure, the SEM image quality, the repeatability of point cloud trimming, the diameter value resolution, the stereo-pair reconstructions repeatability and the stereo-pair technique performed with MeX. Since the uncertainty related to the MeX input parameters, when performing stereophotogrammetry technique, was found to be the most influencing factor, a correction of the systematic error related to the pixel size was performed for the 3D-SEM reconstructions of the WG 260 μm and of the HN. From the experimental results and from the uncertainty budget the following conclusions can be drawn:

Considering 3D-SEM reconstructions of the three cylindrical items:

- The mean value, resulting from 24 stereo-pair reconstructions of the WG with a reference diameter equal to 250 μm, resulted be 251.1 μm with a ± 3.8 μm interval containing the 95% of the diameter values. Therefore a percentage uncertainty equal to 1.5 % was estimated;

- Considering the wire gauge with a reference diameter of 260 μm, the mean diameter value, calculated from the 10 reconstructions, was found to equal to 263.1 μm, if no compensation of the pixel size systematic error was applied and to 261.7 μm in the other case. Therefore the diameter overestimation was calculated to be approx. 1.2% and 0.6% respectively;

- A mean diameter value equal to 262.0 μm was calculated from the 20 stereo-pair reconstructions performed on different views of the hypodermic needle. From this data ±6.9 μm interval containing the 95% of the diameter values was calculated. Comparing the mean diameter value with the one obtained from the calibration procedure (*i.e.* 259.7 μm), a 0.9% overestimation in the diameter calculation was estimated.

Considering <u>the uncertainty budget</u> calculation performed for the three cylindrical items:

- For the case of 3D-SEM reconstructions performed on the two wire gauges, similar results were obtained for the uncertainty budget calculation, taking into account the uncertainty sources listed above. An expanded uncertainty equal to 1.206μm and to 1.561μm were calculated for the smaller and the bigger WG respectively. Considering the different uncertainty contributors it was estimated that the uncertainty due to the surface topography, the stereo-pair technique the non-eucentricity accounts for about 40% to 60% of the combined standard uncertainty, followed by the repeatability of the point cloud trimming procedure which accounts for about 35 to 25% for both the smaller and the bigger WG respectively;

- In the case of uncertainty budget carried out from 3D-SEM reconstructions of the hypodermic needle, an expanded uncertainty equal to 1.967μm was calculated, meaning. In this case the uncertainty to the surface topography, the stereo-pair technique the non-eucentricity accounts for about 75% of the combined standard uncertainty.

The performances of these three pieces of software, Geomagic, Polyworks and the Matlab routine developed by the author, were tested with regards to the accuracy of their feature extraction algorithms. The experimental investigation was performed considering point clouds obtained by MeX, from three different stereo-pairs of the wire gauge (WG) with a reference diameter of 260 μm and three of the hypodermic needles (HN), performing six replications. It can be concluded that the feature extraction algorithm, implemented in Geomagic, leads to lower diameter values, compared to Polyworks and Matlab. Differences range from 0.3 to 0.6 μm. The results obtained using Polyworks and Matlab are very similar with a maximum difference in the diameter calculation in the order of 0.2 μm. Moreover, performing feature extraction, on the same point cloud, but with different software, leads to differences in the resulting diameter calculation, which in same cases could be in the order of 1 μm.

References

Carli L, De Chiffre L, Horsewell A, Carmignato S, Caroli M, Santin D. Improvement of geometrical measurements from 3D-SEM reconstructions. *11th CIRP Conference on Computer Aided Tolerancing*, Annecy, 2009.

Catalogue of TESA Technology. Hexagon Metrology, TESA, 2007/2008.

Geomagic Studio 10. Geomagic Inc., 2008.

ISO/TC 213, ISO/TS 14253-2. Geometrical Product Specifications (GPS) – Inspection by Measurement of Workpieces and Measuring Equipment – Part 2: Guide to the Estimation of Uncertainty in GPS Measurement, in Calibration of Measuring Equipment and in Product, ISO, 1999.

JCGM (Joint Committee for Guides in Metrology)100:2008. Evaluation of measurement data - Guide to the expression of uncertainty in measurement (GUM), 2008.

Matlab® 7.4 (R2007a). MathWorks, 2007.

MeX^{TM} v 5.1. Alicona Imaging, 2007.

Polyworks v.10. InnovMetric Software Inc.,2007.

Trevisan A., Uncertainty Evaluation for 3D-SEM recontructions, M.Sc. Thesis, Department of Mechanical Engineering.Technical University of Denmark, 2010.

9. Fabrication and application of two novel artefacts for 3D-SEM calibration

9.1 Introduction

This chapter deals with the fabrication, calibration and application of two novel artefacts for 3D-SEM calibration. These artefacts are intended for the z-coordinate calibration, which is a crucial issue when performing measurements on 3D reconstructions obtained by employing stereophotogrammetry technique. A state of the art survey was carried out to investigate artefacts for 3D-SEM calibration currently available. The main limitation of such geometries is that, in order to take measurements at different magnifications or at different working distances, they require artefact relocation. The two artefacts proposed in this work, instead, encompass the presence of a central point, located at the intersection of microscope optical axis (z-axis) and the reference x-y plane (SEM focal plane). The artefacts were therefore fabricated, based on the design originally proposed by Bariani (2005) (see Fig.9.1), and calibrated by means of a reference stylus profilometer, to establish measurements traceability when performing 3D-SEM reconstructions. The mean step-heights values, calculated from 3D-SEM measurements, were compared to the ones obtained with the reference ones and with measurements performed using an optical 3D measurement device.
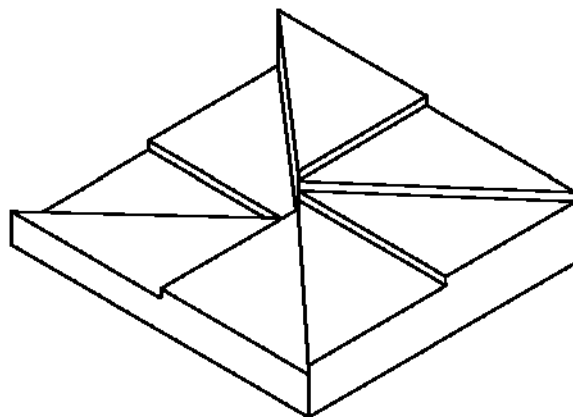

Figure 9.1. Sketch of a proposed geometry for a multiple-step heights calibration artefact with a centre point (Bariani, 2005)

9.2 Survey on artefacts for vertical range calibration

The z-coordinate calibration in SEM can be performed by adopting calibration artefacts and procedures intended for Scanning Probe Microscopy, such as gratings for vertical direction calibration, or the multiple-step solution, consisting of steps with the same height (United States Patent; patent number 6028008). Artefacts intended for the vertical range calibration of stylus instruments can also be employed, such as the ones proposed by the DS/ISO 5436-1:2000 (2000). The usage of calibrated gauge-blocks, wringed together forming different step-heights, was also proposed by Bariani *et al.* (2005). Anyhow, few artefacts are nowadays available, which are specifically intended for 3D-SEM calibration. A micrometer-sized 3D calibration structure was originally proposed by (Sinram *et al.*, 2002). More recently a 3D calibration structure, for the calibration of various 3D micro-range measurement methods was developed by PTB (Physikalisch Technische Bundesanstalt, Braunschweig). It is a 34 x 34 μm base pyramid fabricated using a gas-assisted focused ion beam (FIB) proposed to be the reference artefact for the traceability chain for Scanning Electro Microscopes (Ritter *et al.*, 2004). The pyramidal shaped calibration object has slope steps which approximately measures 6μm in width and length and 3μm in height. It can be used for SEM calibration at magnifications of 8000x to approx. 20000x. The calibration object has up to 38 nano-markers as well distinguishable reference points. Furthermore an artefact, encompassing 3D calibration structures for four-quadrants back scattered Scanning Electron Microscopes (4Q BSD SEMs) for scan widths (FOVs) of 20, 40 and 80 μm, was developed by the m2c Company. This calibration artefact allows simultaneous (one-step) lateral and vertical calibration by means of three pyramidal elements each one consisting of three equal steps in the order of 0.6 μm (MMC40) and of 1.3 μm (MMC80) (Ritter *et al.*, 2007). The One Step 3D Calibration by m2c was also recently implemented in the VDI/VDE guideline 2656 (2008). The MeX by Alicona Imaging GmbH (MeX^TM, 2007), used in this work to performed stereo-pair reconstructions (reference to MeX), allows height measurements from stereo-triplet reconstructions, using the AutoCalibration routine, which was verified using a micro-contour-artefact calibrated by the PTB (Physikalisch Technische Bundesanstalt, Braunschweig) which contains grooves of different depth (from 240nm to 50μm; Schroettner *et al.*, 2006).

9.3 Multi-step heights artefacts design and fabrication

The first multi-step heights artefact was fabricated according to the design proposed by Bariani (2005), patented by (De Chiffre *et al.*, 2004) and considering the different issues concerning manufacturing, calibration and application. In fact the choice of the calibration artefact material and geometry should fulfil some requirements such as the stability over time, a smooth surface topography (*i.e.* low roughness value), and overall x-y and z dimensions making it suitable for the calibration process and for the application transfer into a SEM environment. The artefact weight is also relevant, as the SEM stage should be able to support the calibration artefact without this affecting the translation and tilting capabilities of the stage itself. Moreover, if the multi-step height artefact calibration is intended to be performed by means of a reference stylus profilometer, one further requirement is to have step heights decreasing from the bottom to the top and therefore decreasing as the z direction is increasing. This issue can be seen in Fig.9.2.
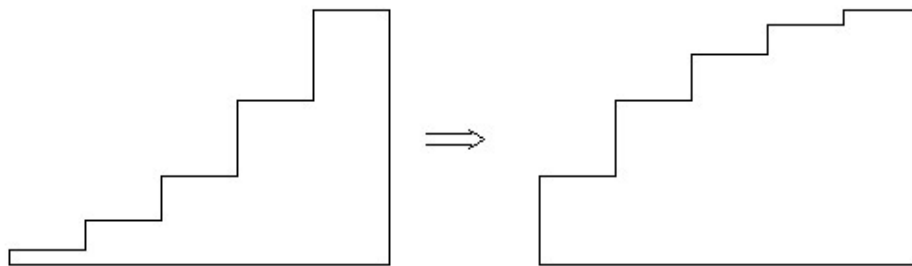
Figure 9.2. An example of two different configurations for a multiple step-height artefact, one with step heights increasing as the vertical direction is also increasing (on the left) and the other with step heights decreasing from the bottom to the top (on the right). The latter configuration was adopted for the multiple-step height artefacts fabrication.

9.3.1. The five step heights "staircase" artefact

Based on the above mentioned configuration the first realization of the five step heights artefact was performed with the characteristics listed in Table 9.1.

Characteristic	Description
Material	ASP60 (high alloyed high speed steel)
Technology	Grinding with a tool radius of 50 μm
Geometry	Cylindrical shape with five step-heights forming a "staircase" shape with a common central point
Overall Dimensions	Diameter Φ=6 mm; Height h=3 mm
Weight	Not measured (estimation: few grams)
Nominal step heights	50 μm; 35μm; 10 μm; 3 μm; 2 μm

Table 9.1. Main characteristics and relative description of the five-step heights artefact for 3D-SEM calibration.

The overall geometry of the five-step artefact was produced by taking advantage of a tool grinding operation, with a tool radius of 50 μm, on super highly alloyed high speed steel with hardness of 60 HRC (VANADIS® 60 from *Uddeholm* Svenska AB). The main characteristics of this steel are:

• high wear resistance;

• high compressive strength;

• good hardening properties;

• good toughness;

• good dimensional stability.

Therefore this material fulfils the requirements for a calibration artefact listed above. More information about ASP60 and the grinding process of this material can be found in (TSO *et al.*, 1999). The step-by-step process for producing the five-step heights artefact, starting from a cylindrical rod, and using grinding by rotating the object around its main axis is shown in Fig.9.3. As the final overall height of the artefact would be generally too high from the 3D-SEM application perspective, the cylindrical rod was cut to ensure the final 3 mm overall height. Values lower than this would make the handling, positioning and fixing processes too difficult, during SEM measurements. In Fig.9.4 a 3D view of the CAD model and the final realization of the artefact are shown, where each of the five steps was named with a letter from A to E to facilitate the understanding of the measuring results. In particular, the nominal step heights values are the ones listed in Table 9.2.
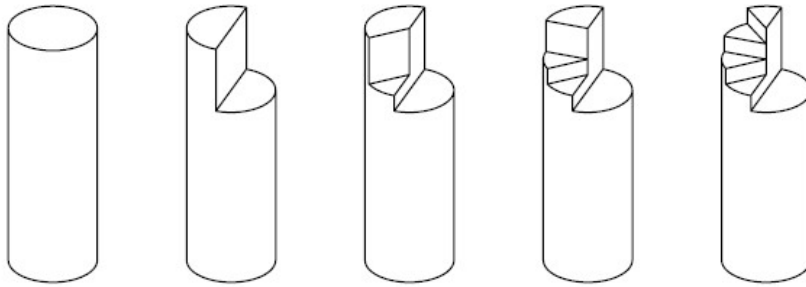
Figure 9.3. The step-by-step process for producing the five-step heights artefact, starting from a cylindrical rod, and using grinding by rotating the object around its main axis.
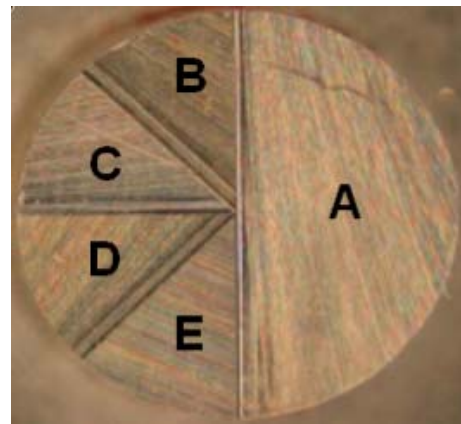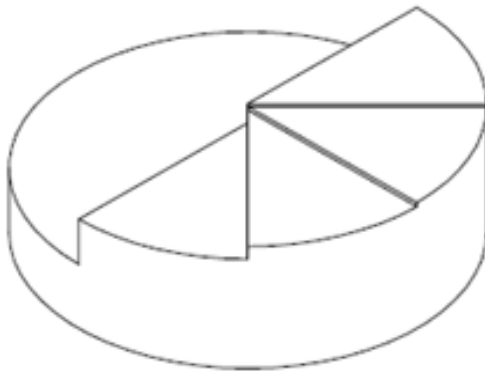
Figure 9.4. 3D view of the CAD model (on the left) and an image of the final realization of the five-step heights artefact by means of grinding operation (on the right). Each of the five steps was named with a letter from A to E to facilitate the understanding of the measuring results.

Step	Height/µm (Design Specifications)
AB	35
BC	10
CD	3
DE	2
AE	50

Table 9.2. Nominal values, for the five-step heights calibration artefact, according to the design specifications.

9.3.2. The three step heights artefact

The second multi-step heights artefact was designed along the lines of the previous one, but considering three-step heights instead of five. In particular the three-step heights were chosen ranging from 2 to 7 μm, therefore being similar to the smaller steps of the previous design. Concerning the fabrication, the Electrical Discharge Machining (EDM) process was chosen to meet the desired requirements. The artefact manufacturing was carried out by 3D Multi-Axis Micro EDM Milling from Sarix SA, at the author's department. This technology, due to the very small size of the electrode (about 45 μm), guarantees side walls almost vertical, with a curvature radius in the order of 3 to 5 μm. Moreover, very smooth surface finishing is obtainable down to Ra 0.05 μm (SX-200-HPM, 2010). In Table 9.3 the main characteristics and relative description concerning the three-step heights artefact for 3D-SEM calibration are reported. Moreover Fig.9.5 shows a 3D model of the three-step heights artefact together with a 2D-view of a measurements performed using a reference stylus profilometer, as it will be discussed in the next section.

Characteristic	Description
Material	Carbide
Geometry	Cylindrical shape and three step heights with a common central point
Overall Dimensions	Diameter Φ=3 mm; Height h=4 mm
Weight	Not measured (estimation: few grams)
Nominal step heights	7 μm; 5μm; 2 μm

Table 9.3. Main characteristics and relative description of the three-step heights artefact for 3D-SEM calibration.
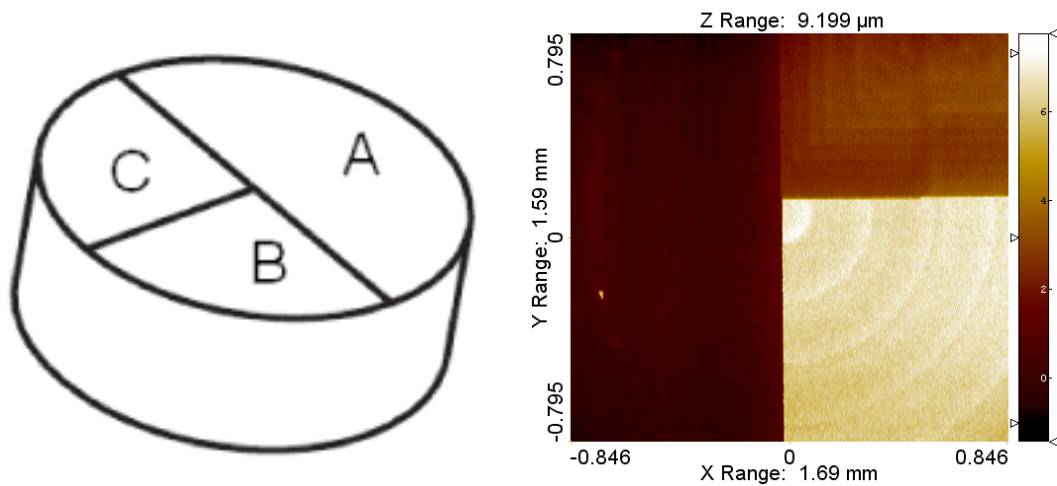
Figure 9.5. 3D model of the three-step heights artefact (on the left) and 2D-view of a measurements performed using a reference stylus profilometer.

9.4 Artefacts calibration by means of a reference stylus profilometer

Reference measurements, on both the proposed artefacts for 3D-SEM calibration, were performed using a stylus profilometer, Form Talysurf Series 2 (FTS) from Taylor Hobson, with a tip radius of 2 μm, at the Center for Geometrical Metrology. Before performing the artefacts calibration, an uncertainty budget was carried out in accordance with the ISO GUM (JCGM 100:2008) following the procedure described below. The calibration, of the reference stylus instrument vertical range, was carried out using an ISO Type A2 step height standard, with 6 grooves ranging from 0.1 to 10 μm (DS/ISO 5436-1:2000). A calibration certificate was provided together with the artefact (reference no. PTB- 5.15-4038109) stating the expanded uncertainty, calculated in accordance with ISO GUM, of the groove depth d and the total height of profile Pt for each of the six grooves. These parameters are evaluated according to DIN EN ISO 5436-1:2000 for the case of d, and to DIN EN ISO 4287:1998 in the case of Pt. In order to perform an uncertainty budget for the calibration of the reference stylus instrument, the following uncertainty contributors must be considered:

- Uncertainty of the calibration standard u_n;
- Uncertainty of the transfer of traceability (repeatability of the instrument) u_r;
- Uncertainty caused by the background noise u_b.

Five repeated measurements were performed to evaluate u_r, at a vertical instrument range of 200 μm which provides a resolution equal to 3nm. This uncertainty contributor was also taken into account for the uncertainty budget performed in accordance with ISO /TS 213, ISO/TS 14253-2 (1999). In particular only the *d* parameter was calculated for the calibration. As the FTS provided an output series of 11 profiles, these were analyzed using the software SPIP^{TM} (Scanning Probe Image Processor v.5.1.3) from Image Metrology. This contains a routine which allows the calculation of the *d*-value, as prescribed by the DIN EN ISO 5436-1:2000, from a given profile. The results of five repeated measurements and the resulting uncertainty budget are shown in Table 9.4. The uncertainty contributors listed above were considered to calculate the expanded uncertainty (k=2) of the instrument. Moreover the calibration factor for each groove was estimated, by dividing the mean calculated groove depth value for the one stated on the calibration certificate. The uncertainty due to the background noise was calculated from five repeated measurements on an optical flat glass, from which an average Rz0=0.045 μm was obtained. Furthermore, the resolution value, equal to 3 nm, was obtained from the FTS reference manual for a measuring range equal to 0.2 mm.

Groove No.	Groove depth d/μm	u_n/nm	u_r/nm	u_b/nm	u_{res}/nm	U_{inst}/nm	U_{inst}%	Cal.factor
R1	0.151	3.5	2.9	13.0	0.9	27.6	18.3	1.036
R2	0.401	3.5	2.8	13.0	0.9	27.5	6.9	1.035
R3	1.059	4	2.9	13.0	0.9	27.9	2.6	1.045
R4	2.555	4.5	2.5	13.0	0.9	28.0	1.1	1.041
R5	5.661	5	1.9	13.0	0.9	28.1	0.5	1.026
R6	9.053	9	4.6	13.0	0.9	33.0	0.4	1.027

Table 9.4. Uncertainty table summarizing the mean value of the groove depth d for the six grooves of the ISO Type A2 step height standard. Five repeated measurements were carried out using a reference FTS stylus profilometer to calculate the different uncertainty contributors. In particular the uncertainty related to the calibration standard (un), to the instrument repeatability (u_r), the background noise (u_b) and the resolution (u_{res}) were taken into account for the evaluation of the expanded uncertainty (k=2).

Once the reference stylus vertical range has been calibrated, six repeated measurements were performed on the two artefacts for 3D-SEM calibration and the expanded uncertainty (k=2) was calculated. Concerning step-height calculation, different strategies were tested in previous works, for their ability to lead to traceable results (Santin (2009) and Trevisan (2010)). The problem arising when step height measurements are performed on a single profile is shown in Fig.9.6. There, an example of two profiles, representing AB and AC steps of the three-step heights artefact, obtained from the reference measurements are shown. It can be seen that the definition of the "real "step height it is not trivial due to the roughness. Hence, for step-height measurements, one of several algorithms may be used. For single-sided steps, a straight line was fitted by the method of least squares to each side of the step transition, and the height was calculated from the relative position of these two lines extrapolated to the step edge, similarly to what proposed by Vorburger *et al.* (2008). Nevertheless, as a parallelism error is typically always present, the resulting fitting lines would not be parallel, introducing an error source when measuring their vertical distance. This error source was considered to be contained into the measuring reproducibility uncertainty.
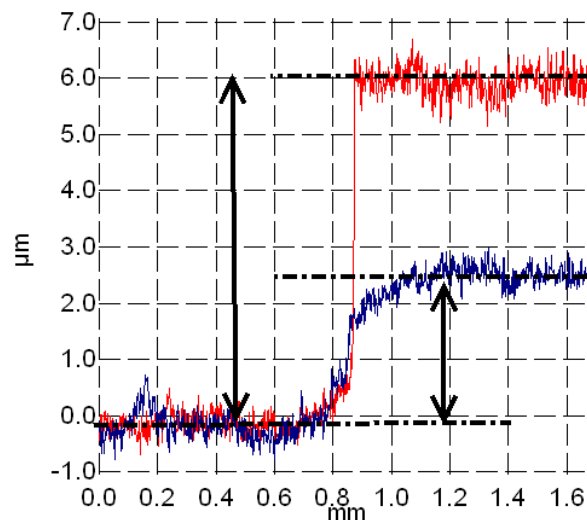

Figure 9.6. Example of two profiles, representing AB and AC steps of the three-step heights artefact, obtained from the reference measurements. For single-sided steps, a straight line is fitted by the method of least squares to each side of the step transition, and the height is calculated from the relative position of these two lines extrapolated to the step edge.

Two measuring strategies were considered for the reference measurements performed on both artefacts for 3D-SEM calibration, since the lateral resolution of the FTS is direction dependent. For this reason both the artefact were measured with the reference plane A positioned first oriented orthogonally to the x-axis measuring direction (strategy 1) and then parallel to it (strategy 2) as shown in Fig.9.7. As the measuring range was 1.68x1.60 mm, the resulting lateral resolution was 1 µm and 10 µm in the x and y measuring direction respectively.

A)

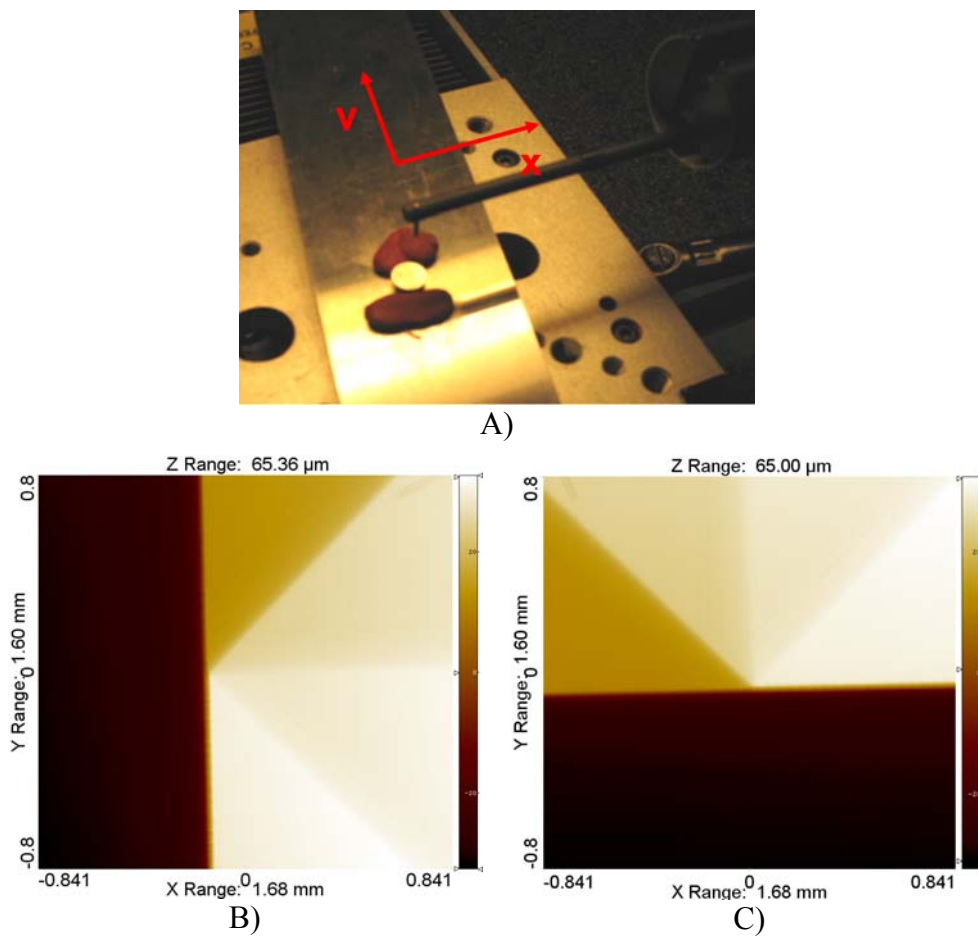B)   C)

Figure 9.7. Image (A) shows the measurements procedure, by means of an FTS reference stylus profilometer. The lateral resolution was 1 µm and 10 µm in the x and y measuring direction respectively. A 2D view of the measurements performed with the reference zero plane A positioned parallel to the x measuring direction (B) and to the y one (C) is shown.

In order to perform an uncertainty budget from reference measurements, the uncertainty related to the instrument calibration u_{ins} (type A) and to the measurements reproducibility u_s (type A) were considered. Moreover, the workpiece surface roughness u_w was also taken into account in terms of Rz-value (type B, rectangular). An Rz=0.050 µm was calculated for the five-step heights artefact produced by grinding, and to Rz=0.160 µm for the three-step heights machined through EDM technique. For the uncertainty related to the FTS calibration, the highest value, among the ones calculated from the Table 9.4., was chosen (*i.e.* U_{ins}=33 nm). The final results of the uncertainty evaluation procedure are reported in Table 9.5 and Table 9.6, together with the mean calculated values for the multiple-step heights. Moreover a 3D rendering, from stylus profilometer measurements for the two artefacts proposed for 3D-SEM calibration, is shown in Fig.9.8.

Step	Height/µm	u_{ins}/nm	u_s/nm	u_w/nm	U/µm (k=2)	U(z)/z
AB	2.235	4.8	91.0	46.2	0.204	9.1 %
BC	3.964	4.8	196.5	46.2	0.404	10.2 %
AC	6.116	4.8	75.6	46.2	0.177	2.9 %

Table 9.5. Experimental results obtained from six replicated measurements, performed on the three-step heights calibration artefact, with the reference stylus profilometer. The mean step-heights values are shown, together with the different uncertainty sources taken into account, the evaluated expanded uncertainty (k=2) and the relative uncertainty U(z)/z.

Step	Height/μm	u_{ins}/nm	u_s/nm	u_w/nm	U/μm (k=2)	U(z)/z
AB	39.268	4.8	85.1	14.4	0.171	0.4 %
BC	11.202	4.8	94.3	14.4	0.213	1.9 %
CD	4.035	4.8	74.0	14.4	0.183	4.5 %
DE	3.225	4.8	68.2	14.4	0.178	5.5 %
AE	57.723	4.8	76.2	14.4	0.153	0.3 %

Table 9.6. Experimental results obtained from six replicated measurements, performed on the three-step heights calibration artefact, with the reference stylus profilometer. The mean step-heights values are shown, together with the different uncertainty sources taken into account, the evaluated expanded uncertainty (k=2) and the relative uncertainty U(z)/z.
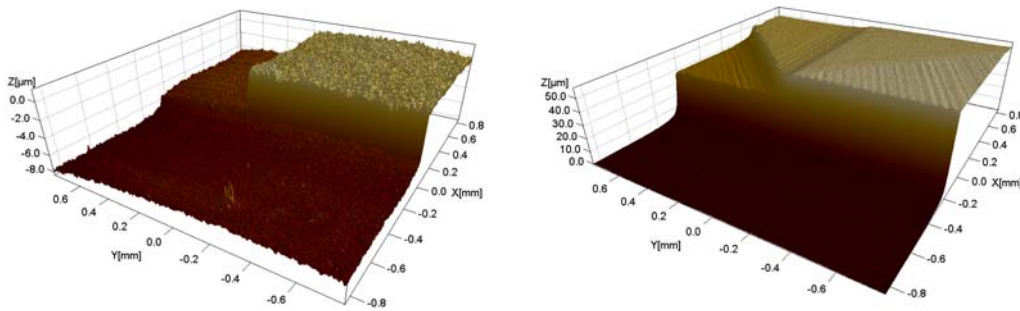

Figure 9.8. 3D rendering from stylus profilometer measurements performed on the three-step heights artefact (on the left) and on the five-step heights artefact (on the right).

224

9.5 Step heights measurements by means of an Infinite Focus instrument

After the calibration procedure, the two artefacts for 3D-SEM calibration were measured using an Infinite Focus instrument by Alicona Imaging GmbH. The Infinite Focus is an optical 3D measurement device which provides dimensional measurements, surface analysis and characterization. The Infinite Focus operating principle combines the small depth of focus of an optical system with vertical scanning to provide topographical and colour information from the variation of focus. A 50x magnification was chosen when performing measurements on both artefacts, which leads to a vertical resolution of approx. 50 nm. The measuring range was 1.0 mm per 0.8 mm with a lateral resolution equal to about 0.7 μm in x and y directions. In order to estimate the different step heights, the measuring strategy, as well as the step-height calculation, for a given profile, were kept the same as for the case of the FTS. This was done to enable a direct comparison of the results with the ones obtained by means of the reference stylus profilometer. Six replicated measurements were performed on each artefact to estimated the reproducibility uncertainty u_s. Furthermore, the following uncertainty sources were taken into account when performing the uncertainty evaluations:

- Uncertainty of the workpiece u_w in terms of surface roughness, which affects the step height estimation (see Fig.9.6). The Rz values considered for the uncertainty calculation where the same estimated from the FTS measurements, *i.e.* Rz=0.050 μm, for the five-step heights artefact and to Rz=0.160 μm for the three-step heights one.

- Uncertainty due to the vertical resolution u_{res}. The vertical resolution achievable by measuring at M=50x is about 50 nm. Therefore u_{res} was calculated assuming a Type B rectangular distribution.

In Table 9.7 and Table 9.8 the average values of the different step heights, resulting from the six replicated measurements, performed on the two artefacts by means of the Infinite Focus instrument are shown. The different uncertainty contributors and the resulting expanded uncertainty (k=2) and the relative uncertainty U(z)/z are also shown. The results are compared to the references one and discussed in section 9.7. Moreover, an example of 3D rendering resulting from Infinite Focus measurements on the three and five-step heights artefacts is given in Fig.9.9.

Step	Height/µm	u_s/nm	u_w/nm	u_{res}	U/µm (k=2)	U(z)/z
AB	2.027	47.7	46.2	14.4	0.133	6.6 %
BC	3.799	98.5	46.2	14.4	0.218	5.7 %
AC	6.052	26.1	46.2	14.4	0.106	1.8 %

Table 9.7. Experimental results obtained from six replicated measurements, performed on the three-step heights calibration artefact, using an Infinite Focus instrument from Alicona. The mean step-heights values are shown, together with the different uncertainty sources taken into account, the evaluated expanded uncertainty (k=2) and the relative uncertainty U(z)/z.

Step	Height/µm	u_s/nm	u_w/nm	u_{res}/nm	U/µm (k=2)	U(z)/z
AB	38.137	87.3	14.4	14.4	0.179	0.5 %
BC	11.295	43.3	14.4	14.4	0.096	0.8 %
CD	3.762	66.1	14.4	14.4	0.138	3.7 %
DE	2.843	53.3	14.4	14.4	0.114	4.0 %
AE	56.270	82.1	14.4	14.4	0.169	0.3 %

Table 9.8. Experimental results obtained from six replicated measurements, performed on the five-step heights calibration artefact, using an Infinite Focus instrument from Alicona. The mean step-heights values are shown, together with the different uncertainty sources taken into account, the evaluated expanded uncertainty (k=2) and the relative uncertainty U(z)/z.
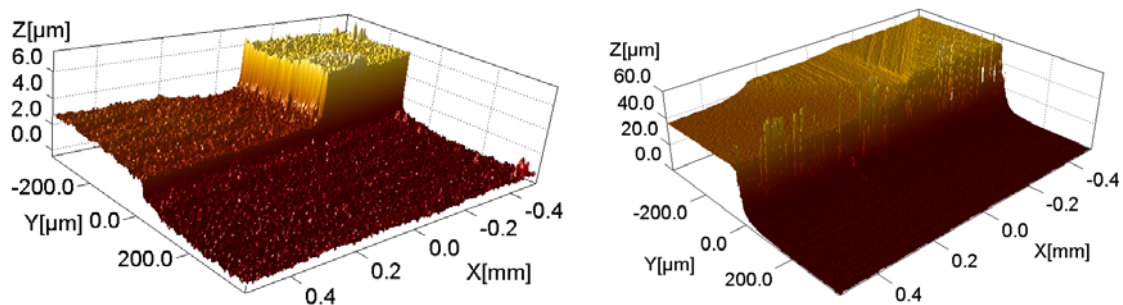

Figure 9.9. Example of 3D rendering obtained from measurements performed using Infinite Focus from Alicona on the three-step heights artefact (on the left) and on the five-step heights one (on the right).

9.6 Artefacts application for 3D-SEM calibration

The three and the five-step heights artefacts were fabricated and calibrated by means of a reference stylus profilometer and then measured using an Infinite Focus instrument. A series of stereo-pair reconstructions were then carried out, starting from SEM images of both the artefacts, to verify the applicability of the proposed designs for 3D-SEM calibration. The SEM used in this work was the Inspect™ from FEI Company, owned by the Center of Electron Nanoscopy (CEN) at the author's University. The stereo-pair reconstructions were performed using MeX Alicona. The procedure leading from two SEM images, forming the stereo-pair, to a 3D reconstruction was already described in chapter 3, together with a description of the input parameters to be set into the software.

A number of preliminary considerations should be made before performing the SEM measurements:

- The SEM instrument setting parameters, in terms of accelerating voltage and spot size, have to be chosen based on the artefacts material and characteristics as described in chapter 5 of this work.

- The magnification is chosen depending on the desired field of view and depth of field. This choice influences the resulting pixel size, which is one of the input parameters to be set into MeX Alicona when performing stereo-pair reconstructions.

- Efforts should be made by the operator, when acquiring the SEM images, to assure the optimum possible image quality, obtained through a proper combination of focus, brightness and contrast, and by reducing the noise to the minimum (*e.g.* by decreasing the scan rate).

- The measuring strategy should guarantee the eucentric tilting of the artefacts to be measured inside the SEM chamber. Different values of the angle, formed between the two images composing the stereo-pair, one tilted with respect to the other, can be set.

Therefore, based on the above mentioned considerations, a number of SEM images at different tilt angles were acquired for both the proposed calibration artefacts.

 The working distance was set equal to 10.1 mm, which was the value experimentally determined to guarantee the eucentric tilting. In this condition, the center point of the artefacts is not shifting when a tilt is applied to the SEM stage, remaining always in the middle of the SEM images.

The five-step heights artefact encompasses the presence of curvature radius in the order of 50 μm between the single steps. This is due to the grinding tool used during the manufacturing process. For this reason, if plane A (Fig.9.4) is chosen as the reference plane when performing step-height measurements, the height of the single profiles should be measured at a certain distance from the side walls, corresponding to the curvature radius. This effect could be seen in Fig.9.10 where a 2D profile was traced on the AB and AC planes from measurements performed using the reference stylus profilometer. Thus, the magnification should be chosen taking into account that the resulting field of view should be sufficient to enable reliable measurements of the step heights, performed using the strategy described in section 9.4. In the case under consideration a FOV≥ 200 μm is needed. This corresponds to magnification values M≤ 1500x for the SEM used in this work. Considering the three-step heights calibration artefact, the smaller curvature radius (~5 µm) enables the acquisition of SEM images, for step-heights calculations, up to 5000x, corresponding to a FOV=60 μm. The measuring strategy adopted for 3D-SEM reconstructions carried out on both the calibration artefacts is summarized in Table 9.9.
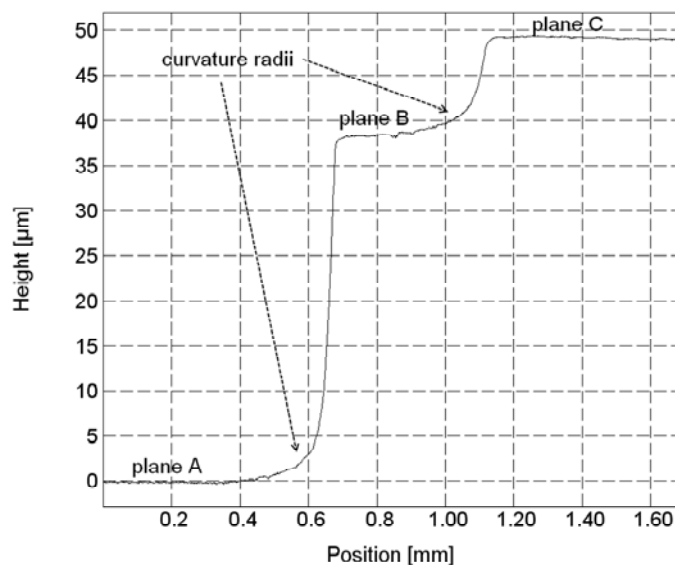

Figure 9.10. Example of 2D profile traced along the ABC plane from measurements performed on the five-step heights artefact with the FTS. The presence of curvature radii of about 50 μm is clearly visible.

Parameter	Symbol	Unit	Value
Accelerating voltage	HV	kV	10.0
Spot Size	SS	nm	4.0
Magnification	M	times	1500
Working distance	d	mm	10.1
Tilt angle	Dphi	deg.	14, 16 and 18

Table 9.9. Summary of the measuring strategy chosen to perform 3D-SEM reconstructions starting from SEM images acquired on the two calibration artefacts: the three-step heights and the five-step heights.

From Table 9.9 it can be seen that tilt angles equal to 14, 16 and 18 degrees between the two stereo-pairs were chosen when performing the 3D-recontructions. Generally speaking, smaller angles could have been chosen for the artefacts with bigger steps, and larger angles for the artefact with smaller steps, since the fewer the heights variations in the SEM image, the higher should be the tilt angle. Nevertheless, these values were chosen as they were suitable for both the calibration artefacts.

Similarly, higher magnification levels could have been used with the three-step heights artefact, nevertheless M=1500x was a trade-off choice, allowing performing preliminary measurements on both the calibration artefacts. SEM images of both calibration artefacts, acquired in the 0 deg. tilt condition are shown in Fig.9.11 where the center point was positioned right in the middle of the field of view. The tilting operation was performed along the xz direction, *e.g.* orthogonal to the y-axis, as shown in Fig.9.11.
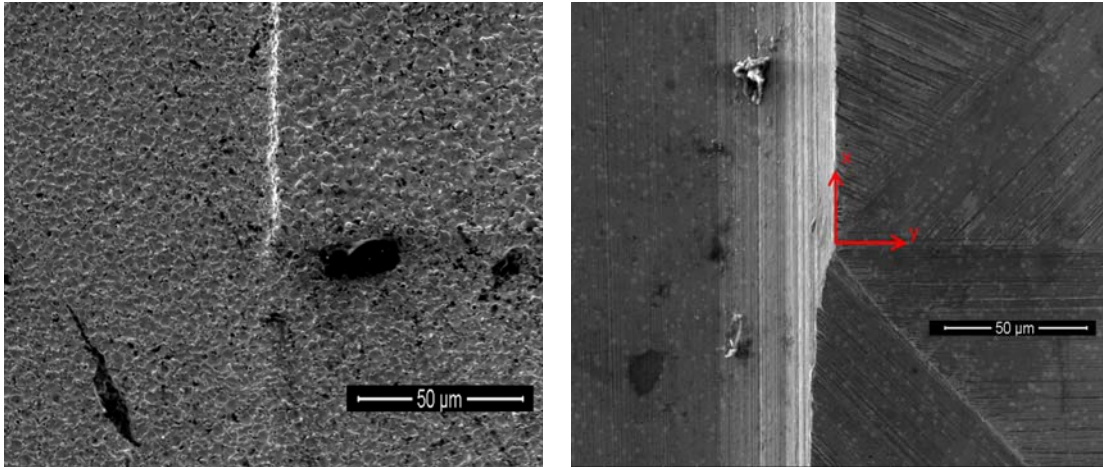
Figure 9.11. SEM images acquired at a 0deg. tilting for the three-step heights artefact (on the left) and for the five-step heights one (on the right). Images were acquired at a working distance d=10.1 mm, magnification M=1500x, accelerating voltage HV=10 kV and spot size SS=4 nm, with the center point positioned in the middle of the field of view. The tilting operation was performed along the xz direction, *e.g.* orthogonal to the y-axis.

At any of the three chosen values of the tilt angle, stereo-pair reconstructions were performed two times, for a total of six replications. This strategy enabled the evaluation of the uncertainty related to 3D reconstructions performed using MeX, in terms of measurements reproducibility. The following uncertainty contributors were then considered:

- Uncertainty related to the measurements reproducibility u_s;

- Uncertainty due to the workpiece roughness, u_w. This value was the same calculated for the uncertainty budget performed from FTS and Infinite Focus measurements;

- Uncertainty due to the vertical resolution u_{res}. Since measurements were performed at M=1500x, the vertical resolution was estimated to be approx. 160 nm.

The mean step-height values calculated from the six replicated reconstructions and measurements are shown in Table 9.10 and Table 9.11 for the two calibration artefacts under consideration. Moreover the uncertainty contributors listed above are also calculated and the resulting expanded uncertainty (K=2) and the relative uncertainty U(z)/z are shown.

Step	Height/µm	u_s/nm	u_w/nm	u_{res}/nm	U/µm (k=2)	U(z)/z
AB	1.878	43.9	46.2	45.6	0.157	8.3 %
BC	3.813	41.4	46.2	45.6	0.154	4.0 %
AC	5.974	29.7	46.2	45.6	0.143	2.4 %

Table 9.10. Experimental results obtained from six replicated measurements, performed on the three-step heights calibration artefact, from 3D-SEM reconstructions. The mean step-heights values are shown, together with the different uncertainty sources taken into account, the evaluated expanded uncertainty (k=2) and the relative uncertainty U(z)/z.

Step	Height/µm	u_s/nm	u_w/nm	u_{res}/nm	U/µm (k=2)	U(z)/z%
AB	38.200	159.2	14.4	45.6	0.332	0.9
BC	10.383	98.0	14.4	45.6	0.218	2.1
CD	3.331	60.0	14.4	45.6	0.153	4.6
DE	2.708	60.5	14.4	45.6	0.154	5.7
AE	56.300	223.6	14.4	45.6	0.457	0.8

Table 9.11. Experimental results obtained from six replicated measurements, performed on the five-step heights calibration artefact, from 3D-SEM reconstructions. The mean step-heights values are shown, together with the different uncertainty sources taken into account, the evaluated expanded uncertainty (k=2) and the relative uncertainty U(z)/z.

An example of 3D reconstruction, obtained using MeX Alicona, for the five-step heights artefact is shown in Fig. 9.12 together with a contour plot representing different heights in different colours, having chosen the plane A as reference zero plane. The areas corresponding to the curvature radii can be distinguished from the ones representing the steps.
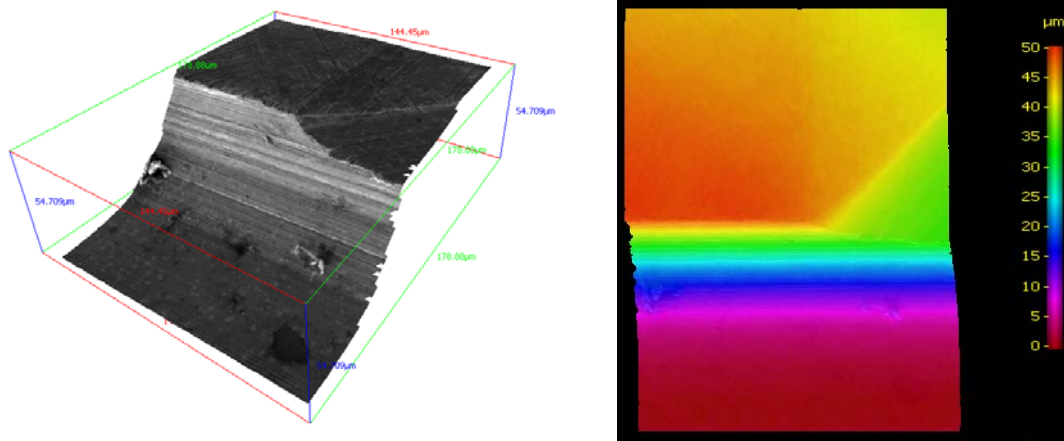
Figure 9.12. Example of a 3D-SEM reconstruction of the five-step heights artefact (on the left) and a contour-plot representing the different heights in different colours. The areas corresponding to the curvature radii can be distinguished.

9.7 Comparison of step-height measurements performed with the three different

Considering the experimental results, obtained by measuring the two proposed calibration artefacts, using the three different instruments, as described in the previous sections, a number of the graphs was produced to allow a direct comparison. In particular, the mean step-heights values calculated from measurements performed with the reference stylus profilometer (FTS), the Infinite Focus instrument (IF) and the 3D-SEM technique (3D-SEM) are shown, together the expanded uncertainty values reported in Tables 9.5, 9.7 and 9.10, for the three-step heights artefact (Fig. 9.13), and in Tables 9.6, 9.8 and 9.11 for the five-step heights one (Fig.9.14 and Fig.9.15). Moreover, for the step-heights measurements, performed using the Infinite Focus and the 3D-SEM technique, the expanded uncertainty was corrected taking into account the presence of the systematic errors as prescribed by ISO/TS 15330-3 (2004) to guarantee measurement traceability.
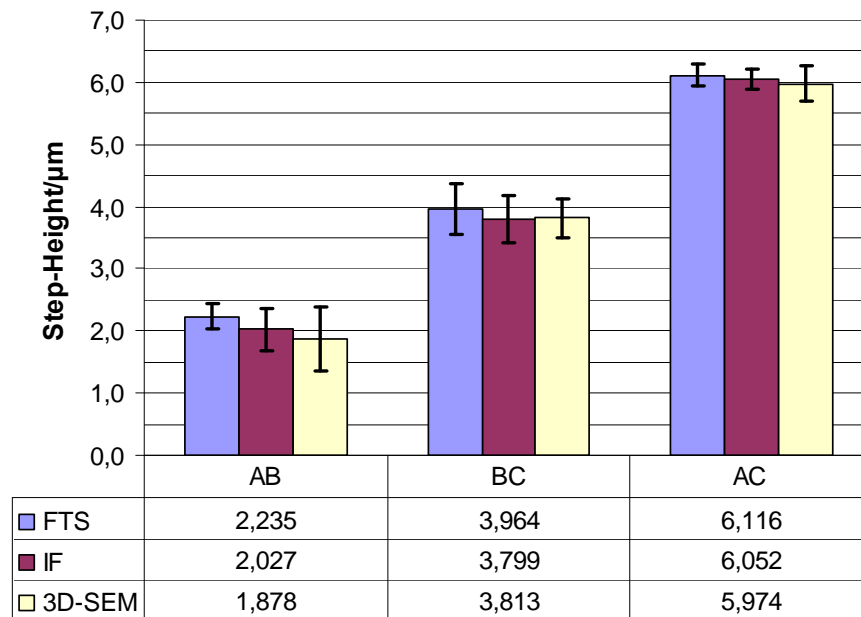
	AB	BC	AC
▣ FTS	2,235	3,964	6,116
■ IF	2,027	3,799	6,052
▢ 3D-SEM	1,878	3,813	5,974

Figure 9.13. Mean step-height values and calculated expanded uncertainties for the case of measurements performed on the three-step heights artefact. Calibrated values, obtained by using a reference stylus instrument (FTS) are compared with the ones obtained by measuring with an Infinite Focus instrument (IF) and from 3D-SEM reconstructions performed using MeX Alicona. For these two measuring techniques, the calculated expanded uncertainty (k=2) was corrected taking into account the presence of systematic errors.

The mean step-height values, calculated from measurements performed by means of the Infinite Focus from Alicona, were shown to be in agreement with the reference ones, taking into account the resulting expanded uncertainty of the mean (k=2). The largest difference, in the mean values, was observed to be about 6% for the case of the BC step-height, which was also the one with the highest expanded uncertainty evaluated (*i.e.* 382 nm). Comparing the resulting step-height mean values and expanded uncertainties for the case of 3D-SEM reconstructions, to the ones obtained from the calibration by means of FTS, the following considerations can be made:

- The mean step-height value, calculated from 3D-SEM reconstructions, for the three steps AB, BC and AC, show a systematic underestimation compared to the calibrated values.

- The expanded uncertainty (k=2) of the mean value, was calculated to be dependant on the step-height. Since the uncertainty due to the resolution and to the surface roughness, were constant, the difference, which is in the order of about 15 nm, is due to the measurements reproducibility, when the systematic error compensation is not considered.

- The relative expanded uncertainty $U(z)/z$, calculated by dividing the calculated expanded uncertainty for the mean step-height value, is in the order of 8.3% for the smallest step AB, of 4.0% for the step BC and 2.4% for the highest step AC.

- The expanded uncertainty for the case of step-heights measurements performed using 3D-SEM technique, can be reduced by performing stereo-pair reconstructions starting from SEM images acquired at higher magnification (*e.g.* 5000x). In this case, in fact, the vertical resolution is decreasing, leading to a decrease in the u_{res} uncertainty contributor. Another possibility would be to increase the number of replicated reconstructions, using MeX, and to increase the number of experiments from which calculating the mean step-heights, to decrease the uncertainty contributor due to the reproducibility (u_s). The systematic error should be also compensated whenever possible.

For the case of measurements performed on the five step-heights calibration artefact, two different graphs were produced, one showing the mean calculated values and the expanded uncertainty for the higher steps AB and AE (Fig.9.14) and one for the smaller steps BC, CD and DE (Fig.9.15). The mean step-height values, calculated from measurements performed by means of the Infinite Focus from Alicona, were shown to be always smaller when compared to the reference ones, except for the case of the BC step-height calculation. The uncertainty budget lead to expanded uncertainties ranging from 100 nm to 180 nm, where the uncertainty due to the measurements reproducibility was found to be the most influencing contributor, when the uncertainty due to the systematic error compensation is not considered.
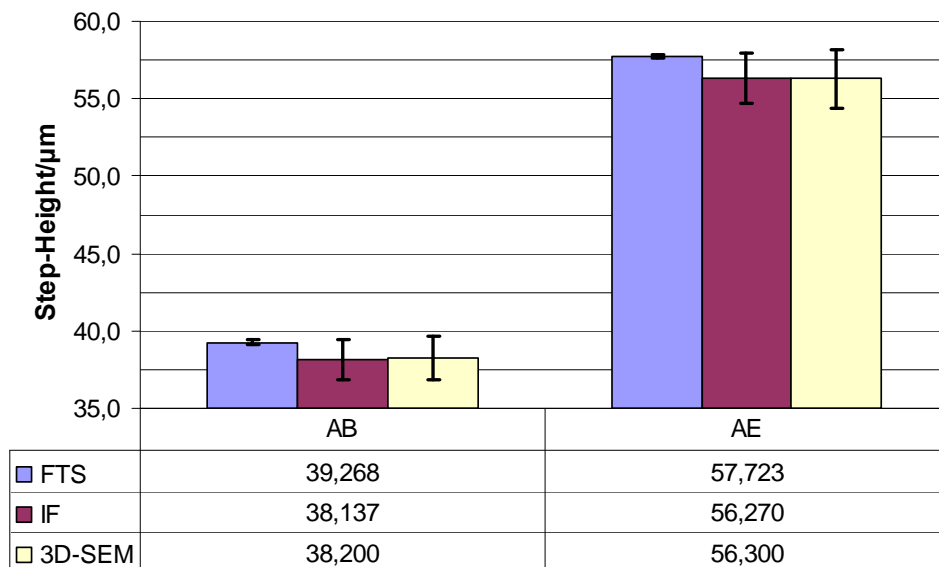
	AB	AE
◻ FTS	39,268	57,723
◼ IF	38,137	56,270
◻ 3D-SEM	38,200	56,300

Figure 9.14. Mean step-height values and calculated expanded uncertainties for the case of measurements performed on the steps AB and AE of the five - step heights artefact. Calibrated values, obtained by using a reference stylus instrument (FTS) are compared with the ones obtained by measuring with an Infinite Focus instrument (IF) and from 3D-SEM reconstructions performed using MeX Alicona. For these two measuring techniques, the calculated expanded uncertainty (k=2) was corrected taking into account the presence of systematic errors.

	BC	CD	DE
■ FTS	11,202	4,035	3,225
■ IF	11,295	3,762	2,843
□ 3D-SEM	10,383	3,331	2,708

Figure 9.15. Mean step-height values and calculated expanded uncertainties for the case of measurements performed on the steps BC, CD and DE of the five -step heights artefact. Calibrated values, obtained by using a reference stylus instrument (FTS) are compared with the ones obtained by measuring with an Infinite Focus instrument (IF) and from 3D-SEM reconstructions performed using MeX Alicona. For these two measuring techniques, the calculated expanded uncertainty (k=2) was corrected taking into account the presence of systematic errors.
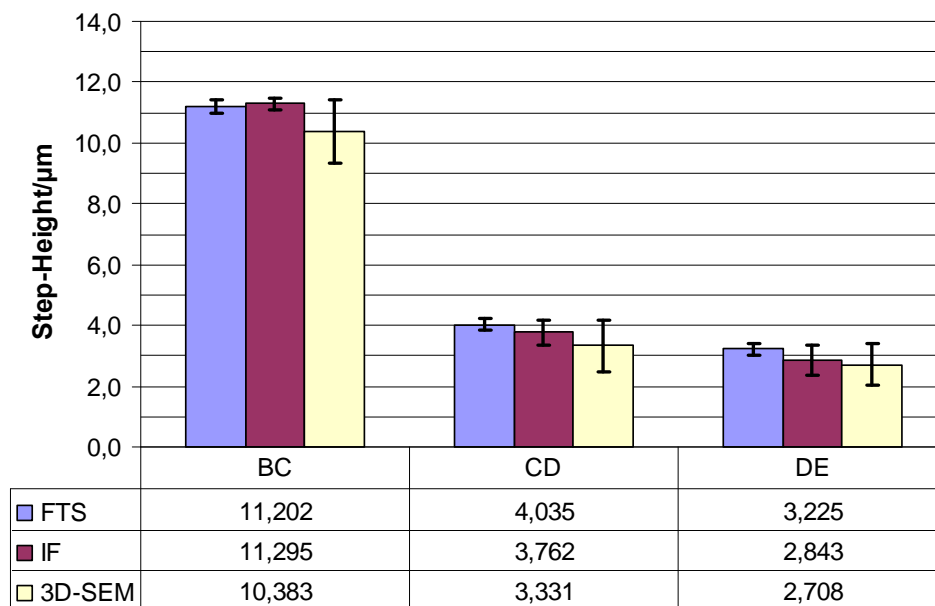
Comparing the resulting step-height mean values and expanded uncertainties for the case of 3D-SEM reconstructions, to the ones obtained from the calibration by means of FTS, the following considerations can be drawn:

- A systematic underestimation of mean step-height values is always present when comparing measurements performed using the 3D-SEM technique, with the reference ones by means of the FTS. Generally speaking, it can be observed that the higher the step-height the higher is this uncertainty of the systematic error correction. This is most likely due to the pixel size value set into MeX when performing the 3D reconstructions, as this affects the calculation of the parallax shift Δy, where $\Delta y=n*s$, being s the pixel size and n the number of pixels.

The parallax shift is proportional to the step height, to the working distance and to the tilt angle as it was shown in chapter 3, where the Piazzesi formula, for calculating the theoretical z-coordinate vertical elevation, in the case of stereo-pair reconstructions, was described;

- For this calibration artefact, consistent differences in the expanded uncertainty calculated values were observed for the different step-heights. In particular the expanded uncertainty ranges from a maximum value of about 1.9 μm for the highest step, to a minimum of about 0.7 μm for the smallest step. Since the uncertainty contributors u_{res} (related to the vertical resolution) and u_w (related to surface roughness) were the same for all the steps, the difference is due to reproducibility uncertainty u_s and to the systematic error compensation. It was observed that, as the step-height is decreasing, the uncertainty contributor u_s is also decreasing;

- The expanded uncertainty for the case of the five-step heights artefacts, resulting from measurements performed using 3D-SEM technique, can not be reduced by performing stereo-pair reconstructions starting from SEM images acquired at higher magnification. In fact, due to the high curvature radii, the reconstructions were performed at the highest possible M-value. Therefore, one possibility for reducing the expanded uncertainty would be to increase the number of replicated reconstructions, using MeX, and to increase the number of experiments from which calculating the mean step-heights, to decrease the uncertainty contributor due to the reproducibility (u_s). Moreover, the systematic error should be compensated whenever possible.

9.8 Five-step heights artefact machining by means of Focused Ion Beam technique

In the case of the five-step heights artefact for 3D-SEM calibration, the tool used for grinding had a radius of 50 μm, which guarantees roughness Sa<50 nm, but results in a radius of the workpiece concave edges of the same size of the tool radius. A Focused Ion Beam (FIB) milling was therefore implemented as a finishing operation, in order to improve surface geometry on concave edges, considering the AE step as a case study. FIB is a technique widely used in the semiconductor and materials science fields for site-specific analysis, deposition, and ablation of materials, using a focused beam of gallium ions to sputter and remove atoms away from a surface (Giannuzzi *et al.*, 2005). Although this technique is commonly used on soft materials such as silicon wafers, FIB machining can also be used as a micro-machining tool, to modify or remove materials at the micro- and nanoscale levels, though this is a new field of application that still needs developments. In this work a Quanta 3D lift-out from FEI Company, available at DTU CEN, was used, which is a versatile dual-beam Scanning Electron Microscope. The dual beam instrument enables FIB milling and SEM imaging without sample repositioning, through in-line sample measurements. The AE step-height curvature radius was previously estimated by means of the reference stylus profilometer FTS. The same curvature radius was also measured after FIB milling, to determine the machining capabilities of the dual beam instrument on the above-mentioned high speed steel. In Fig. 9.16, a SEM image of the AE step, seen from a side at M=1200x, is shown, where the curvature radius to the machining by means of FIB is visualized.
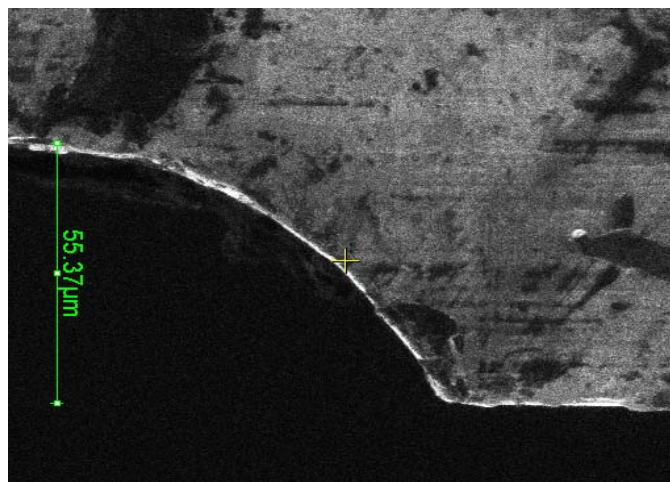

Figure 9.16. SEM image, acquired at M=1200x, showing the curvature radius between the planes A and E of the five-step heights artefact seen from the side.

A section of the curvature radius between A and E planes of the five-step heights artefact, was machined considering FIB milling capabilities and limitations. When a certain milling depth is set into the FIB software, every spot in the working window is lowered down by the same amount. This approach is therefore not feasible when milling is performed from the top for reducing local curvatures. In this case, in fact, a non constant material removal rate, depending on the feature's profile, is required, which up until now, is still not feasible with proper accuracy (Giannuzzi *et al.*, 2005). This effect is shown through a schematic representation in Fig.9.17, where two cases are presented. In the first one (Fig.9.17A) a constant material removed rate is set, in the second (Fig.9.17B), the area to be machined is divided into a number of smaller sections, each one machined using a different etching rate. A further problem that can be encountered when machining from the top, is that the removed material would also redeposit on the surface, affecting its quality. For these reasons it was decided to mill the curvature radius from the external side rather than from the top, as shown in Fig. 9.18.
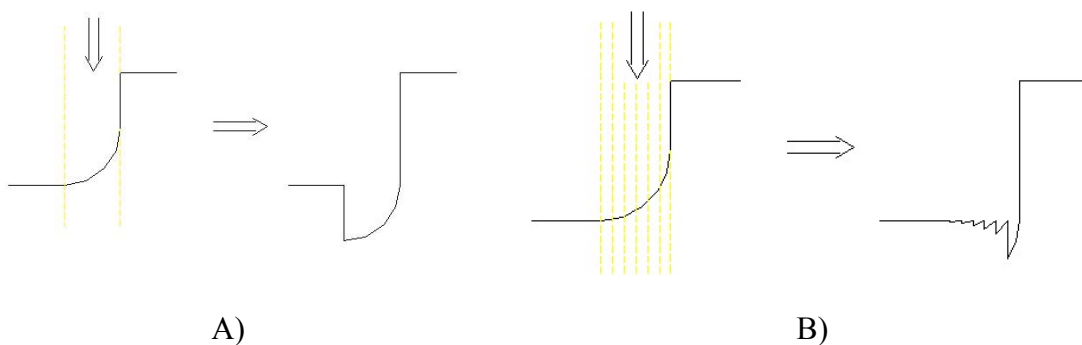

A)   B)

Figure 9.17. Schematic representation of the effects of FIB milling operation performed from the top. In the case (A) a constant material removed rate is set, in case (B) the area to be machined is divided into a number of smaller sections, each one machined using a different etching rate.
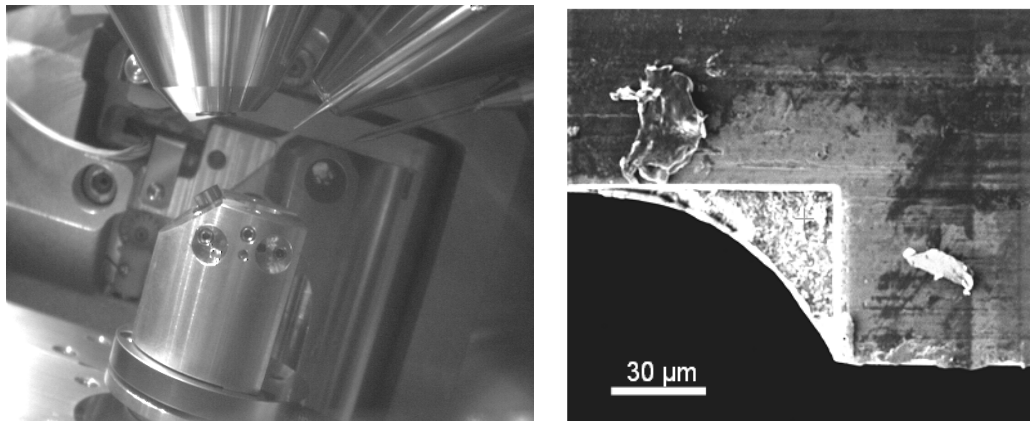
Figure 9.18. Five-step heights artefact positioning inside dual beam instrument chamber (left) and artefact milling viewed from a side with the FIB camera (right).

Different current intensity levels were tested for milling the surface, keeping the acceleration voltage at 30 kV and the spot size constant. After a series of optimization tests, current was set to 20 nA, achieving an etched depth of 10 μm in half an hour, which is an acceptable machining time at the nanoscale level. In order to improve the surface quality and machining accuracy, the current was subsequently lowered to 7 nA just along the corners to refine this area of interest.

After FIB machining, the part was measured using the stylus instrument and visually inspected using the dual beam SEM. A triangular section having a depth of about 10 μm was machined, where the 50 μm curvature radius, due to grinding, was reduced to about 2 μm by FIB milling. These results were estimated using the dual beam SEM, since the stylus profilometer could not properly measure these features due to the stylus tip radius and to its vertex angle (Fig.9.19). Implementation of Atomic Force Microscope technique, properly adapted for the difficultly accessible artefact region, is under study. The depth of the triangular section, machined with FIB, estimated with the dual beam SEM at 1600x is shown in Fig.9.20, where also the preliminary results, of a FIB milling operation, performed on DE step of the same artefact are shown. The work and the experimental results, presented in this section, where published in a paper by the author (Carli *et al.*, 2009).
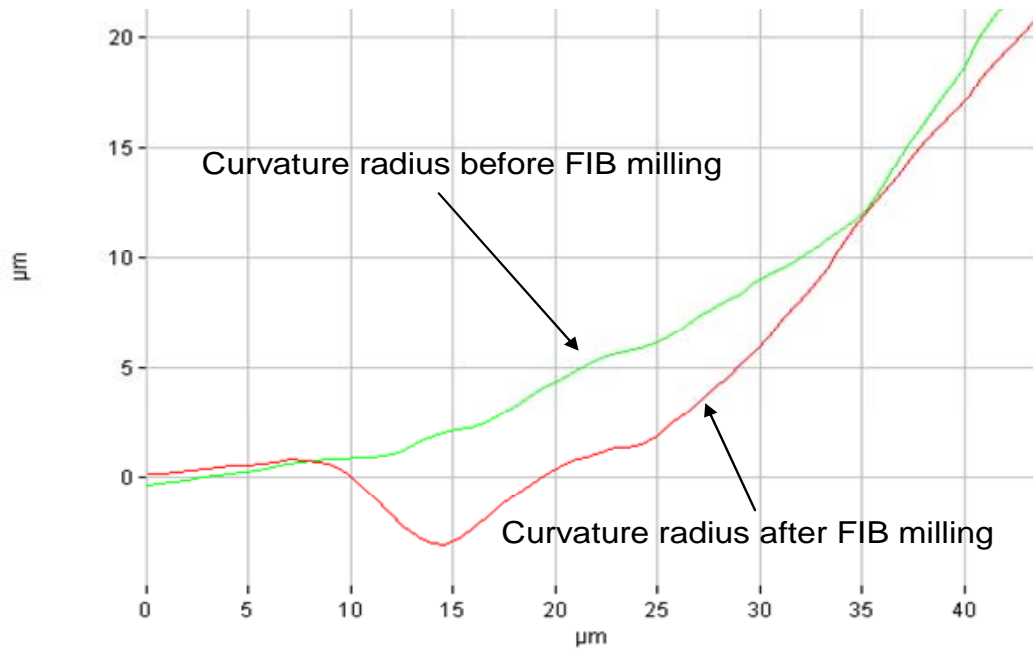
Figure 9.19. Comparison of 2D profiles of the curvature radius measured with the stylus instrument before and after FIB milling.
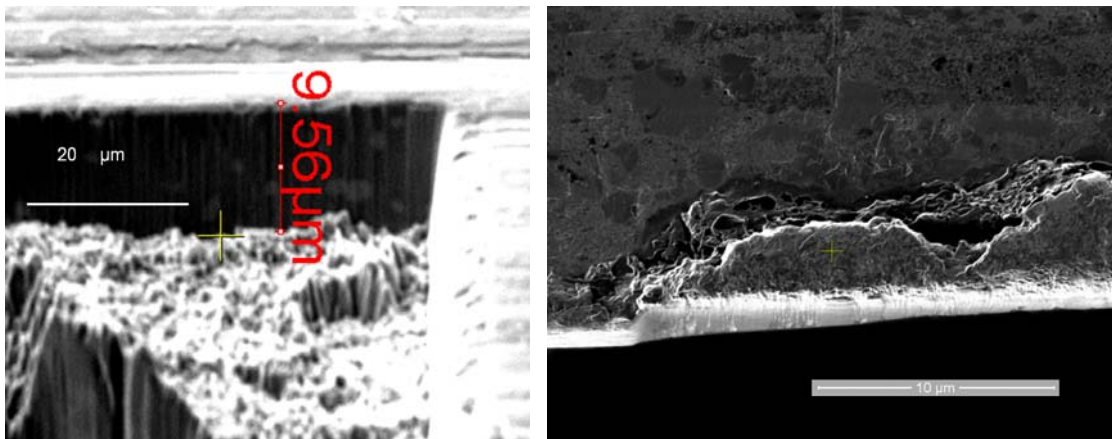

Figure 9.20. Depth of the triangular section, machined with FIB, estimated with the dual beam SEM at 1600x (left) and qualitative inspection of the results of a FIB milling operation, performed on DE step of the five-step heights artefact (right).

9.9 Summary and conclusions

This chapter deals with the fabrication, calibration and application of two novel artefacts for 3D-SEM calibration. These two artefacts encompass the presence of a central point, located at the intersection of microscope optical axis (z-axis) and the reference x-y plane (SEM focal plane). The first artefact, a five-step heights staircase geometry, was fabricated using grinding technology, while the second one, a three-step heights, was designed and manufactured using an Electrical Discharge Machining (EDM) process. After the fabrication, the artefacts were calibrated using a reference stylus profilometer (FTS). The applicability of the two calibration artefacts for 3D-SEM reconstructions was tested and verified. This measuring technique led to 3D-recontructions of the artefacts, enabling the extraction of multiple profiles in order to calculate the different step-heights. An uncertainty evaluation was performed taking into account the different error sources taking place when performing stereo-pair reconstructions. The mean step-heights values, calculated from 3D-SEM measurements, were compared to the ones obtained with the reference ones and with measurements performed using an Infinite Focus instrument. The milling capabilities of the Focused Ion Beam technique, performed on the AE step of the five step-heights artefact, were visually inspected using the dual beam SEM imaging and measured using the stylus instrument to establish traceability. A triangular section having a depth of about 10 μm was machined, where the 50 μm curvature radius produced by grinding was reduced to about 2 μm by FIB milling.

The main results of the mean step-height calculation and of the uncertainty budget, performed from measurements carried out by means of the FTS, the Infinite Focus and the 3D-SEM were the following.

Considering the <u>three step-heights</u> artefacts:

- The mean step-height values, calculated from measurements performed by means of the Infinite Focus from Alicona, were shown to be in agreement with the reference ones, taking into account the resulting expanded uncertainty of the mean (k=2). The largest difference, in the mean values, was observed to be about 4% for the case of the BC step-height, which was also the one with the highest expanded uncertainty evaluated (*i.e.* 382 nm);

- The mean step-height value, calculated from 3D-SEM reconstructions, for the three steps show a systematic underestimation compared to the calibrated values. This underestimation is in the order of about 16 %, 3.8% and 2.3% for the decreasing step-heights mean values respectively;

- The expanded uncertainty (k=2) of the mean value, calculated for the three steps, and corrected by the uncertainty due to the systematic errors, resulted in a difference ranging from about 500 nm to 300 nm.

Considering the <u>five step-heights</u> artefacts:

- The mean step-height values, calculated from measurements performed by means of the Infinite Focus from Alicona, were shown to be always smaller when compared to the reference ones, except for the case of BC step-height calculation. The uncertainty budget lead to expanded uncertainties ranging from 100 nm to 180 nm, where the uncertainty due to the measurements reproducibility was found to be the most influencing contributor, when the uncertainty due to the systematic error compensation is not considered;

- A systematic underestimation of mean step-height values is always present when comparing measurements performed using the 3D-SEM technique, with the reference ones by means of the FTS. In particular, this underestimation is ranging from 2.5% for the highest AB step to 16% for the smallest DE step;

- For this calibration artefact, consistent differences in the expanded uncertainty calculated values were observed for the different step-heights. In particular the expanded uncertainty is ranging from a maximum value of 1.9 μm for the highest step, to a minimum of about 0.7 μm for the smallest step.

For both the proposed calibration artefacts, the expanded uncertainty deriving from the 3D-SEM technique, can be reduced by performing stereo-pair reconstructions starting from SEM images acquired at higher magnifications (*e.g.* 5000x) to reduce the uncertainty related to the vertical resolution. Another possibility would be to increase the number of replicated reconstructions and the number of mean step-heights calculation, to decrease the uncertainty contributor due to the reproducibility. Moreover, the uncertainty due to the systematic error compensation could be reduced by performing a compensation of the bias.

References

Bariani P. Dimensional metrology for microtechnology. Ph.D. Thesis, Department of Manufacturing Engineering and management. Technical University of Denmark, 2005.

Bariani P, De Chiffre L, Hansen HN, Horsewell A. Investigation on the traceability of three dimensional scanning electron microscope measurements based on the stereo-pair technique. *Precis. Engineering* 2005; **29**: 2319-228.

Carli L., MacDonald A.N., De Chiffre L., Marinello F., Carmignato S., Horsewell A. Development of Focused Ion Beam technique for high speed steel 3D-SEM artefact fabrication. Proc.of the 9th euspen Int. Conference, Vol. 2, pp. 295-298, 2009.

De Chiffre L, Bariani P, Sobiecki R, Hansen HN, Horsewell A. A Means for Calibrating a Microscope, a Method of Preparing the Means, and a Method of Calibrating a Microscope, Patent Application, 2004.

EN ISO 5436-1:2000 (German version). Geometrical Product Specifications (GPS) - Surface texture: Profile method; Measurement standards - Part 1: Material measures (ISO 5436-1:2000).

EN ISO 4287:1998 (German version). Geometrical Product Specifications (GPS) - Surface texture: Profile method - Terms, definitions and surface texture parameters (ISO 4287:1997).

Giannuzzi L.A., Stevie F.A. Introduction to focused ion beams: instrumentation, theory, techniques and practice. Springer edition, 2005.

ISO 5436-1:2000. Geometrical Product Specifications (GPS) -Surface texture: Profile method; Measurement standards -- Part 1: Material measures, ISO, 2000.

ISO/TC 213, ISO/TS 14253-2. Geometrical Product Specifications (GPS) – Inspection by Measurement of Workpieces and Measuring Equipment – Part 2: Guide to the Estimation of Uncertainty in GPS Measurement, in Calibration of Measuring Equipment and in Product, ISO, 1999.

ISO/TS 15330-3, Geometrical Product Specifications (GPS) -Coordinate measuring machines (CMM): Techniques for determining uncertainty of measurements – Part3: Uncertainty assessment using calibrated workpieces, ISO, 2004.

JCGM (Joint Committee for Guides in Metrology)100:2008. Evaluation of measurement data - Guide to the expression of uncertainty in measurement (GUM), 2008.

MeX^{TM} v 5.1. Alicona Imaging, 2007.

Ritter M, Hemmleb M, Sinram O, Albertz J, Hohenberg H. A versatile 3D calibration object for various micro-range measurement methods *Proc. 22nd ISPRS Congress* 2004*;* **25**: 696–701.

Ritter M, Dziomba T, Kranzmann A, Koenders L. A landmark-based 3D calibration strategy for SPM. *Meas. Sci. Technol.* 2007; **18**: 404-414.

Santin D. Tracebility of 3D-SEM. Ms.C. Thesis, Department of Manufacturing Engineering and management. Technical University of Denmark, 209.

Schroettner H, Schmied M, Scherer S. Comparison of 3D Surface Reconstruction Data from Certified Depth Standards Obtained by SEM and an Infinite Focus Measurement Machine (IFM). *Microchimica Acta* 2006; **155/1-2**: 279-284.

Sinram O, Ritter M, Schertel A, Hohenberg H, Albertz J. Ein neues Kalibrierobjekt für die Elektronenmikrophotogrammetrie *Photogrammetrie–Fernerkundung Geoinformation* 2002b; **6**: 435-441.

SX-200-HPM, technical specifications and performances. http://sarix.com, 2010.

Trevisan A. Uncertainty evaluation for 3D-SEM reconstructions. Ms.C. Thesis, Department of Manufacturing Engineering and management. Technical University of Denmark, 2010.

Tso PL, Lu CC. Study on the grinding of P/M high speed steel ASP60. *Int. J. Machine Tools and Manufacture* 1999; **39/4**: 627-638(12).

United States Patent; patent number 6028008.

VDI/VDE guideline 2656: Determination of geometrical quantities by using of Scanning Probe Microscopes - Calibration of measurement systems.Technical Division Measurement Technology, 2008-6.

Vorburger TV, Song JF, Renegar TB, Zheng A. Nist surface roughness and step height calibrations. *Measurement Conditions and Sources of Uncertainty*, 2008.

10. Conclusions

10.1 Summary

In this work an investigation was carried out concerning 3D-SEM metrology as a tool for coordinate measurements at the nanometer scale. The relevance of 3D-SEM technique was highlighted, with respect to the other measuring instruments nowadays available for micro and nano-metrology. The latter were also described pointing out main advantages and limitations of the different measuring instruments and techniques.

The importance of multi-sensor and multi-orientation strategy for geometrical reconstructions at the micro and nanoscale was discussed through an experimental example, together with point cloud stitching methodology and the most recent algorithms for feature extraction. In particular, a measuring strategy based on object rotations, performed by the SEM stage, was proposed and implemented, which allows acquiring multi-orientation views of the item to be measured. These multiple-views can then be stitched together using one of the three different approaches described: positioning system as a reference, workpiece as a reference or external reference (fiducial marks).

The main phases involved when stereo-pair technique methodology, based on two SEM images obtained by tilting or rotating the SEM stage of a desired amount, is performed, were described underling the most relevant error sources in the case of 2D and 3D-SEM metrology. In particular, the following sources of uncertainty were considered for their influence on 3D-SEM reconstructions: point cloud processing and feature extraction, instrument setting parameters and image quality. Moreover, a comparison of the results obtained through a theoretical and an experimental uncertainty evaluation of stereo-pair technique was performed. Each of these uncertainty contributors were discussed in separated chapters of this thesis. As a result, a final uncertainty budget table was produced for the case of multi-orientation reconstructions obtained by applying 3D-SEM technique to three cylindrical items: two reference wire gauges and a hypodermic needle.

The fabrication, calibration and application of two novel multiple-step heights artefacts for 3D-SEM calibration, was also addressed. These artefacts are intended for the z-coordinate calibration, which is a crucial issue when performing measurements on 3D reconstructions obtained by employing stereophotogrammetry technique. The key concept of the two artefacts proposed in this work is that they encompass the presence of a central point, that is located at the intersection of microscope optical axis (z-axis) and the reference x-y plane (SEM focal plane). Therefore, they allow SEM measurements at different magnifications and different working distances, without requiring artefact relocation. The step-heights values, calculated from 3D-SEM measurements, were compared to the ones obtained by means of a calibration procedure, carried out using a reference stylus profilometer, and with measurements performed using an Infinite Focus instrument.

10.2 Achievements

The main challenges to be addressed when performing stereophotogrammetry technique were identified and described in the first chapter of this work. The experimental investigations and the analysis performed in this thesis were therefore aimed contributing to solve the issues related to 3D-SEM technique. In this section the above mentioned challenges are summarized and the most relevant achievements of this thesis, related to them, are described.

1) The 3D reconstructions performed using stereophotogrammetry technique, result typically in a very dense point cloud. A point cloud post-processing procedure is then foreseen before carrying out feature extraction and measurements. In this work the following point cloud processing operations were discussed and investigated through the application of a case study, based on a cylindrical item: trimming, outliers removal, filtering, sampling and meshing. It can be concluded that, among the above mentioned post-processing operations, the point cloud trimming and the filtering are the most crucial ones, when aiming to perform feature extraction and measurements on a given object. Regarding the point cloud trimming operation, the influence of the operator results to be consistent as this procedure is usually carried out manually. Moreover, an improper filtering procedure may modify the shape of the given point cloud. A methodology was then proposed helping to address the issues concerning point cloud post-processing for a given measuring task, depending on the shape of the object to be measured.

It was also proven that different software for feature extraction, because of the implementation of different algorithms, lead to consistent differences when measuring the size of the feature. For the case study considered, a wire gauge with a reference diameter of 250 μm, a maximum difference of 1 μm were observed when measuring the diameter, from the same point cloud using three commercial software. Among these three ones, one was a Matlab routine developed by the author;

2) When employing 3D-SEM technique a number of factors are influencing the ability of the software performing stereo-pair reconstruction. Among these, the <u>SEM image quality and the instrument setting parameters</u> were considered as uncertainty contributors. A methodology was proposed to determine the optimum setting of the instrument parameters, in terms of accelerating voltage, spot size and magnification, when acquiring SEM images to be later used for stereophotogrammetry technique. These parameters were demonstrated to affect not only the image formation process and the resolution, but also the pixel nonlinearity, i.e. the mean position error of the pixels composing the SEM image. Considering SEM image quality, it was demonstrated that an improper setting of brightness and contrast influences the 3D reconstructions, leading to a standard deviation of the experimentally calculated diameter in the order of 0.3 μm. Moreover, the presence of noise was proven to influence the ability of the software, performing stereo-pair technique, to find the corresponding features in the two images composing the stereo-pair;

3) For a given measuring task, the uncertainty related to stereophotogrammetry technique can be evaluated through a theoretical and an experimental approach. This investigation was carried out in accordance to ISO GUM considering a wire gauge with reference diameter of 250 μm, as a case study. The <u>theoretical uncertainty evaluation</u> was performed starting from a modified version of Piazzesi's equation, enabling the calculation of the z-coordinate from a given stereo-pair. Metrological characteristics of each input variable (p, n_1, n_2, d and $\Delta\varphi$) were taken into account, and the uncertainty, in terms of bias, resolution and reproducibility for each variable was calculated. Moreover, a calibration of the SEM stage performances in terms of tilting and rotation was performed. An expanded uncertainty of 6.5 μm was evaluated for the case of SEM stage rotation, and of 4.3 μm for the case of tilting. The uncertainty was calculated considering the wire gauge radius (i.e. 125 μm), therefore it can be concluded that a relative uncertainty is equal to about 5.2% and 3.4% for the two cases respectively.

An <u>experimental uncertainty evaluation</u> was also carried out, considering the three input parameters requested by the software for stereo-pair reconstructions: the pixel size, the working distance and the tilt (or rotational) angle. It was proven that, in the case of stereo-pair reconstructions performed at a magnification M=1000x, the uncertainty related to the pixel size is the most relevant one, accounting for about 60% of the experimental uncertainty, followed by the uncertainty of the rotational angle. The uncertainty due to the working distance was found to be negligible. A final uncertainty table was produced taking into account all the uncertainty sources described above, for the case of 3D-SEM reconstructions performed on three cylindrical items. The experimental values of the diameter was calculated from a series of 3D reconstructions performed using the multi-orientation strategy, i.e. by rotating the cylindrical item around its main axis on the SEM stage. The uncertainty due to the measuring procedure, the non-eucentricity and the object's topography, were then quantified and included in the uncertainty evaluation. The expanded uncertainties for the case of the two wire gauges with a reference diameter of 250.0 μm and 260.0 μm and for the hypodermic needle with a calibrated diameter equal to 259.7 μm were calculated to be 1.2 μm, 1.6 μm and 2.0 μm respectively;

4) The <u>z-coordinate calibration</u> in SEM is a crucial issue to establish measurement traceability. Nevertheless, none or few reference artefacts are nowadays available for calibration and performance verification of 3D-SEM technique. In this work two multiple-step heights artefacts, intended for 3D-SEM calibration, were fabricated using grinding and EDM technique and calibrated by means of a reference stylus profilometer to establish traceability. An uncertainty evaluation was performed on the step-heights measurements performed from 3D-SEM reconstructions of both the calibration artefacts. The following results were obtained:

- Considering the <u>three step-heights</u> artefacts, the expanded uncertainty of the mean value, calculated for the three steps, after the systematic error compensation, resulted in a difference ranging from about 500 nm to 300 nm.
- Considering the <u>five step-heights</u> artefacts consistent differences in the expanded uncertainty calculated values were observed for the different step-heights. In particular the expanded uncertainty is ranging from a maximum value of 1.9 μm for the highest step, to a minimum of about 0.7 μm for the smallest step.

A procedure for reducing the uncertainty, deriving from 3D-SEM reconstructions of the two calibration artefacts, was proposed.

10.3 Proposal for future work

Some suggestions for future work in the field of 3D-SEM metrology are given below, based on the experience gained by working at this Ph.D. project within the last three years.

- In this work SEM image quality was proven to be liable of affecting 3D-SEM reconstructions. Thus, a procedure for defining a numerical "quality factor" for a given image should be developed. It would then be possible to quantify the different effects by converting image characteristics into a number. This would allow, for instance, to determine whether two given SEM images are usable for performing a stereo-pair reconstruction or if their overall quality should be improved;

- The possibility of performing point cloud stitching was envisaged in this work. Among the different stitching strategies described in this work, i.e. positioning system as a reference, workpiece as a reference or external reference, only the workpiece based one seems to be feasible in the case of 3D-SEM technique. Thus, the surface topography of the item to be measured plays a relevant role for achieving this goal. In particular, the size and number of the features on the external surface is responsible for affecting the quality of the resulting point cloud stitching operation. For this reason the object' s topography could be machined by means of Focused Ion Beam technique to leave some reference marks which could later used for superimposing the two SEM images forming the stereo-pair;

- The uncertainty table, produced for the case of rotations and tilting, resulting from the theoretical uncertainty evaluation of the stereo-pair technique, was based on a case study. As the metrological characteristics of each input variable were already calculated in this work, it would be relevant to extend this approach, making it more general. For instance, given a measuring task, it should be possible to theoretically calculate the estimated expanded uncertainty. Moreover, efforts should be made to improve the calibration of the SEM rotary stage;

- Two artefacts for 3D-SEM calibration were fabricated and calibrated in this work. A number of reconstructions were performed using 3D-SEM technique to investigate the applicability of these two artefacts and step-height measurements were also performed by means of an infinite focus instrument. The height of the steps for the smaller calibration artefact, with nominal

values of 7 μm, 5 μm and 2 μm, will be in the nearest future measured by means of an atomic force microscope. Moreover those artefacts will be employed for carrying out a performance inter-comparison of the newly developed small and ultra-precision CMMs.

- A new variant of the staircase artefact has been designed and developed for calibration of the height in 3D microscopy by making it possible the application of ISO 5436. The artefact is suitable for transferring traceability to 3D techniques at the micrometer and nanometer scale, e.g. 3D SEM, confocal microscopes etc. The design comprises three different step heights, featuring four, nominally equal, common vertical axes (see Fig.10.1). Two different series of samples were fabricated using EDM technique with three steps of 2, 5 and 7 μm, and 20, 50 and 70 μm, respectively, from a 3 mm diameter carbide wire. The artefact steps will be calibrated on a stylus instrument according to ISO 5436 and measured on a number of 3D microscopes.
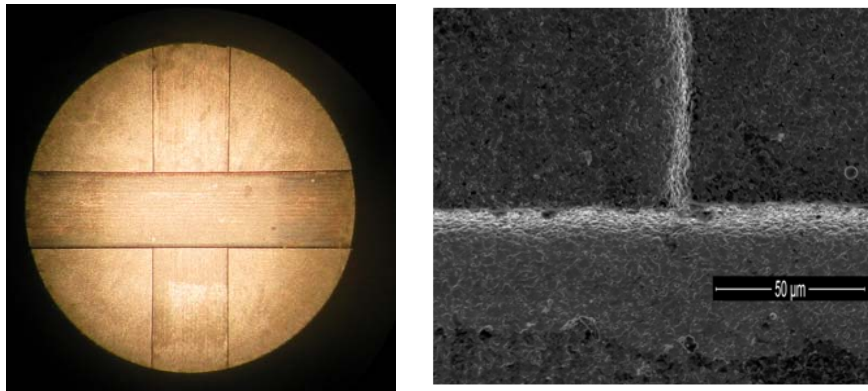
Figure 10.1. Image showing the multiple height calibration artefact for 3D microscopy (left) and a SEM image at 2000x magnification showing the three steps converging in a common point (right).